Discrete dislocation dynamics modelling of hexagonal close-packed zirconium



Daniel Hortelano Roig

St Anne's College

University of Oxford

A thesis submitted for the degree of

Doctor of Philosophy

Trinity 2025

Acknowledgements

A competent PhD thesis is certainly expected to contain stories reflecting generations of diligent investigation and knowledge acquisition. However, this thesis cannot tell the stories of its author. It will not tell of the metamorphic ailments developed throughout, and the consequent fostered impotence and apathy. It will not tell of the years spent in criminal idle. It will not tell of the glimpses of humanity or of God felt through tempered steel. But it must be written – and I have written it.

Publications

The following publications are related to—or have arisen from—this thesis.

Directly related:

- **Daniel Hortelano-Roig**, Rakesh Kumar, Daniel S. Balint, and Edmund Tarleton. Discrete dislocation dynamics simulations of $\langle a \rangle$-type prismatic loops in zirconium. *International Journal of Plasticity*, December 2023. [1]

Moderately or slightly related:

- **Daniel Hortelano-Roig**, Alan Xu, Dhriti Bhattacharyya, Mujan Seif, and Edmund Tarleton. Homogenised dislocation plasticity modelling of micron-scale constitutive relationships under uniaxial loading in hexagonal close-packed zirconium. *In preparation.*
- **Daniel Hortelano-Roig** and Edmund Tarleton. Investigations of linear drag-based dislocation mobility laws and their influence on macroscopic response in zirconium. *In preparation.*
- Rakesh Kumar, **Daniel Hortelano-Roig**, Edmund Tarleton, and Daniel S. Balint. A discrete dislocation plasticity study of irradiation hardening in zirconium alloys. *In preparation.*

Contents

1 Introduction **1**

1.1 Models of plasticity 1

1.2 Zirconium: a crucial nuclear material 3

1.3 Materials modelling 6

2 Literature review **11**

2.1 Deformation modes of zirconium 11

2.2 Prismatic loops and irradiation hardening 14

2.3 Large-scale dislocation dynamics modelling 17

3 Model formulation **23**

3.1 Elements of dislocation dynamics 23

3.2 Forces 25

3.3 Mobility laws 31

3.4 Time integrators 36

3.5 Topological operations 38

3.5.1 Remeshing 39

3.5.2 Collisions 40

3.5.3 Separations 41

3.6 Finite domain simulations 43

3.6.1 DD-FEM coupling 43

3.6.2 Surface exit of dislocations 44

3.6.3 Dislocation-induced displacements 46

4 HCP mobility law **49**

4.1 HCP crystallography 49

4.2 Dislocation kinematics 52

4.2.1 Drag tensor construction 52

4.2.2 Segment decomposition algorithms 57

4.2.3 Drag tensor conditioning . . . 64
4.3 Model extensions and investigations . . . 66
4.3.1 Drag tensor interpolation schemes . . . 66
4.3.2 Resolved drag coefficient distributions . . . 67
4.4 Free spatial distributions of dislocation loops . . . 78
4.4.1 Problem description . . . 78
4.4.2 Analytical relationships between drag functions and spatial dislocation distributions . . . 80
4.4.3 Simulation results and analyses . . . 86
4.5 Conclusions and future work . . . 95

5 A 2.5D model of irradiation hardening 97
5.1 Representations of prismatic loops . . . 97
5.2 The dislocation-loop interaction . . . 107
5.3 Prismatic loop dynamics and stability analysis . . . 112
5.3.1 Segment-segment interactions . . . 115
5.3.2 Core restoring force . . . 117
5.3.3 Double super-jog dragging effect . . . 123
5.3.4 Elastic restoring force . . . 125
5.3.5 Total restoring force . . . 126
5.4 Investigations using the 2.5D DDP model . . . 127
5.4.1 Loop stability analysis . . . 128
5.4.2 Restoring force and loop density effects on flow stress . . . 133
5.5 Conclusions and future work . . . 135

6 Simulations of zirconium tensile tests 139
6.1 Dislocation junctions . . . 139
6.2 Methodology . . . 151
6.2.1 Experimental setup . . . 151
6.2.2 Simulation setup . . . 155
6.2.3 Bug mitigation . . . 163
6.2.4 Computer codes and algorithms . . . 171
6.3 Tensile simulations . . . 178
6.3.1 Basal-prismatic slip . . . 183
6.3.2 Pure prismatic slip . . . 189
6.4 Conclusions . . . 199

7 Conclusion **203**

A A level set approach for investigating dislocation evolution **207**

A.1 Mathematical framework 207

A.2 Example: a self-similarly evolving superelliptical loop 209

Bibliography **212**

List of Symbols

The following notation holds unless otherwise specified.

Computational variables

Δt	Time-step size
Δt_0	Maximum allowed time-step size
$A_{\max}$	Maximum allowed area formed by three consecutive nodes
$A_{\min}$	Minimum allowed area formed by three consecutive nodes
$L_{\max}$	Maximum allowed segment length
$L_{\min}$	Minimum allowed segment length
r_c	Isotropic core spreading radius
r_{ann}	Annihilation distance between segments
$r_{\max}$	Maximum allowed nodal travel distance
r_{tol}	Maximum allowed nodal error based on velocity gradient

Mathematical notation

$\hat{\boldsymbol{V}}$	Normalised (or unit) vector $\boldsymbol{V}$
$\max(a, b, \ldots)$	Maximum among the values a, b, etc.
$\min(a, b, \ldots)$	Minimum among the values a, b, etc.
$\{v_j\}$	Set composed of elements v_j
$x \in V$	x is an element of the set V
$\boldsymbol{\nabla}$	Vector differential operator

$\dot{V}$	Time derivative of $V(t)$
$\mathbb{R}^n$	Vector space of dimension n over field of real numbers
$\otimes$	Outer product operator
$A \Rightarrow B$	Statement A implies statement B

Physical constants

μ	Shear modulus
ν	Poisson's ratio
a, c	HCP lattice parameters
b	Burgers vector magnitude
E_c^s	Core energy per unit length of a screw dislocation

Chapter 1

Introduction

1.1 Models of plasticity

A theoretical formulation for elastic field distortions generated by a particular class of linear crystallographic defects—so-called *dislocations*—was first developed by Vito Volterra in 1907 [2]. In 1934, Sir Geoffrey Ingram Taylor, Egon Orowan, and Michael Polanyi [3, 4, 5] independently connected Volterra's theory to observations of non-reversible shape changes in crystalline solids (i.e. *plastic deformation*), and correctly proposed that the motion of dislocations was one mechanism responsible for material properties of plasticity. Building on these insights, the elastic theory of curved dislocations was developed by several authors, most notably the displacement field equation by Burgers in 1939 [6], the stress field equation by Peach and Koehler in 1950 [7], and the interaction energy equation by Blin in 1955 [8]. Furthermore, advancements to the transmission electron microscope (TEM) led to the first nano-scale experimental observation of dislocations by Hirsch and others in 1956 [9]. Since then, TEM [10] and various other imaging methods such as X-ray topography [11] and etch-pit techniques [12] have become fundamental tools in materials science for visualising dislocations and validating dislocation-based models.

Upon their discovery, dislocations provided microscopic explanations to pre-existing empirical theories of macroscopic plasticity, such as the one already formulated by von Mises in 1913 [13]. Understanding dislocation mechanics has enabled the mechanistic investigation of a wide range of important plastic phenomena that were previously observed but poorly understood, such as the Bauschinger effect [14], creep [15], crystal growth [16], and strain hardening [17]. Furthermore, this understanding has facilitated the study and development of a wide range of functional and structural materials with modern technological applications in fields such as architecture [18],

semiconductors [19], concrete structural analysis [20], and nuclear energy [21, 22], among many others.

Strain hardening is a phenomenon in which an increase in dislocation density corresponds to an increase in a material's strength and its resistance to deformation. An understanding of this process is crucial for accurately predicting the mechanical behaviour of materials. Strain hardening is therefore known as one of the most important problems in materials science, and also one of the most challenging in physics [23]. In general, hardening is understood to be caused by an increased resistance to dislocation motion, such as that arising from junction formation and other strengthening mechanisms. A large body of experimental evidence has validated a simple relationship between the material strength and the dislocation density, known as the Taylor hardening model [24], which is given by

$$\tau = \alpha \mu b \sqrt{\rho} \tag{1.1}$$

where τ is the flow stress required to sustain plastic slip, ρ is the dislocation density, μ is the shear modulus, b is the Burgers vector magnitude, and α is a dimensionless parameter associated with the particular hardening mechanism (and is typically approximately $0.2 - 1$). Here, α can subsume (in a phenomenological sense) various types of hardening mechanisms, such as dislocation pile-ups, tangles, jogs, and junctions [25].

When dislocations on non-coplanar slip systems interact—known as so-called *forest* interactions—a junction may form, which acts as a strengthening mechanism. Experimental [24, 26], analytical [27], and numerical [28, 29, 30, 31] studies have supported a strong association between forest interactions and strain hardening. Forest-related hardening can be modelled by a generalised Taylor hardening law [32] given by

$$\tau^i = \mu b \sqrt{\sum_j a_{ij} \rho^j} \tag{1.2}$$

where τ^i is the flow stress required to sustain plastic slip on slip system i, ρ^j is the dislocation density in slip system j, and a_{ij} is the so-called interaction coefficient corresponding to the interaction between slip systems i and j.

Because of its importance in materials science, various models have been developed to predict and explain hardening behaviour [33, 17, 34, 35]. Ideally, the development of a hardening law is grounded in at least a partial mechanistic understanding of the behaviours underlying macroscopic observations. Based on this understanding, appropriate laws can then be formulated. Hardening laws [36, 37, 38] form the

foundation of many macroscopic-scale models of plasticity [39], notably crystal plasticity (CP) [40, 38], which can, for example, be used to simulate irradiation-induced hardening in nuclear materials [41].

1.2 Zirconium: a crucial nuclear material

The UK Climate Change Act of 2008 aims to reduce the country's greenhouse gas emissions to net zero by 2050 [42]. In this effort, carbon-free nuclear power is a key contributor for future energy security in the UK. Safe, efficient, reliable, and long-term operational nuclear energy depends on the selection and development of appropriate structural and functional materials capable of withstanding the extreme environments inside a reactor. Nuclear materials must endure intense thermomechanical stresses, high neutron fluxes, and radiation-induced embrittlement, among other phenomena [43]. Although nuclear fusion research has advanced in recent years [44], it has yet to demonstrate a net-positive energy output at scale. As a result, nuclear fission remains the sole source of commercial nuclear power, and fission reactors therefore provide the primary motivation for the work presented in this text.

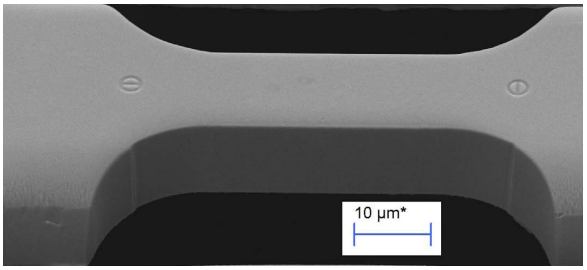
In a typical nuclear fission reactor, the radioactive fissionable material (such as uranium) is physically encapsulated in fuel cladding tubes, which are grouped into fuel assemblies. Large commercial reactors often contain on the order of 100 such assemblies, each comprising hundreds of individual fuel rods [45]. The fuel cladding itself forms the first structural barrier that both retains fission products and transfers heat to the surrounding coolant. Cladding materials must meet a demanding set of design criteria: low neutron absorption cross-section, microstructural stability, high thermal conductivity, low thermal expansion coefficient, and resistance to high temperatures, corrosion/oxidation, radiation, and thermal creep [46]. Various candidates have been proposed as nuclear cladding materials, such as stainless steels, ceramic materials, and refractory alloys [47, 46]. Zirconium (Zr) alloys have been found to be excellent for this purpose, and they are the primary components of the cladding material in the fuel assemblies of modern light water reactors (LWRs), which constitute the majority of all western nuclear power plants [48, 46, 49, 22].

Commercial nuclear-grade zirconium alloys typically consist of over 95% pure zirconium, with the remainder comprising various alloying elements added to improve mechanical strength, corrosion resistance, and other properties which enhance their application as cladding materials [50, 51]. Alloying elements incorporated in modern zirconium alloys include tin, niobium, oxygen, iron, sulfur, chromium, and nickel.

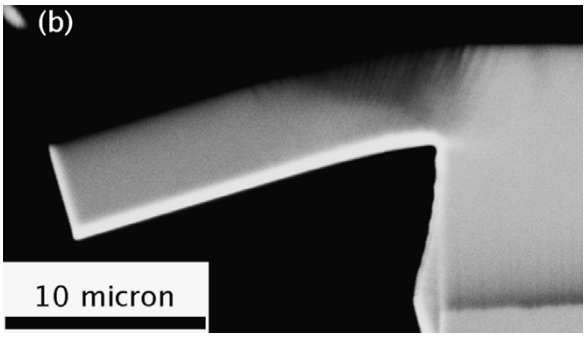
Due to the high zirconium content across these alloys, they are often assumed to share similar properties for some modelling purposes. The most commonly used alloys include Zircaloy-2 in boiling water reactors (BWRs), Zircaloy-4 and M5 in pressurised water reactors (PWRs), Zr–2.5Nb in Canada Deuterium Uranium (CANDU) reactors, and E635 in water-water energetic reactors (VVERs). More recent commercial alloys such as M5, Zirlo, and E635 have been specifically developed to further enhance in-reactor performance.

At normal LWR operating temperatures (less than approximately 700 K), Zr exhibits a hexagonal close-packed (HCP) α-phase [22]. HCP systems exhibit lower symmetries and a limited number of available slip systems compared to those of face-centred cubic (FCC) and body-centred cubic (BCC) systems, which complicates dislocation motion [52]. The situation is further confounded by reactor-specific phenomena that affect structural integrity, such as hydride precipitation [53] and radiation-induced formation of prismatic loop defects [54], which can lead to irradiation-related hardening and softening. Indeed, there is currently a lack of well-validated mechanistic models to predict failure of Zr-based fuel assemblies. To stay within safety margins, operators often remove fuel assemblies long before the fuel is fully expended, increasing costs and waste production. Therefore, improved understanding of Zr degradation—and, more broadly, of irradiation hardening mechanisms in HCP systems—is essential for the safe and effective operation of LWRs.

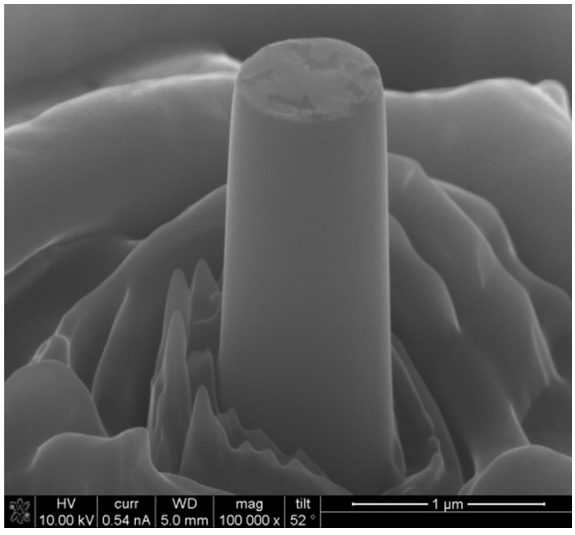
Ion irradiation can be used to replicate irradiation-induced dislocation structures, which avoids neutron-related transmutation while still having a similar effect on defect generation [58, 59]. This is often how experiments are used to study irradiation systems. However, ion penetration depth is generally too shallow to conduct traditional mechanical testing. As a result, micro-mechanical tests must be conducted on small material volumes such as micro-tensile samples, micro-cantilevers, and micro-pillars (see figure 1.1) [60]. Micro-mechanical tests also allow for the isolation of individual material constituents by, for example, investigating single crystal samples, thereby enabling mechanistic insights into the macroscopic behaviour of polycrystals [61]. However, small sample sizes introduce "smaller is stronger" size effects, which complicate the extrapolation of information gained from small-scale tests to bulk materials [62, 63, 64, 59, 65]. In practice, experiments must be combined with analytical and computational modelling approaches to fully understand irradiation-induced phenomena.



(a)



(b)



(c)

Figure 1.1: Examples of images of micro-mechanical samples. (a) TEM image of a dog-bone shaped micro-tensile sample (obtained from [55]) (b) scanning electron microscope (SEM) image of a bending micro-cantilever (obtained from [56]). (c) SEM image of a nano-pillar (obtained from [57]).

1.3 Materials modelling

Experiments provide insights into materials behaviour but are heavily limited with respect to delivering complete mechanistic models. On the other hand, computer simulations offer predictive and explanatory capabilities that are essential for investigating plastic phenomena and for developing robust materials models. However, no single computational model can capture behaviour seamlessly across all length and time scales: coarse-scale simulations may fail to describe fine-scale physics accurately, whereas fine-scale simulations can become prohibitively computationally expensive for large systems. Consequently, modern materials modelling adopts a multiscale approach, linking atomistic, mesoscopic, and continuum models to capture behaviour across multiple scales [66, 67]. The basic strategy is hierarchical: results from lower-scale models feed into higher-scale models, ultimately bridging from the single-atom scale up to complex multiphysics models of, for instance, designs of entire nuclear reactors [68].

At the smallest scales, *ab initio* approaches—which can model $10^2 - 10^3$ atoms—directly solve the Schrödinger equation, and include methods such as density functional theory (DFT) and Hartree-Fock theory [69]. Molecular dynamics (MD) simulations use empirical or semi-empirical potentials to model $10^6 - 10^9$ atoms, targeting length and time scales on the order of 10^{-9}m and 10^{-9}s; at most only a few dislocations can be simulated [70]. Dislocation dynamics (DD) simulations—which are the primary focus of this text—capture the mesoscopic-scale dynamics of dislocation networks, targeting length and time scales on the order of 10^{-6}m and 10^{-6}s. Crystal plasticity simulations capture the averaged effect of dislocation activity on polycrystalline plasticity, targeting length and time scales on the order of at least 10^{-3}m and 10^{-3}s [40, 38].

Continuum dislocation dynamics (CDD) theories—in which ensembles of discrete dislocation lines are averaged over space—were first developed in the 1950s, notably by Nye [71] and Kröner [72] in their tensorial descriptions of dislocation densities. CDD was eventually shown to encounter various theoretical issues associated with averaged representations of moving curved dislocations in three dimensions [73], although recent mathematical developments [74, 75] have led to a resurgence of interest; see [76] for a recent review. Despite these advances, most contemporary DD models continue to resolve individual dislocation lines explicitly, which is the modelling framework adopted throughout this text.

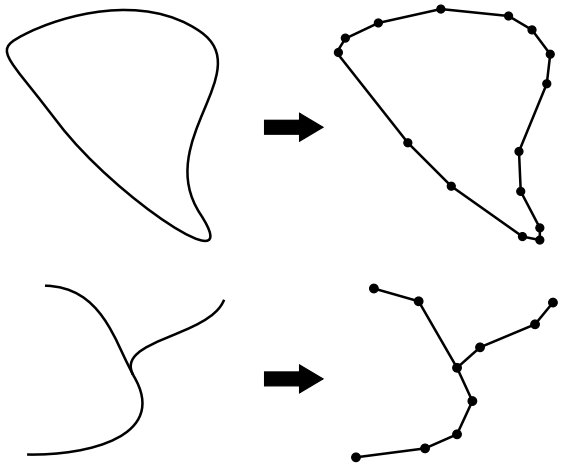


Figure 1.2: Schematic of examples of discretisations for a nodal-based DD model.

DD is a discrete model of material plasticity which treats dislocation line defects explicitly as discretised segments embedded within an elastic medium (see figure 1.2) [77, 78, 79]. It is designed to operate at a scale at which dislocation-mediated processes, such as strain hardening, can be directly probed to reveal mechanistic insights. DD simulations have proven valuable for investigating the role and/or origin of a variety of phenomena including junction formation [80], size effects [65], plastic strain localisation [81], cross slip [82], twinning [83], elastic instabilities of composite dislocations [84], and dislocation interactions with irradiation-induced defects [85]. DD simulations are typically conducted either in a finite domain via the finite element method (FEM) (see section 3.6), or by using periodic boundary conditions (PBCs), in which dislocation evolution is simulated in a computational cell which is repeated infinitely in every direction [86], effectively representing bulk domains. The latter has historically received the most attention in the literature [87, 81]. However, DD has also been useful in modelling finite domains such as during micro-pillar compression [88, 57, 89] and tension [90, 82], micro-cantilever bending [56, 65], and nanoindentation [91, 92].

There are currently various available 3D DD codes which can be split into two categories distinguished by their method of discretisation of dislocations. In lattice-based codes, dislocation lines are constrained to lie on a spatially fixed, Eulerian-style lattice that discretises the simulated volume [78]. In nodal-based codes—which are inherently more flexible to topological changes—dislocation lines are explicitly tracked as they evolve, and are represented as nodes connected by straight line segments (see figure 1.2). Lattice-based codes include TRIDIS [93], microMegas [94], and MobiDiC [95]. Nodal-based codes include micro3D [96], PARANOID [97], parametric DD [98],

MDDP [99], ParaDiS [100, 101, 102], El-Numodis [103], and, notably, the newly-released open-source code OpenDiS [104]. Throughout this text, 3D DD simulations are performed using EasyDD, which is a MATLAB-based code developed at the University of Oxford [105]. EasyDD uses a nodal-based discretisation, incorporates GPU acceleration, and is capable of modelling finite domains.

There are several computational challenges associated with the DD approach. Three-dimensional (3D) DD simulations must be capable of modelling complex physics at a mesoscopic scale [106]. Additionally, 3D DD must achieve a sufficient level of computational efficiency required to model plastic strains large enough to understand macroscopic bulk plastic deformation behaviour. 3D DD simulations have a large computational cost, making parallelisation essential for large-scale simulations. Directly computing the interactions between N dislocation segments is expensive, with order $\mathcal{O}(N^2)$ scaling. In addition, the number of nodes and segments must change during run-time in order to achieve a balance between accuracy and performance; finding the optimal topological operations can be challenging. Although advances in 3D DD have increased feasible plastic strains, most modern 3D DD simulations are only capable of achieving plastic strains of approximately 0.5% for a reasonable set of initial conditions [77, 101]. On the other hand, planar (2D) dislocation dynamics, often referred to as discrete dislocation plasticity (DDP)[1], tracks fewer degrees of freedom and is thus computationally faster. It is also inherently flexible with respect to boundary conditions and the inclusion of microstructures, and hence can be used to solve more complicated boundary value problems that may otherwise be inaccessible to 3D methods [107, 108, 65, 109]; dislocation structures and interactions are also more readily identified, elucidating mechanisms and scaling relationships.

At the time of writing, no studies have been identified which perform large-scale 3D DD simulations of HCP Zr that fully incorporate finite domains via FEM. Likewise, no studies have been identified which conduct large-scale DD simulations—neither 2D nor 3D—to investigate defect-induced irradiation hardening of Zr. This represents a significant gap in the literature, as the complex and anisotropic dislocation slip behaviour of Zr remains poorly explored at the mesoscopic scale, particularly under irradiation conditions. Building DD models capable of capturing critical aspects of dislocation-mediated phenomena of HCP Zr will therefore lay a foundation for future investigations of irradiation hardening. In chapter 2, a review of the literature

[1]Although DDP commonly refers to 2D simulations, it has also been used to refer to finite-domain 3D simulations.

is presented to contextualise and motivate the research problem. In chapter 3, a description of the 3D DD model is formulated. In chapter 4, a dislocation kinematic law for 3D DD simulations of HCP materials is developed and elucidated upon. In chapter 5, a 2.5D model is developed for the purpose of producing large-scale simulations of irradiation hardening. In chapter 6, 3D DD simulations are conducted to support experimental tensile tests of HCP zirconium, thereby building towards the first of these kinds of computational investigations.

Chapter 2

Literature review

2.1 Deformation modes of zirconium

In HCP materials, the most commonly observed Burgers vector is of type $\langle a \rangle = \frac{a}{3}\langle 11\bar{2}0 \rangle$ (see figure 4.1 for a visualisation of the HCP slip systems) [110]. In zirconium—and also in titanium (Ti), which exhibits similar deformation modes—the conditions for the activation of slip systems is a complex phenomenon that is not fully understood, and has been observed to be significantly dependent on temperature and crystal orientation [111]. It is known that, regardless of temperature, prismatic slip is the primary slip system for dislocation glide and it has the lowest critical resolved shear stress (CRSS) [112]. However, the prismatic slip systems are alone geometrically insufficient to generate an arbitrary three-dimensional plastic deformation. Other possible slip modes include $\langle a \rangle$-type basal, $\langle a \rangle$-type pyramidal, and $\langle c + a \rangle$-type pyramidal slip systems. The flow stress for prismatic and basal slip systems decreases with increasing temperature, though this dependence becomes less significant at higher temperatures [113, 114]. At room temperature, it has been determined that the CRSS of the slip systems increase in the following order: $\langle a \rangle$-type prismatic, $\langle a \rangle$-type basal, and $\langle c + a \rangle$-type pyramidal [115]. Furthermore, $\langle a \rangle$-type pyramidal slip has been observed at higher temperatures and has a higher CRSS than prismatic and basal slip [111]. Above room temperature, basal slip has been observed to become the secondary slip mode [116], and becomes increasingly prevalent as the temperature increases [114]. The activation of secondary slip systems has been in part attributed to cross slip from prismatic to basal (and, more rarely, pyramidal) slip systems, the activity of which increases with temperature [117, 118, 111]. Furthermore, CP-based modelling approaches have shown that basal slip must be introduced to account for experimental results under high strain deformation at room temperature [119].

Khater and Bacon [120] used MD simulations of pure α-Zr to show that, at a temperature of 600 K and applied stresses below 200 MPa, the steady-state dislocation velocity is approximately linearly dependent on the applied stress in both prismatic and basal planes and for both edge and screw orientations. They also found that edge dislocations have a smaller Peierls stress compared to screw dislocations in both prismatic and basal slip systems, and exhibit higher mobilities. The propagation of screw dislocations is thus the rate-limiting mode, and at lower temperatures they are subject to thermally activated processes. MD simulations have been used to determine that the easy glide in prismatic slip systems can in part be attributed to the stability and low Peierls stress barrier of screw dislocations when dissociated in prismatic planes [121, 122, 123]. Furthermore, *ab initio* calculations and atomistic simulations indicate that the stacking fault energy is lower on prismatic planes compared to basal planes [120, 122], which supports the observation of preferential dissociation on prismatic planes. Screw dislocations can also partially dissociate in pyramidal planes, but this mode is less stable than in prismatic planes [124, 125]. The dissociation of screw dislocations on basal planes has been shown to be unstable [122]. At high applied stresses, screw dislocations that on average glide on basal planes remain dissociated in either prismatic or pyramidal planes [125]. However, at low stresses, screw dislocations can nucleate and propagate kink-pairs into the basal plane, thereby confining their motion to this plane and enabling true basal glide [123].

In pure zirconium, the mobilities of edge and screw dislocations gliding in prismatic planes are comparable [118]. However, *ab initio* calculations have shown that, in zirconium alloys, $\langle a \rangle$-type screw dislocations gliding on prismatic planes exhibit significant friction resulting from short-ranged elastic interactions with solute atoms (particularly oxygen) [126]. Furthermore, at lower temperatures, and in basal and pyramidal slip systems, dislocations have been observed to be typically composed of long, straight screw dislocations and faster, curved non-screw dislocations [118, 111]. In these slip systems, screw dislocations appear to be rate-limited by kink-pair mechanisms [111]. A thermally activated dislocation mobility—as opposed to an athermal drag-mediated mobility—can be described by a so-called Arrhenius form [127, 128]. This type of mobility model has effectively been used in some DD studies of Zr [129, 82]. It is expected that motion becomes increasingly rate-limited by athermal drag-related mechanisms as the temperature increases. Indeed, there is some observational evidence that basal slip becomes increasingly athermal at higher temperatures [111].

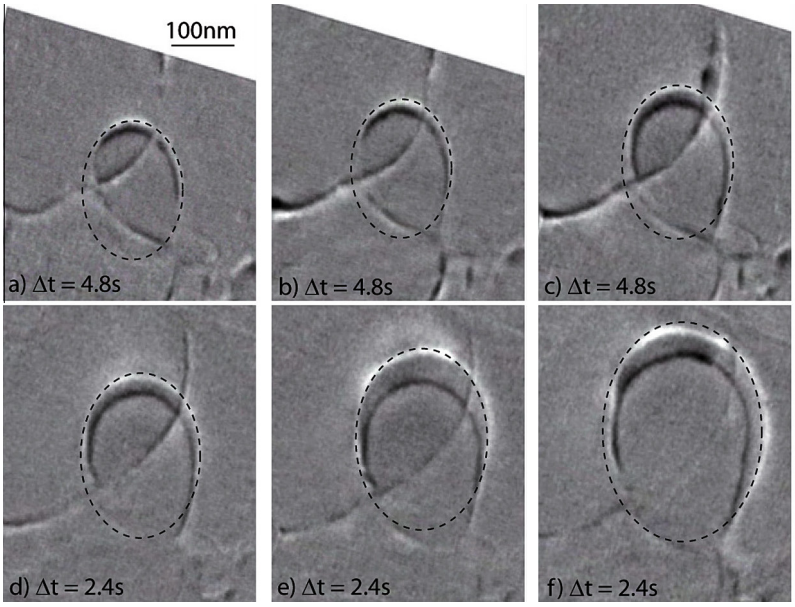
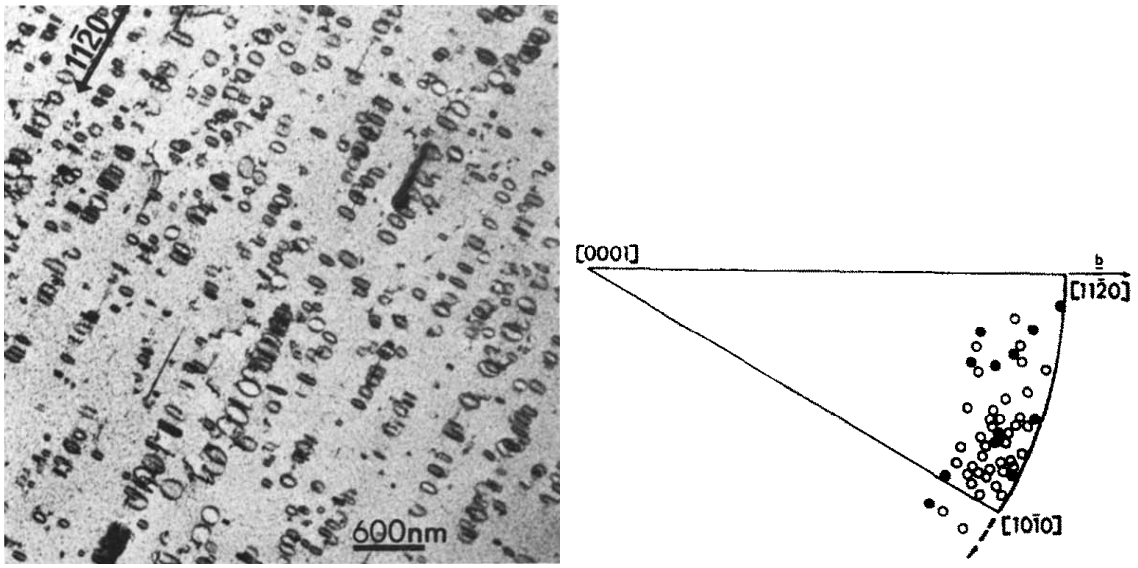


Figure 2.1: Dislocation loop in a zirconium alloy expanding on a prismatic plane and exhibiting an approximately self-similarly-growing elliptical shape (obtained from [130]).

Caillard *et al.* [130] investigated the kinematics of dislocations gliding on prismatic planes in an M5 zirconium alloy with a fairly high oxygen content of 1507 ppm and at a range of temperatures. At a fairly high temperature of approximately 673 K, they observed multiple expanding $\langle a \rangle$-type prismatic dislocation loops which exhibited elliptical shapes with ratios between screw and edge directions of approximately 1.5, and which expanded self-similarly at dynamic equilibrium, i.e. without changing aspect ratio (see figure 2.1). In addition, they showed that the glide velocity of these loops is linearly dependent on the local driving stress [130]. Therefore, at high temperatures, and as a first approximation, it is likely appropriate to model dislocation motion through a drag-mediated mobility (discussed in section 3.3), and with comparable orders of magnitude for the edge and screw mobilities.

It is important to note that, since $\langle a \rangle$-type dislocations cannot accommodate strain in the $\langle c \rangle$ direction on their own, such deformation requires the activation of mechanical twinning or $\langle c+a \rangle$-type dislocations. The former is an important deformation mode in zirconium, especially at lower temperatures [113, 131]. Furthermore, in HCP materials, $\langle c + a \rangle$ dislocations are believed to be strongly correlated with twins, and the two may mutually enhance each others nucleation [132]. As the temperature increases, $\langle c + a \rangle$ dislocations become increasingly active [133]. Furthermore, $\langle c + a \rangle$ dislocations have a large Burgers vectors magnitude, which leads to their elastic



(a) (b)

Figure 2.2: Experimental observations of $\langle a \rangle$-type prismatic loops at 668 K in zirconium irradiated to a neutron fluence of $6.4 \times 10^{23}\,\mathrm{m}^{-2}$ for $E > 1$ MeV (obtained from [137]). (a) TEM image of a collection of prismatic loops. (b) Prismatic loop plane normals (open and full circles respectively represent vacancy and interstitial loops).

instability and the possible decomposition reaction $\langle c + a \rangle \rightarrow \langle c \rangle + \langle a \rangle$ [134].

2.2 Prismatic loops and irradiation hardening

In a nuclear fission reaction core, Zr is subjected to fast neutron irradiation at energies $E > 1$ MeV [54]. The neutrons interact elastically with the atoms in the Zr crystal and displace them from their equilibrium positions, creating point defects without transmutation. This leads to a distribution of defect clusters in the sample, such as voids, stacking fault tetrahedra (SFT), and prismatic loops. Radiation damage of Zr alloys at low neutron fluences (less than $3 \times 10^{25}\,\mathrm{m}^{-2}$ for $E > 1$ MeV) has been shown to generate mostly $\langle a \rangle$-type prismatic loops on prismatic habit planes [135, 136]. A typical Zr alloy cladding with a thickness of less than a centimetre which receives a fast neutron flux of $5 \times 10^{17}\,\mathrm{m}^{-2}\,\mathrm{s}^{-1}$ may receive this upper bound of fast neutron fluence in approximately two years [54].

The microstructure and corresponding characteristics of distributed prismatic loops in neutron-irradiated Zr alloys has a complex dependence on irradiation temperature, purity, and thermo-mechanical history of the sample (see figure 2.2a) [137, 135, 54, 136]. At the low neutron fluences and temperatures as similar to those

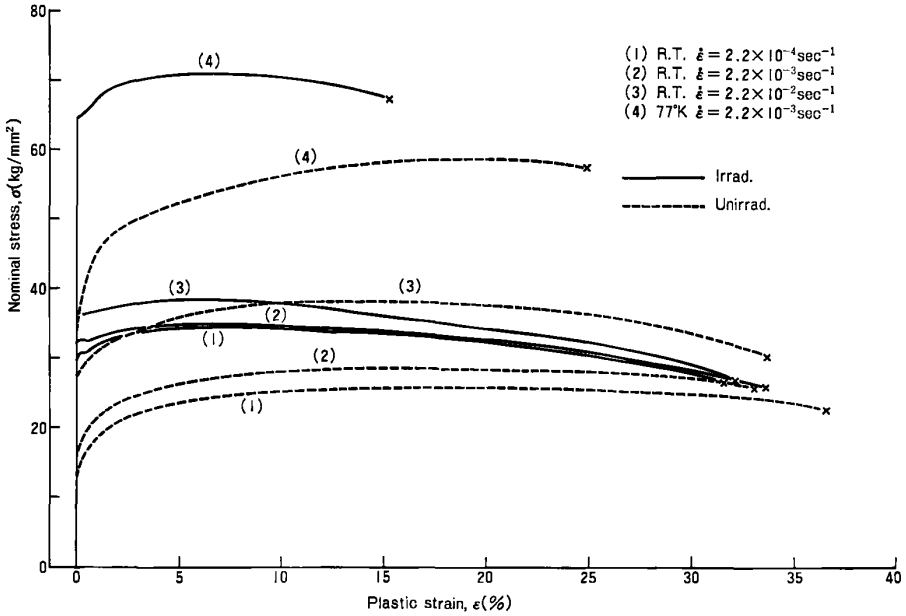


Figure 2.3: Stress-strain curves comparing irradiated and unirraditated Zr under tensile deformation for varying strain rates at room temperature (RT) and at 77 K (obtained from [139]). The irradiated samples have an increased yield stress and a decreased ductility compared to the corresponding unirradiated samples.

seen at LWR operating conditions, neutron irradiation-induced prismatic loops lie on prismatic planes distributed between 1st ($\{10\bar{1}0\}$) and 2nd ($\{11\bar{2}0\}$) order prismatic planes (see figure 2.2b). They have perfect $1/3\langle 11\bar{2}0\rangle$ Burgers vectors distributed equally among the three $\langle a\rangle$-type directions. It has also been found experimentally that the normal vector of the habit plane of these prismatic loops may have a small basal component [138, 137]. They are distributed as both interstitial and vacancy-type loops, with the proportion depending on the irradiation temperature. They are in general elliptical in shape, with eccentricities depending on the loop size, irradiation temperature, and on whether the loops are of interstitial or vacancy-type. For instance, in one "round-robin" study of nuclear-grade Zr alloys, at irradiation temperatures ranging from $523 - 673$ K it was found that loop diameters ranged from $8.5 - 20$ nm and loop densities were approximately on the order of $1 \times 10^{22}\,\text{m}^{-3}$ [135]. See [54] for a review of the microstructural evolution in irradiated Zr alloys.

Irradiation hardening is manifested macroscopically, in part, as an increase in yield stress and decrease in ductility (see figure 2.3) [139, 140]. It is well known that prismatic loops act as obstacles to dislocation motion [141, 142], which contributes to hardening in the irradiated material [143, 144]. For a sufficiently high applied stress, dislocations can overcome the prismatic loop barriers. This results in the formation

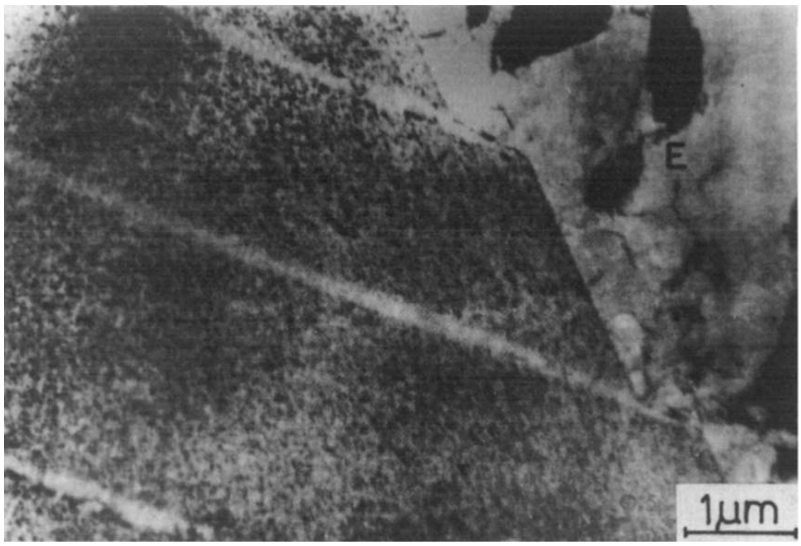


Figure 2.4: TEM image of defect-free dislocation channels in a neutron irradiated copper single crystal under tensile strain (obtained from [140]). Surface slip steps are also visible along the intersection between the dislocation channels and the surface.

of defect-free channels facilitating further dislocation motion, leading to plastic strain localisation (see figure 2.4) [140]. In combination with other irradiation-induced phenomena, these dislocation channels can have a significant impact on the properties of irradiated Zr, such as in early material fracture [145]. In unirradiated Zr alloys, the prismatic slip systems are the preferred planes for dislocation glide [112, 110]. However, when irradiated, the preferred glide planes become the basal slip systems [146, 147]. This has been associated with a greater increase in the critical resolved shear stress of prismatic slip systems compared to basal slip systems after irradiation.

In order to obtain a better understanding of irradiation hardening, the interactions between gliding dislocations and defect clusters such as prismatic loops has been the subject of much recent numerical investigation. Dislocation-defect interactions involve mechanisms which operate at multiple length scales, and have consequently been modelled using both MD and DD simulations. At the atomic scale, individual dislocation-defect interactions have been classified and described extensively by [148] and [149]. MD simulations of dislocations interacting with prismatic loops have been performed in face-centred cubic (FCC) metals [150, 151], body-centred cubic (BCC) metals [152, 153, 154, 155], and, of particular relevance to this text, HCP Zr [156, 157]. At the mesoscopic scale, DD simulations have been performed to investigate dislocation-loop interactions in FCC [158, 151], BCC [159], and HCP [85, 160, 1, 161] metals.

Drouet *et al.* conducted DD simulations in Zr to study the interactions between prismatic loops and both edge and screw dislocations gliding on basal and prismatic planes. These mechanisms were subsequently validated through TEM observations of ion-irradiated Zr alloy samples [162]. They showed on a statistical basis that dislocations gliding on basal slip systems have a greater probability of triggering loop-clearing mechanisms compared to dislocations gliding on prismatic slip systems. Building on this work, Onimus *et al.* [160] performed an extensive DD study of prismatic loop interactions with mixed character dislocations, also considering glide on both basal and prismatic planes. More recently, Dupuy *et al.* [161] developed an atomistically informed DD simulation framework to model dislocation–loop interactions in Zr. Through detailed comparison with MD simulations, they incorporated a series of material-specific features necessary to capture this interaction mechanism with increased accuracy.

In the literature it is understood from analytical [163, 164], atomistic [157, 165, 166], and experimental [138, 137, 167] analyses that the tilt angle between the habit plane normal vector and Burgers vector of prismatic dislocation loops tends to adopt a stable point which is influenced by the presence of external stress fields. The precise mechanism of prismatic loop tilting and stability is currently not fully understood. The tilt angle of prismatic loops has a significant impact on their interaction with other dislocations [164]. The stability of the prismatic loop habit plane may depend on the loop size, loop shape, and the degree of material anisotropy. At the time of writing, the only study in the literature which systemically computes stable loop tilt angles as a function of loop sizes is the one conducted by Hortelano-Roig *et al.* [1], and this study is incorporated as part of chapter 5 of this text.

2.3 Large-scale dislocation dynamics modelling

The incorporation of multiple slip systems increases the probability of junction formation and thus the potential contribution to forest hardening. Most studies of junction formation pertain to FCC and BCC systems [168, 28, 168, 169], although recent efforts have led to the probing of the more complicated dislocation arrangements found in HCP systems. Multiple studies have conducted combined line-tension analyses and small-scale 3D DD simulations of dislocation-dislocation interactions in HCP systems, including in Zr, ice, Mg, Cd, Zn, Co, Ti, and Be [129, 170, 171, 172, 173, 80]. Furthermore, Wu *et al.* [80] developed an analytical model describing the resistance of junctions to applied stress in a general HCP-based

framework. It is understood that junction formation in HCP systems is sensitive to the slip system geometry and Burgers vectors of interacting dislocations. Unlike the highly symmetric geometries exhibited by FCC or BCC systems, HCP systems may exhibit unique forest hardening behaviours which are associated with their limited slip symmetries. In contrast to the thoroughly investigated FCC systems [174], there are not many HCP-specific (and, notably, none concerning Zr) large-scale DD studies which directly quantify relations between individual junction configurations and strain hardening behaviour.

The first large-scale 3D DD simulation concerning an HCP material was conducted in 2004 by Monnet *et al.* [129] for pure prismatic slip in bulk Zr. The authors assumed a simplified orthorhombic HCP crystallography and operated within the low temperature regime wherein dislocation networks have sometimes been observed to be composed of mostly long screw dislocations. It was found that screw-screw dislocation interactions rarely form junctions, leading to small amounts of forest hardening. This is consistent with the small hardening rate which has been experimental observed in the initial deformation stage of micro-pillar compression of oxygen-doped Ti [175] and Zr [129] under similar conditions.

There have since been other large-scale 3D DD studies concerning HCP materials. Bertin *et al.* [176] and Devincre *et al.* [173] conducted bulk simulations to obtain interaction coefficients pertaining to forest interactions in pure magnesium and ice, respectively. Aitken *et al.* [57] conducted simulations of single crystal magnesium alloy nano-pillars in uniaxial compression to investigate dislocation-mediated size and orientation effects. They coupled their DD model to FEM (through a method described by [177]), although they assigned an equivalent mobility to dislocations in every slip system. Aubry *et al.* [84] investigated the $\langle c+a \rangle \rightarrow \langle c \rangle + \langle a \rangle$ decomposition mode in beryllium, and found that its inclusion resulted in significant contributions to hardening. To capture this behaviour, they developed a mobility law tailored for HCP materials, though easily generalisable to other crystallographic systems. This mobility law is a central focus of the present work and is further elaborated in chapter 4. Furthermore, Capolungo *et al.* conducted bulk simulations in c-axis tension to investigate the impact of elastic anisotropy on various HCP metals, including Zr [178]; it was found that anisotropic calculations have a moderate impact on Zr. However, anisotropic elasticity is outside of the scope of this text, and all calculations herein assume isotropic media.

Some studies have conducted large-scale 3D DD simulations to investigate the impact of twin boundaries (TBs) and grain boundaries (GBs) in polycrystalline HCP

magnesium [83, 179, 180]. Traditional 3D DD frameworks do not explicitly model the generation or evolution of twins, but Fan *et al.* [83] incorporated TBs as static, pre-inserted regions in the domain with a specified dislocation transmission criterion, and in which the crystal axes are rotated. Furthermore, grain boundaries have been implemented as interfaces which require a critical stress for dislocations to penetrate. 3D DD simulations have shown that TBs act as strong barriers to dislocation motion, substantially increasing the flow stress. This hardening effect competes with the softening effect associated with twin growth, which accommodates a portion of the imposed strain in the presence of dislocation slip. These competing phenomena have been used to explain the experimentally observed "concave" stress-strain curves in Mg [181]: twin growth softening dominates at small strains, while TB-induced hardening dominates at higher strains. Twinning is a relevant deformation mode of Zr, but is outside of the scope of the present text.

More recently, Li *et al.* [182] developed an atomistically informed 3D DD model incorporating cross slip in HCP Zr. Furthermore, the authors conducted 3D DD simulations of single crystal Zr micro-pillar tension tests to investigate the plastic slip transitions between slip systems [82]. Their mobility law incorporated a screw dislocation mobility which was partially thermally activated and dependent on the slip system, treated edge dislocation mobility as solely drag-mediated, and assigned an equivalent drag mobility to dislocations in every slip system. The authors did not fully couple their DD model to FEM, and instead treated the finite domain as a perfect dislocation sink with no image stresses. They incorporated thermally activated cross slip between prismatic and basal slip systems. They used an asymmetric activation energy for (prismatic $\rightarrow$ basal) and (basal $\rightarrow$ prismatic) cross slip calibrated to experiments [111] and which reflects the observed difference in stacking fault energies between both slip systems. They found that, at higher temperatures, a prismatic-to-basal plastic slip transition occurs which is enabled by the asymmetric cross slip conditions.

There are few studies that have used 2D DDP to investigate Zr. Tarleton *et al.* [65] used DDP to investigate the bending of single crystal micro-cantilevers in Ti and Zr, and validated their model with experiments. Their DDP simulations were able to reproduce the experimentally observed strengthening as the beam size decreased. Notably, the authors found that the size effect in micro-cantilevers is strongly controlled by the initial dislocation source density: when the beam size becomes comparable to the mean source spacing, the flow stress increases due to the limited availability of sources to accommodate the imposed strain. In addition,

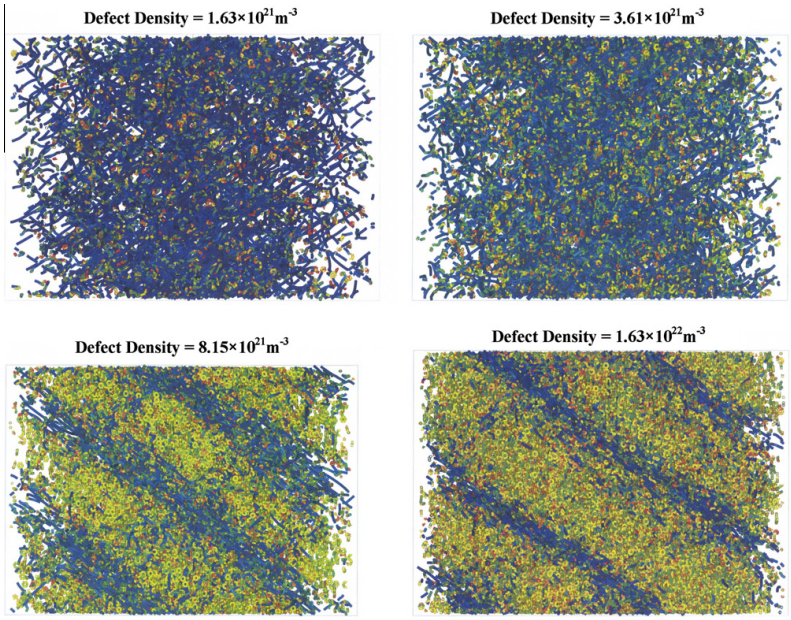


Figure 2.5: Images from 3D DD bulk simulations depicting progressive dislocation channelling in irradiated BCC iron (obtained from [81]). Green and yellow colours represent prismatic loop defects. Blue colours represent network dislocations.

dislocation-free regions near the free surfaces, whose volume is independent of the beam size, occupy a proportionally larger volume in smaller beams, further restricting plastic deformation. Furthermore, Reali *et al.* developed a series of DDP models for the purpose of capturing reactor-specific phenomena in Zr alloys, such as hardening related to hydrogen pickup [183, 184, 185]. At the time of writing, however, no studies have been identified which use 2D DDP to investigate irradiation hardening related to prismatic loop defects.

Being capable of capturing both long-ranged elastic dislocation-dislocation interactions and short-ranged dislocation-defect interactions, DD is an ideal method for investigating dislocation-mediated hardening mechanisms related to irradiation-induced defects. However, a significant multi-scale challenge exists: the characteristic size of irradiation-induced defects is about an order of magnitude smaller than that of typical dislocation segment lengths in DD [186]. Furthermore, dislocation channel initiation is a rare event, and only occurs above approximately 1% plastic strains [186]. Diligent computational optimisation and GPU acceleration are necessary to manage such large-scale simulations. For these reasons, large-scale DD studies which capture dislocation channel formation and plastic slip localisation through the discrete representation of prismatic loop defects[1] are somewhat limited

[1]Note that some studies have investigated irradiation hardening related to other irradiation-

[187, 188, 81, 189, 89]. Recent developments have attempted to circumvent this difficulty by, for instance, incorporating a spatially averaged continuum defect field [190]. Although some authors have incorporated such solutions [191], most existing DD studies of irradiation hardening have treated prismatic loop defects as discrete structures.

At the time of writing, only one large-scale study has been identified which fully couples DD with FEM to investigate hardening related to discrete prismatic loop defects. Specifically, Cui *et al.* [89] investigated intermittent plastic flow in irradiated single crystal BCC iron micro-pillars. Furthermore, Nogaret *et al.* [187] conducted 3D DD simulations to investigate dislocation channel formation mechanisms in irradiated FCC copper single crystal grains under tensile deformation. Notably, mobile screw dislocations were shown to absorb prismatic loops as helical turns (effectively acting as jogs) on the dislocation lines, which act as pinning sites. As these screw dislocations unpin and glide forward, they carry the jogs along the lines, clearing out a defect-free channel behind them. At the bulk scale, Arsenlis *et al.* [81] conducted 3D DD bulk simulations of irradiated BCC iron to investigate the impact of varying loop-defect concentrations (see figure 2.5). They found that a transition to plastic strain localisation occurs at a critical loop density above which dislocation channelling takes place. Furthermore, they determined that such localisation occurs as a result of a coarsening of prismatic loops upon their interaction with dislocations, eventually growing to become indistinguishable from the dislocation network.

Irradiation hardening is a complex, multi-scale phenomenon that remains challenging to model. Indeed, no large-scale 3D DD investigations of irradiation hardening in Zr have been identified. Although 3D DD simulations are limited by computational ability, 2D DDP appears as a promising alternative to model aspects of irradiated materials, since it may be capable of simulating large strains at the mesoscopic scale while simultaneously preserving dislocation-based insights. However, no 2D DDP studies have been identified which explore irradiation hardening mechanisms by directly incorporating representations of prismatic loop defects. The development of a 2D model which is capable of investigating such systems is the aim of chapter 5. Furthermore, no studies have been identified which conduct large-scale 3D DD simulations of HCP Zr that are fully coupled to FEM. Establishing such a simulation framework is, in part, the aim of chapter 6, which forms a step toward the broader

induced defects such as SFTs [88]; however, the methodology differs, as SFTs cannot be directly modelled as dislocation structures in a traditional sense, unlike prismatic loops.

objective of modelling irradiation hardening in HCP Zr. Building a foundation to address these gaps in the literature is a central aim of this text.

Chapter 3

Model formulation

Chapter introduction

In this chapter, the general framework of a 3D DD model is presented, with a specific focus on the implementation underlying EasyDD. In section 3.1, the basic elements and degrees of freedom in the DD model are introduced. In section 3.2, the theoretical formulations and implementations of energies and forces are outlined. In section 3.3, the mobility laws that govern dislocation kinematics are discussed. In section 3.4, the time integration methods used to evolve the system are outlined. In section 3.5, the topological operations applied to maintain and update the discrete nodal dislocation network are described. In section 3.6, the treatment of finite simulation domains and associated boundary conditions is explained.

3.1 Elements of dislocation dynamics

For a large subset of DD models which includes EasyDD, the smooth dislocation structure is represented as a nodal network C consisting of a set of nodes $\mathcal{N} = \{n_k\}$ and piecewise straight segments (or links/edges) $\mathcal{L} = \{\Gamma_{ij}\}$, each of which connects node n_i at position $\boldsymbol{x}_i$ to node n_j at position $\boldsymbol{x}_j$. Although the segments represent the conceptual picture, the computations themselves are performed on the nodes. Note that the following presentation will apply for EasyDD, but is general enough that it also applies to a majority of existing DD codes, with some alterations. A framework of isotropic linear elasticity is assumed.

Each segment $\Gamma_{ij} = (n_i, n_j) \in \mathcal{L}$ is directed in the sense that it represents a connection between two nodes in the direction $n_i \rightarrow n_j$. Each segment is assigned a Burgers vector $\boldsymbol{b}_{ij} \neq \boldsymbol{0}$, such that $\boldsymbol{b}_{ij}$ refers to the Burgers vector of a segment with the line sense in the direction $n_i \rightarrow n_j$. To impose Burgers vector conservation at

junctions, one asserts that $\boldsymbol{b}_{ij} = -\boldsymbol{b}_{ji}$. The conservation law is then conveniently expressed as $\sum_j \boldsymbol{b}_{ij} = 0$, where the sum is over all nodes connected to node n_i. Furthermore, each node is assigned an integer flag which specifies its mobility. A node which is connected to more than two segments is referred to as a *physical* node. If it is connected to two segments, it is referred to as a *discretisation* node.

The line vector and normal vector of every segment Γ_{ij} may be computed via

$$\boldsymbol{l}_{ij} = \frac{\boldsymbol{L}_{ij}}{|\boldsymbol{L}_{ij}|} \qquad \text{and} \qquad \boldsymbol{n}_{ij} = \frac{\boldsymbol{b}_{ij} \times \boldsymbol{l}_{ij}}{|\boldsymbol{b}_{ij} \times \boldsymbol{l}_{ij}|} \tag{3.1}$$

where $\boldsymbol{L}_{ij} = \boldsymbol{x}_j - \boldsymbol{x}_i$ is the segment length vector. The normal vector $\boldsymbol{n}_{ij}$ is normal to the glide plane on which the dislocation segment undergoes easy glide motion[1]. This is in contrast to climb motion, which is usually much more difficult, and occurs in the direction parallel to $\boldsymbol{n}_{ij}$. For screw segments, in which the line and Burgers vectors are parallel, the normal vector cannot be constructed from geometric quantities in this manner. In EasyDD, a normal vector is assigned to every segment and is therefore treated as a pre-defined additional degree of freedom.

The aim is to develop a coherent and consistent mesoscopic description of the mechanics and dynamics of the dislocation network. An important challenge is to translate continuum-scale physical descriptions into discrete representations. This framework must account for applied forces, kinematics, and the evolving topology of the network. A typical generic DD loop is comprised of the following steps:

1. *Force calculation*: The forces acting on the dislocations are obtained.

2. *Mobility law*: The resulting kinematics (including accelerations and/or velocities) of the dislocations are obtained.

3. *Time integration*: The updated positions of the dislocations are obtained.

4. *Topological operations*: The topology of the dislocation nodal network is modified to account for dislocation reactions and mesh coarsening/refining.

For the remainder of this chapter we will provide an overview of each of these steps.

[1] As noted by Bromage [192], calculating the normal vector for non-screw segments in the manner described by equation (3.1) yields the *habit* plane normal of a segment, and does not necessarily coincide with its *glide* plane normal. This distinction becomes relevant when a segment undergoes climb motion and deviates from its original glide plane, such that it is no longer entirely parallel to it.

3.2 Forces

We begin by introducing the total energy, $\mathcal{E} = \mathcal{E}(C)$, associated with a dislocation network C. In general, this quantity depends on several factors, such as the size and connectivity of the network, properties of the material in which it is embedded, the temperature, and the size of the crystal sample. However, for this presentation, let us consider an idealised case in which the dislocation network is contained within an infinite, perfectly homogeneous, linearly elastic medium.

The theory of elasticity can only describe domains which may be adequately modelled as a continuous medium. This excludes a small cylindrical region around a dislocation, the so-called dislocation *core*, within which large and nonlinear strains occur[2]. Within the dislocation core, the discrete nature of the lattice becomes significant and continuum elasticity theory becomes invalid. Consequently, the total energy $\mathcal{E}$ is often conveniently decomposed into two contributions: the nonlocal elastic energy $\mathcal{E}^{\mathrm{e}}$, stored outside of the dislocation cores, and the local inelastic core energy $\mathcal{E}^{\mathrm{c}}$, stored within the dislocation cores. The former contribution, $\mathcal{E}^{\mathrm{e}}$, is associated with the nonlocal elastic strain fields produced by the dislocation network, and gives rise to all long-ranged interactions between dislocations. The latter contribution, $\mathcal{E}^{\mathrm{c}}$, is associated with the distortion of the local atomic configuration surrounding the core region, which stores a short-ranged inelastic energy.

We shall first consider the elastic energy contribution. Since the classical elastic field expressions associated with dislocations exhibit singularities at the dislocation core[3] [193], they are unsuitable for computational implementation. EasyDD instead uses the non-singular continuum elastic theory expressions derived by Cai *et al.* [194] at the cost of requiring one additional input parameter: the isotropic Burger's vector spreading radius r_c. Here, r_c represents the radius of the cylinder enveloping the dislocation core, within which linear elasticity is invalid. The non-singular elastic

[2]The dislocation core region usually only extends a few atomic distances away from the dislocation line.

[3]These singularities arise from the so-called Volterra dislocation model, in which a given dislocation generates a displacement field which exhibits a discontinuity at its core, and hence a singularity in the resulting strain field.

energy of a dislocation loop C is given by

$$\begin{aligned}\mathcal{E}^{\mathrm{e}} = &\frac{\mu}{16\pi}\oint_C\oint_C b_i b'_j \partial_k\partial_k R_a \mathrm{d}x_i \mathrm{d}x'_j \\ &- \frac{\mu}{8\pi}\oint_C\oint_C \epsilon_{ijq}\epsilon_{mnq} b_i b'_j \partial_k\partial_k R_a \mathrm{d}x_m \mathrm{d}x'_n \\ &- \frac{\mu}{8\pi(1-\nu)}\oint_C\oint_C \epsilon_{ikl}\epsilon_{jmn} b_k b'_m \partial_i\partial_j R_a \mathrm{d}x_l \mathrm{d}x'_n\end{aligned} \tag{3.2}$$

where $R_a \equiv \sqrt{R^2 + r_c^2}$ and $R \equiv |\boldsymbol{x} - \boldsymbol{x}'|$, ϵ_{ijk} is the Levi-Civita symbol, and index notation is used. It should be noted that for the system to remain strictly thermodynamically consistent, the elastic energy must include a term representing the work done by the elastic tractions exerted on the surface of the inelastic cylindrical core region [195, 196]. Because the non-singular continuum elastic theory formulation has been shown to be self-consistent [194], this term is naturally incorporated.

The local core energy contribution $\mathcal{E}^c$ can be expressed as

$$\mathcal{E}^c = \sum_{\text{all segments}} \epsilon^c(\boldsymbol{b}_{ij}, \boldsymbol{l}_{ij})|\boldsymbol{L}_{ij}| \tag{3.3}$$

where $\boldsymbol{L}_{ij} = \boldsymbol{x}_j - \boldsymbol{x}_i$ is the segment length vector and $\epsilon^c(\boldsymbol{b}_{ij}, \boldsymbol{l}_{ij})$ is the non-negative, empirically-determined core energy per unit length for a segment with a given Burger's vector $\boldsymbol{b}_{ij}$ and unit line vector $\boldsymbol{l}_{ij} = \boldsymbol{L}_{ij}/|\boldsymbol{L}_{ij}|$. To understand the magnitudes of the energies associated with the dislocation core, consider an infinitely long straight dislocation. Define the following two cylindrical regions around the dislocation line: the inelastic region which surrounds the immediate neighbourhood of the core up to the cut-off distance r_c, and an elastic region which surrounds the core (excluding the inelastic region) up to some radial distance $\mathcal{R}_c$ which is characteristic of the microstructure [197]. The latter elastic region has an associated energy per unit length given by

$$E^{\text{line}} = \frac{\mu b^2}{4\pi\,(1-\nu)} \ln\left(\frac{\mathcal{R}_c}{r_c}\right)\left(1 - \nu\cos^2\theta\right) \tag{3.4}$$

where θ is the character angle. This is the elastic energy per unit length of an infinite straight dislocation, and is typically on the order of $\alpha\mu b^2$, where $\alpha \approx 0.5 - 1$. In contrast, the energy per unit length corresponding to the former (inelastic) region is usually approximately ten times lower [198, 193, 122, 199]. Consequently, for the purposes of dislocation dynamics the former core energy per unit length term is sometimes neglected. However, many codes (including EasyDD) do not neglect this term, as it can have a significant impact on phenomena such as dislocation-dislocation collision reactions and prismatic loop rotational dynamics.

The total energy is usually decomposed as an additive superposition of the elastic and core energies, such that $\mathcal{E} = \mathcal{E}^{\mathrm{e}} + \mathcal{E}^{\mathrm{c}}$. Implicit in this formulation is the assumption that the two energy contributions are independent——that is, no nonlinear coupling exists between them. In the linear elastic regime, it is assumed that dislocation-generated elastic fields satisfy the superposition principle, ensuring that, at least to leading order, the elastic energy does not influence the core energy. Conversely, the dislocation core involves strong interactions and highly nonlinear atomic rearrangements, and thus lies outside the scope of linear elasticity [200, 201, 202, 196]. However, the fields generated by the core decay much more rapidly with distance than the long-ranged elastic strain fields, and are effectively confined to the dislocation core [201]. As a result, their influence on the surrounding lattice is minimal beyond this region, and the core energy does not introduce additional terms from interactions with the elastic energy. Therefore, to leading order, cross terms between the elastic and core energies can be neglected, thereby justifying the use of the superposition principle in DD models[4].

With a total energy that satisfies the necessary criteria to constitute a state variable[5], the total force $\boldsymbol{f}_i$ on a node n_i can then be determined formally via

$$\boldsymbol{f}_i = -\boldsymbol{\nabla}_i \mathcal{E} \tag{3.5}$$

where the gradient operator $\boldsymbol{\nabla}_i \equiv \partial/\partial \boldsymbol{x}_i$ is assumed to act in a way such that the nodal connectivity is preserved[6]. It follows from the linearity of differentiation that the total nodal force can be expressed in terms of an elastic contribution $\boldsymbol{f}_i^{\mathrm{e}}$ and a core contribution $\boldsymbol{f}_i^{\mathrm{c}}$ via the summation $\boldsymbol{f}_i = \boldsymbol{f}_i^{\mathrm{e}} + \boldsymbol{f}_i^{\mathrm{c}}$. It is convenient to express the force on a node in terms of the contributions due to its connection to the segments which are connected to it, given by

$$\boldsymbol{f}_i = \sum_{j}^{k_i} \boldsymbol{f}_{ij} \tag{3.6}$$

[4]It should be noted that the superposition principle breaks down in scenarios involving significant core overlap, such as during dislocation–dislocation reactions. In such cases, nonlinear interactions between cores can no longer be neglected. However, in DD simulations, the detailed atomic-scale processes underlying these reactions are effectively coarse-grained. Only the initial and final dislocation topologies are explicitly resolved, while the intermediate states are not modelled in detail; these states are not relevant at the scales of DD.

[5]A quantity constitutes a state variable if and only if it is fully determined by the spatial degrees of freedom of the current configuration.

[6]The preservation of nodal connectivity during the gradient operation is necessary to maintain the smoothness of the energy function, and thus its differentiability. As with the superposition principle, the notion of the nodal force breaks down during discrete changes in topological connectivity.

where k_i is the number of segments connected to node n_i and $\boldsymbol{f}_{ij}$ is the force contribution to node n_i due to its connection to node n_j.

Of the two types of contributions to the total force, the core force $\boldsymbol{f}_{ij}^{\mathrm{c}}$ is the simplest to calculate. Computing the negative gradient of the core energy for a single isolated segment Γ_{ij} yields the core force contribution to node n_i due to its connection to node n_j given by

$$\boldsymbol{f}_{ij}^{c} = \epsilon^{c}(\boldsymbol{b}_{ij}, \boldsymbol{l}_{ij})\boldsymbol{l}_{ij} + (I - \boldsymbol{l}_{ij} \otimes \boldsymbol{l}_{ij}) \cdot \frac{\partial \epsilon^{c}(\boldsymbol{b}_{ij}, \boldsymbol{l}_{ij})}{\partial \boldsymbol{l}_{ij}} \tag{3.7}$$

where I is the 3×3 identity matrix. The first and second terms in equation (3.7) represent the longitudinal and torsional core forces, respectively. Expressions for $\epsilon^{c}(\boldsymbol{b}_{ij}, \boldsymbol{l}_{ij})$ may be determined phenomenologically by fulfilling a certain set of criteria such as interpolating smoothly between regimes defined by fitting parameters obtained from atomistic simulations [203]. In EasyDD and ParaDiS, the interpolation proceeds as

$$\epsilon^{c}(\theta) = E_e^{c} \sin^2 \theta + E_s^{c} \cos^2 \theta \tag{3.8}$$

where θ is the character angle and the empirical parameters E_e^{c} and E_s^{c} are respectively the core energy per unit length of an edge and screw dislocation[7]. This relation is identical in interpolation to expression (3.4), which is the elastic energy per unit length of an infinitely long mixed dislocation. In the elastic case, the relation $E_s^{\mathrm{line}} = E_e^{\mathrm{line}}(1 - \nu)$ holds, where E_s^{line} and E_e^{line} are respectively the elastic energy per unit length of an infinite edge and screw dislocation. By analogy, assuming the phenomenological relation $E_s^{c} = E_e^{c}(1 - \nu)$ results in the expression

$$\epsilon^{c}(\theta) = \frac{E_s^{c}}{1 - \nu}\left(1 - \nu \cos^2 \theta\right) \tag{3.9}$$

In EasyDD and ParaDiS, the core energy per unit length can be equivalently derived by replacing $\frac{\mu b^2}{4\pi} \ln\left(\frac{\mathcal{R}_c}{r_c}\right)$ with E_s^{c} in expression (3.4).

The elastic force contribution is more difficult to calculate. It can be formally defined by

$$\boldsymbol{f}_i^{\mathrm{e}} = -\boldsymbol{\nabla}_i \mathcal{E}^{\mathrm{e}} \tag{3.10}$$

but it shall be calculated in a different manner by considering the following argument which invokes thermodynamics. The change in elastic energy $\delta\mathcal{E}^{\mathrm{e}}$ associated with a displacement $\delta\boldsymbol{r}(\boldsymbol{x})$ in the network is by definition given by

$$\delta\mathcal{E}^{\mathrm{e}} = -\oint_C \boldsymbol{f}^{\mathrm{PK}} \cdot \delta\boldsymbol{r}(\boldsymbol{x})\, \mathrm{d}L(\boldsymbol{x}) \tag{3.11}$$

[7]Note that other interpolations may be more suitable depending on the material [204, 205].

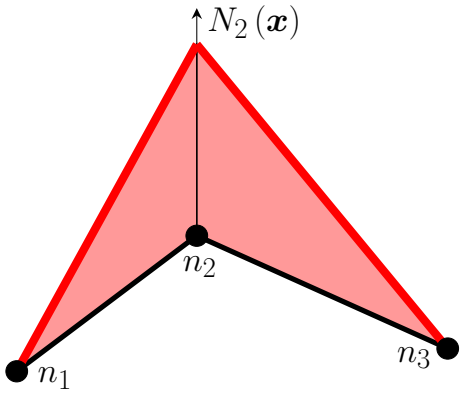


Figure 3.1: Schematic of a shape function $N_2(\boldsymbol{x})$ (in thick red lines) defined along segments Γ_{12} and Γ_{23}. The shape function varies linearly from $N_2(\boldsymbol{x}_2) = 1$ to $N_2(\boldsymbol{x}_1) = 0$ along segment Γ_{12} and from $N_2(\boldsymbol{x}_2) = 1$ to $N_2(\boldsymbol{x}_3) = 0$ along segment Γ_{23}.

where the displacement $\delta\boldsymbol{r}(\boldsymbol{x})$ is necessarily small such that the domain of evaluation of the line integral is approximately equivalent to the new position of the network after the displacement. The segments of the network are constrained by the motion of the nodes in a manner such that the displacement along segments connected to node n_i is given by $\delta\boldsymbol{r}(\boldsymbol{x}) = N_i(\boldsymbol{x})\,\delta\boldsymbol{r}_i$, where the shape functions $N_i(\boldsymbol{x})$ are defined along each segment connected to node n_i as

$$N_i(\boldsymbol{x}) := \frac{|\boldsymbol{x} - \boldsymbol{x}_j|}{|\boldsymbol{x}_i - \boldsymbol{x}_j|} \tag{3.12}$$

such that $N_i(\boldsymbol{x})$ varies linearly from $N_i(\boldsymbol{x}_i) = 1$ to $N_i(\boldsymbol{x}_j) = 0$ (see figure 3.1) [206]. It therefore follows that

$$\boldsymbol{f}_i^{\mathrm{e}} \equiv -\lim_{\delta\boldsymbol{r}_i \to 0} \frac{\delta\mathcal{E}^{\mathrm{e}}}{\delta\boldsymbol{r}_i} = \oint_C N_i(\boldsymbol{x})\,\boldsymbol{f}^{\mathrm{PK}}(\boldsymbol{x})\,\mathrm{d}L(\boldsymbol{x}) \tag{3.13}$$

This method allows one to account for the field contributions to n_i due to all of its connected segments. As a validity check, note that the total elastic force on the network satisfies the equivalence given by

$$\sum_{i=1}^{N} \boldsymbol{f}_i^{\mathrm{e}} = \oint_C \boldsymbol{f}^{\mathrm{PK}}(\boldsymbol{x})\,\mathrm{d}L(\boldsymbol{x}) \tag{3.14}$$

where N is the total number of nodes in the network; this relation is expected and conceptually desirable.

The Peach-Koehler force expression [7] is given by

$$\boldsymbol{f}^{\mathrm{PK}}(\boldsymbol{x}) = (\sigma(\boldsymbol{x}) \cdot \boldsymbol{b}) \times \boldsymbol{l} \tag{3.15}$$

where $\boldsymbol{b}$ and $\boldsymbol{l}$ are the Burgers and line vectors, and σ is the elastic stress field. What remains is to relate the Peach-Koehler force field $\boldsymbol{f}^{\mathrm{PK}}(\boldsymbol{x})$ with any given configuration of the network. The dislocation network C generates an elastic stress field, here expressed in its non-singular formulation given by

$$\begin{aligned}\sigma_{\alpha\beta}(\boldsymbol{x}) = \frac{\mu}{8\pi}\oint_C \partial_i\partial_p\partial_p R_a \left(b_m\epsilon_{im\alpha}\mathrm{d}x'_\beta + b_m\epsilon_{im\beta}\mathrm{d}x'_\alpha\right) \\ \frac{\mu}{4\pi(1-\nu)}\oint_C b_m\epsilon_{imk}\left(\partial_i\partial_\alpha\partial_\beta R_a - \delta_{\alpha\beta}\partial_i\partial_p\partial_p R_a\right)\mathrm{d}x'_k\end{aligned} \tag{3.16}$$

which is used to determine $\boldsymbol{f}^{\mathrm{PK}}$ via equation (3.15). This solves the problem of defining the discrete forces on the network. Arsenlis *et al.* [101] have derived analytical expressions for the forces $\boldsymbol{f}_{ij}^{kl}$ on a node at position $\boldsymbol{x}_i$ that terminates a dislocation segment that begins at position $\boldsymbol{x}_j$ due to the elastic stress field of a dislocation segment that begins at position $\boldsymbol{x}_k$ and terminates at position $\boldsymbol{x}_l$.

Each segment generates an elastic stress field which influences every other segment in a pairwise fashion, resulting in an N-body problem that must be solved, where N is the number of segments. Because of the corresponding order $\mathcal{O}(N^2)$ scaling, this is typically the largest computational bottleneck in a DD simulation. It is not unusual for the forces module to consume $> 80\%$ of the computation time in simulations which exhibit at least up to moderate dislocation densities[8].

One approach to resolve this computational bottleneck is to apply a spatial field "cut-off" distance, beyond which elastic interactions are not considered. This method exhibits $\mathcal{O}(Nm)$ time scaling, where m is the number of interactions within the cut-off distance. However, dislocation stress fields are long-ranged in nature; they decay as $1/r$ for evaluations at a distance r from a dislocation. Indeed, it has been shown for DD that applying a field cut-off yields numerical artefacts [207]. On the other hand, approximate solutions to the N-body problem with improved scaling have been studied extensively in the literature. For instance, the Barnes-Hut algorithm exhibits $\mathcal{O}(N\log N)$ scaling [208, 209], and the fast multipole method (FMM) can in principle achieve $\mathcal{O}(N)$ scaling [210, 211, 212]. FMM has successfully been implemented in various dislocation dynamics codes [213, 101, 214, 215]. At the time of writing, EasyDD performs a direct $\mathcal{O}(N^2)$ calculation of the forces—this is an important limitation of EasyDD, and future improvements should be considered in this regard.

[8] In dense dislocation networks, where most nodes have a large number of connections, topological operations can become the dominant factor in the computation time.

The line tension model

The concept of dislocation line tension provides a simplified yet useful model for describing the energy associated with a dislocation configuration. While several formulations exist [216], one which is occasionally referenced in this text is the simplest: it neglects all nonlocal interaction energies and assigns a local energy per unit length (i.e., an energy density) to the dislocation, given by expression (3.4). Since the form of interpolation with respect to the character angle of the core energy density is identical to that of the elastic energy density, the two can be combined without further modifying the theoretical framework. When incorporating the core energy, one can simply additively subsume both contributions to obtain a total energy per unit length given by

$$E(\theta) = \left(E_e^{\text{line}} + E_e^c\right) \sin^2\theta + \left(E_s^{\text{line}} + E_s^c\right) \cos^2\theta \tag{3.17}$$

where θ is the character angle. Because of the similarities in form between the core and line tension energies, the core energy and its associated forces are, in this text, occasionally referred to interchangeably to as the line tension energies and forces, respectively. Any potential ambiguity is either irrelevant or resolved by context.

3.3 Mobility laws

Given a complete set of nodal forces acting on the dislocation network, the resulting nodal kinematics must be computed in order to determine the dislocation dynamics. The response of each node depends on local fields such as stress, temperature, and the line, Burgers, and normal vectors of its connected segments. In general, this leads to nonlinear nodal equations of motion which must be solved by a mobility law. The mobility law is an essential module of a dislocation dynamics code, in part because the macroscopic plastic flow is proportional to the average speed of dislocations [217].

The dislocation core response to forces depends on inelastic atomistic interactions which cannot be directly modelled by the linear elastic theory. In order to incorporate these atomic-scale effects into linear elasticity, mesoscopic theories of dislocation mobility have been derived with a set of free parameters which are empirically determined from finer-scale theories. For instance, MD simulations can be performed in which dislocation velocities are calculated as functions of a given stress state for different dislocation orientations.

Dislocation segments can in general have an anisotropic mobility response which strongly depends on the segment's line orientation and crystal lattice structure [197, 193]. In principle, MD simulations can be performed to determine the dislocation mobility parameters for any dislocation orientation. However, in practice, mobility parameters are known for only a finite number of dislocation orientations. This is due to computational difficulties and relatively limited parametric studies available in the literature. These empirically-determined parameters must be interpolated and extrapolated in order to obtain a continuous distribution of mobility parameters so that a general dislocation orientation may be used in DD simulations.

The general kinematic equation of motion at every position $\boldsymbol{x}$ along a dislocation line is given by

$$\boldsymbol{f}(\boldsymbol{x}) = \boldsymbol{\mathcal{I}}(\dot{\boldsymbol{v}}(\boldsymbol{x})) + \boldsymbol{\mathcal{B}}(\boldsymbol{v}(\boldsymbol{x})) \tag{3.18}$$

where $\boldsymbol{f}$, $\boldsymbol{\mathcal{I}}$, and $\boldsymbol{\mathcal{B}}$ are respectively the driving, inertial, and drag forces per unit length acting on the dislocation line [218]. When dislocations accelerate, they radiate elastic waves throughout the medium which travel at the speed of sound (on the order of $3\,\mathrm{km\,s^{-1}}$ in zirconium [219]), and which eventually dissipate and relax to a static state after a sufficiently long time scale [220]. The inclusion of the dislocation inertia term $\boldsymbol{\mathcal{I}}$ gives rise to elastodynamic simulations wherein the elastic fields generated by dislocations are treated as fully time-dependent and thus their retardation effects become significant [221]. This can be used to model systems where the velocity of dislocations is comparable to the speed of elastic wave propagation, or where the time scale associated with the acceleration of dislocations is comparable to the relevant time scale of the simulation. This includes systems such as materials subjected to high strain rates and shock loading [221, 222].

Elastodynamic simulations are computationally expensive and challenging to implement. Therefore, in most dislocation dynamics simulations it is commonly assumed that the dislocation inertia term is negligible, which corresponds to $\boldsymbol{\mathcal{I}}(\dot{\boldsymbol{v}}) \approx \boldsymbol{0}$. This inertia-free regime is equivalent to asserting that the relevant time scales are much longer than the time scale during which the elastic waves reach a static form. Therefore, the evolution of the elastic field waves is assumed to happen instantaneously relative to the evolution of the dislocations, and elastostatic field solutions are used. This is known as the *quasistatic* regime, and is equivalent to assuming that the system is always approximately in mechanical equilibrium. In this text, it is always assumed that systems under consideration operate within the quasistatic regime.

Indeed, except for in conditions of high strain rates, dislocation inertia may be ignored due to the effects of phonon-induced drag [197]. In these so-called over-damped regimes, the dislocation velocity $\boldsymbol{v}(\boldsymbol{x})$ at position $\boldsymbol{x}$ on the dislocation line can be expressed in terms of the total instantaneous driving force per unit length $\boldsymbol{f}(\boldsymbol{x})$ at that point via

$$\boldsymbol{v}(\boldsymbol{x}) = \boldsymbol{\mathcal{M}}(\boldsymbol{f}(\boldsymbol{x})) \tag{3.19}$$

Note that, in this context, $\boldsymbol{f}$ contains information representing all of the interactions influencing dislocation motion, including both elastic and core effects. The mobility function $\boldsymbol{\mathcal{M}}$ depends on several factors such as the material crystallography, temperature, and dislocation character angle. Although $\boldsymbol{\mathcal{M}}$ is in general a nonlinear function, linear mobility laws have been implemented for BCC [223], FCC [101, 224], and HCP [84, 1] crystals. Nonlinear mobility laws with closed-form expressions for $\boldsymbol{\mathcal{M}}$ have also been implemented [225, 226].

If $\boldsymbol{\mathcal{M}}$ is a bijective function, then a unique inverse exists, known as the drag function $\boldsymbol{\mathcal{B}}$. If $\boldsymbol{\mathcal{M}}$ is a linear function, as will be assumed in this presentation, then it is bijective if its matrix representation can be inverted. In the over-damped regime, a dislocation drag force per unit length $\boldsymbol{f}^{\text{drag}}$ is given by

$$\boldsymbol{f}^{\text{drag}}(\boldsymbol{x}) = -\boldsymbol{\mathcal{B}}(\boldsymbol{v}(\boldsymbol{x})) \tag{3.20}$$

and exactly cancels the driving force per unit length $\boldsymbol{f}(\boldsymbol{x})$ at each point of the dislocation line, i.e.

$$\boldsymbol{f}^{\text{drag}}(\boldsymbol{x}) + \boldsymbol{f}(\boldsymbol{x}) = 0 \tag{3.21}$$

Due to the discrete nature of DD models, the velocity $\boldsymbol{v}(\boldsymbol{x})$ can only vary independently at each node, and not along segments which connect them. Therefore, we may enforce condition (3.21) only at the nodes. Using shape functions $N_i(\boldsymbol{x})$ to account for this constraint, the velocity $\boldsymbol{v}(\boldsymbol{x})$ at an arbitrary point on a segment can be expressed as

$$\boldsymbol{v}(\boldsymbol{x}) = \sum_i \boldsymbol{v}_i \; N_i(\boldsymbol{x}) \tag{3.22}$$

where $\boldsymbol{v}_i$ is the velocity of node n_i and the sum is over both nodes to which the segment is connected to.

Weighing the driving force per unit length with shape functions leads to a weaker drag condition given by

$$\boldsymbol{f}_i = \oint_C N_i(\boldsymbol{x}) \; \boldsymbol{f} \; \mathrm{d}L = \oint_C N_i(\boldsymbol{x}) \; \boldsymbol{\mathcal{B}}(\boldsymbol{v}(\boldsymbol{x})) \; \mathrm{d}L \tag{3.23}$$

where $\boldsymbol{f}_i$ represents the driving force acting on node n_i and C represents the entire dislocation network. Since $N_i(\boldsymbol{x})$ is non-zero only along segments connected to node n_i, equation (3.23) can be expressed as

$$\boldsymbol{f}_i = \sum_j^{k_i} \int_{\Gamma_{ij}} N_i(\boldsymbol{x})\ \boldsymbol{\mathcal{B}}\left(\boldsymbol{v}\left(\boldsymbol{x}\right)\right)\ \mathrm{d}L \tag{3.24}$$

where the summation is over all k_i nodes n_j which are connected to node n_i. For a sufficiently finely discretised nodal network, it is reasonable and highly convenient to assume that the dislocation velocity of positions along segments are approximately equivalent to the velocity of node n_i. This results in a constant drag function $\boldsymbol{\mathcal{B}}\left(\boldsymbol{v}\left(\boldsymbol{x}\right)\right) \approx \boldsymbol{\mathcal{B}}_{ij}\left(\boldsymbol{v}_i\right)$ along each segment, leading to

$$\boldsymbol{f}_i \approx \sum_j^{k_i} \boldsymbol{\mathcal{B}}_{ij}\left(\boldsymbol{v}_i\right) \int_{\Gamma_{ij}} N_i(\boldsymbol{x})\ \mathrm{d}L = \sum_j^{k_i} \boldsymbol{\mathcal{B}}_{ij}\left(\boldsymbol{v}_i\right) \frac{1}{2}\ |\boldsymbol{L}_{ij}| \tag{3.25}$$

where $\boldsymbol{L}_{ij} = \boldsymbol{x}_j - \boldsymbol{x}_i$ is the segment length vector. Note that the assumption that the velocities of neighbouring nodes are approximately equivalent can be problematic in certain situations, such as at nodes connected to more than two segments with dramatically different velocities. However, this assumption should still be considered, as it greatly reduces the computational requirements of 3D DD simulations.

Furthermore, for low nodal velocities we may assume a linear mobility response, i.e. a mobility relation given by $\boldsymbol{\mathcal{B}}_{ij}\left(\boldsymbol{v}_i\right) = \mathcal{B}_{ij} \cdot \boldsymbol{v}_i$ for the drag tensor $\mathcal{B}_{ij}$ of segment Γ_{ij} (with units of $\mathrm{Pa} \cdot \mathrm{s}$). Consequently, the weak condition simplifies to become

$$\boldsymbol{f}_i = \frac{1}{2} \sum_j^{k_i} |\boldsymbol{L}_{ij}|\ \mathcal{B}_{ij} \cdot \boldsymbol{v}_i \tag{3.26}$$

To obtain the nodal velocities, one must solve equation (3.26). What remains is to construct the drag tensor $\mathcal{B}_{ij}$. The motion of a dislocation segment Γ_{ij} may be decomposed into three directions which form an orthonormal basis in three dimensions: the line vector $\boldsymbol{l}_{ij}$, the normal vector $\boldsymbol{n}_{ij}$, and the glide vector $\boldsymbol{m}_{ij} = \boldsymbol{n}_{ij} \times \boldsymbol{l}_{ij}$. Therefore, in the standard method (which is typically used in non-HCP mobility laws), the drag tensor of a segment is constructed as the linear combination

$$\mathcal{B}_{ij} = B_l \boldsymbol{l}_{ij} \otimes \boldsymbol{l}_{ij} + B_c \boldsymbol{n}_{ij} \otimes \boldsymbol{n}_{ij} + B_g \boldsymbol{m}_{ij} \otimes \boldsymbol{m}_{ij} \tag{3.27}$$

The eigenvalues B_l, B_c, and B_g are drag coefficients which determine the stiffness of the dislocation segment in the line, climb, and glide directions, respectively. Since

nodal motion in the line direction does not produce a change in the dislocation shape, the line drag B_l in a sense has no physical significance. However, its inclusion is necessary to ensure that the drag tensor is nonsingular. In the most basic formulation, B_l and B_c are set to constant values and $B_g = B_g(\theta)$ (where θ is the character angle) is interpolated between pure edge and pure screw configurations. Typically, the orders of magnitude of the drag coefficients are assigned such that $B_l \ll B_g$ and $B_g \ll B_c$. The latter condition makes climb motion much more difficult than glide motion[9], while the former condition is intended to facilitate nodal distribution along a dislocation line. However, a large disparity between drag coefficients can result in numerical instabilities related to the ill-conditioning of the drag matrix. For this reason, in EasyDD it is usually recommended to assign B_l to be of a similar order of magnitude as B_g.

Depending on the desired sophistication of the model, variations on this formulation can be produced. For instance, the line and glide drag coefficients may be interpolated between pure glide and pure climb configurations such that segments becomes increasingly stiff as they lie further off of their slip planes [192]. Furthermore, extensions may be incorporated depending on the nature of the physics involved, such as to model cross slip [227, 223], kink diffusion [225], and climb mechanisms mediated by core and lattice diffusion [228, 229, 230].

In EasyDD, every segment is assigned a pre-defined normal vector, although it can be unreliable, as will be discussed in chapter 6. On the other hand, the normal vector of non-screw dislocations can in principle be calculated from other geometric quantities, such as the line and Burgers vectors. For instance, the glide plane of a non-screw dislocation can be determined by first computing $\hat{\boldsymbol{b}}_{ij} \times \boldsymbol{l}_{ij}$ and then comparing this habit plane normal vector to a set of admissible glide plane normals; the closest match is then assigned as the current glide plane for the segment [192]. In contrast, when cross slip is neglected, screw dislocations always present a challenge in defining an appropriate normal vector, as their glide plane is not uniquely determined by geometry alone. In such cases, the force acting on the dislocation can be used to infer the slip plane direction [192]. In practice, the optimal formulation will depend on the specific system being modelled and the desired level of resolution.

In principle, formulation (3.27) can be extended to accommodate multiple slip systems with anisotropic mobilities by assigning different mobility parameters to

[9] An alternative to this approach is to explicitly enforce glide constraints by projecting nodal velocities onto their glide planes.

segments associated with different slip systems. One could, for instance, treat non-screw segments by first detecting the closest slip system to which it belongs based on its orientation, and then treat this segment as strictly gliding on solely that single slip system. However, it is not immediately clear how one should interpolate drag properties across transitions between slip systems in a mathematically consistent way. Furthermore, a robust mobility law framework should enable the simple incorporation of additional slip systems as required by the physics of the material. To address these considerations, the HCP mobility law adopts an alternative construction of the drag tensor, which differs from that of equation (3.27). The HCP mobility law will be described in chapter 4.

3.4 Time integrators

Once the kinematics are determined through the mobility law, the nodal positions must then be updated. From the nodal velocities $\boldsymbol{v}_i$, the updated nodal positions $\boldsymbol{r}_i$ must be obtained by solving the ODE given by

$$\boldsymbol{v}_i \equiv \frac{\mathrm{d}\boldsymbol{x}_i}{\mathrm{d}t} = \boldsymbol{g}_i\left(\{\boldsymbol{x}_j\}\right) \tag{3.28}$$

where an evaluation of the function $\boldsymbol{g}_i$ involves solving for both the nodal forces and the mobility model. In general, the function $\boldsymbol{g}_i$ depends nonlinearly on the position of every node in the network. Because each node in the network in general moves at potentially drastically different rates, equation (3.28) is *stiff*[10], meaning that it involves a large range of disparate timescales. To numerically solve stiff ODEs, one must resolve the shortest timescale [231]. In DD, this corresponds to nodes with large velocities, especially during dislocation reactions or large stress conditions. These nodes can be very problematic, and induce drastic slowdowns of the simulation. This phenomenon may for instance arise from a large disparity between the line and glide drag coefficients, which can lead to undesired simulation stiffness wherein the velocity of nodes travelling in the fictitious line direction is much larger than those travelling in the glide direction. Apart from mitigating numerical instabilities related to inverting the drag tensor, this is another reason for assigning the line drag coefficient B_l to be of a similar order of magnitude as the glide drag coefficient B_g.

Explicit time integration methods solve for the updated nodal positions by only using information from the current time-step [231]. They tend to have small, finite

[10]This notion of stiffness is distinct from mechanical stiffness. When any confusion is possible in this text, the former will be referred to as *simulation* or *system* stiffness.

bounds on the time-step sizes which correspond to stable solutions, meaning that highly stiff ODEs typically require small time-steps to solve. *Implicit* methods solve for the updated nodal positions by using information from both the current time-step *and* the updated time-step; they tend to have large (sometimes infinite) bounds on the time-step sizes which correspond to stable solutions. The drawback is that each time-step requires solving an algebraic equation for the unknown updated time-step variables which can be computationally expensive and analytically challenging if $\boldsymbol{g}_i$ is a complicated function, which is often the case in DD.

Various strategies for alleviating stiffness in DD systems have been proposed and implemented in the literature [232, 233, 234, 235, 236]. While implicit solvers can accommodate larger time-step sizes, the increased computational cost and implementation complexity often diminish the overall benefit [233, 234, 235]. Furthermore, time-step subcycling—in which different nodes advance using different time-step sizes—has demonstrated significant computational speedups [233, 235, 236].

EasyDD uses the Euler-trapezoid method[11], which is an explicit time integration method commonly employed by DD codes such as ParaDiS [101]. The solution to the Euler-trapezoid method converges as $\mathcal{O}\left(\Delta t^2\right)$, which improves upon the $\mathcal{O}\left(\Delta t\right)$ convergence of the simple explicit Euler method [231]. It involves calculating the explicit *predictor* $\boldsymbol{x}_i^P$ and *corrector* $\boldsymbol{x}_i^C$ nodal positions, respectively given by

$$\boldsymbol{x}_i^P = \boldsymbol{x}_i^0 + \boldsymbol{g}_i\left(\{\boldsymbol{x}_j^0\}\right)\Delta t \tag{3.29}$$

$$\boldsymbol{x}_i^C = \boldsymbol{x}_i^0 + \frac{\boldsymbol{g}_i\left(\{\boldsymbol{x}_j^0\}\right) + \boldsymbol{g}_i\left(\{\boldsymbol{x}_j^P\}\right)}{2}\Delta t \tag{3.30}$$

where $\boldsymbol{x}_i^P$ predicts the solution using a potentially unstable explicit Euler method, and $\boldsymbol{x}_i^C$ is used to estimate the solution error. Here, Δt and $\boldsymbol{x}_i^0$ respectively denote the time-step size and the initial (or current) position of node n_i. The disadvantage of this method is that it requires performing two potentially expensive evaluations of $\boldsymbol{g}_i$ at each time-step. However, the trade-off is that, if the difference between $\boldsymbol{x}_i^P$ and $\boldsymbol{x}_i^C$ is outside some specified accuracy range, Δt may be decreased or increased to maximise computational efficiency. This provides an estimate of an appropriate size for Δt which solely depends on the current system configuration. Consequently, one may impose the conditions given by

$$\max_i\left\{|\boldsymbol{x}_i^C - \boldsymbol{x}_i^P|\right\} \leq r_{\text{tol}} \tag{3.31}$$

[11]The Euler-trapezoid method is also sometimes referred to as the Heun method or the explicit trapezoidal method.

and

$$\max_i \{|\boldsymbol{x}_i^P - \boldsymbol{x}_i^0|\} \leq r_{\max} \tag{3.32}$$

where r_{tol} and $r_{\max}$ are numerical tolerances.

During a given time-step, nodes are assumed to move with constant velocity. Condition (3.31) ensures that the time-step size remains small enough to preserve the constant velocity assumption, effectively detecting large nodal velocity *gradients*. In contrast, condition (3.32) prevents nodes from traveling excessive distances within a single time step, effectively detecting large nodal velocity *magnitudes*. Here, $r_{\max}$ represents the maximum permissible nodal displacement during a time-step. When the tolerances r_{tol} and $r_{\max}$ are appropriately assigned[12], the former condition is triggered by large velocity gradients (so-called "r_{tol}-dominated" states), while the latter condition is triggered by large velocity magnitudes (so-called "$r_{\max}$-dominated" states).

In EasyDD, if the time-step size Δt results in conditions which meet criteria (3.31) or (3.32), it is considered too large and is halved. If neither of these criteria are met, the time-step size is increased according to the rule given by

$$\Delta t \to \Delta t \Lambda_{\max} \left(1 + \frac{\epsilon_{\max}}{r_{\text{tol}}} \left(\Lambda_{\max}^q - 1\right)\right)^{-1/q} \tag{3.33}$$

where $\epsilon_{\max} \coloneqq \max_i \{|\boldsymbol{x}_i^C - \boldsymbol{x}_i^P|\}$ is the error associated with the nodal velocity gradient, $\Lambda_{\max} = 2$ is the maximum allowed time-step factor increase, and $q = 10$ parametrises the rate at which the time-step changes as a function of $\epsilon_{\max}$ [237, 192]. Furthermore, a maximum allowed time-step size of Δt_0 is enforced. For the simulations conducted in this text, a modified version of the time integrator described here was used and is presented in algorithm 2.

3.5 Topological operations

In DD simulations, changes in nodal connectivity are required to enable dislocation reactions and to optimise computational efficiency. EasyDD performs topological operations in roughly the following order:

1. Remeshing

2. Collisions

[12]The assignment of r_{tol} and $r_{\max}$ depend on the nature of the simulation and on the desired level of plasticity.

3. Separations

This order is fairly non-commutative, although it may be altered for some applications. In this section, these topological operations will be summarised in brief; for an in-depth overview, see the culmination of work conducted by Bromage [192] and Celis-Garza [237].

3.5.1 Remeshing

The remeshing module balances accuracy and efficiency by refining or coarsening the DD network discretisation. It is applied only to discretisation nodes (those with two connections) to maintain resolution of dislocation curvature while minimising force evaluations—physical nodes remain unaltered. Nodes connecting two segments with different normal vectors are never coarsened. Furthermore, when a segment is refined into two, both new segments inherit the normal vector of the original segment. The discrete topology of the DD network necessitates the introduction of four additional computational parameters: the minimum and maximum allowed segment length $L_{\min}$ and $L_{\max}$, and the minimum and maximum allowed area formed by three consecutive nodes $A_{\min}$ and $A_{\max}$.

If the length of a segment is greater than $L_{\max}$, a node is created at its midpoint, thus dividing it in two. If the length of a segment is less than $L_{\min}$, it is merged with an adjacent segment, which involves deleting a node. This implicitly introduces the necessary input constraint $L_{\max} > 2L_{\min}$. A node is never created or deleted if this would result in a segment length being shorter than $L_{\min}$ or longer than $L_{\max}$.

The remeshing algorithm identifies regions of high curvature in the network by computing the area A_i of the triangle formed by the discretization node n_i and its two neighbours n_j and n_k. The corresponding area given by

$$A_i = \frac{1}{2} \left| \left(\boldsymbol{x}_j - \boldsymbol{x}_i \right) \times \left(\boldsymbol{x}_k - \boldsymbol{x}_i \right) \right| \tag{3.34}$$

is computed for every discretisation node in a remeshing step. If $A_i > A_{\max}$, a discretisation node is placed at the midpoint of the longest attached segment (Γ_{ij} or Γ_{ik}). On the other hand, if $A_i < A_{\min}$ and $\dot{A}_i < 0$[13], the two segments Γ_{ij} and Γ_{ik} are combined to form a single segment Γ_{jk} connecting the node at position $\boldsymbol{x}_j$ to the node at position $\boldsymbol{x}_k$.

[13]The area rate of change $\dot{A}_i$ can easily be determined through the identity given by

$$\frac{\mathrm{d}}{\mathrm{d}t} |\boldsymbol{u} \times \boldsymbol{v}| = \frac{(\boldsymbol{u} \times \boldsymbol{v})}{|\boldsymbol{u} \times \boldsymbol{v}|} \cdot \left(\frac{\mathrm{d}\boldsymbol{u}}{\mathrm{d}t} \times \boldsymbol{v} + \boldsymbol{u} \times \frac{\mathrm{d}\boldsymbol{v}}{\mathrm{d}t} \right)$$

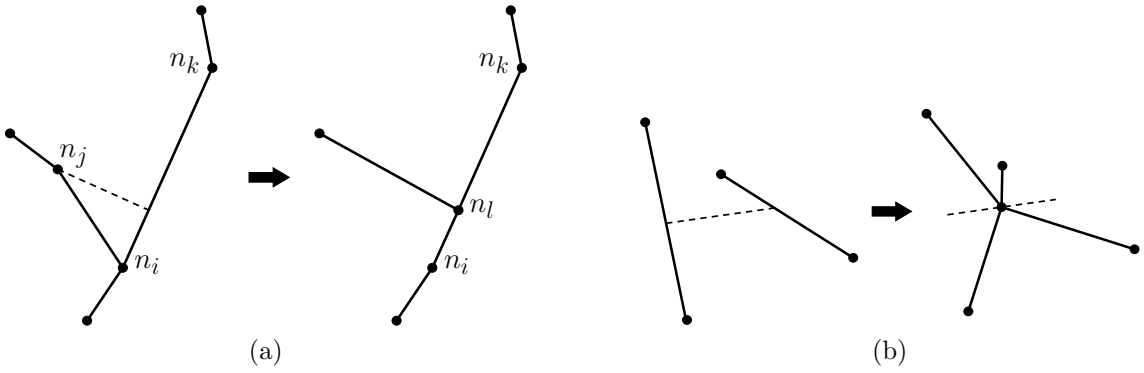


Figure 3.2: Diagram depicting the treatment of (a) a hinge collision and (b) a two-line collision. The solid black lines and circles respectively represent the dislocation segments and nodes. For each case, the dotted black line respectively represents (a) the minimum distance between node n_j and segment Γ_{ik} and (b) the minimum distance between the two segments in the initial configuration.

3.5.2 Collisions

To accurately model dislocation reactions, a correct treatment of segment-segment collisions is essential. In EasyDD, there are two types of collisions: those between segments which are connected to each other—so-called *hinge* collisions—and those between segments which are *not* connected to each other—so-called *two-line* collisions. Overall, the collisions module exhibits $\mathcal{O}(M^2)$ time scaling, where M is the number of segments.

To maintain network stability, all possible hinge collisions in a network are always detected and resolved before treating two-line collisions. Consider two segments Γ_{ij} and Γ_{ik} which are mutually attached at node n_i (see figure 3.2a). The following two quantities are calculated: (1) the minimum distance between node n_j and segment Γ_{ik} and (2) the minimum distance between node n_k and segment Γ_{ij}. If one of these distances is less than the annihilation distance r_{ann}, which is an additional input parameter, a new node is created at the point on the corresponding segment which is closest to the node from which the distance calculation was made. For instance, if distance (1) is less than r_{ann}, a node n_l is created at the point on segment Γ_{ik} which is closest to node n_j. Furthermore, node n_j is merged with node n_l, meaning that node n_j is deleted and all of its connections are transferred to node n_l while preserving Burgers vector conservation. If both of these distances are less than r_{ann}, then the minimum of the two is selected and the corresponding operation is conducted.

Two segments are treated as a two-line collision if their minimum mutual distance is less than r_{ann}. Furthermore, their minimum mutual distances must be decreasing,

which can be determined from the velocities of all four of the involved nodes. To ensure the uniqueness of the final configuration, two-line collisions are resolved in order of increasing minimum mutual distances. Suppose two segments are selected to be processed as a two-line collision. Nodes are created at the points on each segment which are closest to the opposing segment. These nodes are then merged as shown in figure 3.2b.

3.5.3 Separations

The separation module is necessary to separate every highly connected node into two nodes which each has fewer connections, thereby enabling the modelling of dislocation reactions. In EasyDD, any node connected to more than three segments is a candidate for separation. Once a node is flagged for separation, all of the ways that it can be split into two nodes—so-called *splitting modes*—are determined. A single splitting mode is created by assigning each of the segments attached to the initial node to one of the two new nodes created by the split.

The total power dissipation of the network is given by

$$\dot{\mathcal{P}} = \sum_{i=1}^{N} \boldsymbol{f}_i \cdot \boldsymbol{v}_i \tag{3.35}$$

where N is the total number of nodes in the network. The final configuration is then selected based on the maximum power dissipation criterion, i.e. the splitting mode which maximises $\dot{\mathcal{P}}$ is selected [101]. If necessary, a sequence of splitting operations will take place until, in principle, the mode corresponding to the maximum power dissipation is achieved. For a single node with k_i connections, the total number of possible splitting modes is given by

$$M_{\text{split}} = \sum_{j=2}^{\lfloor k_i/2 \rfloor} \frac{k_i!}{(k_i - j)!j!} \tag{3.36}$$

where $\lfloor \cdot \rfloor$ denotes the floor function. This means that, in densely connected networks, the separation module exhibits a poor time scaling with a worst-case upper bound of $\mathcal{O}\left(N!\right)$[14]. However, in EasyDD, two important assumptions are made which greatly minimise computational costs. First, it is assumed that a splitting event does not affect the forces and velocities of nodes which are not involved in the split. Second, a greedy algorithm [238] is used: the locally optimal choice is made at each step of the splitting tree, and backtracking is forbidden.

[14]This assumes that the average number of connections per node scales with the number of nodes.

Splitting procedure

Consider a splitting operation that acts on node n_A (at position $\boldsymbol{x}_A$) to create two child nodes n_B and n_C. The velocities $\boldsymbol{v}_B$ and $\boldsymbol{v}_C$ of the child nodes are evaluated while they are both temporarily coincident with position $\boldsymbol{x}_A$. If the creation of a segment Γ_{BC} is required to preserve Burgers vector conservation, this segment is instantiated with zero length at this intermediary stage and therefore does not influence $\boldsymbol{v}_B$ or $\boldsymbol{v}_C$. However, because the child nodes differ in connectivity, these nodal velocities may nevertheless be distinct.

Upon calculation of the nodal velocities $\boldsymbol{v}_B$ and $\boldsymbol{v}_C$, the node with the greatest speed is displaced from position $\boldsymbol{x}_A$ along its velocity direction by a distance $r_{\text{dis}} = r_{\text{ann}} + \delta$ for some small $\delta > 0$; the other node remains at position $\boldsymbol{x}_A$. If a segment must connect nodes n_B and n_C, its normal vector $\boldsymbol{n}_{BC}$ must be calculated. For a non-screw segment it is calculated via $\boldsymbol{n}_{BC} = \boldsymbol{l}_{BC} \times \hat{\boldsymbol{b}}_{BC}$ (modulo normalisation) and for a pure screw segment it is calculated via

$$\boldsymbol{n}_{BC} = \boldsymbol{l}_{BC} \times (\boldsymbol{v}_B + \boldsymbol{v}_C) \tag{3.37}$$

Because the line direction $\boldsymbol{l}_{BC}$ depends on the nodal velocities, the normal vector assignment is strongly coupled with the mobility law. Consequently, when climb is enabled and thus nodal velocities can have climb components, the resulting normal vector assignments for segments created from a splitting procedure can be unexpected. Furthermore, if $\boldsymbol{v}_B$ and $\boldsymbol{v}_C$ are both parallel to $\boldsymbol{l}_{BC}$ in the pure screw case, the resulting normal vector becomes zero and thus spurious. If improperly treated, these issues can present major challenges to a DD simulation, and lead to a large population of unreliable or spurious normal vectors throughout the dislocation network.

Dislocation reactions in HCP

It should be noted that the topological operations described thus far cannot model the decomposition of composite dislocations. Consequently, EasyDD cannot model the dissociation of the elastically unstable $\langle c+a \rangle$ dislocation configurations, which are believed to be important dissociation modes in HCP materials [239, 132, 240, 241]. Aubry *et al.* [84] defined a new topological operator which is necessary to capture the decomposition $\langle c+a \rangle \rightarrow \langle c \rangle + \langle a \rangle$. The implementation of this topological operator into EasyDD should be considered as an avenue of future work. In this text, only $\langle a \rangle$-type dislocations are considered.

3.6 Finite domain simulations

3.6.1 DD-FEM coupling

DD models can be coupled to finite element methods (FEMs), thereby enabling the modelling of finite domains. The two most common coupling methods are the superposition principle method (SPM) [109, 242, 243, 232] and the discrete-continuous method (DCM) [244, 177, 245, 246, 247]. In the DCM, the plastic strain resulting from dislocation motion is incorporated directly into an elastic FEM model to compute the total stress, thereby circumventing the expensive segment-segment interaction force calculation. The trade-off is that the resolution of the DCM is limited by the size of the elements in the finite element (FE) mesh. As the number of dislocation segments increases relative to the resolution of the finite elements, the DCM becomes increasingly computationally efficient compared to the SPM.

EasyDD employs the SPM, which is outlined in the following. Consider a finite volume V consisting of a linearly elastic medium bounded by a surface S. Let the surface be partitioned into two components: S_U, on which displacement boundary conditions $\boldsymbol{U}$ are specified, and S_T, on which traction boundary conditions $\boldsymbol{T}$ are specified. This problem can be solved via FEM using standard methods [248], which introduces a population of FE nodes and elements within the domain. Furthermore, suppose that a dislocation network is introduced within V. Let us denote by $\tilde{(\cdot)}$ the fields generated by the dislocation network inside an infinite medium. Since the dislocation-induced fields are non-zero on the boundary S, they modify the imposed boundary conditions, and hence introduce corrective image fields associated with the finite domain, here denoted by $\hat{(\cdot)}$. The dislocation-induced displacements $\tilde{\boldsymbol{U}}$ [249] and tractions $\tilde{\boldsymbol{T}}$ [250] can be solved analytically on the FE surface nodes for any arbitrary dislocation configuration. Subsequently, one can use the modified boundary conditions $\hat{\boldsymbol{U}} = \boldsymbol{U} - \tilde{\boldsymbol{U}}$ and $\hat{\boldsymbol{T}} = \boldsymbol{T} - \tilde{\boldsymbol{T}}$ to solve the linear elastic field equations given by

$$\boldsymbol{\nabla} \cdot \hat{\sigma} = 0 \quad \text{in} \quad V \tag{3.38}$$

$$\hat{\sigma} = \mathcal{C} : \hat{\epsilon} \quad \text{in} \quad V \tag{3.39}$$

$$\hat{\epsilon} = \frac{1}{2}\left(\boldsymbol{\nabla}\hat{\boldsymbol{u}} + (\boldsymbol{\nabla}\hat{\boldsymbol{u}})^{\intercal}\right) \quad \text{in} \quad V \tag{3.40}$$

$$\hat{\sigma} \cdot \boldsymbol{n} = \hat{\boldsymbol{T}} \quad \text{on} \quad S_T \tag{3.41}$$

$$\hat{\boldsymbol{u}} = \hat{\boldsymbol{U}} \quad \text{on} \quad S_U \tag{3.42}$$

to obtain the corrective stress field $\hat{\sigma}$. Here, $\hat{\epsilon}$ represents the corrective strain field, $\hat{\boldsymbol{u}}$ the corrective displacement field, $\mathcal{C}$ the fourth-rank elasticity tensor, and $\boldsymbol{n}$ the outward-facing surface normal vector of the surface S. Furthermore, the dislocation-induced stress field $\tilde{\sigma}$ can be computed at any field point using equation (3.16). The dislocation-induced tractions can be calculated at the surface using $\tilde{\boldsymbol{T}} = \tilde{\sigma} \cdot \boldsymbol{n}$; the calculation of the dislocation-induced displacements is more involved and will be discussed in section 3.6.3. Following from the linearity of the elastic equations, one may then construct the total stress field within the domain via the additive superposition $\sigma = \tilde{\sigma} + \hat{\sigma}$.

3.6.2 Surface exit of dislocations

To create realistic DD simulations in a finite domain, dislocations must be allowed to exit the domain; this is how plastic slip steps are generated on the surface of a material. The SPM necessitates the calculation of dislocation-induced displacement fields $\tilde{\boldsymbol{u}}$ on the domain surface. However, these fields and their corresponding analytical expressions can only be fully evaluated for closed dislocation loops [251, 252, 253]. Therefore, to enable the calculation of dislocation-induced displacement fields, so-called *virtual* dislocations are necessary to complete a dislocation loop which has partially exited [249]. These virtual dislocation segments extend to a distance very far away from the domain, and do not generate a stress field. In EasyDD, virtual segments are tracked during the entire duration of a DD simulation.

Furthermore, this framework also necessitates the proper treatment of dislocation segments intersecting the domain boundary. When a segment intersects a surface, a *surface node* is created at the point of intersection. Surface nodes mostly follow similar kinematic rules as other nodes in the network but are constrained to remain on the surface throughout the simulation. Surface nodes are simultaneously connected to both internal nodes and virtual (external) nodes.

Exited nodes become virtual nodes through the process depicted in figure 3.3. Once a previously internal and non-virtual node is detected outside of the domain, surface nodes are created at the points of intersection between its connected segments and the surface. The normal vectors of the newly-created internal surface connecting segments are assigned using part of the splitting procedure discussed in section 3.5.3; for a pure screw segment, equation (3.37) is used for the assignment, where the two velocities used are those of the exited node and the internal node. The exited node is then moved to the point through which it penetrated the surface, which is determined from its velocity. From this point, the exited node is extended outwards

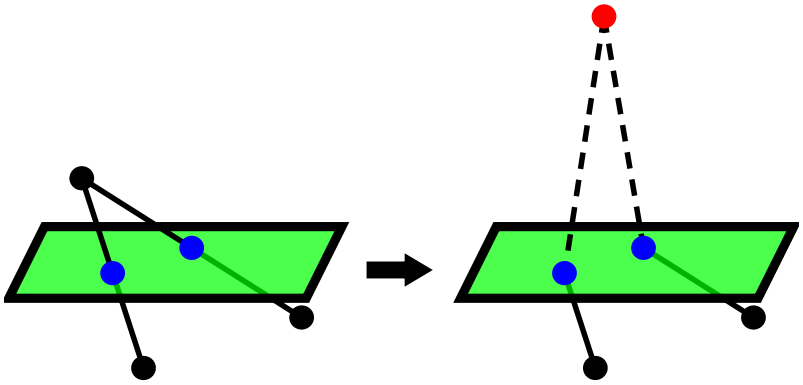


Figure 3.3: Diagram depicting the transformation of an exited internal node into a virtual node. The black, blue, and red solid circles respectively represent internal, surface, and virtual nodes; the black solid and dotted lines respectively represent internal (i.e. non-virtual) and virtual segments. The green parallelogram with the solid black border represents a surface of the domain.

in the direction of the surface normal vector by a distance which is very large relative to the domain size. Finally, the exited node is designated as virtual. If a surface node is connected to only virtual nodes, it is similarly extended and designated as virtual. Since the virtual node extension distance is fixed throughout a simulation, all virtual nodes corresponding to dislocations that have exited out of a given surface have the same shortest distance to that surface. Virtual segments are those which connect virtual nodes to either surface nodes or other virtual nodes.

If a dislocation penetrates S_U, it leaves a localised slip step at the point where it exited. Consequently, the corrective FE system must align the slip step to satisfy the displacement boundary conditions, which generates a large and unphysical stress within the domain. Furthermore, displacement-controlled surfaces present in DD simulations often represent faces where the test sample connects to the rest of the bulk material. For instance, in DD simulations of micro-tensile tests (such as those presented in chapter 6), the test sample (see figures 6.10 and 6.11) includes two opposing faces that connect to the bulk, but which are usually modelled as displacement-controlled. Since dislocations experience significant repulsion from these surfaces, their presence in this type of DD simulation introduces unphysical artefacts even if dislocations do not penetrate them.

There exist multiple strategies of dealing with dislocations colliding with displacement-controlled boundaries. A commonly used [65, 249, 237, 192] solution is to permanently fix any dislocations which collide with S_U, thereby treating these surfaces as fully impenetrable. This method is implemented in the DD simulations

conducted in chapter 6.

3.6.3 Dislocation-induced displacements

Consider an arbitrary dislocation loop C which bounds some surface A with an area vector $\boldsymbol{A} = \hat{\boldsymbol{s}}A$, where $\hat{\boldsymbol{s}}$ is a surface unit normal vector oriented such that its positive direction—pointing away from the positive side of A—is related to the unit line direction $\boldsymbol{l}'$ along the dislocation loop via the right hand rule. The resulting displacement field $\tilde{\boldsymbol{u}}$ evaluated at a field point $\boldsymbol{r}$ is given by [251]

$$\tilde{\boldsymbol{u}}\left(\boldsymbol{r}\right) = \tilde{\boldsymbol{u}}^{\Omega}\left(\boldsymbol{r}\right) + \tilde{\boldsymbol{u}}^{e}\left(\boldsymbol{r}\right) \tag{3.43}$$

where

$$\tilde{\boldsymbol{u}}^{\Omega}\left(\boldsymbol{r}\right) \coloneqq -\frac{\boldsymbol{b}}{4\pi}\Omega\left(\boldsymbol{r}\right) \tag{3.44}$$

$$\tilde{\boldsymbol{u}}^{e}\left(\boldsymbol{r}\right) \coloneqq -\frac{1}{8\pi\left(1-\nu\right)}\oint_{C}\frac{1}{R}\left[\left(1-2\nu\right)\boldsymbol{b}\times\boldsymbol{l}' + \left[\hat{\boldsymbol{R}}\cdot\left(\boldsymbol{b}\times\boldsymbol{l}'\right)\right]\hat{\boldsymbol{R}}\right]\mathrm{d}L' \tag{3.45}$$

such that $\boldsymbol{R} \equiv \boldsymbol{r} - \boldsymbol{r}'$, $R \equiv |\boldsymbol{R}|$, and $\hat{\boldsymbol{R}} \equiv \boldsymbol{R}/R$. Furthermore,

$$\Omega\left(\boldsymbol{r}\right) = \int_{A}\frac{\boldsymbol{R}\cdot\mathrm{d}\boldsymbol{A}}{R^{3}} \tag{3.46}$$

is the solid angle through which the positive side of A is observed from the field point $\boldsymbol{r}$. The solid angle displacement term $\tilde{\boldsymbol{u}}^{\Omega}$—which exhibits a discontinuity of $\pm\boldsymbol{b}/2$ across the slip plane area bounded by the loop—accounts for the permanent plastic deformation of the material as the loop evolves, in addition to the plastic slip step produced by a loop which has partially or fully exited from the domain. At distances r from the loop centroid which are large relative to the loop size, the solid angle term decays as $1/r^2$. On the other hand, the line integral term $\tilde{\boldsymbol{u}}^{e}$ accounts for the elastic displacements produced by the segments of the loop, and is independent of its slip history. It is unambiguously defined for an isolated finite dislocation segment, for which it tends towards zero as the field point moves to infinity.

Equation (3.43) can be evaluated for a general dislocation network composed of piecewise straight segments (both internal and virtual) by decomposing the network into triangular loops, each consisting of a network segment and two non-network segments joined to a closure point [254, 249]. Barnett's formula [252, 253] for the displacement field generated by an arbitrary triangular loop is then evaluated at a field point on the domain surface and summed for each network segment contribution. Only a single closure point within the domain is necessary to compute

the contribution due to all internal segments. In contrast, a unique closure point must be created outside the domain for each exterior virtual segment that does not connect to an internal segment [249]. The elastic displacements from virtual segments are ignored, while the total solid angle has non-zero contributions from all segments. Therefore, the determination of $\tilde{\boldsymbol{u}}^e$ on the domain surface depends purely on the internal segments, while the determination of $\tilde{\boldsymbol{u}}^\Omega$ additionally depends on the location and orientation of exited segments, and hence necessitates the tracking of virtual segments.

The overall computation of $\tilde{\boldsymbol{u}}$ time scales as $\mathcal{O}(N_T)$, where N_T is the total number of network segments including virtual segments. In certain conditions, this can lead to very poor computational efficiency. This issue is particularly prevalent in uniaxial loading conditions, since dislocation sources therein are not naturally limited by pile-up mechanisms as in cantilever bending conditions, in which the neutral axis is a pile-up zone. In some cases, such as in a single-source or source-limited strengthening [255, 256] regime, dislocations can freely exit the domain without restriction, resulting in a rate of generation of virtual segments that is much larger than the rate of generation of internal segments. In such conditions, achieving large strains can become computationally infeasible even when the internal dislocation density is small.

To account for this issue, topological operations can be conducted on the virtual network to minimise its degrees of freedom. In EasyDD, virtual segments are remeshed in a manner similar to section 3.5.1: a virtual segment is merged with an adjacent virtual segment if (1) its length is below a critical threshold of $10b$ and (2) both segments are near parallel. However, EasyDD does not conduct topological recombinations of non-connected virtual segments, which would be necessary to address computational issues associated with resolving multiple exited loops. For instance, the virtual network could undergo a collision-type process and recombine non-connected virtual segments by superposing their Burgers vectors. Although this approach can result in information loss, the computational enhancements would in some cases be drastic. This should be considered as an area of future improvements to EasyDD.

Chapter 4

HCP mobility law

Chapter introduction

In this chapter, the HCP mobility law is thoroughly elucidated. In section 4.1, the geometry of the HCP crystal structure is described and visualised. In section 4.2, the basic framework of the HCP mobility law is described in detail. In section 4.3, the implications of the methods employed by the HCP mobility law are articulated, and the basic framework is extended. In section 4.4, a method of deriving analytical relationships between drag functions and their corresponding spatial dislocation distributions is proposed. Finally, simulations are conducted and analysed to further investigate the HCP mobility law. In section 4.5, conclusions and future work regarding the HCP mobility law are discussed. Note that all of the content in this chapter is original work, and large portions (section 4.1 and much of section 4.2) are published in Hortelano-Roig *et al.* [1].

4.1 HCP crystallography

The geometry of the HCP crystal may be described by the Miller-Bravais system, which denotes families of planes using the four indices $(hkil)$ such that $h + k + i = 0$ [257]. The direct HCP lattice vectors are conventionally defined as the linearly

dependent set of vectors given by

$$\begin{aligned} \boldsymbol{a}_1 &= a\left(-\frac{1}{2}\hat{\boldsymbol{x}} + \frac{\sqrt{3}}{2}\hat{\boldsymbol{y}}\right) \\ \boldsymbol{a}_2 &= a\left(-\frac{1}{2}\hat{\boldsymbol{x}} - \frac{\sqrt{3}}{2}\hat{\boldsymbol{y}}\right) \\ \boldsymbol{a}_3 &= a\hat{\boldsymbol{x}} \\ \boldsymbol{a}_4 &= c\hat{\boldsymbol{z}} \end{aligned} \tag{4.1}$$

where $\hat{\boldsymbol{x}}$, $\hat{\boldsymbol{y}}$, and $\hat{\boldsymbol{z}}$ are the unit Cartesian basis vectors, and a and c are the two HCP lattice parameters. The redundant index i facilitates the identification of symmetries present in the HCP system. Therefore, a given set of Miller-Bravais indices denotes the family of planes perpendicular to the normal vector which may be constructed via

$$\boldsymbol{n} = h\boldsymbol{a}_1^* + k\boldsymbol{a}_2^* + l\boldsymbol{a}_4^* \tag{4.2}$$

where $\{\boldsymbol{a}_1^*, \boldsymbol{a}_2^*, \boldsymbol{a}_4^*\}$ denotes the reciprocal lattice basis corresponding to the direct basis $\{\boldsymbol{a}_1, \boldsymbol{a}_2, \boldsymbol{a}_4\}$. The notation $[hkil]$ refers to a vector $\boldsymbol{b}$ expressed as a linear combination of the direct HCP lattice vectors via

$$\boldsymbol{b} = h\boldsymbol{a}_1 + k\boldsymbol{a}_2 + i\boldsymbol{a}_3 + l\boldsymbol{a}_4 \tag{4.3}$$

Table 4.1 contains all the possible HCP slip systems (i.e. all combinations of Burgers and normal vectors) considered in this text. See figure 4.1 for a visualisation of all the slip systems and corresponding slip planes. The notation for plane types used in this text is based on the notation used by [84] and [1], which consists of an integer referring to the glissile Burgers vector, followed by a combination of letters and Roman numerals which refer to the slip plane. There are five different slip plane types considered: $\{0001\}$ basal (Ba), $\{10\bar{1}0\}$ prismatic (Pr), $\{10\bar{1}1\}$ primary pyramidal type I (PyI), $\{10\bar{1}1\}$ primary pyramidal type II (PyII), and $\{11\bar{2}2\}$ secondary pyramidal (sP). The three types of Burgers vectors — $\langle a\rangle$, $\langle a+c\rangle$, and $\langle c\rangle$ — are labelled according to the lattice parameters which must be used to describe them, and respectively correspond to Burgers vectors $\boldsymbol{b}_1$ to $\boldsymbol{b}_3$, $\boldsymbol{b}_4$ to $\boldsymbol{b}_9$, and $\boldsymbol{b}_{10}$ in Table 4.1[1].

[1]Some errors present in Hortelano-Roig *et al.* [1] have been corrected in this table.

Table 4.1: HCP slip systems. $\rho = c/a$ represents the HCP axes ratio. The Cartesian representation of the Burgers vector is expressed as $\boldsymbol{b}_i/a$.

Burgers vector		**Normal vector**		**Plane type**
Miller-Bravais	Cartesian	Miller-Bravais	Cartesian	
$\boldsymbol{b}_1 = 1/3\left[2\bar{1}\bar{1}0\right]$	$\left[-\frac{1}{2}, \frac{\sqrt{3}}{2}, 0\right]$	$\left(0001\right)$	$\left[0, 0, 1\right]$	1Ba
		$\left(01\bar{1}0\right)$	$\left[-\frac{\sqrt{3}}{2}, -\frac{1}{2}, 0\right]$	1Pr
		$\left(01\bar{1}1\right)$	$\left[-\sqrt{3}\rho, -\rho, \sqrt{3}\right] / \sqrt{3+4\rho^2}$	1PyI
		$\left(0\bar{1}11\right)$	$\left[\sqrt{3}\rho, \rho, \sqrt{3}\right] / \sqrt{3+4\rho^2}$	1PyII
$\boldsymbol{b}_2 = 1/3\left[\bar{1}\bar{1}20\right]$	$\left[-\frac{1}{2}, -\frac{\sqrt{3}}{2}, 0\right]^1$	$\left(0001\right)$	$\left[0, 0, 1\right]$	2Ba
		$\left(1\bar{1}00\right)$	$\left[0, 1, 0\right]$	2Pr
		$\left(1\bar{1}01\right)$	$\left[0, 2\rho, \sqrt{3}\right] / \sqrt{3+4\rho^2}$	2PyI
		$\left(\bar{1}101\right)$	$\left[0, -2\rho, \sqrt{3}\right] / \sqrt{3+4\rho^2}$	2PyII
$\boldsymbol{b}_3 = 1/3\left[\bar{1}2\bar{1}0\right]$	$\left[1, 0, 0\right]^2$	$\left(0001\right)$	$\left[0, 0, 1\right]$	3Ba
		$\left(\bar{1}010\right)$	$\left[\frac{\sqrt{3}}{2}, -\frac{1}{2}, 0\right]$	3Pr
		$\left(\bar{1}011\right)$	$\left[\sqrt{3}\rho, -\rho, \sqrt{3}\right] / \sqrt{3+4\rho^2}$	3PyI
		$\left(10\bar{1}1\right)$	$\left[-\sqrt{3}\rho, \rho, \sqrt{3}\right] / \sqrt{3+4\rho^2}$	3PyII
$\boldsymbol{b}_4 = 1/3\left[2\bar{1}\bar{1}3\right]$	$\left[-\frac{1}{2}, \frac{\sqrt{3}}{2}, \rho\right]^3$	$\left(01\bar{1}0\right)$	$\left[-\frac{\sqrt{3}}{2}, -\frac{1}{2}, 0\right]$	4Pr
		$\left(\bar{1}011\right)$	$\left[\frac{\sqrt{3}}{2}, -\frac{1}{2}, 0\right]$	4PyI
		$\left(\bar{1}101\right)$	$\left[0, -2\rho, \sqrt{3}\right] / \sqrt{3+4\rho^2}$	4PyII
		$\left(\bar{2}112\right)$	$\left[\rho, -\sqrt{3}\rho, 2\right] / \sqrt{4+4\rho^2}$	4sP
$\boldsymbol{b}_5 = 1/3\left[2\bar{1}\bar{1}\bar{3}\right]$	$\left[-\frac{1}{2}, \frac{\sqrt{3}}{2}, -\rho\right]$	$\left(01\bar{1}0\right)$	$\left[-\frac{\sqrt{3}}{2}, -\frac{1}{2}, 0\right]$	5Pr
		$\left(10\bar{1}1\right)$	$\left[-\sqrt{3}\rho, \rho, \sqrt{3}\right] / \sqrt{3+4\rho^2}$	5PyI
		$\left(1\bar{1}01\right)$	$\left[0, 2\rho, \sqrt{3}\right] / \sqrt{3+4\rho^2}$	5PyII
		$\left(2\bar{1}\bar{1}2\right)$	$\left[-\rho, \sqrt{3}\rho, 2\right] / \sqrt{4+4\rho^2}$	5sP
$\boldsymbol{b}_6 = 1/3\left[\bar{1}\bar{1}23\right]$	$\left[1, 0, \rho\right]$	$\left(1\bar{1}00\right)$	$\left[0, 0, 1\right]$	6Pr
		$\left(10\bar{1}1\right)$	$\left[-\sqrt{3}\rho, \rho, \sqrt{3}\right] / \sqrt{3+4\rho^2}$	6PyI
		$\left(01\bar{1}1\right)$	$\left[-\sqrt{3}\rho, -\rho, \sqrt{3}\right] / \sqrt{3+4\rho^2}$	6PyII
		$\left(11\bar{2}2\right)$	$\left[-2\rho, 0, 2\right] / \sqrt{4+4\rho^2}$	6sP
$\boldsymbol{b}_7 = 1/3\left[\bar{1}\bar{1}2\bar{3}\right]$	$\left[1, 0, -\rho\right]$	$\left(1\bar{1}00\right)$	$\left[0, 0, 1\right]$	7Pr
		$\left(\bar{1}011\right)$	$\left[\frac{\sqrt{3}}{2}, -\frac{1}{2}, 0\right]$	7PyI
		$\left(0\bar{1}11\right)$	$\left[\sqrt{3}\rho, \rho, \sqrt{3}\right] / \sqrt{3+4\rho^2}$	7PyII
		$\left(\bar{1}\bar{1}22\right)$	$\left[2\rho, 0, 2\right] / \sqrt{4+4\rho^2}$	7sP
$\boldsymbol{b}_8 = 1/3\left[\bar{1}2\bar{1}3\right]$	$\left[-\frac{1}{2}, -\frac{\sqrt{3}}{2}, \rho\right]$	$\left(\bar{1}010\right)$	$\left[\frac{\sqrt{3}}{2}, -\frac{1}{2}, 0\right]$	8Pr
		$\left(1\bar{1}01\right)$	$\left[0, 2\rho, \sqrt{3}\right] / \sqrt{3+4\rho^2}$	8PyI
		$\left(0\bar{1}11\right)$	$\left[\sqrt{3}\rho, \rho, \sqrt{3}\right] / \sqrt{3+4\rho^2}$	8PyII
		$\left(1\bar{2}12\right)$	$\left[\rho, \sqrt{3}\rho, 2\right] / \sqrt{4+4\rho^2}$	8sP

Burger's vector		**Normal vector**		**Plane type**
Miller-Bravais	Cartesian	Miller-Bravais	Cartesian	
$\boldsymbol{b}_9 = 1/3\left[\bar{1}2\bar{1}\bar{3}\right]$	$\left[-\frac{1}{2}, -\frac{\sqrt{3}}{2}, -\rho\right]$	$\left(\bar{1}101\right)$	$\left[0, -2\rho, \sqrt{3}\right] / \sqrt{3+4\rho^2}$	9Pr
		$\left(01\bar{1}1\right)$	$\left[-\sqrt{3}\rho, -\rho, \sqrt{3}\right] / \sqrt{3+4\rho^2}$	9PyI
		$\left(\bar{1}101\right)$	$\left[0, -2\rho, \sqrt{3}\right] / \sqrt{3+4\rho^2}$	9PyII
		$\left(\bar{1}2\bar{1}2\right)$	$\left[-\rho, -\sqrt{3}\rho, 2\right] / \sqrt{4+4\rho^2}$	9sP
$\boldsymbol{b}_{10} = \left[0001\right]$	$\left[0, 0, \rho\right]$	$\left(01\bar{1}0\right)$	$\left[-\frac{\sqrt{3}}{2}, -\frac{1}{2}, 0\right]$	10PrI
		$\left(\bar{1}010\right)$	$\left[\frac{\sqrt{3}}{2}, -\frac{1}{2}, 0\right]$	10PrII
		$\left(1\bar{1}00\right)$	$\left[0, 0, 1\right]$	10PrIII

4.2 Dislocation kinematics

4.2.1 Drag tensor construction

As discussed in section 3.3, the construction of the drag tensor is a necessary step in solving the dislocation kinematics within the mobility law. In non-HCP mobility laws, the drag tensor is typically constructed according to expression (3.27). This approach is often adequate for FCC and BCC crystal structures, where it is reasonable to assume that anisotropies in mobility are not significant across different slip systems. However, in HCP crystal structures—where dislocation mobilities exhibit strong anisotropy depending on the slip system—this construction method may lack the necessary sophistication to accurately capture these anisotropic effects. To address this, an alternative method for constructing the drag tensor should be considered which, if necessary, facilitates the incorporation of additional slip systems to the model. This is one advantage of the HCP mobility law presented in this chapter. In this section, the drag tensor construction method originally proposed by Aubry *et al.* [84], which was developed as part of the HCP mobility law, will be presented and elucidated in detail. Note that cross slip is not included in this model.

The drag tensor depends on empirically-determined data which in practice is obtained for pure screw and pure edge dislocations for a limited set of glide planes. Consider a pure screw and a pure edge segment with respective drag tensors $\mathcal{B}^s_{ij}$ and $\mathcal{B}^{eq}_{ij}$ with orientations on slip systems for which there exists empirical data. Suppose that, for a segment with a given Burgers vector, there are N available edge-type

[1] (Table row for $\boldsymbol{b}_2$) Corrected from $\left[1, 0, 0\right]$ in [1].

[2] (Table row for $\boldsymbol{b}_3$) Corrected from $\left[-\frac{1}{2}, -\frac{\sqrt{3}}{2}, 0\right]$ in [1].

[3] (Table row for $\boldsymbol{b}_4$) Corrected from $\left[-\frac{1}{2}, \frac{\sqrt{3}}{2}, 0\right]$ in [1].

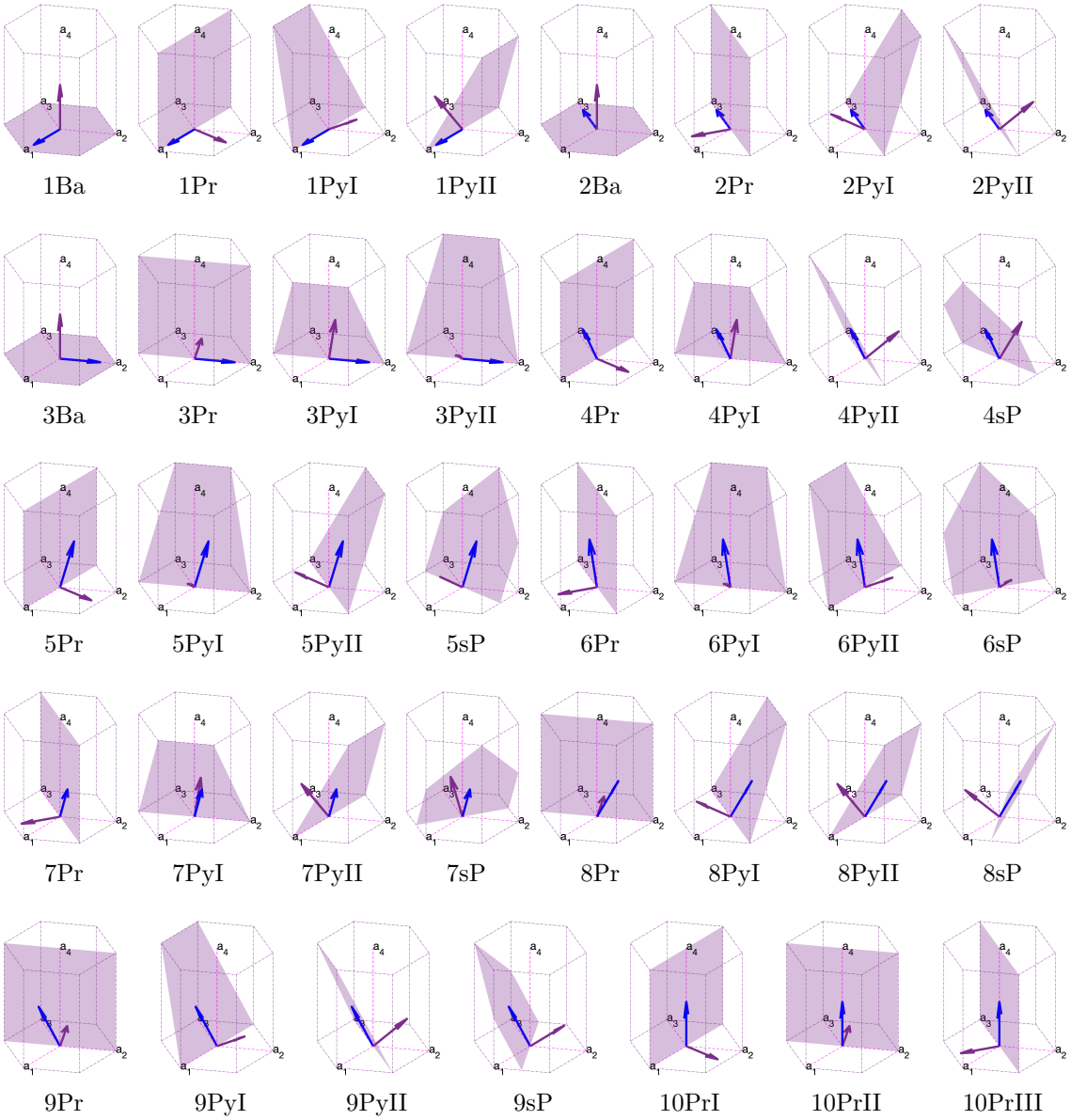


Figure 4.1: Geometry of HCP slip systems including corresponding slip planes. The blue and magenta vectors are of arbitrary magnitude and respectively represent the direction of the burgers and normal vectors.

orientations denoted by the index q. These drag tensors may be constructed via a linear combination of rank-1 symmetric matrices expressed as

$$\begin{aligned} \mathcal{B}^{s}_{ij} &= B^{\text{line}} \boldsymbol{l}_s \otimes \boldsymbol{l}_s + B^{\text{glide}}_{\text{screw}}(\boldsymbol{b}_{ij}, \boldsymbol{n}_s) \boldsymbol{m}_s \otimes \boldsymbol{m}_s + B^{\text{climb}} \boldsymbol{n}_s \otimes \boldsymbol{n}_s \\ \mathcal{B}^{e_q}_{ij} &= B^{\text{line}} \boldsymbol{l}_{e_q} \otimes \boldsymbol{l}_{e_q} + B^{\text{glide}}_{\text{edge}}(\boldsymbol{b}_{ij}, \boldsymbol{n}_{e_q}) \boldsymbol{m}_{e_q} \otimes \boldsymbol{m}_{e_q} + B^{\text{climb}} \boldsymbol{n}_{e_q} \otimes \boldsymbol{n}_{e_q} \end{aligned} \tag{4.4}$$

For the following discussion, let $\boldsymbol{l}_k$, $\boldsymbol{m}_k$, $\boldsymbol{n}_k$, and $\mathcal{B}^{k}_{ij}$ respectively denote the line vector, glide vector, normal vector, and drag tensor for the corresponding segment

character as expressed in equation (4.4). The drag coefficients B^{line}, $B^{\text{glide}}_{\text{screw}}$, $B^{\text{glide}}_{\text{edge}}$, and B^{climb} are the empirically-determined parameters. In principle, all of the drag coefficients could depend on the slip system of the segment, but in this model this dependency only applies to the glide drag coefficients. The fictitious drag coefficient B^{line} represents the stiffness of the nodes when moving in the line direction. This term is necessary in order to construct a full rank drag tensor. If the set $\{\boldsymbol{l}_k, \boldsymbol{m}_k, \boldsymbol{n}_k\}$ forms an orthonormal basis, the drag coefficients are the eigenvalues of the drag tensor $\mathcal{B}^k_{ij}$. Because the drag coefficients must be real and greater than zero to be physically meaningful, this drag tensor will always be positive-definite. If the set $\{\boldsymbol{l}_k, \boldsymbol{m}_k, \boldsymbol{n}_k\}$ is not linearly independent, the matrix $\mathcal{B}^k_{ij}$ is non-invertible and solving a corresponding linear system introduces singularities.

For general segment orientations, the mobility law must be capable of interpolating through all orientations for which there exists drag coefficient data. Therefore, the general drag tensor $\mathcal{B}_{ij}$ expressed in equation (3.26) will be a linear combination of tensors consisting of a form represented by equations (4.4). For a pure screw segment, $\boldsymbol{l}_s = \hat{\boldsymbol{b}} = \frac{\boldsymbol{b}}{|\boldsymbol{b}|}$, $\boldsymbol{m}_s = \boldsymbol{l}_s \times \boldsymbol{n}_s$, and $\boldsymbol{n}_s = \boldsymbol{n}$, where the Burgers vector $\boldsymbol{b}$ and normal vector $\boldsymbol{n}$ are pre-defined, i.e. they are not calculated in the mobility law from more fundamental parameters. For a pure edge segment of orientation q, $\boldsymbol{n}_{e_q} = \boldsymbol{m}_{e_q} \times \boldsymbol{l}_{e_q}$ and $\boldsymbol{m}_{e_q} = \hat{\boldsymbol{b}}$.

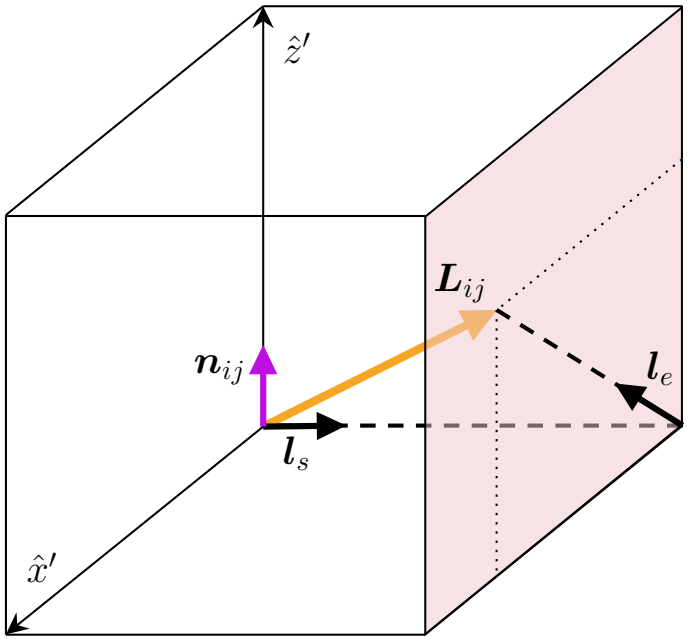


Figure 4.2: Segment line vector decomposition.

In this model, a segment is considered glissile if its Burgers and normal vectors are

respectively parallel to a pair of Burgers and normal vectors which appear in a row of Table 4.1; otherwise, it is considered sessile. Consider a general, mixed-character segment Γ_{ij} with its line, Burgers, and normal vectors $\{\boldsymbol{l}_{ij}, \boldsymbol{b}_{ij}, \boldsymbol{n}_{ij}\}$ pre-defined. Suppose that $\boldsymbol{b}_{ij}$ is parallel to a Burgers vector contained in Table 4.1. For a glissile segment, every Burgers vector has a corresponding set of normal vectors according to this table. Let us define the map Υ which takes a Burgers vector as input and outputs the set of corresponding normal vectors according to Table 4.1. Suppose that $\boldsymbol{n}_{ij}$ is parallel to a normal vector contained in $\Upsilon(\boldsymbol{b}_{ij})$. The segment now fulfils the criteria required to be considered glissile. The segment length vector $\boldsymbol{L}_{ij}$ may be represented as a decomposition in terms of perpendicular pure screw and pure edge components via $\boldsymbol{L}_{ij} = L^s_{ij}\boldsymbol{l}_s + L^e_{ij}\boldsymbol{l}_e$, where $\boldsymbol{l}_s \parallel \boldsymbol{b}_{ij}$ and $\boldsymbol{l}_e \perp \boldsymbol{b}_{ij}$ are unit vectors. To study a general case, suppose that the segment is lying off-plane (see, for instance, figure 4.2), i.e. $\boldsymbol{l}_{ij} \times \boldsymbol{b}_{ij}$ is not parallel to any normal vector contained in $\Upsilon(\boldsymbol{b}_{ij})$ and, thus, $\boldsymbol{l}_{ij} \times \boldsymbol{b}_{ij} \nparallel \boldsymbol{n}_{ij}$. This is possible for instance in the case that node n_i experiences an asymmetric climb with respect to its connected node n_j. In such a case, the normal vector $\boldsymbol{n}_{ij}$ would still be pre-defined and should still be parallel to a normal vector contained in $\Upsilon(\boldsymbol{b}_{ij})$. Since the edge component $\boldsymbol{L}^e_{ij} = L^e_{ij}\boldsymbol{l}_e$ would not lie on any plane contained in $\Upsilon(\boldsymbol{b}_{ij})$, an algorithm must be devised to appropriately decompose this edge component into further edge components $L^{e_q}_{ij}\boldsymbol{l}_{e_q}$ which lie on the planes contained in $\Upsilon(\boldsymbol{b}_{ij})$. The set of all unit vectors $\bigcup_q \{\boldsymbol{l}_{e_q}\}$ for which the edge component $\boldsymbol{L}^e_{ij}$ may be decomposed into is obtained via $\boldsymbol{l}_{e_q} = \hat{\boldsymbol{b}}_{ij} \times \boldsymbol{n}_{e_q}$ for all $\boldsymbol{n}_{e_q} \in \Upsilon(\boldsymbol{b}_{ij})$. Note that, since the screw component $L^s_{ij}\boldsymbol{l}_s$ can always lie on any plane contained in $\Upsilon(\boldsymbol{b}_{ij})$, the screw component does not need to be further decomposed.

Upon application of the chosen decomposition algorithm, the length vector for this segment may be written without loss of generality as

$$\boldsymbol{L}_{ij} = L^s_{ij}\boldsymbol{l}_s + L^{e_a}_{ij}\boldsymbol{l}_{e_a} + L^{e_b}_{ij}\boldsymbol{l}_{e_b} \tag{4.5}$$

The drag tensor for an arbitrary segment is then interpolated via

$$\mathcal{B}_{ij} = \frac{|L^s_{ij}|}{|\boldsymbol{L}_{ij}|}\mathcal{B}^s_{ij} + \frac{|L^{e_a}_{ij}|}{|\boldsymbol{L}_{ij}|}\mathcal{B}^{e_a}_{ij} + \frac{|L^{e_b}_{ij}|}{|\boldsymbol{L}_{ij}|}\mathcal{B}^{e_b}_{ij} \tag{4.6}$$

The drag tensors corresponding to the decomposition are

$$\begin{aligned}
\mathcal{B}^s_{ij} &= B^{\text{line}}\hat{\boldsymbol{b}}_{ij} \otimes \hat{\boldsymbol{b}}_{ij} + B^{\text{glide}}_{\text{screw}}(\boldsymbol{b}_{ij}, \boldsymbol{n}_{ij})\boldsymbol{m}_s \otimes \boldsymbol{m}_s + B^{\text{climb}}\boldsymbol{n}_{ij} \otimes \boldsymbol{n}_{ij} \\
\mathcal{B}^{e_a}_{ij} &= B^{\text{line}}\boldsymbol{l}_{e_a} \otimes \boldsymbol{l}_{e_a} + B^{\text{glide}}_{\text{edge}}(\boldsymbol{b}_{ij}, \boldsymbol{n}_{e_a})\hat{\boldsymbol{b}}_{ij} \otimes \hat{\boldsymbol{b}}_{ij} + B^{\text{climb}}\boldsymbol{n}_{e_a} \otimes \boldsymbol{n}_{e_a} \\
\mathcal{B}^{e_b}_{ij} &= B^{\text{line}}\boldsymbol{l}_{e_b} \otimes \boldsymbol{l}_{e_b} + B^{\text{glide}}_{\text{edge}}(\boldsymbol{b}_{ij}, \boldsymbol{n}_{e_b})\hat{\boldsymbol{b}}_{ij} \otimes \hat{\boldsymbol{b}}_{ij} + B^{\text{climb}}\boldsymbol{n}_{e_b} \otimes \boldsymbol{n}_{e_b}
\end{aligned} \tag{4.7}$$

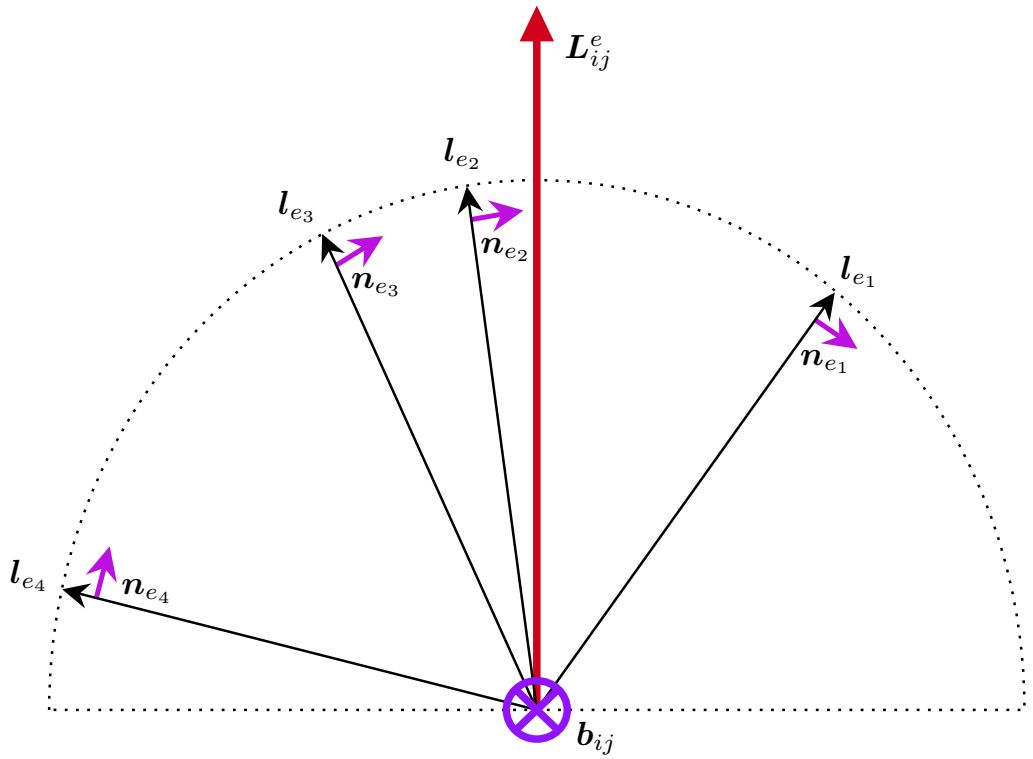


Figure 4.3: Edge vector decomposition. Unit line vectors $\boldsymbol{l}_{e_q}$ can always be represented as lying on a half-circle without loss of generality.

where $\boldsymbol{m}_s = \boldsymbol{l}_s \times \boldsymbol{n}_{ij}$. Finally, in the case of a sessile segment, it is treated as stiff in all directions such that the drag tensor is defined as

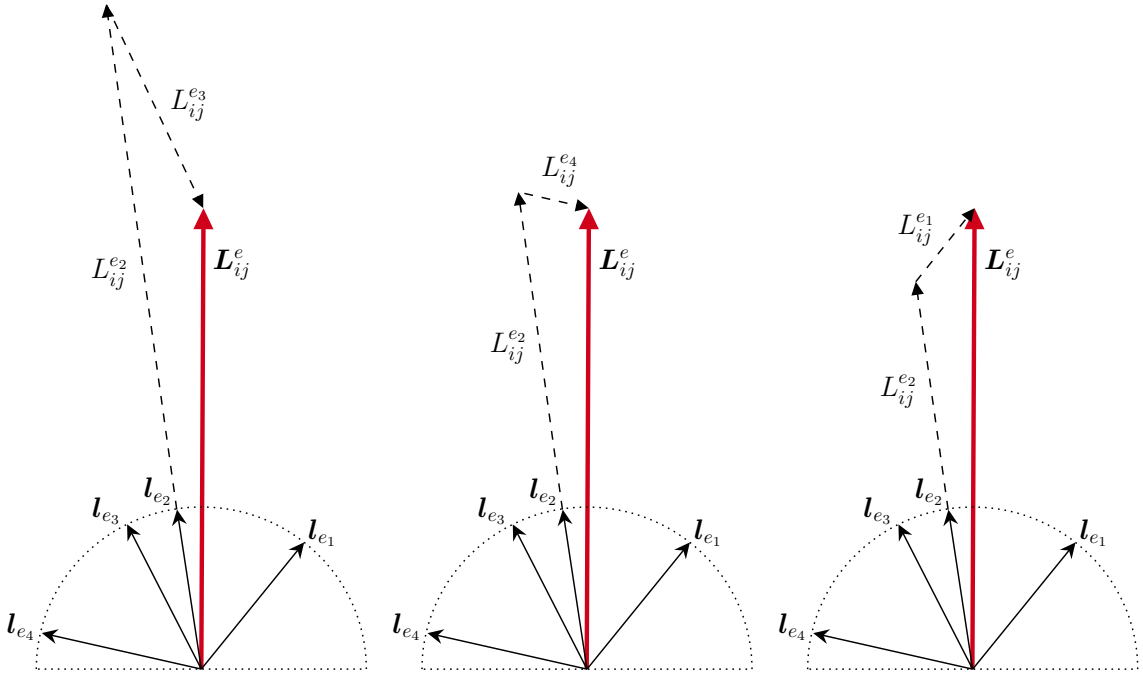
$$\mathcal{B}_{ij} = B^{\text{line}} \boldsymbol{l}_{ij} \otimes \boldsymbol{l}_{ij} + B^{\text{glide}}_{\text{sess}} (I - \boldsymbol{l}_{ij} \otimes \boldsymbol{l}_{ij}) \tag{4.8}$$

where $B^{\text{glide}}_{\text{sess}}$ is the drag coefficient in all directions perpendicular to the line vector and is set to a large finite value.

As a result of the interpolation procedure, the weak condition (3.26) may be expressed as

$$\boldsymbol{f}_i = \frac{1}{2} \sum_j^{k_i} \left(|L^s_{ij}| \; \mathcal{B}^s_{ij} + |L^{e_a}_{ij}| \; \mathcal{B}^{e_a}_{ij} + |L^{e_b}_{ij}| \; \mathcal{B}^{e_b}_{ij} \right) \cdot \boldsymbol{v}_i \tag{4.9}$$

It should be noted that the way in which the drag tensor $\mathcal{B}_{ij}$ is interpolated may result in artefacts in the segment mobility which do not reflect the physical reality. In particular, from equation (4.9), it can be seen that the drag which a given segment experiences depends on the algorithm which determines the decomposition given by equation (4.5). An ideal decomposition algorithm is one which minimises the norm of the set $\bigcup_q \{L^{e_q}_{ij}\}$, and thus minimises the effective length of the segment components which contribute to the segment drag.



(a) Decomposition outcome of simple projection-based minimisation algorithm. See algorithm A1.

(b) Decomposition outcome of altered simple projection-based minimisation algorithm. See algorithm A2.

(c) Decomposition outcome of perimeter minimisation algorithm (which is functionally equivalent to the L^1 norm minimisation algorithm). See algorithm A3.

Figure 4.4: Optimal edge vector decompositions given a set of basis line vectors according to different algorithms. Basis line vectors can be depicted without loss of generality to be emanating from a single source and lying at the edges of a half unit circle.

4.2.2 Segment decomposition algorithms

In the HCP mobility law, it is important to select a segment decomposition algorithm which minimises artefacts in the segment mobility. These artefacts arise from the fact that the force on a segment scales with its length, while the drag on a segment scales with the norm of the post-decomposition set $\bigcup_q \{L_{ij}^{e_q}\}$, i.e. its *effective* length. When a segment has an effective length which is significantly larger than its actual length, mobility artefacts will occur. The aim is to select a decomposition algorithm which minimises the effective segment length.

The general optimisation problem to solve is

$$\arg\min_{\{L_{ij}^{e_q}\}} \mathcal{F}(\{L_{ij}^{e_q}\}) \quad \text{such that} \quad \boldsymbol{L}_{ij}^{e} = L_{ij}^{e_1}\boldsymbol{l}_{ij}^{e_1} + \ldots + L_{ij}^{e_N}\boldsymbol{l}_{ij}^{e_N} \quad \text{and} \quad \bigcup_{q=1}^{N} \{\boldsymbol{l}_{ij}^{e_q}\} \subseteq \mathbb{R}^2 \tag{4.10}$$

where the N unit vectors contained in the set $\bigcup_q \{\boldsymbol{l}^{e_q}\}$ are in general linearly dependent and lie on the same two-dimensional plane with normal vector $\boldsymbol{b}_{ij}$. There are several potential candidates for an algorithm which finds an optimal decomposition for the edge component $\boldsymbol{L}_{ij}^e$. These algorithms are formally distinguished by the choice of the objective function $\mathcal{F}$. For the following discussion, let $\boldsymbol{L} = (L_{ij}^{e_1}, \ldots, L_{ij}^{e_N})^\intercal \in \mathbb{R}^N$ and $\mathcal{L} = (\boldsymbol{l}^{e_1}, \ldots, \boldsymbol{l}^{e_N}) \in \mathbb{R}^{3\times N}$ such that $\boldsymbol{L}_{ij}^e = \mathcal{L}\boldsymbol{L}$.

Problem (4.10) may be solved using the L^p norm objective functions $\mathcal{F}(\{L_{ij}^{e_q}\}) = (\sum_k^N |L_{ij}^{e_k}|^p)^{1/p}$. The HCP mobility law developed by [84] and [1] uses the L^1 norm objective function. It can be shown that the standard L^1 norm minimisation problem may be cast into a linear programming format given by

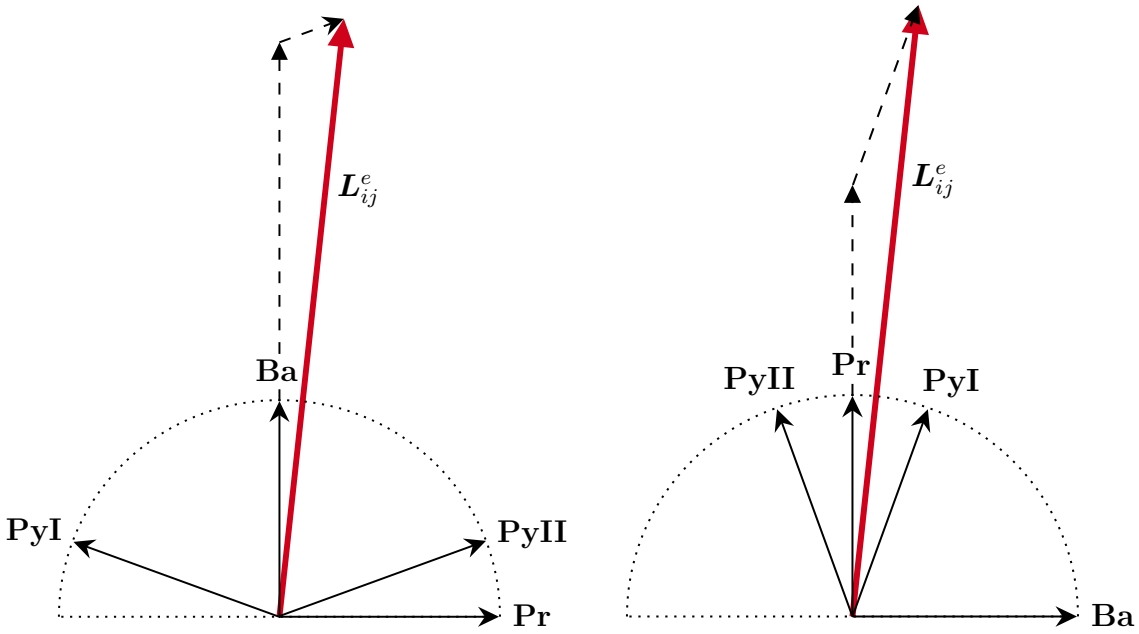
$$\underset{\boldsymbol{L},\boldsymbol{H}}{\arg\min} \begin{bmatrix}\boldsymbol{0} & \boldsymbol{1}\end{bmatrix} \begin{bmatrix}\boldsymbol{L}\\ \boldsymbol{H}\end{bmatrix} \quad \text{such that}$$
$$\begin{bmatrix} I_N & -I_N \\ -I_N & -I_N\end{bmatrix} \begin{bmatrix}\boldsymbol{L}\\ \boldsymbol{H}\end{bmatrix} \leq \begin{bmatrix}\boldsymbol{0}\\ \boldsymbol{0}\end{bmatrix}, \ \begin{bmatrix}\mathcal{L} & \boldsymbol{0}\end{bmatrix} \begin{bmatrix}\boldsymbol{L}\\ \boldsymbol{H}\end{bmatrix} = \boldsymbol{L}_{ij}^e, \ \begin{bmatrix}\boldsymbol{L}\\ \boldsymbol{H}\end{bmatrix} \geq \begin{bmatrix}-\boldsymbol{\infty}\\ \boldsymbol{0}\end{bmatrix} \quad (4.11)$$

where $\boldsymbol{0} = (0, \ldots, 0)^\intercal$, $\boldsymbol{1} = (1, \ldots, 1)^\intercal$, $\boldsymbol{\infty} = (\infty, \ldots, \infty)^\intercal$, the entries of $\boldsymbol{H} \in \mathbb{R}^N$ and $\boldsymbol{L}$ are related via $H_i = |L_i|$, and I_N denotes the $N \times N$ identity matrix. This linear program may then be solved by applying standard optimisation techniques or software packages such as the MATLAB function `linprog`. A simple alternative to the L^1 norm minimisation algorithm proceeds as follows.

Algorithm A1 (Simple projection-based optimisation)**.** First, the set consisting of the projections $\bigcup_{q=1}^N \{\varrho_q = |\boldsymbol{L}_{ij}^e \cdot \boldsymbol{l}^{e_q}|\}$ is generated. $\boldsymbol{L}_{ij}^e$ is then decomposed with respect to the basis $\{\boldsymbol{l}^{e_a}, \boldsymbol{l}^{e_b}\}$ consisting of two basis vectors which correspond to the two greatest projection magnitudes ϱ_a and ϱ_b.

See figure 4.4a for a depiction of a decomposition outcome of algorithm A1. The corresponding decomposition outcome does not necessarily favour the minimisation of the effective length of the segment components which contribute to the segment drag, and can thus lead to artefacts. It can be shown that this simple optimisation algorithm in general yields a different decomposition compared to the L^1 norm algorithm (see figure 4.4c for a counter-example). A minor amendment to the simple projection-based algorithm described above can yield a significant improvement with regards to minimising mobility-related artefacts. The procedure is as follows.

Algorithm A2 (Altered simple projection-based optimisation)**.** First, as in the original algorithm, compute the set of projections $\bigcup_{q=1}^N \{\varrho_q = |\boldsymbol{L}_{ij}^e \cdot \boldsymbol{l}^{e_q}|\}$. Next, decompose $\boldsymbol{L}_{ij}^e$ with respect to the basis $\{\boldsymbol{l}^{e_a}, \boldsymbol{l}^{e_b}\}$ consisting of two basis vectors: one



(a) Primarily Ba slip system.

(b) Primarily Pr slip system.

Figure 4.5: Edge vector decompositions via algorithm A3 in an HCP system with significant crystallographic anisotropy.

corresponding to the greatest projection magnitude ϱ_a, and the other corresponding to the smallest projection magnitude ϱ_b. See figure 4.4b for a depiction of a decomposition outcome of this algorithm.

In order to reduce mobility-related artefacts, it may be favourable to select an algorithm which instead minimises the perimeter of triangles generated by $\boldsymbol{L}^e_{ij}$ and its two decomposed components. This is precisely what the L^1 norm minimisation algorithm achieves, but an equivalent deterministic algorithm is presented in the following.

Algorithm A3 (Perimeter minimisation)**.** First, the set consisting of the projections $\bigcup_{q=1}^{N}\{\varrho_q = |\boldsymbol{L}^e_{ij} \cdot \boldsymbol{l}^{e_q}|\}$ is generated. The greatest projection magnitude ϱ_a is then selected and stored. Next, a copy of the edge vector, $\boldsymbol{P}$, is rotated by 90 degrees anti-clockwise with respect to the Burgers vector, and the sign value $s_a = \text{sign}(\boldsymbol{P} \cdot \boldsymbol{l}^{e_a})$ is calculated and stored. The set consisting of the projections $\bigcup_{q=1,q\neq a}^{N}\{\eta_q = s_a \boldsymbol{P} \cdot \boldsymbol{l}^{e_q}\}$ is generated. The line vector $\boldsymbol{l}^{e_b}$ corresponding to the greatest projection which is less than zero, η_b, is then selected. $\boldsymbol{L}^e_{ij}$ is then decomposed with respect to the basis $\{\boldsymbol{l}^{e_a}, \boldsymbol{l}^{e_b}\}$.

Algorithm A3 will result in a decomposition outcome which selects the basis line vectors with the two greatest projection magnitudes which are on opposite

sides of $\boldsymbol{L}_{ij}^{e}$ as seen in figure 4.4c. This algorithm will generate a decomposition corresponding to the minimum possible effective segment length, and thus minimise mobility-related artefacts.

Crystallography-based drag anisotropy

In an HCP system, as the ratio c/a increases, the Pr and Ba planes will remain orthogonal, but the PyI and PyII planes will increasingly align with the Pr plane, becoming equivalent as $c/a \to \infty$. Consider an $\langle a \rangle$-type pure edge segment within a significantly anisotropic HCP system ($c/a \gg 1$). Suppose that the segment is lying off-plane due to climb. The segment line vector will be decomposed into two of four possible basis vectors lying on the Ba, Pr, PyI, and PyII planes, as shown in figure 4.5. It is evident that there is a decomposition asymmetry with regards to segments primarily gliding in Ba planes (see figure 4.5a) compared to those primarily gliding in Pr planes (see figure 4.5b). The Pr plane lies closer to the PyI and PyII planes compared to the Ba plane. It follows that segments primarily gliding in Pr planes will have a lower effective length, and thus will typically undergo less drag. Note that this anisotropy is of a purely computational nature. The anisotropic drag effect becomes more significant as c/a increases, and disappears when $c/a = 1$. This effect can significantly impact the disparity in velocity between dislocations, and has been seen to even inhibit certain dislocation-dislocation reactions. It should be noted that a large disparity in drag coefficients between slip systems can also lead to unexpected effects related to crystallographic anisotropy. For instance, compared to segments on primarily Ba planes, segments on primarily Pr planes decompose in such a way that a greater portion of their effective length involves secondary slip systems, such as PyI or PyII. These secondary systems differ not only in type but also, potentially, in their drag coefficients, thus contributing to anisotropic behaviour.

Let us now compare the influence of the chosen decomposition algorithm on the velocity of a segment as a function of crystallographic anisotropy. This influence becomes apparent when the available slip systems have reduced symmetry. Figure 4.6a depicts an $\langle a \rangle$-type pure edge segment line vector lying off-plane. The possible decomposition planes are Ba, Pr, and PyII; PyI is intentionally neglected to accentuate the influence of the choice of the decomposition algorithm. Let ψ represent the angle between the Pr plane and $\boldsymbol{L}_{ij}^{e}$; consider only cases wherein the condition $0 \leq \psi \leq \pi/2$ holds. Let ς represent the angle between the Pr plane and the PyII plane; it is related to the c/a ratio via $\tan\varsigma = a/c$. Algorithm A1 predicts a Pr-PyII decomposition when the condition $\psi < \pi/4 - \varsigma/2$ holds, while algorithm A3 (resulting in the

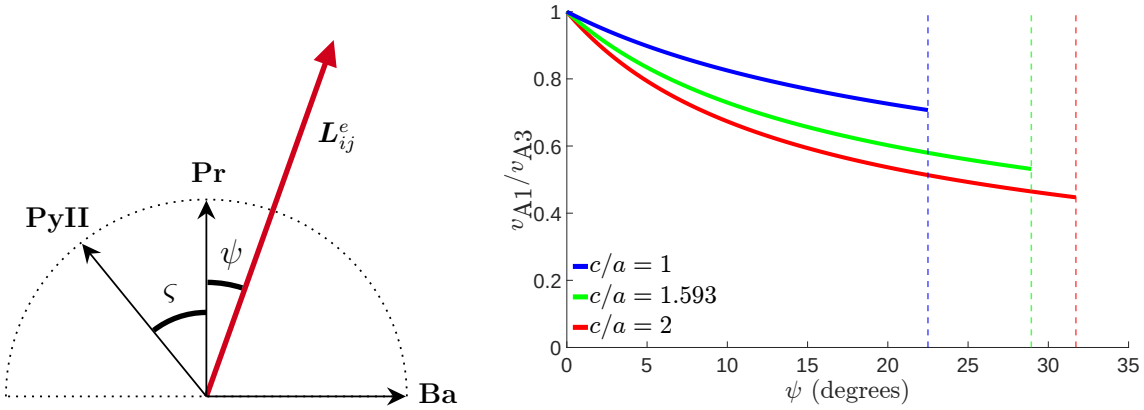


Figure 4.6: (a) Geometry of an off-plane $\langle a \rangle$-type pure edge segment. Here, ψ is the angle between the Pr plane and the segment; $\varsigma = \arctan(a/c)$ is the angle between the Pr and PyII planes. (b) Plots (as solid curves) of the velocity ratio described by equation (4.13) as a function of the angle ψ for varying values of c/a. The vertical dotted lines correspond to the limiting angle $\psi = \pi/4 - \varsigma/2$.

minimal effective length) always predicts a Pr-Ba decomposition under the assumed conditions. Note that, when the available slip systems are fully symmetric (e.g. when the PyI plane is available), algorithm A1 and algorithm A3 predict the same decomposition, and no algorithm-dependent differences appear in the simulation.

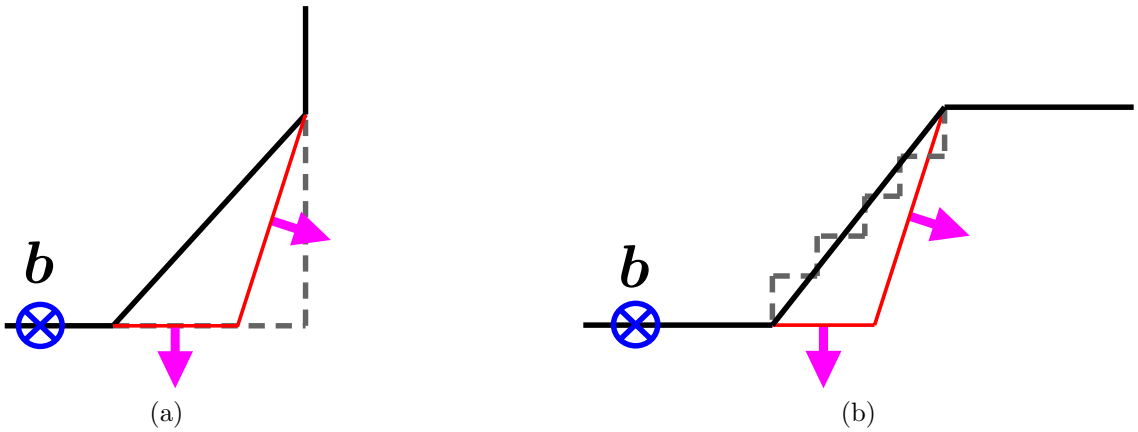
Assuming that (1) a spatially uniform force per unit length $\boldsymbol{f} = f\hat{\boldsymbol{b}}$ acts on the segment (of length L) in its slip direction $\hat{\boldsymbol{b}}$ and (2) all glide drag coefficients are equivalent, equation (4.9) becomes

$$v = \frac{fL}{B\,(L_1 + L_2)} \tag{4.12}$$

where v is the segment velocity magnitude (the direction of which is parallel to the force), L_1 and L_2 are the lengths of the two edge decompositions, and B is the glide drag coefficient. The ratio between the velocity obtained from algorithm A1 (resulting in a Pr-PyII decomposition) and algorithm A3 (resulting in a Pr-Ba decomposition) is given by

$$\frac{v_{\mathrm{A1}}}{v_{\mathrm{A3}}} = \frac{\cos\psi + \sin\psi}{\cos\psi + \sin\psi\left(\rho + \sqrt{1+\rho^2}\right)} \tag{4.13}$$

where $\rho = c/a$. This velocity ratio is plotted in figure 4.6b for three values of c/a. For the case of $c/a = 1.593$ (i.e. that of Zr), a small deviation of $\psi = 6°$ results in a velocity reduction of approximately 20% when using algorithm A1 compared



(a) (b)

Figure 4.7: Schematics of pure edge dislocations with off-plane segments. The solid black lines represent segments composing the DD model. The dotted black lines represent examples of the actual line configuration which could not be resolved by the DD model. As a result of the HCP mobility law, off-plane segments are decomposed into two segments which are shown as solid red lines. Each segment decomposition has an associated normal vector which lies in the plane of the figure, and is depicted as a magenta arrow. The Burgers vector $\boldsymbol{b}$ of the structures point into the page and are depicted in blue. (a) The DD model fails to resolve two in-plane segments, and the off-plane segment estimates their glide planes. (b) Climb leads to a "staircase" of jogs which is represented by an off-plane segment.

to algorithm A3, which is substantial. The ratio $v_{\mathrm{A1}}/v_{\mathrm{A3}}$ always decreases with increasing ψ; its rate of decrease increases as c/a increases. Therefore, for larger values of c/a, and in cases in which the available slip systems have reduced symmetry, the choice of the decomposition algorithm can have a significant effect on segments with off-plane components. This phenomenon is amplified when climb is enabled, owing to the corresponding increase in population of off-plane segments.

An interpretation of off-plane components

The $L_{ij}^{e_b} \neq 0$ case corresponds to the case in which the considered segment has an off-plane component. A physical interpretation of this situation is important, as its treatment marks a fundamental deviation from the formulations used in some non-HCP mobility laws. As discussed in section 3.3, one strategy for handling segments that lie between well-defined glide planes is to determine the closest slip system based on segment orientation and treat the segment as gliding solely on that plane (possibly with some interpolation procedure involved to account for its deviation from the glide plane). In contrast, the HCP mobility law adopts a different approach: off-plane segments are regarded as simultaneously occupying a weighted

mixture of multiple slip systems, from which they inherit glissile drag properties.

To understand possible interpretations of this approach, consider the following two examples involving pure edge segments. In the first example, shown in figure 4.7a, the DD model fails to resolve multiple in-plane segments, and instead represents them as a single off-plane segment. In the HCP mobility law, the off-plane segment is decomposed into two pure edge segments, each gliding on different glissile planes. In this interpretation, the HCP mobility law effectively infers the slip systems of such segments using a minimum effective length criterion. In the second example, shown in figure 4.7b, a segment undergoes asymmetric climb such that it acquires an off-plane component. Climb processes involve the generation of short jogged segments that are non-parallel to the non-jogged segments, in this case creating a "staircase" of jogs. Here, the jogged component of the line is effectively coarse-grained and treated as being a part of a segment occupying two glissile planes.

Figure 4.7 presents two illustrative cases in which the decomposed segments lie on crystallographic planes that differ from those of the original, finer segments prior to coarse-graining. For instance, in figure 4.7b, the horizontal jogs are partially represented with some accuracy, but the vertical jogs are not. In practice, the currently considered DD model lacks the resolution required to accurately capture the physics of these types of climb mechanisms at this scale. However, in both examples, the decompositions reproduce some physically plausible behaviour: the off-plane segments are mostly confined to move along the Burgers vector direction. However, it remains unclear whether assigning distinct glide coefficients in this way is physically meaningful.

In the current model, algorithm A3 should be selected because it minimises the effective segment length and, hence, related mobility artefacts. With respect to the climb example (figure 4.7b), the decomposition algorithm controls the interpretation of the orientation of the jogged components. In this model, jogs on edge and screw dislocations always respectively behave in a glissile and sessile manner, which matches what is generally expected [258, 259]. The decomposition decision is based purely on geometric criteria: jogged components will occur such that the effective segment length is minimised. However, the difference between the effective and actual segment length is not compensated by additional forces as would be required to preserve physical consistency.

While founded in some degree of reason, this model is not entirely physics-based and therefore cannot accurately capture the orientations of jogs, which are assumed to lie on different glide planes, and which in reality are determined by several factors

such as local stress fields, the diffusion paths of point defects, and the local core atomic structure [193, 260]. The situation is further complicated by the anisotropic nature of the HCP Zr crystallography [110]. Although this level of resolution is outside of the scope of the current model, the explicit representation of jogs and their orientations has been incorporated in some DD models by coupling the conventional glide-based framework with point defect transport [261, 262]. Finally, the current model does not capture the increased drag which has been observed at dislocation lines bending across intersecting non-coplanar glide planes, which is believed to arise due to the complex core structure at those lattice sites [263, 161].

Regardless of the specific interpretation, the HCP mobility law remains valuable due to its mathematically convenient formulation and its flexibility in seamlessly accommodating additional slip systems into the DD model. Furthermore, in simulations where other factors more significantly limit overall fidelity, it is not necessary to resolve climb-related behaviours with high precision.

4.2.3 Drag tensor conditioning

To determine the nodal velocities of a node connected to glissile segments, one must invert the full drag tensor given by

$$\boldsymbol{B}_i = \frac{1}{2}\sum_{j}^{k_i}\left(|L_{ij}^{s}|\ \mathcal{B}_{ij}^{s} + |L_{ij}^{e_a}|\ \mathcal{B}_{ij}^{e_a} + |L_{ij}^{e_b}|\ \mathcal{B}_{ij}^{e_b}\right) \tag{4.14}$$

for each node of the network. Since $\boldsymbol{B}_i$ is composed of a linear combination of symmetric positive-definite matrices, $\boldsymbol{B}_i$ will also be symmetric positive-definite. Because of the large amount of times that this inversion may be performed during a simulation, it is crucial that $\boldsymbol{B}_i$ is constructed in such a way so as to not be singular or ill-conditioned.

The condition number $\kappa\left(\boldsymbol{B}_i\right)$ associated with solving for $\boldsymbol{v}_i$ in the linear system $\boldsymbol{f}_i = \boldsymbol{B}_i\boldsymbol{v}_i$ gives a measure for how sensitive the output $\boldsymbol{v}_i$ is to a change in the input $\boldsymbol{f}_i$. The condition number is roughly the factor by which any noise in the input vector $\boldsymbol{f}_i$ will be magnified when computing the solution. In the context of linear systems, $\kappa\left(\boldsymbol{B}_i\right) = \|\boldsymbol{B}_i^{-1}\|\ \|\boldsymbol{B}_i\|$ for some matrix norm $\|\cdot\|$. Using the L^2 norm, and assuming that the linear system is symmetric (such as the one in equation (4.9)), the condition number is given by $\kappa\left(\boldsymbol{B}_i\right) = |\lambda_{\max}|/|\lambda_{\min}|$, where $\lambda_{\max}$ and $\lambda_{\min}$ are respectively the maximal and minimal eigenvalues of the matrix $\boldsymbol{B}_i$. In the optimal case that the condition number is $\kappa\left(\boldsymbol{B}_i\right) = 1$, the output vector can be found with a precision which is no worse than that of the input vector. On the other hand, for

finite large condition numbers, i.e. $\kappa(\boldsymbol{B}_i) \gg 1$, small errors in $\boldsymbol{f}_i$ may result in large errors in $\boldsymbol{v_i}$. The solutions of linear systems involving matrices with large condition numbers are prone to numerical error due to the amplification of errors inherent in computers using finite machine precision. When the condition number $\kappa(\boldsymbol{B}_i)$ is infinite, matrix $\boldsymbol{B}_i$ is non-invertible. Note that the maximal and minimal eigenvalues of $\boldsymbol{B}_i$ will respectively be on the order of the climb and line drag coefficients.

Because the line drag coefficient B_{ij}^{line} is not physically meaningful, it may be selected in order to optimise the stability of the mobility law. It is often set to a relatively low value to facilitate nodal distribution along segments, but not low enough such that the condition number becomes too large. Setting drag coefficients to typical values $B_{ij}^{\text{climb}} \approx 10$ and $B_{ij}^{\text{line}} \approx 10^{-5}$ yields a condition number $\kappa(\boldsymbol{B}_i) \approx 10^6$. This condition number is reasonable assuming that the error in $\boldsymbol{f}_i$ is only due to finite machine precision, i.e. it contains noise up to a factor of 10^{-16} when using double-precision floating-point arithmetic.

Even when the drag coefficients are selected with stability in mind, there may still be cases where $\kappa(\boldsymbol{B}_i)$ is very large, and other stability techniques should be considered. In the mobility law implemented in this text, the linear system is regularised once a predetermined threshold for ill-conditioning is reached via some transformation $\boldsymbol{B}_i^{\mathcal{R}} = \mathcal{T}(\boldsymbol{B}_i)$, and the linear system $\boldsymbol{f}_i = \boldsymbol{B}_i^{\mathcal{R}} \boldsymbol{v}_i$ is instead solved. This will increase the stability of the mobility law in exchange for decreasing the accuracy of the solution. Note that calculating the L^2-based condition number of a matrix involves a costly computation of its eigenvalues. The mobility law in this text instead uses the MATLAB function `rcond` (based on [264]) which gives a more cost-efficient approximation involving the L^1-based condition number.

Given a regularisation matrix $\mathcal{R}$, the transformation

$$\boldsymbol{B}_i^{\mathcal{R}} = \boldsymbol{B}_i + \mathcal{R} \tag{4.15}$$

provides a simple regularisation which can be computed quickly and can induce a potentially dramatic improvement in stability. An example of a useful regularisation matrix is an isotropic noise matrix $\mathcal{R} = cI$, where $c \geq 0$ is a regularisation parameter. This physically corresponds to an increase in the isotropic stiffness of the nodes. Another possibility is the matrix $\mathcal{R} = b\boldsymbol{l}_{ij} \otimes \boldsymbol{l}_{ij}$, where $b \geq 0$ parametrises the increase in line drag coefficient for the segments connected to the node. This will increase the minimal eigenvalue of the full drag tensor $\boldsymbol{B}_i$, and hence reduce its condition number.

A distinction is made between ill-conditioned cases, where $1 \ll \kappa(\boldsymbol{B}_i) < \infty$, and singular cases, where $\det(\boldsymbol{B}_i) = 0$ to within machine precision. In the singular case, the known components of the linear system, $\boldsymbol{B}_i$ and $\boldsymbol{f}_i$, are transformed into the eigenbasis of $\boldsymbol{B}_i$, and the dimensions corresponding to its nullspace are truncated. The solution $\boldsymbol{v}_i$ is solved for in the truncated eigenbasis, after which $\boldsymbol{v}_i$ is transformed to its original coordinate system. This is equivalent to setting node n_i to be infinitely stiff in its nullspace direction.

4.3 Model extensions and investigations

4.3.1 Drag tensor interpolation schemes

Aubry *et al.* [84] and Hortelano-Roig *et al.* [1] interpolate the drag tensor for an arbitrary segment according to equation (4.6). This interpolation scheme is a subset of a general class of schemes given by

$$\mathcal{B}_{ij} = \frac{|L_{ij}^{s}|^{\eta}}{|\boldsymbol{L}_{ij}|^{\eta}}\mathcal{B}_{ij}^{s} + \frac{|L_{ij}^{e_a}|^{\eta}}{|\boldsymbol{L}_{ij}|^{\eta}}\mathcal{B}_{ij}^{e_a} + \frac{|L_{ij}^{e_b}|^{\eta}}{|\boldsymbol{L}_{ij}|^{\eta}}\mathcal{B}_{ij}^{e_b} \tag{4.16}$$

for some free parameter $\eta > 0$. This yields the full drag tensor given by

$$\boldsymbol{B}_i = \frac{1}{2}\sum_{j}^{k_i}\left(\frac{|L_{ij}^{s}|^{\eta}}{|\boldsymbol{L}_{ij}|^{\eta-1}}\mathcal{B}_{ij}^{s} + \frac{|L_{ij}^{e_a}|^{\eta}}{|\boldsymbol{L}_{ij}|^{\eta-1}}\mathcal{B}_{ij}^{e_a} + \frac{|L_{ij}^{e_b}|^{\eta}}{|\boldsymbol{L}_{ij}|^{\eta-1}}\mathcal{B}_{ij}^{e_b}\right) \tag{4.17}$$

Interpolation (4.6) effectively corresponds to scheme $\eta = 1$. However, other choices of η should be considered. For instance, the choice $\eta = 2$ offers the favourable property in that it results in an interpolation which enjoys the benefit of laying strictly within the range provided by the data, i.e.

$$\min\left(\mathcal{B}_{ij}^{s}, \mathcal{B}_{ij}^{e_a}, \mathcal{B}_{ij}^{e_b}\right) \leq \mathcal{B}_{ij} \leq \max\left(\mathcal{B}_{ij}^{s}, \mathcal{B}_{ij}^{e_a}, \mathcal{B}_{ij}^{e_b}\right) \tag{4.18}$$

which is conceptually desirable, and for $\eta \neq 2$ is not in general guaranteed[2]. At the time of writing, the $\eta \neq 1$ schemes have not been explored in the literature as potential candidates for an HCP mobility law. Therefore, in the following section comparisons will be made between different HCP mobility law candidates, and their implications will be investigated.

[2]This property is particularly evident when representing the generalised out-of-plane problem in spherical coordinates—the scheme becomes

$$\mathcal{B}_{ij} = \mathcal{B}_{ij}^{s}\sin^2\phi\sin^2\psi + \mathcal{B}_{ij}^{e_a}\sin^2\phi\cos^2\psi + \mathcal{B}_{ij}^{e_b}\cos^2\phi$$

where ϕ and ψ are respectively the polar and azimuthal angles. The drag tensor element is formulated as a convex combination of $\mathcal{B}_{ij}^{s}$, $\mathcal{B}_{ij}^{e_a}$, and $\mathcal{B}_{ij}^{e_b}$, from which it follows that property (4.18) is satisfied [265].

4.3.2 Resolved drag coefficient distributions

Consider an isolated segment in an ideal case in which there is no out-of-plane component, i.e. $L_{ij}^{e_b} = 0$, and let us denote quantities referring to the (now entirely on-plane) edge component via the superscript e. The interpolation for a general η is given by

$$\mathcal{B}_{ij} = \mathcal{B}_{ij}^{s} |\cos\theta|^{\eta} + \mathcal{B}_{ij}^{e} |\sin\theta|^{\eta} \tag{4.19}$$

where we have used $L_{ij}^{s} = |\boldsymbol{L}_{ij}| \cos\theta$, $L_{ij}^{e_a} = |\boldsymbol{L}_{ij}| \sin\theta$, and θ is the character angle.

Suppose the segment lies with respect to a coordinate system as shown in figure 4.8. In the pure edge case, the drag tensor is

$$\mathcal{B}_{ij} = \begin{pmatrix} B_{\text{edge}}^{\text{glide}} & 0 & 0 \\ 0 & B^{\text{line}} & 0 \\ 0 & 0 & B^{\text{climb}} \end{pmatrix} \tag{4.20}$$

Similarly, in the pure screw case, the drag tensor is

$$\mathcal{B}_{ij} = \begin{pmatrix} B^{\text{line}} & 0 & 0 \\ 0 & B_{\text{screw}}^{\text{glide}} & 0 \\ 0 & 0 & B^{\text{climb}} \end{pmatrix} \tag{4.21}$$

Finally, in the mixed case, the drag tensor is

$$\mathcal{B}_{ij} = \begin{pmatrix} \left(B^{\text{line}} |\cos\theta|^{\eta} + B_{\text{edge}}^{\text{glide}} |\sin\theta|^{\eta}\right) & 0 & 0 \\ 0 & \left(B_{\text{screw}}^{\text{glide}} |\cos\theta|^{\eta} + B^{\text{line}} |\sin\theta|^{\eta}\right) & 0 \\ 0 & 0 & g^{c}(\theta) \end{pmatrix} \tag{4.22}$$

where $g^{c}(\theta) = B^{\text{climb}} \left(|\cos\theta|^{\eta} + |\sin\theta|^{\eta}\right)$. In coordinate-free form, the drag tensor can be equivalently expressed as

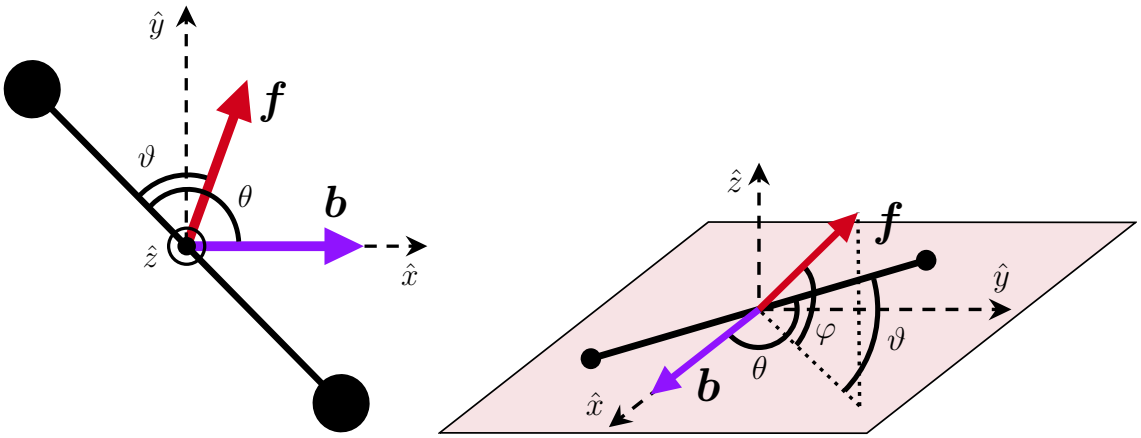
$$\mathcal{B}_{ij} = A_e \boldsymbol{b}_{ij} \otimes \boldsymbol{b}_{ij} + A_s \boldsymbol{s}_{ij} \otimes \boldsymbol{s}_{ij} + A_c \boldsymbol{n}_{ij} \otimes \boldsymbol{n}_{ij} \tag{4.23}$$

where $\boldsymbol{s}_{ij} = \boldsymbol{b}_{ij} \times \boldsymbol{n}_{ij}$, $\boldsymbol{n}_{ij} = \boldsymbol{b}_{ij} \times \boldsymbol{l}_{ij}$, and the coefficients A_e, A_s, and A_c are respectively the diagonal elements of the drag tensor (4.22) such that $\mathcal{B}_{ij} = \text{diag}(A_e, A_s, A_c)$.

Assuming that $B^{\text{climb}} \gg \max\left(B^{\text{line}}, B_{\text{screw}}^{\text{glide}}, B_{\text{edge}}^{\text{glide}}\right)$, the condition number of matrix (4.22) is given by

$$\kappa\left(\mathcal{B}_{ij}\left(\theta\right)\right) = \frac{\left|g^{c}\left(\theta\right)\right|}{\left|\min\left(B^{\text{line}} |\cos\theta|^{\eta} + B_{\text{edge}}^{\text{glide}} |\sin\theta|^{\eta}, B_{\text{screw}}^{\text{glide}} |\cos\theta|^{\eta} + B^{\text{line}} |\sin\theta|^{\eta}\right)\right|} \tag{4.24}$$

In the case that the dislocation network is sufficiently fine and each node has at most two connections, the condition number of matrix (4.22) is the same as the condition



(a) Point of view parallel to the z-axis.

(b) The segment lies entirely in its glide plane (the red parallelogram) such that $\boldsymbol{n}_{ij} = \hat{z}$.

Figure 4.8: Schematic depicting a dislocation segment with an associated coordinated system. The force vector $\boldsymbol{f}$ and Burgers vector $\boldsymbol{b}$ are respectively shown in red and blue. The Burgers vector always lies on the x-axis.

number of the full drag tensor $\boldsymbol{B}_i$. The maximum upper bound for the condition number is given by

$$\max(\kappa) = \begin{cases} B^{\text{climb}}/B^{\text{line}} & \text{if } B^{\text{line}} < \min(B^{\text{glide}}_{\text{edge}}, B^{\text{glide}}_{\text{screw}}) \\ B^{\text{climb}}/\min(B^{\text{glide}}_{\text{edge}}, B^{\text{glide}}_{\text{screw}}) & \text{if } B^{\text{line}} \geq \min(B^{\text{glide}}_{\text{edge}}, B^{\text{glide}}_{\text{screw}}) \end{cases} \tag{4.25}$$

which exhibits the same behaviour as that of non-HCP mobility laws.

Suppose that a force $\boldsymbol{f}$ is applied equally to each end node of the considered isolated segment such that $\boldsymbol{f}_i = \boldsymbol{f}_j = \boldsymbol{f}$, and thus $\boldsymbol{v}_i = \boldsymbol{v}_j = \boldsymbol{v}$ for the resultant velocity. The general expression for an applied force on this segment is given by

$$\boldsymbol{f} = |\boldsymbol{f}|\hat{\boldsymbol{f}} = |\boldsymbol{f}|\left(\cos(\theta - \vartheta)\cos(\varphi), \sin(\theta - \vartheta)\cos(\varphi), \sin(\varphi)\right)^{\intercal} \tag{4.26}$$

where $\hat{\boldsymbol{f}}$ is the force unit vector and ϑ and φ are angles corresponding to figure 4.8. One may calculate the resulting velocity magnitude by applying the weak condition (3.26), resulting in

$$|\boldsymbol{v}| = \frac{|\boldsymbol{f}|}{\frac{1}{2}|\boldsymbol{L}_{ij}|}\left|\left(\mathcal{B}_{ij}\right)^{-1} \cdot \hat{\boldsymbol{f}}\right| \tag{4.27}$$

We are interested in a quantity which measures the magnitude of the velocity response relative to the magnitude of the applied force at varying character angles. This quantity should directly relate to the drag coefficients $B^{\text{glide}}_{\text{screw}}$, $B^{\text{glide}}_{\text{edge}}$, and B^{line}, which are given as inputs to a DD simulation, as well as be independent of the segment length. Therefore, in order to connect to the essential features of the drag

tensor, we shall introduce the *resolved* drag coefficient β[3] of the segment, which is defined as

$$\beta \coloneqq \left| \left(\boldsymbol{\mathcal{B}}_{ij}\right)^{-1} \cdot \hat{\boldsymbol{f}} \right|^{-1} = \frac{|\boldsymbol{f}|}{\frac{1}{2}|\boldsymbol{L}_{ij}||\boldsymbol{v}|} \tag{4.28}$$

This quantity is effectively the drag coefficient of a segment resolved in the direction of the velocity $\boldsymbol{v}$. It should be noted that expression (4.28) is a general definition not limited to the HCP mobility law. In the HCP mobility law, mixed segments have a general resolved drag coefficient given by

$$\beta = \left(\left(\frac{\cos\left(\theta - \vartheta\right)\cos\left(\varphi\right)}{B^{\text{line}}|\cos\theta|^{\eta} + B^{\text{glide}}_{\text{edge}}|\sin\theta|^{\eta}} \right)^2 + \left(\frac{\sin\left(\theta - \vartheta\right)\cos\left(\varphi\right)}{B^{\text{glide}}_{\text{screw}}|\cos\theta|^{\eta} + B^{\text{line}}|\sin\theta|^{\eta}} \right)^2 + \left(\frac{\sin\left(\varphi\right)}{g^{c}(\theta)} \right)^2 \right)^{-\frac{1}{2}} \tag{4.29}$$

If the applied force $\boldsymbol{f}$ is parallel to an eigenvector of $\boldsymbol{\mathcal{B}}_{ij}$, then $\boldsymbol{v}$ will be parallel to $\boldsymbol{f}$. This observation leads to an elucidating connection to other mobility law models. Consider the drag tensor construction method typically used in non-HCP mobility laws, which is given by (3.27). In that formulation, $\boldsymbol{l}_{ij}$, $\boldsymbol{n}_{ij}$, and $\boldsymbol{m}_{ij} = \boldsymbol{l}_{ij} \times \boldsymbol{n}_{ij}$ are respectively the line, normal, and glide vectors of the segment Γ_{ij}. They are assumed to be orthonormal and are thus the eigenvectors of $\boldsymbol{\mathcal{B}}_{ij}$, while the line drag B_l, climb drag B_c, and glide drag B_g are the corresponding eigenvalues. Typically, all eigenvalues are set to constants except for $B_g = B_g\left(\theta\right)$, which is interpolated between pure edge and pure screw characters. In the non-HCP mobility law, when $\boldsymbol{f} \parallel \boldsymbol{m}_{ij}$, $\boldsymbol{f} \parallel \boldsymbol{l}_{ij}$, or $\boldsymbol{f} \parallel \boldsymbol{n}_{ij}$, it follows that $\boldsymbol{v} = \boldsymbol{f}/B_g$, $\boldsymbol{v} = \boldsymbol{f}/B_l$, or $\boldsymbol{v} = \boldsymbol{f}/B_c$, respectively. In the HCP mobility law, when $\boldsymbol{f} \parallel \boldsymbol{m}_{ij}$, $\boldsymbol{f} \parallel \boldsymbol{l}_{ij}$, or $\boldsymbol{f} \parallel \boldsymbol{n}_{ij}$, the resulting β-distributions β^{glide}, β^{line}, or β^{climb} each respectively have an analogous interpretation corresponding to the eigenvalues B_g, B_l, or B_c. However, as we shall see, most of the possible distributions for β^{line} and β^{climb} (determined by the space of free parameter choices) vary with respect to θ. This stands in contrast to the corresponding eigenvalues B_l and B_c, which are constant.

Furthermore, in the non-HCP formulation, a general resolved drag coefficient can also be calculated for mixed segments. The problem can be formulated in the same coordinate system as figure 4.8 by using $\boldsymbol{l}_{ij} = (\cos\theta, \sin\theta, 0)^{\intercal}$ and $\boldsymbol{m}_{ij} =$

[3]In this text, this quantity is also sometimes simply referred to as the *drag function*. Any potential confusion with the identically named function $\boldsymbol{\mathcal{B}}$ will be clarified based on context.

$(\sin\theta, -\cos\theta, 0)^\intercal$. The associated general resolved drag coefficient is given by

$$\beta_{\text{non-hcp}} = \Bigg(\Bigg(\left(B_l^{-1}\cos^2\theta + B_g^{-1}\sin^2\theta\right)\cos(\theta-\vartheta)\cos(\varphi) + \left(B_l^{-1} - B_g^{-1}\right)\cos\theta\sin\theta\sin(\theta-\vartheta)\cos(\varphi)\Bigg)^2 + \Bigg(\left(B_l^{-1} - B_g^{-1}\right)\cos\theta\sin\theta\cos(\theta-\vartheta)\cos(\varphi) + \left(B_l^{-1}\sin^2\theta + B_g^{-1}\cos^2\theta\right)\sin(\theta-\vartheta)\cos(\varphi)\Bigg)^2 + \left(B_c^{-1}\sin(\varphi)\right)^2 \Bigg)^{-\frac{1}{2}} \quad (4.30)$$

From this expression it can be verified that (1) $\boldsymbol{f} \parallel \boldsymbol{m}_{ij} \Rightarrow \beta_{\text{non-hcp}} = B_g$[4], (2) $\boldsymbol{f} \parallel \boldsymbol{l}_{ij} \Rightarrow \beta_{\text{non-hcp}} = B_l$, and (3) $\boldsymbol{f} \parallel \boldsymbol{n}_{ij} \Rightarrow \beta_{\text{non-hcp}} = B_c$.

Let us now investigate the HCP formulation in the $\{\boldsymbol{l}_{ij}, \boldsymbol{n}_{ij}, \boldsymbol{m}_{ij}\}$ basis. The HCP drag tensor can be expressed in coordinate-free form via

$$\mathcal{B}_{ij} = \boldsymbol{m}_{ij}\otimes\boldsymbol{m}_{ij}\left[A_e\sin^2\theta + A_s\cos^2\theta\right] + \boldsymbol{l}_{ij}\otimes\boldsymbol{l}_{ij}\left[A_e\cos^2\theta + A_s\sin^2\theta\right] + \boldsymbol{n}_{ij}\otimes\boldsymbol{n}_{ij}A_c + (\boldsymbol{m}_{ij}\otimes\boldsymbol{l}_{ij} + \boldsymbol{l}_{ij}\otimes\boldsymbol{m}_{ij})\left[(A_e - A_s)\sin\theta\cos\theta\right] \quad (4.31)$$

where the coefficients A_e, A_s, and A_c are the same as those in equation 4.23. Therefore, the HCP drag tensor is not in general diagonal in the $\{\boldsymbol{l}_{ij}, \boldsymbol{n}_{ij}, \boldsymbol{m}_{ij}\}$ basis unless $A_e = A_s$ (which is only true when $B^{\text{glide}}_{\text{edge}} = B^{\text{glide}}_{\text{screw}} = B^{\text{line}}$), $\theta = 0$ (which corresponds to a pure screw segment), or $\theta = \pi/2$ (which corresponds to a pure edge segment). Consequently, in the HCP formulation, when $\boldsymbol{f} \parallel \boldsymbol{m}_{ij}$ or $\boldsymbol{f} \parallel \boldsymbol{l}_{ij}$, it follows that the resulting velocity is *not* necessarily parallel to the force[5]. The deviation in direction is parametrised by $|(A_e - A_s)\sin\theta\cos\theta|$. For illustration, consider the following example: the $\boldsymbol{v} \parallel \boldsymbol{m}_{ij}$ case yields a force $\boldsymbol{f} = f_m\,\boldsymbol{m}_{ij} + f_l\,\boldsymbol{l}_{ij}$; selecting values of $B^{\text{glide}}_{\text{edge}} = 1$, $B^{\text{glide}}_{\text{screw}} = 2$, and $B^{\text{line}} = 1$, the maximum value of $|f_l|/|\boldsymbol{f}|$ (over all possible values of θ) is approximately 20%. This is a moderately large deviation, but for some calculations it may be small enough to ignore, especially if the anisotropy between edge and screw glide directions (i.e. between $B^{\text{glide}}_{\text{edge}}$ and $B^{\text{glide}}_{\text{screw}}$) is smaller. Note that, for the remainder of this section, the focus will be exclusively on the HCP

[4]Here, the notation $A \Rightarrow B$ means that statement A implies statement B.

[5]However, it does indeed follow from $\boldsymbol{f} \parallel \boldsymbol{n}_{ij}$ that $\boldsymbol{v} \parallel \boldsymbol{f}$.

$$
\begin{aligned}
&\text{—}(\eta, R_l) = \left(1, 10^{0}\right)\\
&\text{—}(\eta, R_l) = \left(2, 10^{0}\right)\\
&\text{—}(\eta, R_l) = \left(3, 10^{0}\right)\\
&\text{- -}(\eta, R_l) = \left(1, 10^{-1}\right)\\
&\text{- -}(\eta, R_l) = \left(2, 10^{-1}\right)\\
&\text{- -}(\eta, R_l) = \left(3, 10^{-1}\right)\\
&\text{----}(\eta, R_l) = \left(1, 10^{-2}\right)\\
&\text{----}(\eta, R_l) = \left(2, 10^{-2}\right)\\
&\text{----}(\eta, R_l) = \left(3, 10^{-2}\right)
\end{aligned}
$$

Figure 4.9: Legend corresponding to the polar plots shown in section 4.3.2.

formulation, although several of the results discussed herein are also applicable to the non-HCP formulation.

The distribution of β with respect to θ is closely related to the spatial distribution of dislocations. As we shall see in section 4.4, the β-distribution not only affects the scale-free[6] shape of the spatial distribution, but also the speed at which the bulk distribution travels. It is therefore important to select an appropriate distribution of β which either reflects the physical reality of how dislocations evolve during experiments, or at least which provides some computational advantage. There remains two free parameters which further determine the distribution of β: the interpolation scheme η and the line drag coefficient B^{line}. As discussed previously, B^{line} may be selected freely for computational convenience, numerical stability, managing system stiffness, and/or ensuring physical correspondence.

In the following discussions—and in particular for plotting—we frequently make reference to the (semi-) normalised resolved drag coefficient distribution given by

$$
\hat{\beta} = \frac{\beta}{\min\left(B^{\text{glide}}_{\text{screw}}, B^{\text{glide}}_{\text{edge}}\right)} \tag{4.32}
$$

We always assume that $B^{\text{glide}}_{\text{screw}} \geq B^{\text{glide}}_{\text{edge}}$, as is most typical in HCP simulations. Therefore, it will always be the case that $\hat{\beta} = c \Rightarrow \beta = cB^{\text{glide}}_{\text{edge}}$ for some constant c. Figure 4.9 contains the colour legend for the polar plots in this section.

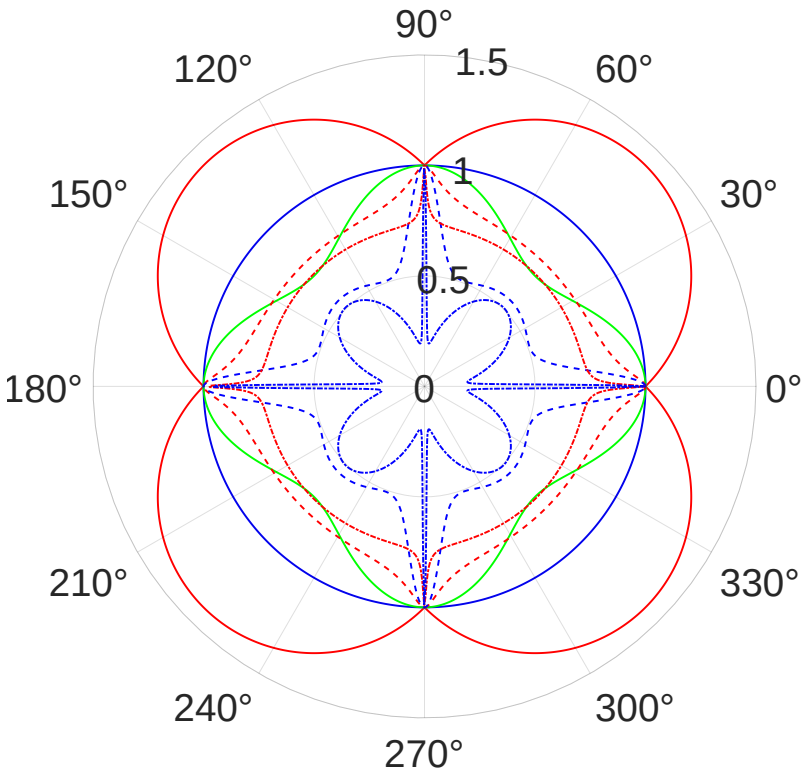


Figure 4.10: Polar plot containing $\hat{\beta}^{\text{glide}}$ interpolations between equal regimes ($R_g = 1$) with no interpolations used for B^{line}. The radial axis is $\hat{\beta}^{\text{glide}}$ while the angular axis is the character angle (in degrees). The red, blue, and yellow colours respectively correspond to $\eta = 1$, $\eta = 2$, and $\eta = 3$; η is the new free parameter introduced in this section that determines the interpolation of the drag tensor. The solid lines, dotted lines, and half-solid-half-dotted lines respectively correspond to $R_l = 1$, $R_l = 10^{-1}$, and $R_l = 10^{-2}$.

Pure glide direction

Let us first consider a climb-free, pure glide force for our considered segment—i.e. one which acts solely in the glide direction, perpendicular to the line and normal vectors. Such a force corresponds to $(\vartheta, \varphi) = (\frac{\pi}{2}, 0)$ and is explicitly given by $\boldsymbol{f} = |\boldsymbol{f}|\,(\sin\theta, -\cos\theta, 0)^{\intercal}$. For pure edge and pure screw segments, the resolved glide drag coefficients are respectively given by $\beta^{\text{glide}} = B^{\text{glide}}_{\text{edge}}$ and $\beta^{\text{glide}} = B^{\text{glide}}_{\text{screw}}$. For mixed segments, the resolved glide drag coefficient is

$$\beta^{\text{glide}} = \left(\left(\frac{\sin\theta}{B^{\text{line}}|\cos\theta|^{\eta} + B^{\text{glide}}_{\text{edge}}|\sin\theta|^{\eta}} \right)^2 + \left(\frac{-\cos\theta}{B^{\text{glide}}_{\text{screw}}|\cos\theta|^{\eta} + B^{\text{line}}|\sin\theta|^{\eta}} \right)^2 \right)^{-\frac{1}{2}} \tag{4.33}$$

[6] A *scale-free* shape is the shape of a spatial distribution after normalising the length scale such that the maximum radial distance from its centroid is unity.

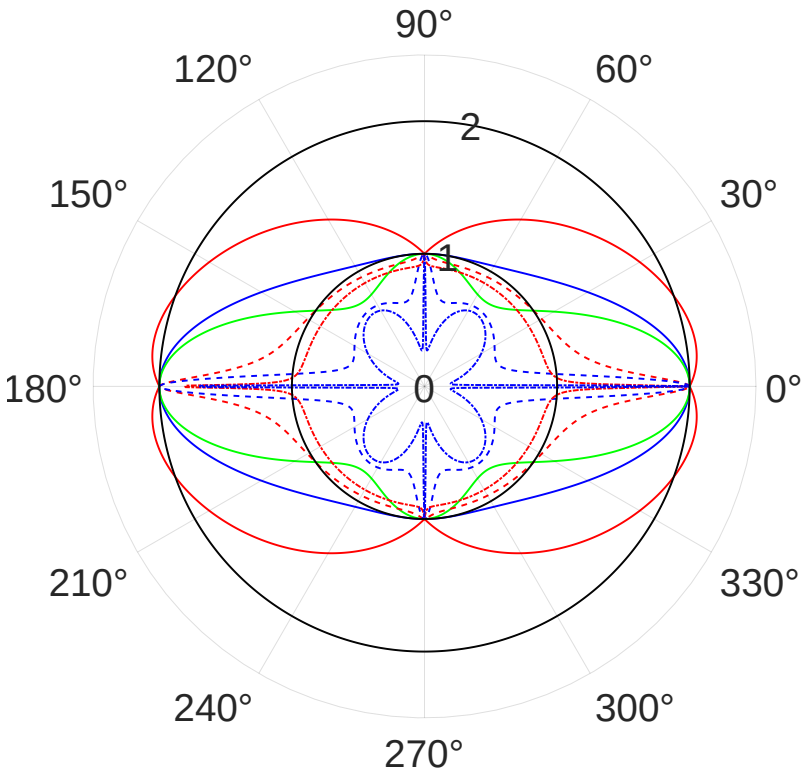


Figure 4.11: Polar plot containing $\hat{\beta}^{\text{glide}}$ interpolations between unequal regimes ($R_g = 2$) with no interpolations used for B^{line}. The radial axis is $\hat{\beta}^{\text{glide}}$ while the angular axis is the character angle (in degrees). The red, blue, and yellow colours respectively correspond to $\eta = 1$, $\eta = 2$, and $\eta = 3$. The solid lines, dotted lines, and half-solid-half-dotted lines respectively correspond to $R_l = 1$, $R_l = 10^{-1}$, and $R_l = 10^{-2}$.

We shall now analyse the β-distributions corresponding to varying η and B^{line}. Let us first study the effect of the fixed ratios

$$R_l \coloneqq B^{\text{line}}/B^{\text{glide}}_{\text{edge}} \qquad \text{and} \qquad R_g \coloneqq B^{\text{glide}}_{\text{screw}}/B^{\text{glide}}_{\text{edge}} \tag{4.34}$$

on the β-distributions. Note that β^{glide} can be re-written in the form

$$\beta^{\text{glide}} = B^{\text{glide}}_{\text{edge}} \left(\left(\frac{\sin\theta}{R_l|\cos\theta|^\eta + |\sin\theta|^\eta} \right)^2 + \left(\frac{-\cos\theta}{R_g|\cos\theta|^\eta + R_l|\sin\theta|^\eta} \right)^2 \right)^{-\frac{1}{2}} \tag{4.35}$$

Figures 4.10 and 4.11 display plots showing the resolved glide drag coefficient for varying R_l between equal regimes ($R_g = 1$) and unequal regimes ($R_g = 2$) respectively. In each case, varying the magnitude of the drag coefficients while maintaining their ratio R_g will not change the normalised distribution.

One important consideration is that the ideal β-distribution should only depend on R_g, and not on the independent magnitude of the drag coefficients. From these

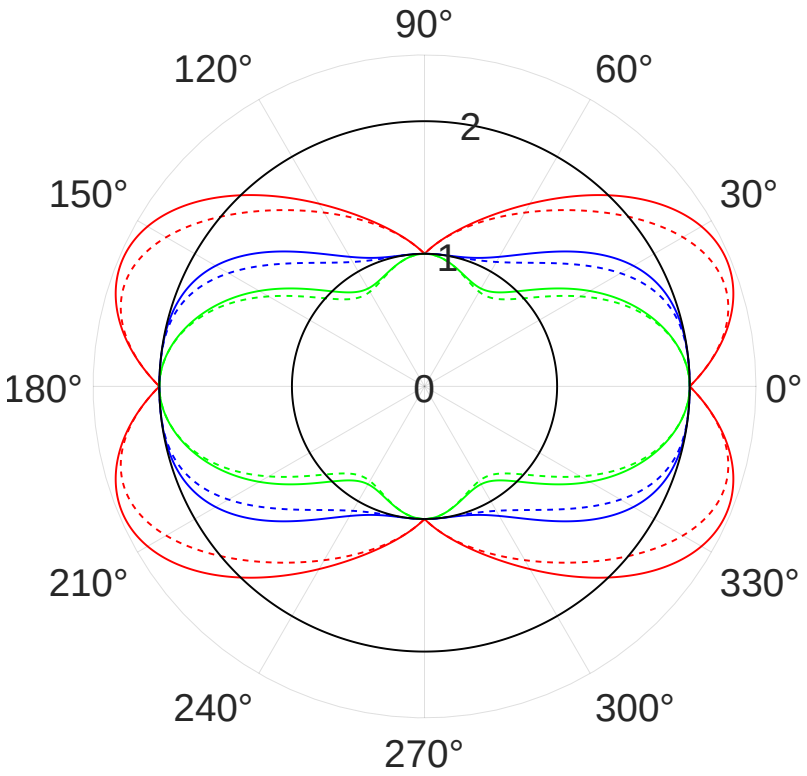


Figure 4.12: Polar plot containing $\hat{\beta}^{\text{glide}}$ interpolations between unequal regimes ($R_g = 2$) with interpolations used for B^{line}. The red, blue, and yellow colours respectively correspond to $\eta = 1$, $\eta = 2$, and $\eta = 3$. The solid lines use the quadratic trigonometric interpolation (4.38) and the dotted lines use the elliptical interpolation (4.39).

plots it can be seen that for fixed R_g the β-distribution is sensitive to R_l. This means that, if a single global value for B^{line} is assigned for all slip systems, the spatial distribution of loops in different slip systems which have the same value for R_g will differ, as they will have different values for R_l. This is unphysical, and should be avoided. It should be noted that the HCP mobility law as presented by Aubry *et al.* [84] should suffer from this phenomenon, although the extent of the impact is unclear from the information provided pertaining to the conducted simulations.

One alternative is to fix a global R_l for a given simulation, and assign B^{line} accordingly for each slip system. This will maintain a consistent β-distribution for each slip system. Another alternative is to concurrently interpolate B^{line} between two regimes as the segment character varies. A natural range is given by

$$\min\left(B^{\text{glide}}_{\text{screw}}, B^{\text{glide}}_{\text{edge}}\right) \leq B^{\text{line}} \leq \max\left(B^{\text{glide}}_{\text{screw}}, B^{\text{glide}}_{\text{edge}}\right) \tag{4.36}$$

which has the benefit of minimising the stiffness of the simulation. In fact, for $\eta = 2$

in particular, if condition (4.36) holds, it follows that condition

$$\min\left(B_{\text{screw}}^{\text{glide}}, B_{\text{edge}}^{\text{glide}}\right) \leq \beta^{\text{glide}} \leq \max\left(B_{\text{screw}}^{\text{glide}}, B_{\text{edge}}^{\text{glide}}\right) \tag{4.37}$$

must hold, which is a conceptually desirable property.

We present two interpolations for B^{line} which fulfill condition (4.36) but which yield different β-distributions. The interpolations are given by

$$B^{\text{line}} = B_{\text{screw}}^{\text{glide}} |\cos\theta|^2 + B_{\text{edge}}^{\text{glide}} |\sin\theta|^2 \tag{4.38}$$

$$B^{\text{line}} = \left(\left(\frac{\cos\theta}{B_{\text{screw}}^{\text{glide}}}\right)^2 + \left(\frac{\sin\theta}{B_{\text{edge}}^{\text{glide}}}\right)^2\right)^{-\frac{1}{2}} \tag{4.39}$$

The quadratic trigonometric interpolation (4.38) is inspired by the $\eta = 2$ scheme, while interpolation (4.39) is the radius of an ellipse with semi-major and semi-minor axes given respectively by $\max\left(B_{\text{screw}}^{\text{glide}}, B_{\text{edge}}^{\text{glide}}\right)$ and $\min\left(B_{\text{screw}}^{\text{glide}}, B_{\text{edge}}^{\text{glide}}\right)$. Figure 4.12 displays a polar plot showing the resolved glide drag coefficient interpolations between unequal regimes ($R_g = 2$) and using interpolations (4.38) and (4.39).

A more thorough analysis of the resolved glide drag coefficient, supported by simulations, will be presented in section 4.4.

Pure line direction

Let us now consider a climb-free, pure line force for our considered segment—i.e. one which acts solely in the line direction, parallel to the line vector and perpendicular to the normal vector. Such a force corresponds to $(\vartheta, \varphi) = (0, 0)$ and is explicitly given by $\boldsymbol{f} = |\boldsymbol{f}|\,(\cos\theta, \sin\theta, 0)^\intercal$. For pure edge and pure screw segments, the resolved line drag coefficients are respectively both $\beta^{\text{line}} = B^{\text{line}}$. For mixed segments, the resolved line drag coefficient is given by

$$\beta^{\text{line}} = \left(\left(\frac{\cos\theta}{B^{\text{line}}|\cos\theta|^\eta + B_{\text{edge}}^{\text{glide}}|\sin\theta|^\eta}\right)^2 + \left(\frac{\sin\theta}{B_{\text{screw}}^{\text{glide}}|\cos\theta|^\eta + B^{\text{line}}|\sin\theta|^\eta}\right)^2\right)^{-\frac{1}{2}} \tag{4.40}$$

Figures 4.13 and 4.14 display plots showing the resolved line drag coefficient for varying R_l between equal regimes ($R_g = 1$) and unequal regimes ($R_g = 2$) respectively. From the plots it is evident that β^{climb} interpolates between edge and screw orientations. However, as has been asserted earlier in this text, line drag has no physical meaning, and thus has no clear physical connection to the character of the segment. Therefore, this interpolation is an odd consequence—the variation of β^{line} with the character angle is a purely trigonometric artifact. However, note that

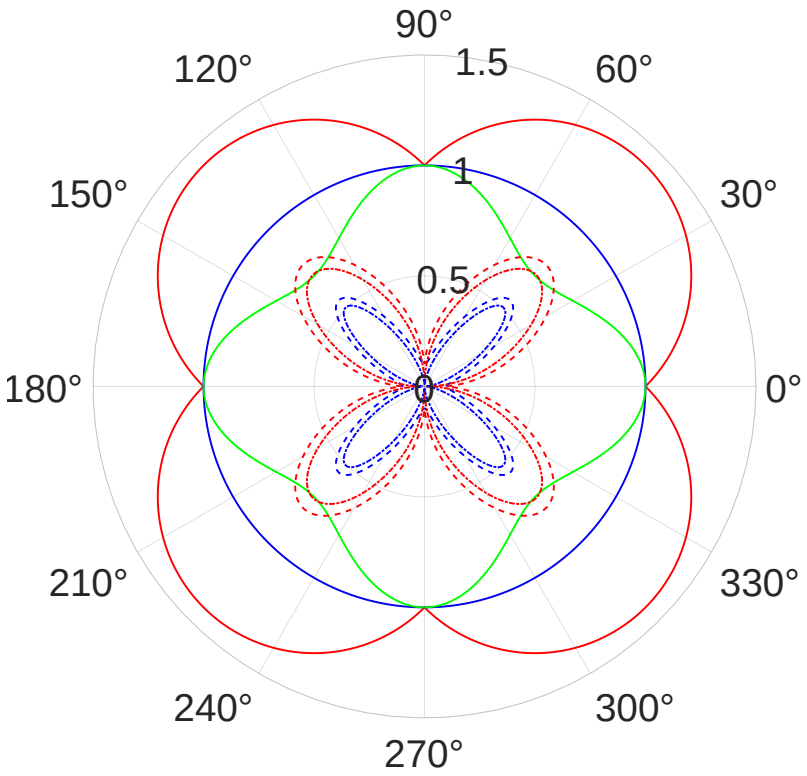


Figure 4.13: Polar plot containing $\hat{\beta}^{\text{line}}$ interpolations between equal regimes ($R_g = 1$) with no interpolations used for B^{line}. The radial axis is $\hat{\beta}^{\text{line}}$ while the angular axis is the character angle (in degrees). The red, blue, and yellow colours respectively correspond to $\eta = 1$, $\eta = 2$, and $\eta = 3$. The solid lines, dotted lines, and half-solid-half-dotted lines respectively correspond to $R_l = 1$, $R_l = 10^{-1}$, and $R_l = 10^{-2}$.

in the $R_g = 1$ case, β^{line} is constant for all θ only when $\eta = 2$. When considering the pure line direction case, a natural choice is therefore $(\eta, R_l) = (2, 1)$. This ensures that the inequality

$$\min\left(B^{\text{glide}}_{\text{screw}}, B^{\text{glide}}_{\text{edge}}\right) \leq \beta^{\text{line}} \leq \max\left(B^{\text{glide}}_{\text{screw}}, B^{\text{glide}}_{\text{edge}}\right) \tag{4.41}$$

is satisfied. Additionally, this choice prevents B^{line} from becoming a limiting factor in the conditioning of the drag tensor.

Pure climb direction

Let us now consider a pure climb force for our considered segment—i.e. one which acts solely in the normal direction, perpendicular to the line and normal vectors. Such a force corresponds to $\vartheta = \frac{\pi}{2}$ and is explicitly given by $\boldsymbol{f} = |\boldsymbol{f}|\,(0, 0, 1)^{\intercal}$. The corresponding resolved drag coefficient is given by

$$\beta^{\text{climb}} = B^{\text{climb}}\left(|\cos\theta|^{\eta} + |\sin\theta|^{\eta}\right) \tag{4.42}$$

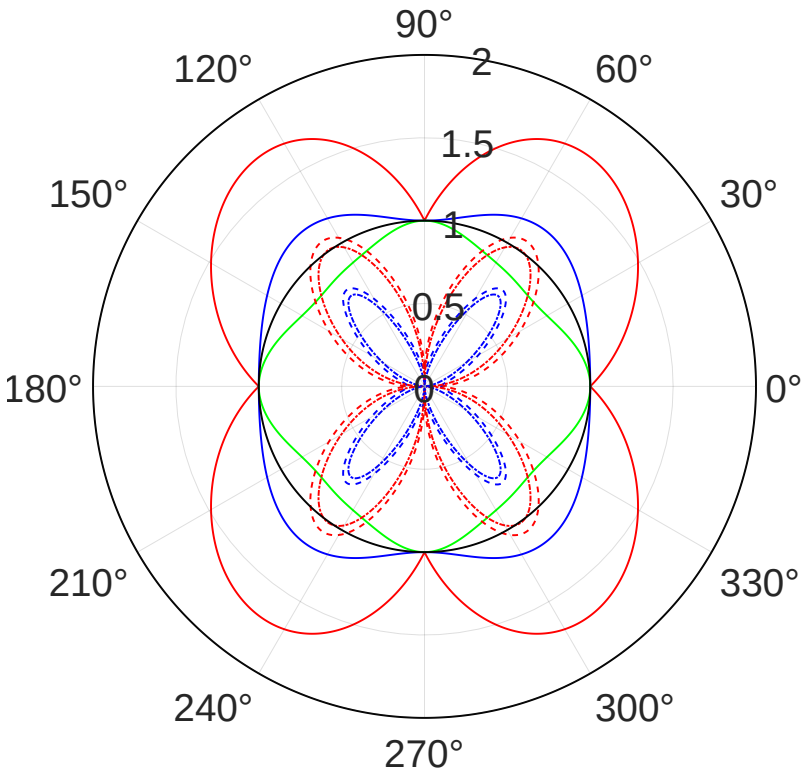


Figure 4.14: Polar plot containing $\hat{\beta}^{\text{line}}$ interpolations between unequal regimes ($R_g = 2$) with no interpolations used for B^{line}. The radial axis is $\hat{\beta}^{\text{line}}$ while the angular axis is the character angle (in degrees). The red, blue, and yellow colours respectively correspond to $\eta = 1$, $\eta = 2$, and $\eta = 3$. The solid lines, dotted lines, and half-solid-half-dotted lines respectively correspond to $R_l = 1$, $R_l = 10^{-1}$, and $R_l = 10^{-2}$.

First, note that B^{line} has no effect in the pure climb case. Next, β^{climb} is only equivalent to B^{climb} for all θ when $\eta = 2$. For $\eta \neq 2$, this property is not guaranteed. Through an argument similar to that of the pure line direction case, the climb drag has no clear physical connection to the segment orientation which can be represented by a proper choice of free parameters in this model—a more sophisticated climb model would be required. When considering the pure climb case, the most natural choice in this model is therefore $\eta = 2$.

The distributions for β^{climb} are plotted in figure 4.15 for a range of integer values of η. For $\eta < 2$, $\beta^{\text{climb}} \geq B^{\text{climb}}$, and for $\eta > 2$, $\beta^{\text{climb}} \leq B^{\text{climb}}$. At $\eta = 0$, $\beta^{\text{climb}} = 2B^{\text{climb}}$. The impact of the choice of η has little effect on β^{climb} until η becomes too large. It is therefore advised to keep $\eta \leq 3$ in order to prevent large unintended oscillation artifacts in the climb drag.

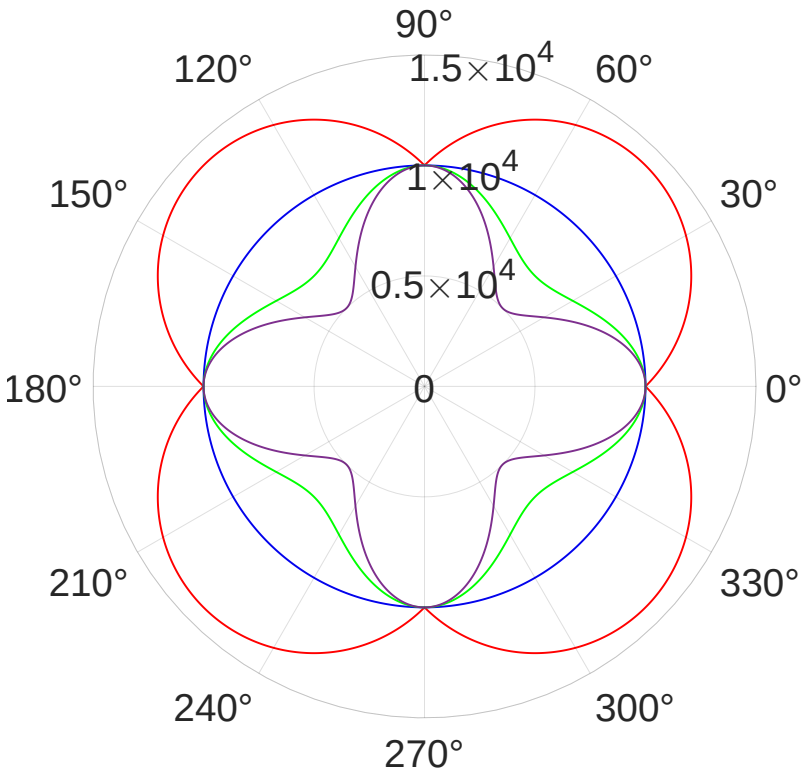


Figure 4.15: Polar plot containing $\hat{\beta}^{\text{climb}}$ distributions at $(\vartheta, \varphi) = \left(\frac{\pi}{2}, \frac{\pi}{2}\right)$ in the radial axis and the character angle (in degrees) in the angular axis. The red, blue, yellow, and purple solid lines respectively correspond to $\eta = 1$, $\eta = 2$, $\eta = 3$, and $\eta = 4$.

4.4 Free spatial distributions of dislocation loops

4.4.1 Problem description

In section 4.3, drag function distributions for the HCP mobility law are analytically derived and plotted for a variety of cases and free parameters. The natural extension to this analysis is to corroborate it with simulations. As we shall see in this section, the choice of drag function can have a significant effect on the evolution of spatial dislocation distributions[7]. Our aim is to make meaningful measurements of these distinctions using a framework which is reproducible in as many different external conditions as possible.

To further understand the influence of the mobility law on dislocations, we shall introduce the notion of a *free* dislocation loop distribution. This is the spatial distribution of an initially circular dislocation loop which is solely acted upon by a

[7] In the context of closed dislocation loops, a spatial dislocation distribution refers to dislocation loop shapes.

spatially uniform stress field such that the loop is growing quasistatically. Although the shape of such a dislocation loop will change over time, in section 4.4.3 we observe that its change in scale-free shape per unit time eventually decreases, thus allowing one to infer the effectively asymptotic distribution over the relevant time-scales of an experiment. This definition ignores other sources of stress—other dislocations, defects, and free surfaces are not included. In a DD simulation, the free distribution will largely depend on the specific mobility law used, and directly reflects the assignment of drag coefficients and applied interpolations. It can be a useful test in order to validate a considered mobility law.

To simulate a free distribution, one constructs an initial circular dislocation loop and allows it to evolve quasistatically under a spatially uniform applied stress. The segments composing a free distribution should be as fine as possible in order to properly resolve its shape, as well as to ensure fulfillment of the assumptions required by the mobility law. As discussed by Hirth *et al.* [216], the approximate total elastic energy of a circular shear dislocation loop of radius R is given by

$$W = \frac{2-\nu}{1-\nu}\frac{\mu b^2}{4} R \left(\ln \frac{4R}{r_c} - 2 \right) \tag{4.43}$$

It follows that the initial conditions of the loop must be such that the external applied shear stress τ^{ext} exerted on the loop fulfills the inequality given by[8]

$$\tau^{\text{ext}} > \frac{2-\nu}{1-\nu}\frac{\mu b}{8\pi R_0} \left(\ln \frac{4R_0}{r_c} - 1 \right) \tag{4.44}$$

where R_0 is the initial radius of the loop. This is the condition for unbounded growth of a circular shear dislocation loop under a spatially uniform applied shear stress. This is an approximation which assumes that the loop will stay circular during its growth. It should be noted that the interaction (arising from the interaction energy) and line tension forces per unit length acting to contract a circular loop respectively follow the approximate relations

$$f^{\text{int}} \sim \frac{\ln R}{R} \qquad \text{and} \qquad f^{\text{line}} \sim \frac{1}{R} \tag{4.45}$$

where R is the radius of the loop [266, 193]. As the loop radius R approaches infinity, both the interaction and line tension forces decrease asymptotically towards zero [266].

[8] This inequality is obtained by invoking the definition of the total outward radial internal force of the loop $F^{\text{self}} = -\partial W/\partial R$ and asserting a balance with an external force given by $-F^{\text{self}} < 2\pi R \tau^{\text{ext}} b$.

In the dynamic case, the chosen drag function β will have a significant impact on the resulting free spatial distribution. When there is a lack of experimentally-obtained data regarding the shape of dislocation curves, a choice of fit for the free spatial distribution should be supported by physical reasoning when possible. Consider first that, in the static case, an ellipse is the minimum length configuration of a shape constrained to enclose a given area and to have positions at given semi-major and semi-minor axes [267]. In addition, it is known that even when one considers a nonlocal interaction energy (in addition to an isotropic local line energy), the ellipse is a minimum energy configuration (under small perturbations) of an isolated closed pure-edge dislocation loop [268, 269]. Therefore, when data is lacking, one relevant selection criterion for the optimal free distribution is the similarity it bears to an ellipse.

Furthermore, it can be shown that the most salient additional phenomena affecting the loop will act to maintain the same type of symmetry as an ellipse[9] (known as D_2 symmetry). The anisotropy introduced by a line energy which interpolates between edge and screw segments has the same type of symmetry as an ellipse. In a dynamic situation, and assuming pure glide, the dislocation loop will be affected by the anisotropy of the drag function β and the drag coefficients, which must also necessarily have the same type of symmetry as an ellipse. It is hence expected that in the case of isotropic linear elasticity, and under the influence of isotropic external forces (such as due to a spatially uniform applied shear stress), this symmetry will be maintained.

4.4.2 Analytical relationships between drag functions and spatial dislocation distributions

Consider a shear dislocation loop as in figure 4.16a. Let the coordinate system lie on the loop centroid, and let the x-axis be parallel to the Burgers vector (the blue arrow in the figure). First, assume that the discretisation of the loop is fine enough such that adjacent segments have approximately equivalent drag matrices $\mathcal{B}_i = \mathcal{B}_{ij}$. Let $\tilde{L}_i$ denote the average of the lengths of each segment attached to node n_i. From the application of the forward Euler algorithm and equation (3.26), it follows that

[9] An ellipse has bilateral symmetry with 2-fold rotational symmetry—it specifically belongs to the dihedral group D_2 [270].

the displacement of node n_i is given by

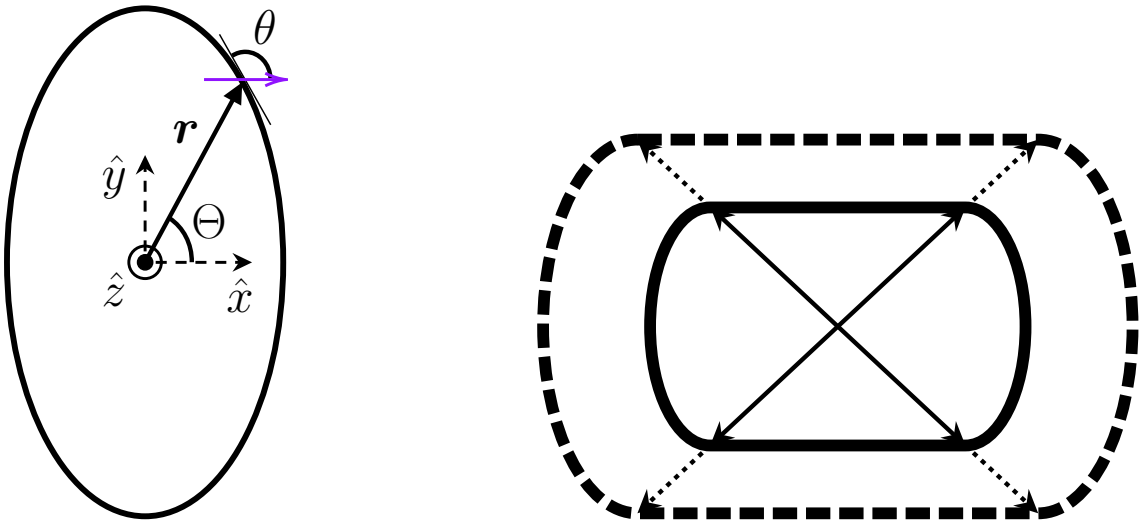
$$\begin{aligned}\Delta \boldsymbol{r}_i &= \boldsymbol{v}_i \Delta t \\ &= \left(\frac{1}{2} \sum_j^2 |L_{ij}| \, \mathcal{B}_{ij} \right)^{-1} \cdot \boldsymbol{f}_i \Delta t \\ &= \frac{1}{\tilde{L}_i} \left(\mathcal{B}_i^{-1} \cdot \hat{\boldsymbol{f}}_i \right) |\boldsymbol{f}_i| \Delta t \\ &= \frac{1}{\tilde{L}_i} \beta^{-1} |\boldsymbol{f}_i| \hat{\boldsymbol{v}}_i \Delta t \end{aligned} \tag{4.46}$$

where $\beta = \beta(\theta)$ is the general resolved drag coefficient from equation (4.28). From the above expression, it is evident that the displacement at each point of the dislocation line is directly proportional to the inverse of the resolved drag coefficient. In the non-HCP formulation, when the force $\boldsymbol{f}_i$ is parallel to an eigenvector of $\mathcal{B}_i$, the forces and velocities are parallel and the resolved drag coefficient is of type pure glide, pure line, or pure climb, depending on the direction of $\boldsymbol{f}_i$. For instance, suppose the forces act perpendicular to the line and climb vectors at each node. This is equivalent to an idealised situation wherein the interaction and core forces are ignored, and a uniform shear stress is applied to the loop. The displacement equation then becomes

$$\Delta \boldsymbol{r}_i = \frac{1}{\tilde{L}_i} \beta^{-1} \boldsymbol{f}_i \Delta t \tag{4.47}$$

As discussed in section 4.3, in the HCP formulation it is not guaranteed that the forces and velocities are parallel when the force $\boldsymbol{f}_i$ is parallel to the pure glide direction $\hat{\boldsymbol{m}}_{ij}$. Consequently, the present discussion is primarily restricted to the standard (non-HCP) formulation. However, suitable approximations may be introduced under which the analysis becomes applicable to the HCP formulation as well.

When selecting the drag coefficients and interpolations used by a mobility law, one typically begins from microscopic observations informed by finer-scale theories (such as MD simulations). The resulting spatial distribution of the dynamic dislocation loop is thus in a sense an emergent phenomenon arising from locally assigned properties. However, from equation (4.47), one may conceive of some procedure by which a scientist elects some β-distribution which results in a global fit for his desired free distribution. For instance, one may select some initial dislocation configuration consisting of a small circular loop with spatial distribution $\boldsymbol{r} \propto \epsilon \hat{\boldsymbol{r}}$ (for $\epsilon \ll 1$) which, in the subsequent time-step, grows to adopt a dislocation configuration $\boldsymbol{r}' \propto \beta^{-1} \hat{\boldsymbol{r}}$. One may hence attempt to construct a distribution β such that $\boldsymbol{r}'$ is of some desired shape which matches an experiment, such as an ellipse. It should be noted that this



(a) (b)

Figure 4.16: Schematics of closed planar dislocation loops. (a) A dislocation loop. The blue arrow represents the Burgers vector $\boldsymbol{b}$, which is parallel to the x-axis. (b) A dislocation loop exhibiting self-similar growth.

method fails to take into account the discrepancy between the character angle θ and the polar angle Θ which occurs after the first time-step. Beyond achieving a rough understanding of the dynamic evolution of the loop, this attempt at adopting a precise free distribution is not very useful.

Self-similar evolution

In order to further study this problem, we consider the regime of *self-similar* (or *homothetic*) evolution, defined as the state during which the spatial dislocation distribution is uniformly scaled by some factor between time-steps (see figure 4.16b). Under such a condition, the proportions of the shape of a dislocation do not change during its growth, thus maintaining self-similarity. For simplicity, we assume an idealised case such that the only force on the line is due to the external applied shear stress, and ignore interaction and line tension forces. Therefore, all forces act purely in the glide plane and perpendicular to the line vector at every point on the line. It follows that the forces must also be parallel to the velocity at every point on the line. For these reasons, the drag function β always refers to the resolved glide drag coefficient β^{glide}. For analyses of this system to remain perspicuous, we operate in the continuum regime, and hence $\boldsymbol{f}_i/\tilde{L}_i \to \boldsymbol{f}$ becomes a force per unit length evaluated at every point on the line, and the displacement equation becomes

$$\Delta \boldsymbol{r} = \beta^{-1} \boldsymbol{f} \Delta t \tag{4.48}$$

where $\Delta \boldsymbol{r} = \Delta \boldsymbol{r}(\boldsymbol{x})$ is now understood to be the displacement at every point $\boldsymbol{x}$ on the line.

There are two pictures of description which must be clearly differentiated in order to develop a coherent model. The first is the physical picture: each point on the line moves a displacement $\Delta \boldsymbol{r}$ perpendicular to the line, with a magnitude depending on the inverse of the drag function β^{-1}. The second picture is a geometric one: during self-similar evolution, the new shape is a scaled version of the original shape, and the geometric displacement vector $\Delta \boldsymbol{R}$ connecting corresponding scaled points on the initial and final shapes is proportional to the radial vector of the initial shape (see figure 4.17). This condition can be stated as $\Delta \boldsymbol{R} = \boldsymbol{R}_s(\gamma - 1)$, where γ is a constant related to the growth rate and $\boldsymbol{R}_s = \boldsymbol{R}_s(\Theta)$ is the spatial distribution of the dislocation loop. Note that we restrict the treatment of this system to dislocation loops for which the radial spatial function $\boldsymbol{R}_s$ that describes them is injective.

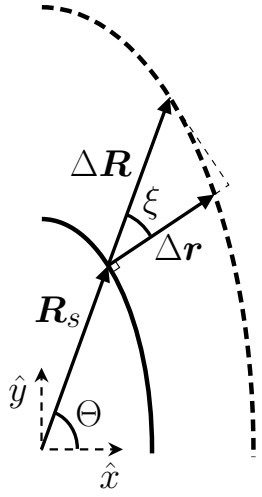


Figure 4.17: Schematic of a portion of a dislocation loop exhibiting self-similar growth.

The self-similar evolution condition is most conveniently stated in the geometric picture. To close the system, we must relate the physical line displacement Δr with the geometric displacement ΔR, i.e. we must impose some relationship

$$\Delta r = \Delta r(\Delta R) \tag{4.49}$$

where $\Delta r \coloneqq |\Delta \boldsymbol{r}|$ and $\Delta R \coloneqq |\Delta \boldsymbol{R}|$. This leads to the general relationship

$$\Delta r(R_s) = \beta^{-1} |\boldsymbol{f}| \Delta t \tag{4.50}$$

At any given point on the line, Δr depends on purely local information—namely, the drag function and the curvature at that point. On the other hand, relating Δr to ΔR in general requires nonlocal information. For instance, one would at least need the position of the point which lies on the intersection between the line defined by the vector $\boldsymbol{R}_s + \Delta \boldsymbol{r}$ and the dislocation loop. However, special cases can be considered where the relation becomes local, either approximately or even exactly. For example, for a rectangular loop, the relation becomes (except for at the corners) exactly

$$\Delta r = \Delta \boldsymbol{R} \cdot \hat{m} = \Delta R \cos \xi \tag{4.51}$$

where $\hat{m} = \hat{m}(\Theta)$ is the unit vector perpendicular to both the line and climb vectors at every point on the line, and $\xi = \xi(\Theta)$ is the angle between $\hat{m}$ and the radial unit vector $\hat{r}$. This relation can be used approximately for convex shapes which do not have extreme curvature at any point on the line. If the local closure relation (4.51) is imposed, the displacement equation becomes

$$R_s = \frac{K}{\beta \cos \xi} \tag{4.52}$$

where $K = |\boldsymbol{f}|\Delta t/(\gamma - 1)$ is a constant that is independent of the position on the dislocation line.

The aim is to construct a drag function $\beta(\theta)$ given a spatial distribution $R_s(\Theta)$ and a closure relation $\Delta r(R_s)$. The general procedure is outlined in the following. The drag function is in general expressed in terms of the polar angle Θ via

$$\beta(\theta(\Theta)) \propto \frac{1}{\Delta r(R_s)} \tag{4.53}$$

up to some scaling constant. Note that for a local closure relation, equation (4.53) becomes explicit. One must then determine the relationship between the polar angle Θ and the character angle θ. The tangent vector $\boldsymbol{l}$ at any point on the line is obtained by performing the differentiation

$$\boldsymbol{l} = \begin{bmatrix} l_x \\ l_y \\ l_z \end{bmatrix} = \frac{\mathrm{d}}{\mathrm{d}\Theta} \begin{bmatrix} R_s(\Theta) \cos \Theta \\ R_s(\Theta) \sin \Theta \\ 0 \end{bmatrix} \tag{4.54}$$

It follows that the relationship

$$\tan \theta = \frac{l_y(\Theta)}{l_x(\Theta)} \tag{4.55}$$

must be satisfied. One can always analytically express θ in terms of Θ, but determining the inverse relationship $\Theta = \Theta(\theta)$ may require numerical methods.

Note that the inverse problem of finding the distribution $R_s(\Theta)$ given a drag function $\beta(\theta)$ and a closure relation $\Delta r(R_s)$ is more challenging. This is because this requires solving an implicit equation given by

$$\Delta r(R_s) \propto \left[\beta \left(\arctan \left(\frac{\frac{\mathrm{d}}{\mathrm{d}\Theta}(R_s(\Theta) \cos \Theta)}{\frac{\mathrm{d}}{\mathrm{d}\Theta}(R_s(\Theta) \sin \Theta)} \right) \right) \right]^{-1} \tag{4.56}$$

which in most cases must be solved using numerical methods. Note that even for a local closure relation, equation (4.56) remains implicit. Solving this problem may be useful in order to determine the self-similar spatial distribution corresponding to a proposed drag function, but this will not be considered further in this text.

A level set approach

In practice, obtaining an exact analytical closure relation $\Delta r\left(R_s\right)$ is challenging, and likely impossible for most loop shapes. On the other hand, adopting a level set based approach results in a conversion of the dislocation front tracking framework considered above into a standard PDE system, which enables the calculation of analytical solutions in some cases. While some computational studies have applied level set methods to simulate dislocation dynamics [271, 272, 273], no studies have been identified which use this approach to derive or justify analytical drag function expressions, which are largely selected ad hoc. In the following, only a brief presentation of a relevant result will be provided; for a more thorough explanation of this method, as well as a detailed example, see appendix A.

The assumptions made are as follows: (1) the only force on the dislocation loop is due to a spatially uniform external applied shear stress (interaction and line tension forces are ignored) and (2) a significant glide-climb drag anisotropy is present, so that the contribution of climb forces can be ignored. The main idea is to solve the so-called *level set equation* for a closed dislocation loop, which, when applying these assumptions, is given by

$$u_t - |\nabla u| \beta^{-1} f = 0 \tag{4.57}$$

where $f = |\boldsymbol{f}\left(\boldsymbol{x}\right)|$ is the spatially uniform force per unit length, β is the drag function, and $u = u\left(\boldsymbol{x}, t\right)$ is an auxillary time-dependent scalar function. We assume that the spatial domain of u is the two-dimensional glide plane of the one-dimensional dislocation loop. The spatial position of the dislocation loop is then defined to be the zero level set of the auxillary function, i.e. $u = 0$.

Let us consider the specific example of an ellipse, which is derived in appendix A.2. The target distribution $R_s\left(\Theta\right)$ is given by

$$R_s\left(\Theta\right) \propto \left(\left(\frac{\cos\Theta}{a_1} \right)^2 + \left(\frac{\sin\Theta}{a_2} \right)^2 \right)^{-1/2} \tag{4.58}$$

up to some scaling constant. The screw and edge glide drag coefficients respectively satisfy $a_1 = B_{\text{screw}}^{\text{glide}}$ and $a_2 = B_{\text{edge}}^{\text{glide}}$ to obtain the desired proportions of the ellipse. Through an appropriate choice of initial conditions for u, it can be shown that β must be

$$\beta\left(\theta\right) = \left(\left(\frac{\cos\theta}{B_{\text{screw}}^{\text{glide}}} \right)^2 + \left(\frac{\sin\theta}{B_{\text{edge}}^{\text{glide}}} \right)^2 \right)^{-1/2} \tag{4.59}$$

Equation (4.59) is the radial equation of an ellipse in terms of θ. This is an expression commonly used to interpolate the glide drag coefficient, especially in BCC materials [223, 206, 101, 192].

Because the external stress state is isotropic, in this self-similar evolution model it is assumed that all anisotropies arise from the drag function β. In an actual simulation, as the loop increases in size, the magnitude of the (anisotropic) interaction and line tension forces decay asymptotically towards zero, but the isotropic applied shear stress remains unchanged. It follows that, as the loop increases in size, the anisotropy arising from the drag function becomes increasingly dominant. Therefore, this self-similar evolution model becomes more accurate as the loop size increases. One could feasibly extend the model by taking into account anisotropic forces which vary along the line according to the character angle and curvature, thus determining a more realistic self-similar distribution.

One can derive any such drag function $\beta(\theta)$ as long as $R_s(\Theta)$ is injective and has D_2 symmetry. However, during a simulation it is not likely that dislocation loops will achieve their self-similar evolution state in a physically realisable time. It is difficult to know a priori how long it will take for this to happen. Therefore, this method should only be used to obtain an approximate understanding of the asymptotic spatial distribution of a dislocation loop. This method is most useful when applied to the conditions found in tensile simulations, since dislocation loops therein grow under approximately spatially uniform isotropic shear stresses. In addition, it is expected that it will take longer to achieve a self-similar evolution state if the corresponding shape exhibits high curvature, as the line tension will be stronger and take longer to decay as the loop grows. Because of this, as well as the limitations associated with a local physical-geometric closure relation, the self-similar evolution model is most useful for convex dislocation loops which have fairly low curvature. Finally, it is important to note that the presently considered self-similar evolution model applies primarily to non-HCP formulations. This is because, under the HCP formulation, the velocities will not necessarily be parallel to the forces which arise in this model, which is an underlying assumption. However, the self-similar evolution model may still be applicable to the HCP formulation when the anisotropy between edge and screw glide directions is sufficiently small.

4.4.3 Simulation results and analyses

Simulations were conducted and analysed in order to test the HCP mobility law for an assortment of values for the parameters η, R_l and R_g. Each simulation proceeds

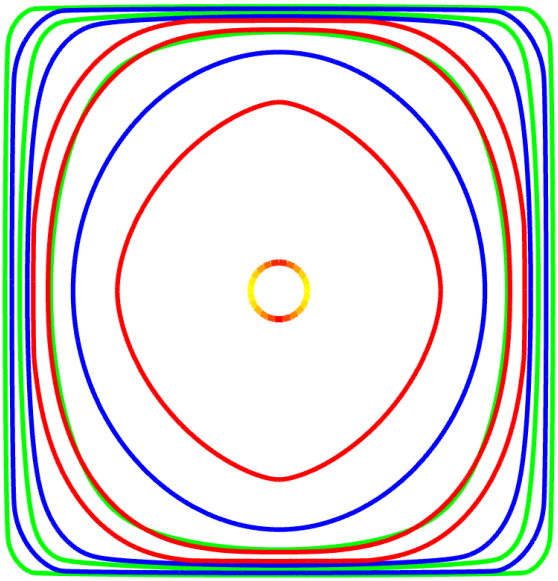
as follows. The initial condition consists of a 24-segment circular shear dislocation loop of radius $R_0 = 175\,\text{nm}$ placed within an infinite domain. Note that, according to equation (4.44), the minimum spatially uniform external shear stress τ^{ext} required for unbounded growth of a loop of this initial size is approximately 45 MPa. A spatially uniform external shear stress of $\tau^{\text{ext}} = 200\,\text{MPa}$ is applied on the loop, and it is allowed to evolve on the 1Ba slip system. For all slip systems, the edge drag coefficients are set to unity, the screw drag coefficients are set to R_g, and the climb drag coefficients are set to 10^6. The simulation is interrupted after a total time of $\Delta t_{\text{total}} = 2 \times 10^{-9}\,\text{s}$, and the results are saved. This process is repeated for the case of no B^{line} interpolation for all possible combinations of $\eta : \{1, 2, 3\}$, $R_l : \{1, 10^{-1}, 10^{-2}\}$, and $R_g : \{1, 2, 10\}$ (27 runs), and the case of quadratic trigonometric (equation (4.38)) and elliptical (equation (4.39)) B^{line} interpolations for all possible combinations of $\eta : \{1, 2, 3\}$ and $R_g : \{1, 2, 10\}$ (18 runs). A total of 45 simulation runs were conducted.

Figure 4.18 displays the spatial superposition of the results of all simulation runs separately for each R_g. It should be noted that the difference in R_l is not made visually distinct in the spatial plots. However, for all loops, a smaller R_l leads to a larger maximum distance travelled. In addition, loops which use the elliptical B^{line} interpolation travel further than those which use the quadratic trigonometric B^{line} interpolation.

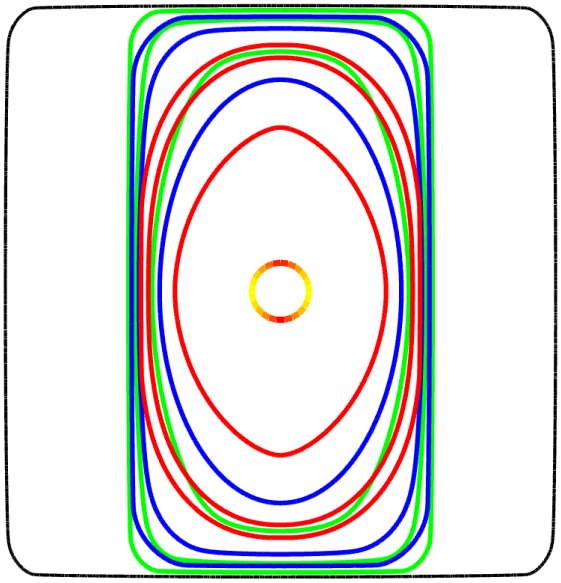
Total distance travelled

The first observation of note is that there is a significant difference in the maximum distance travelled by each loop. Figure 4.19 displays plots of R/R_0 for each loop, where R is the maximum distance from its centroid to any position on the loop and R_0 is the radius of the initial loop. The plotted results are separated based on R_g, and, independently for each R_g, ordered from smallest to largest R.

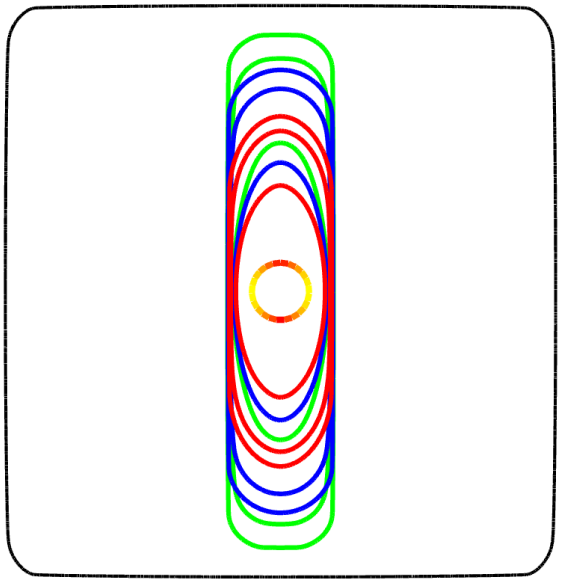
The difference in the distance each loop travels can be partially explained through line tension arguments. The larger the anisotropy in the spatial distribution—such as when one direction becomes more elongated that the other—the more the line tension will restrict the elongated side from moving. In general, the smaller the value for R_g (and thus the smaller the anisotropy), the faster the loop will travel overall. This difference can also be partially explained through an analysis of the difference in glide drag coefficient interpolations. Examining the distributions for β^{glide} (figure 4.11) reveals that some free parameters correspond to interpolations which deviate significantly from the range $\left[B^{\text{glide}}_{\text{edge}}, B^{\text{glide}}_{\text{screw}}\right]$. In general, $\eta \geq 2$ yields distributions



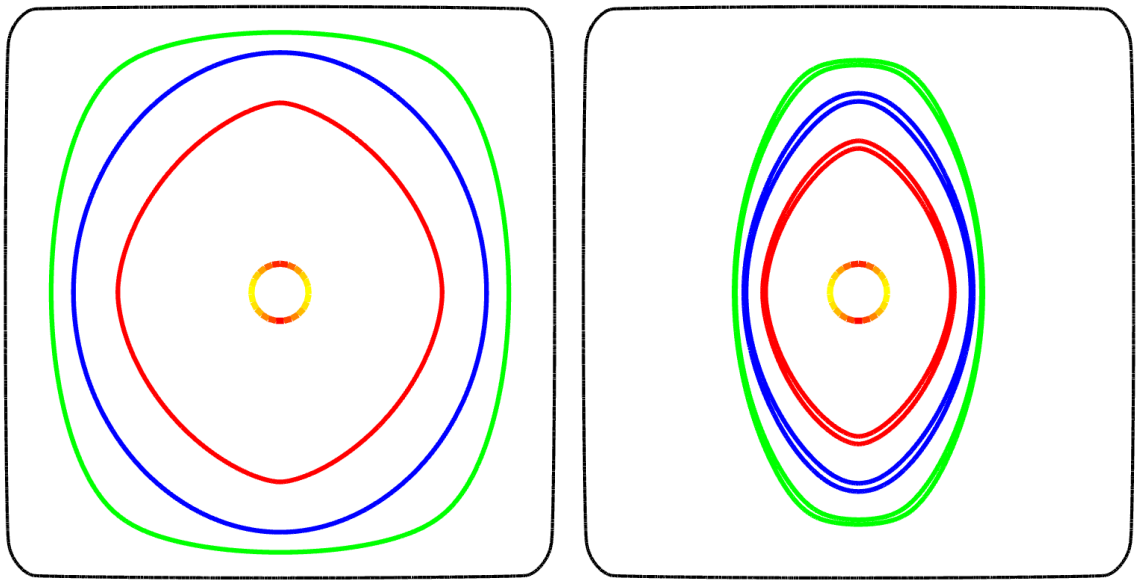
(a) $R_g = 1$; $\eta : \{1, 2, 3\}$ $R_l : \{1, 10^{-1}, 10^{-2}\}$.



(b) $R_g = 2$; $\eta : \{1, 2, 3\}$ $R_l : \{1, 10^{-1}, 10^{-2}\}$.

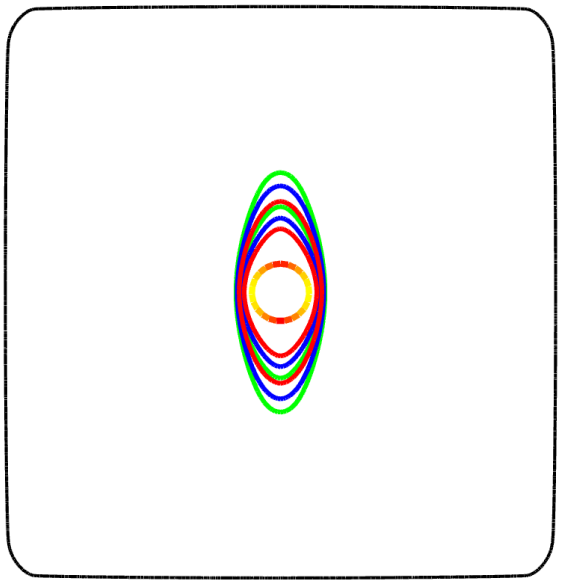


(c) $R_g = 10$; $\eta : \{1, 2, 3\}$; $R_l : \{1, 10^{-1}, 10^{-2}\}$.



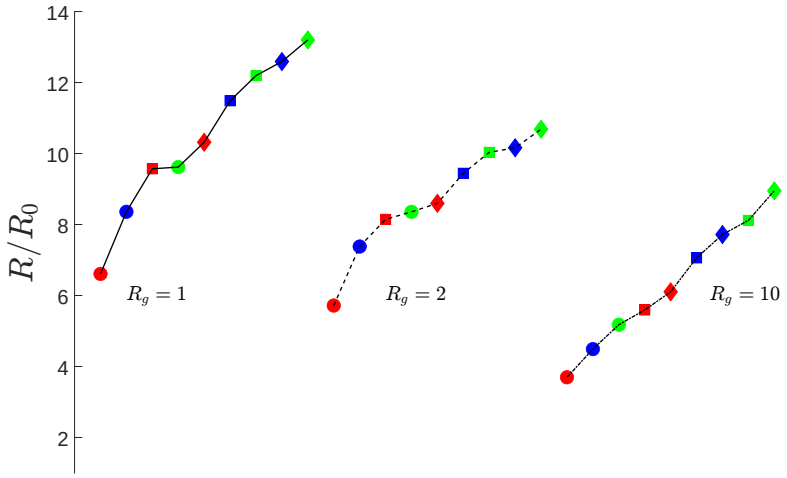
(d) $R_g = 1$; $\eta : \{1, 2, 3\}$; R_l : N/A.

(e) $R_g = 2$; $\eta : \{1, 2, 3\}$; R_l : N/A.

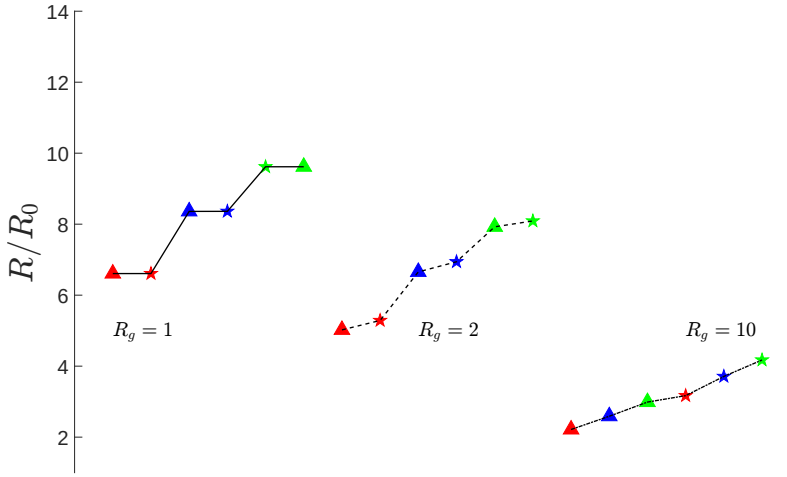


(f) $R_g = 10$; $\eta : \{1, 2, 3\}$; R_l : N/A.

Figure 4.18: Free spatial dislocation loop distributions corresponding to different β-distributions with varying values of η, R_l, and R_g. Distributions (a-c) use no interpolations for B^{line}. Distributions (d-f) use interpolations (4.38) and (4.39) for B^{line}. The central segmented circular loop present in all figures represents the initial dislocation configuration for all tests—it follows the red-edge and yellow-screw colour scheme. The red, blue, and yellow loops respectively correspond to $\eta = 1$, $\eta = 2$, and $\eta = 3$. The black dotted line represents the dislocation loop which travelled the furthest distance, for comparison.



(a) Plots corresponding to no B^{line} interpolation.



(b) Plots corresponding to B^{line} interpolation.

Figure 4.19: Plots containing R/R_0 for varying values of η, R_l, and R_g. The red, blue, and yellow colours respectively correspond to $\eta = 1$, $\eta = 2$, and $\eta = 3$. The circles, squares, and diamonds respectively correspond to $R_l = 1$, $R_l = 10^{-1}$, and $R_l = 10^{-2}$. The triangles and pentagrams respectively correspond to quadratic trigonometric and elliptical B^{line} interpolations.

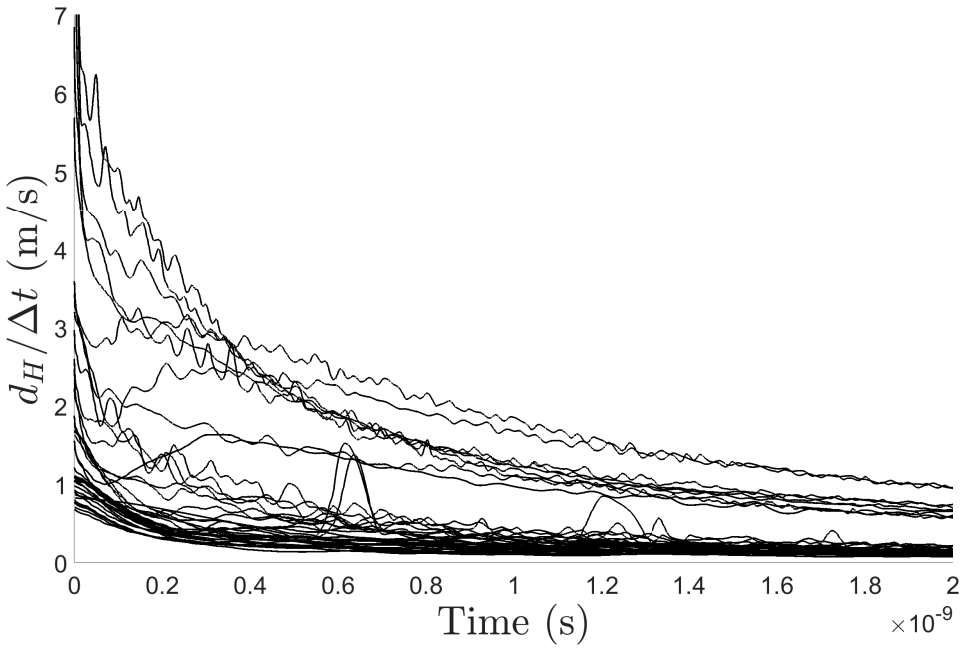


Figure 4.20: Superimposed plots of the normalised Hausdorff distance as a function of time for all simulation runs.

for which $\varsigma \leq \beta^{\text{glide}} \leq B^{\text{glide}}_{\text{screw}}$ such that $\varsigma \leq B^{\text{glide}}_{\text{edge}}$ (equality applies for $\eta = 2$ only). On the other hand, $\eta < 2$ yields distributions for which $B^{\text{glide}}_{\text{edge}} \leq \beta^{\text{glide}} \leq \varsigma$ such that $B^{\text{glide}}_{\text{screw}} < \varsigma$. The larger the value for η, the greater the degree of deviation from the interval $\left[B^{\text{glide}}_{\text{edge}}, B^{\text{glide}}_{\text{screw}}\right]$. Therefore, the larger the value for η, the faster the corresponding loop will travel. Across all η, a similar reasoning applies to R_l. The smaller the value for R_l, the smaller the lower bound of β^{glide} will be, and thus the faster the corresponding loop will travel. These analytically-informed inferences are clearly reflected in the simulation results.

Self-similar evolution regime identification

By simply visually observing the simulation as it progresses, it can be seen that each free spatial distribution roughly approaches a self-similar evolution state. However, this should be substantiated with a more precise and quantitative detection technique. We pursue a useful metric which measures the distance between two sets of points: set A, the set of points describing the position of the dislocation loop at one time-step, and set B, the set of points describing the position of the dislocation loop at the subsequent time-step. An example of such a metric is given by the Hausdorff distance d_H [274]. The Hausdorff distance between two finite discrete sets A and B is given

by

$$d_H(A,B) = \max\left[\max_{a\in A} d(a,B),\ \max_{b\in B} d(A,b)\right] \tag{4.60}$$

where $d(x,B) = d(B,x) \coloneqq \min_{y\in B} d(x,y)$ is the smallest Euclidean distance between the point x to any point in the set B, and $d(x,y)$ is the Euclidean distance between points x and y. Roughly speaking, this metric determines the maximum of all the minimum Euclidean distances between the points in one set to the other. One reason that this is a good metric is that it is robust with respect to irregular shapes. It can intelligibly measure the distance between the two sets of points when they are non-planar (e.g. during significant climb), when there is no symmetry, and when there is a significant disparity in the size of each set. It is also invariant with respect to translations of the coordinate origin, and to coordinate rotations. Another advantage is that this metric is simple to implement since it does not require interpolation techniques or any special ordering of the data set.

In the simulations conducted in this section, the Hausdorff distance d_H was computed at every time-step, comparing the set consisting of the positions of the nodes of the dislocation loop at the current time-step with those of the loop in the previous time-step. The scale-free loop was used for this computation, determined via a normalisation of its positions with respect to R (the maximum distance from the centroid to any position on the loop). In order to eliminate the dependency on the varying time-step size Δt, d_H was normalised through $d_H^k/\Delta t^k$, where the superscript k refers to the current time-step number in the simulation. This quantity can be interpreted as a measure of how quickly the scale-free loop changes in shape. Figure 4.20 displays superimposed plots of the normalised Hausdorff distance as a function of time for all simulation runs. For increased visibility, Gaussian smoothing was applied to each plot, using a moving average filter with a window containing 100 elements. However, significant noise and oscillations are still present in the figure plots, which likely arises due to two common computational phenomena. First, small variations in the time-step occur that oscillate about a stable average during time integration (see figure 6.18 for an example), with respect to which $d_H/\Delta t$ is highly sensitive. Second, irregular and largely unpredictable nodal remeshing occurs during loop evolution, which may impact d_H. However, these effects are transient with respect to the relevant time scale of loop evolution, and the loop shape change should be accurately captured on average. Therefore, their impact on the important results inferred from this figure are minor.

The most important observation is that all plots display a tendency to decay asymptotically towards a small value—as time progresses, each loop shape approaches a self-similar evolution state. It is expected that, as time progresses, the self-similar state assumption would become increasingly valid, and that the spatial distribution of each dislocation loop would increasingly approach the one derived from the β-distribution as described by equation (4.50). However, it is possible that the self-similar state is reached neither in a finite time nor in a physically realisable time. That is, it may be physically implausible for a single-grain sample to be large enough to contain even approximately self-similar dislocation loops. The time until a self-similar state is reached will be even greater for free spatial distributions which contain pieces of greater curvature. However, it is expected that increasing the magnitude of the external applied shear stress will increase the rate at which loops reach their self-similar state, since the isotropic external stress will increasingly dominate over the anisotropic internal forces.

Deviation from an ellipse

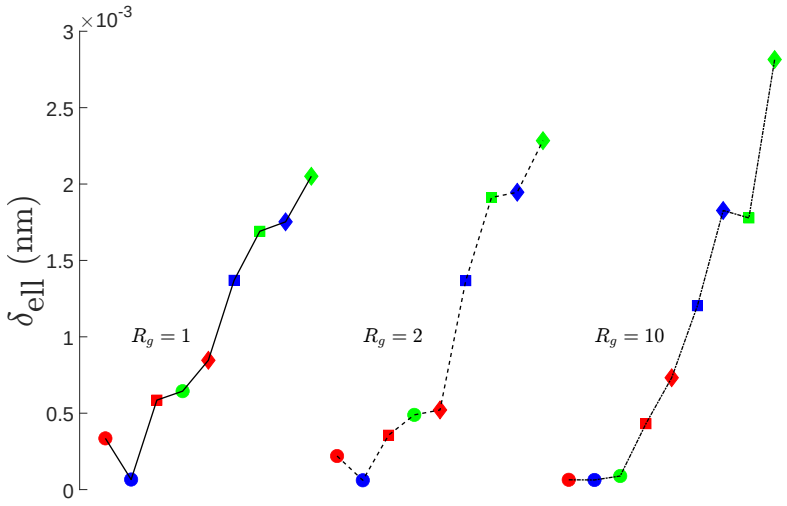
The next observation is that there is a significant difference in the scale-free shape of the loops, as expected. The shapes appear to range from deviations of ellipses, to rectangles with curved corners. To quantify the deviation of each shape to an ellipse, the following procedure was conducted for each loop. An ellipse was first fitted to the set of points describing the loop (normalised with respect to R, as usual) $\mathcal{A}_{\text{loop}}$. This was performed by using the least squares criterion for the conic representation of an ellipse, which is the set of points $(x_1, x_2) \in \mathcal{A}_{\text{ell}}$ which satisfies the equation

$$Ax_1^2 + Bx_1x_2 + Cx_2^2 + Dx_1 + Ex_2 + F = 0 \tag{4.61}$$

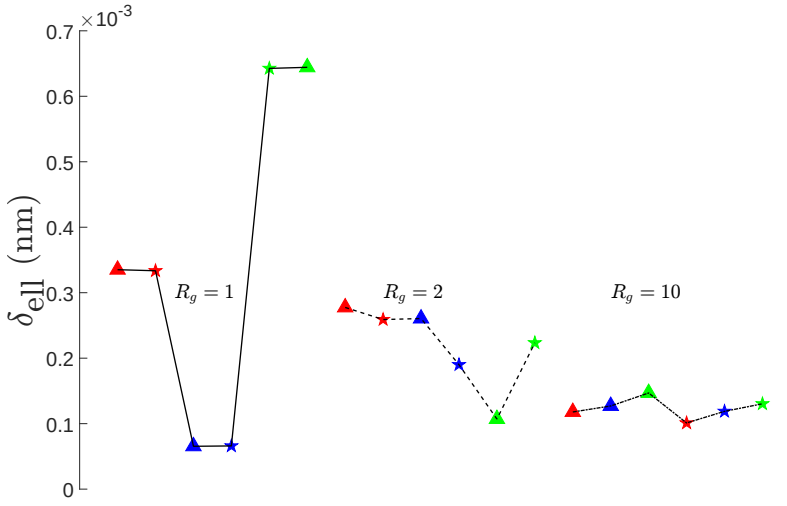
Note that the points $\mathcal{A}_{\text{loop}}$ were all projected onto the glide plane of the loop in order to convert it to an effectively 2D system. This will have a negligible effect on the calculation, as climb motion was heavily restricted during the simulation. Finally, the Hausdorff distance between the sets $\mathcal{A}_{\text{loop}}$ and $\mathcal{A}_{\text{ell}}$ was obtained, necessitating the computation of

$$\delta_{\text{ell}} = d_H\left(\mathcal{A}_{\text{loop}}, \mathcal{A}_{\text{ell}}\right) \tag{4.62}$$

Figure 4.21 displays plots which have the same horizontal data ordering as in figure 4.19, but which instead plot the deviation of each loop from an ellipse, given by δ_{ell}. One observation from these plots is that the free parameters which correspond to the least deviation from the ellipse, for the widest range of R_g, are $(\eta, R_l) = (2, 1)$.



(a) Plots corresponding to no B^{line} interpolation.



(b) Plots corresponding to B^{line} interpolation.

Figure 4.21: Plots containing δ_{ell} (see equation (4.62)) for varying values of η, R_l, and R_g. The red, blue, and yellow colours respectively correspond to $\eta = 1$, $\eta = 2$, and $\eta = 3$. The circles, squares, and diamonds respectively correspond to $R_l = 1$, $R_l = 10^{-1}$, and $R_l = 10^{-2}$. The triangles and pentagrams respectively correspond to quadratic trigonometric and elliptical B^{line} interpolations.

It should be noted that, of the free parameters tested, this selection is the one which yields a β^{glide} distribution which fits closest to an ellipse, i.e. equation (4.59). Note however that this equation cannot in general be fitted exactly by the HCP mobility law (equation (4.33)) via an appropriate selection of free parameters. Next, the choice $\eta = 1$ corresponds to the lowest sensitivity in δ_{ell} to any other parameter. This can be predicted by examining the corresponding β^{glide} distributions—compared to $\eta > 1$, the choice $\eta = 1$ corresponds to less variation in β^{glide} when changing R_l or the B^{line} interpolation method.

4.5 Conclusions and future work

This chapter introduces and elucidates upon the HCP mobility law, which is necessary in the implementation of 3D DD simulations in HCP materials. The development and formulation of this mobility law therefore constitutes a foundational component of the simulation framework used throughout the remainder of this text, as all subsequent chapters are based upon it. However, some potential areas of investigation remain which should be discussed.

In contrast to FCC and BCC crystal structures, HCP systems are both geometrically and kinematically anisotropic, as dislocation mobility can vary greatly across different slip systems. To capture this complex anisotropy, the HCP mobility law treats the mobility of dislocation segments as a length-weighted mixture of multiple slip system mobilities. Furthermore, it sacrifices the relative simplicity of the drag tensor construction method of the non-HCP formulation in favour of a greater inherent mathematical flexibility in accommodating additional slip systems to the model. In principle, the HCP mobility law presented in this chapter can be extended and applied to any crystallography in a straightforward manner. In the absence of off-plane segment components, the parameter selection $(\eta, R_l) = (2, 1)$ was found to be optimal because it is the only selection for which: (1) isotropic input drag coefficients correspond to an isotropic drag function, and (2) the drag function lays strictly within the range provided by the input drag coefficients.

An important aspect of the HCP mobility law is that it effectively assigns normal vectors to each edge decomposition of a segment without reference to pre-defined normal vectors. Therefore, in contrast to other potential methods, the pre-defined normal vector plays less of a role in strictly defining the glide plane of segments. In principle, this allows pure edge segments that deviate from the pre-defined glide plane to freely glide on different planes. While this flexibility may offer certain advantages,

considerations should be made about whether a more restrictive mobility law—one that enforces glide strictly along pre-defined planes—would yield more accurate results. This issue affects the quality of the simulations conducted in chapter 6; the consequences are discussed therein.

The representation of climb in most drag-based DD mobility laws—that is, as an off-plane velocity component that is always linearly proportional to the applied nodal force—is not entirely physics-based. The HCP mobility law presented in this chapter suffers from this same type of nonphysicality, and the physical interpretation of off-plane segments is not always clear. Furthermore, the presence of climb in a DD simulation greatly complicates the treatment of various segment processes, particularly topological operations. Improper treatment of these processes can lead to spurious dislocation arrangements and computational difficulties, some of which are discussed in chapter 6. On the other hand, physically consistent climb motion has been incorporated in some DD models as a thermally activated process described by an Arrhenius form [129, 225, 128, 82]. Therefore, since climb is not entirely physics-based in the HCP mobility law presented in this chapter, in some cases it is advised to disable it entirely when conducting large-scale DD simulations.

It is notable that disabling climb limits some of the attractive qualities of the HCP mobility law—for instance, it reduces the proportion of off-plane segments, the treatment of which partly motivates its use. However, this mobility law formulation remains valuable because of (1) its flexibility in seamlessly accommodating additional slip systems into the model and (2) its ability to approximate the mobility of spurious or unresolved segments, as depicted in figure 4.7a.

Chapter 5

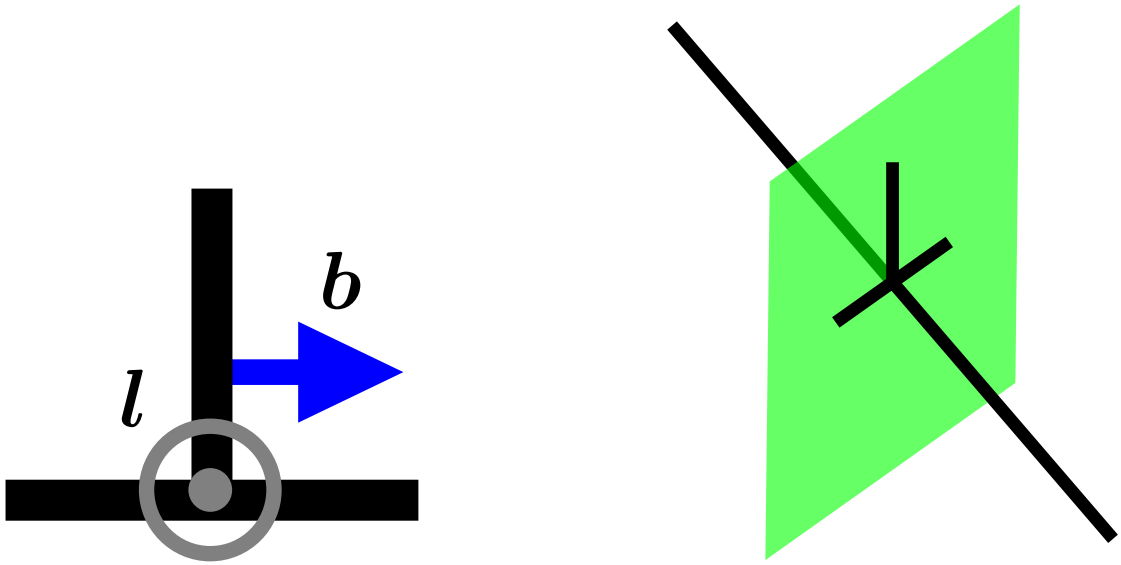
A 2.5D model of irradiation hardening

Chapter introduction

In this chapter, a 2.5D model of irradiation hardening which incorporates realistic prismatic loop physics is described and implemented. In section 5.1, the basic framework of the 2.5D model is introduced, and the fields generated by the dislocation structures of interest are analysed. In section 5.2, a 3D simulation is conducted and analysed to inform the 2.5D model with information pertaining to dislocation-loop reactions. In section 5.3, prismatic loops are analysed in detail to inform the 2.5D model with information pertaining to prismatic loop rotation physics. In section 5.4, 2.5D DD simulations are conducted and analysed. In section 5.5, limitations of the 2.5D model are examined, and potential future work is explored. Note that large portions of the content in this chapter (most of sections 5.2, 5.3, and 5.4) are published in Hortelano-Roig *et al.* [1], although there are new results as well. Rakesh Kumar and Daniel Balint at Imperial College London conducted the 2.5D DD simulations contained in this chapter and created figures 5.23 and 5.27.

5.1 Representations of prismatic loops

3D DD is associated with significant computational and theoretical challenges which are circumvented in DDP models. In 2D DD, all dislocations are modelled as infinitely long straight edge dislocations with line direction perpendicular to the plane of the simulation (see figure 5.1), thereby remaining fully compatible with the plane strain condition. The planar 2D DD model can therefore not model screw dislocations, dislocations parallel to the plane of the simulation, self-interaction



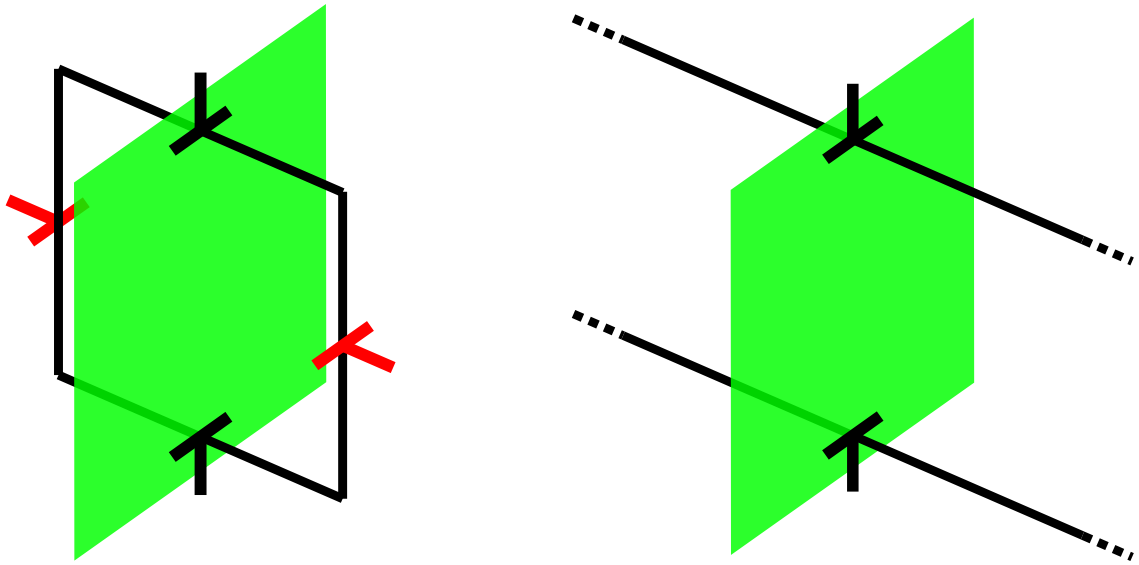
(a) (b)

Figure 5.1: Schematics of a positive edge dislocation in a 2D DD model seen from different perspectives. (a) The 2D DD simulation plane corresponds to the page. The blue arrow is the Burgers vector $\boldsymbol{b}$ and the grey annulus with a central disc is the line direction $\boldsymbol{l}$ pointing out of the page. (b) The green plane represents a finite subset of the 2D DD simulation plane.

terms, and complex dislocation-dislocation reactions. The aim of this chapter is to inform an otherwise planar model of discrete edge dislocations interacting with 2D representations of irradiation loop defects with the essential 3D mechanics of dislocation-loop interactions to thereby construct a 2.5D model with sufficient fidelity to identify the salient mechanisms of irradiation hardening.

In the planar model, irradiation loops are represented as planar cuts of square prismatic loops (see figure 5.2a), which are captured by edge dislocation dipoles in climb configurations (see figure 5.2b). For the case of the loop habit plane being perpendicular to the simulation plane, all four loop segments cannot be explicitly modelled due to the planar nature of DDP. The segments parallel to the simulation plane cannot be modelled by 2D DD, while the segments perpendicular to the simulation plane can only be partially modelled by 2D DD. In this section, we shall make comparisons between some properties of prismatic loops and edge dipoles to, in part, understand to what degree the latter can approximate the former in a 2.5D DD model.

Let us consider a square prismatic vacancy loop with side length (also referred to as diameter or size) L absent of external stress fields as in figures 5.15a and



(a) (b)

Figure 5.2: Schematics of a subset of the 2D simulation plane (the green plane) which bisects (a) a prismatic vacancy loop and (b) a vacancy edge dipole. In the prismatic loop, the dislocations (in red) parallel to the plane cannot be modelled by 2D DD, while the dislocations (in black) perpendicular to the plane can be partially modelled by 2D DD. The simulation plane bisects each respective structure.

5.15b. The loop consists of four segments. In the purely elastic regime, the only difference between a vacancy and interstitial loop is an equal and opposite Burgers vector. Because the character of the field solutions of general Volterra dislocation loops with respect to such a transformation of the Burgers vector is odd [275, 276], the components of the elastic fields generated by vacancy and interstitial loops are equal and opposite in magnitude. Let the loop habit plane initially lie on a 2^{nd} order prismatic plane, and let the loop have the capacity to tilt towards the 1^{st} order prismatic plane; ignore tilting towards the basal plane. Let this tilting process be purely conservative, i.e. let each segment be fixed to its glide plane. As the loop tilts, it will therefore become increasingly rectangular. Assume also that the loop maintains a planar shape regardless of its tilt. The tilt angle θ is defined as the angle between the Burger's vector and habit plane normal vector of the loop. In the corresponding edge dipole case, a similar description applies (see figure 5.15c).

Consider an infinitely long chain of prismatic loops, each containing a segment that overlaps with a segment of the next loop in the sequence, as shown in figure 5.3. Since the overlapping segments have the same Burgers vector but opposite line directions, their respective fields cancel out, leaving only the remaining segments

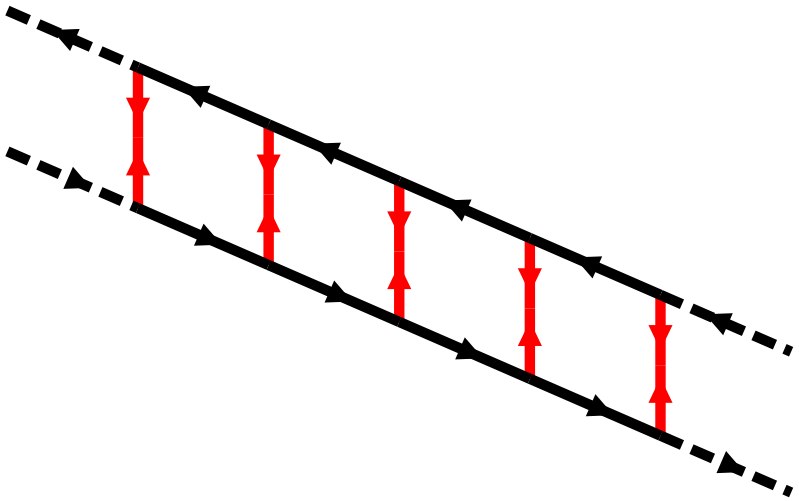


Figure 5.3: Schematic of part of an infinite chain of identical square prismatic loops. The separation distance d_s between the centroids of adjacent loops is equal to the side length L of each loop. The red segments annihilate each other and the remaining (net) black segments compose an infinitely deep prismatic loop (i.e. approximately an edge dipole).

which form an infinitely deep rectangular prismatic loop. Such a dislocation structure is nearly identical to an edge dipole except for the two segments which are infinitely far away from the simulation plane and thus have a negligible effect. Therefore, these two structures can be considered equivalent and will be referred to interchangeably as an edge dipole in this text. In the more general case, and as is more representative of real crystals, one may consider an array of prismatic loops such that the separation distance d_s between the centroids of adjacent loops is greater than the side length of each loop, as shown in figure 5.4. Therefore, in a 2.5D DD model, an edge dipole is in a sense equivalent to a limiting case of such array configurations.

One may conceive of a transition between two limiting cases of prismatic loop array configurations parametrised by the separation distance d_s between adjacent loops. One limiting case corresponds to the separation distance approaching the loop size L, which results in an edge dipole. The other limiting case corresponds to the separation distance approaching infinity, which results in a single prismatic loop. As the latter limiting case transitions to the former, the plane strain assumption becomes increasingly valid, reaching exactness in the edge dipole case. In what remains of this section, we shall compare the properties of single prismatic loops with edge dipoles to determine their similarities and differences.

The non-singular stress field components generated by a prismatic loop and an edge dipole with $L = 10\,\text{nm}$ and $\theta = 0°$ are respectively plotted in figures 5.5 and 5.6.

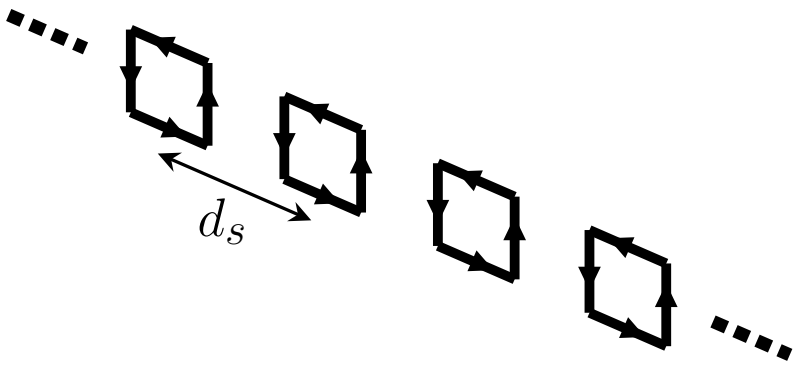


Figure 5.4: Schematic of part of an array of identical square prismatic loops extending infinitely in the direction of the dotted lines. The separation distance d_s between the centroids of adjacent loops is greater than the side length L of each loop.

Similarly, the stress field components for both structures with $\theta = 45°$ are plotted in figures 5.7 and 5.8. The stress fields for these plots were computed by using an isotropic Burgers vector spreading radius of $r_c = L/5$ to avoid excessively large stresses at the dislocation core region so that the colour resolution at other regions could be differentiated. Visual inspection of these field plots reveals that the stress fields have similar shapes. The stress field magnitudes are also similar, although both the lower and upper bounds of stress magnitudes are lower in the edge dipole for both tilt angle cases.

Another characteristic of interest is the capacity of a prismatic loop to resist the motion of incoming dislocations (see figure 5.9). A complete elastic model of this phenomenon must account for the curvature of the dislocation as it approaches the loop, which cannot be captured in conventional 2D DD. Nonetheless, when the dislocation is not too close to the loop ($d > L$), analytical studies on both prismatic loops [277, 278, 141] and edge dipoles [279, 280] which assume a curvature-free configuration have yielded useful insights. It is known that, at large distances r from the centroid of a prismatic loop, the stress decays as $1/r^3$ and the total force on the dislocation decays as $1/r^2$. In comparison, the long-ranged stress due to an edge dipole follows a $1/r^2$ decay, while that of a straight isolated dislocation follows a $1/r$ decay. However, when $d \lesssim L$, the interactions between dislocations and prismatic loops are more complicated and 3D simulation is often necessary to study the interaction processes, as is performed in section 5.2.

One difficulty in comparing the resistance to dislocation motion of edge dipoles and isolated prismatic loops is that the former is fully compatible with the plane strain assumption, whereas the latter is not. In particular, the forces exerted by an isolated prismatic loop on a dislocation are localised near the loop [278], which

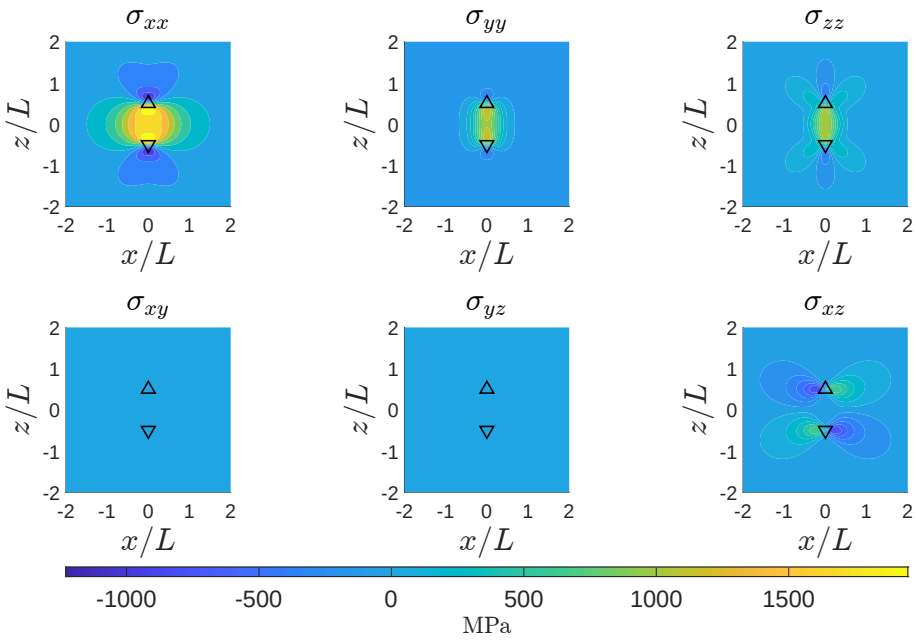


Figure 5.5: Stress field components of a prismatic vacancy loop with $L = 10\,\text{nm}$ and $\theta = 0°$ evaluated on the 2D DD simulation plane. The triangles on the top and bottom respectively represent the positive and negative edge dislocations which intersect the 2D DD simulation plane.

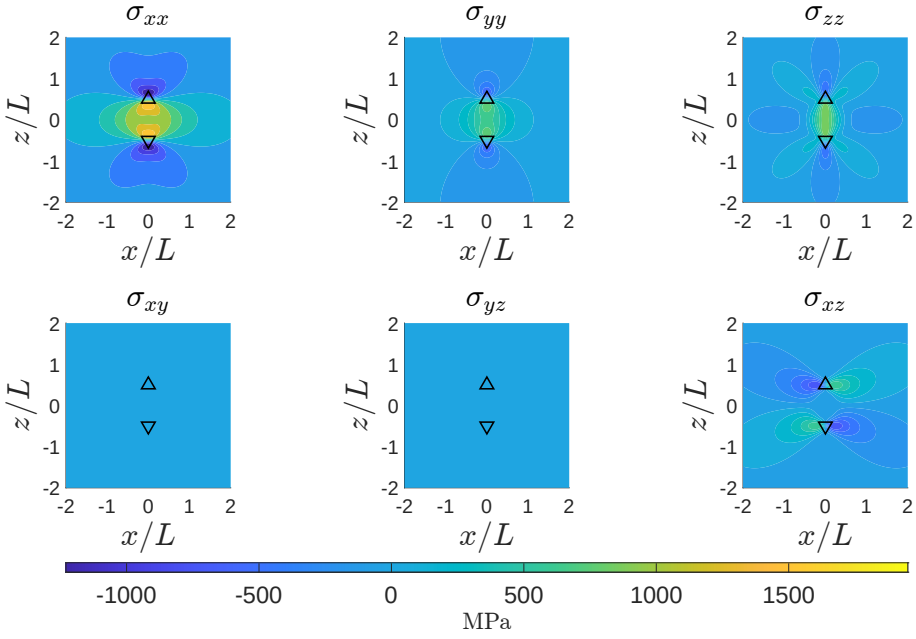


Figure 5.6: Stress field components of a vacancy edge dipole with $L = 10\,\text{nm}$ and $\theta = 0°$ evaluated on the 2D DD simulation plane. The triangles on the top and bottom respectively represent the positive and negative edge dislocations which intersect the 2D DD simulation plane.

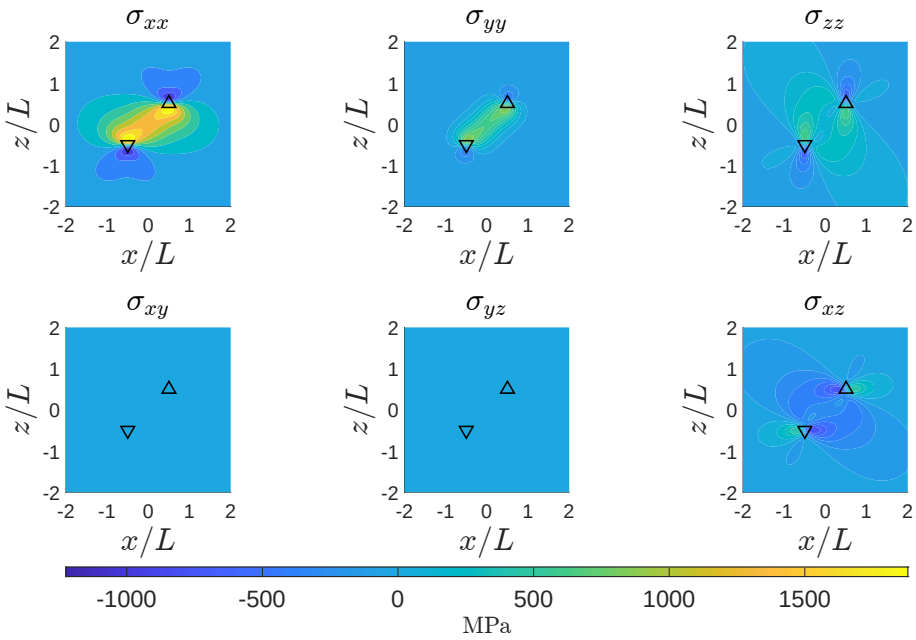


Figure 5.7: Stress field components of a prismatic vacancy loop with $L = 10\,\text{nm}$ and $\theta = 45°$ evaluated on the 2D DD simulation plane. The triangles on the top and bottom respectively represent the positive and negative edge dislocations which intersect the 2D DD simulation plane.

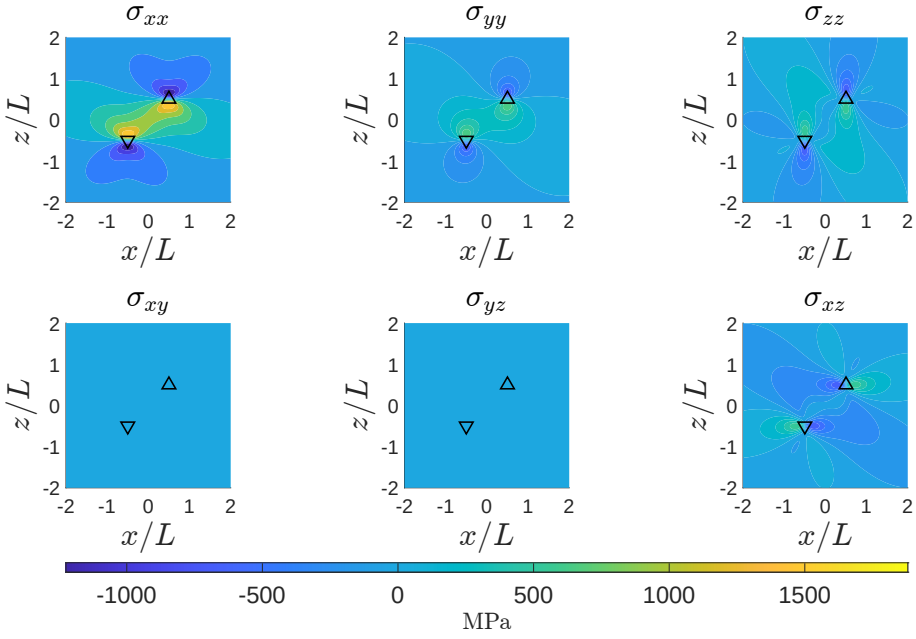


Figure 5.8: Stress field components of a vacancy edge dipole with $L = 10\,\text{nm}$ and $\theta = 45°$ evaluated on the 2D DD simulation plane. The triangles on the top and bottom respectively represent the positive and negative edge dislocations which intersect the 2D DD simulation plane.

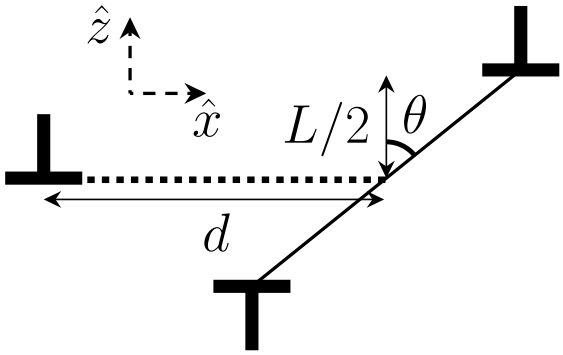


Figure 5.9: Schematic of the interaction between a positive dislocation (left) and a loop or edge dipole (right) resolved on the 2D DD simulation plane. The dotted line emanating from the dislocation represents the trace of the dislocation slip plane along which the position of the dislocation is varied for calculations, and which intersects the habit plane of the loop or edge dipole at its midpoint.

contrasts with the edge dipole case, where the plane strain assumption remains valid. With regards to dislocation resistance, a more adequate analog to an edge dipole would be that of a prismatic loop array as discussed previously. Some authors [281, 282, 283] have investigated the impact that prismatic loop arrays have on dislocation resistance as a function of a variety of relevant geometric parameters, such as the loop size, adjacent loop separation distance, and distance of the array to the dislocation glide plane. Note that these studies ignored collision reactions. In summary, prismatic loop arrays are approximated with increasing accuracy by edge dipoles as (1) their distance from the glide plane increases compared to the loop size and (2) the spacing of adjacent prismatic loops approaches the loop size. In addition, prismatic loop arrays generally act as weaker obstacles than edge dipoles when their distance from the glide plane is large compared to their size. Note that situation (1) is likely to be the most common in practice. At the time of writing, no studies exist which systematically study the critical stress as a function of loop size and inter-loop spacing for the case of dislocation-loop collision reactions.

Taking the aforementioned caveats into account, numerical calculations are performed in the following to compare some simple properties pertaining to dislocation resistance of both a single isolated prismatic loop and an edge dipole by measuring the stress—and thus the PK force—generated by the loop (and the dipole) at the intersection point between a given dislocation and the 2D simulation plane. Consider a system as shown in figure 5.9 such that the dislocation slip plane bisects the habit plane of the respective structure (i.e. a prismatic loop or an edge dipole). The line of measurement is the line of intersection between the dislocation slip plane

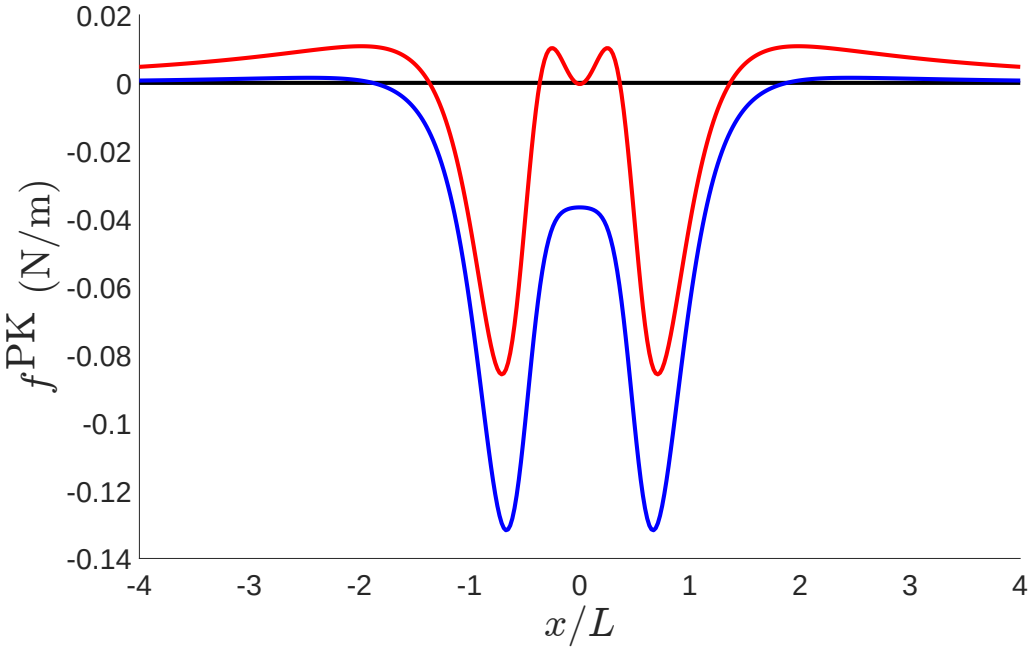


Figure 5.10: Plot of the Peach-Koehler force acting on an incoming dislocation due to a prismatic loop (blue solid line) and an edge dipole (red solid line) with $L = 10\,\mathrm{nm}$ and $\theta = 45°$. The $\theta = 0°$ case (black solid line lying on the x-axis) is plotted; it is equivalent for both structures.

and the 2D simulation plane. Note that in this configuration, only the σ_{xz} stress component contributes to the PK force computation, resulting in a PK force that mirrors the shape of this stress component. The PK force acting on an incoming dislocation as a function of its distance from the centroid of both a prismatic loop and an edge dipole with $L = 10\,\mathrm{nm}$ and $\theta = 45°$ is plotted in figure 5.10. This plot was produced by constructing the corresponding piecewise dislocation structure and evaluating the resulting non-singular stress field along the line of measurement. The PK force $\boldsymbol{f}^{\mathrm{PK}}$ acting on the dislocation was then obtained using equation (3.15). In this configuration, a positive PK force $f^{\mathrm{PK}} = \boldsymbol{f}^{\mathrm{PK}} \cdot \hat{\boldsymbol{x}}$ corresponds to one that is codirectional to the x-axis as shown in figure 5.9. Both force curves have similar shapes. In particular, both cases share the characteristic that they are slightly attractive at large distances and significantly repulsive at short distances. However, the prismatic loop provides a greater repulsive force than the edge dipole. Note that if one changes the relative sign of the two structures (thus changing the system to, for instance, a negative incoming dislocation paired with a vacancy loop or a positive incoming dislocation paired with an interstitial loop), the sign of the resulting PK force is reversed.

Figure 5.11 displays a contour plot of the PK force for a range of tilt angles and

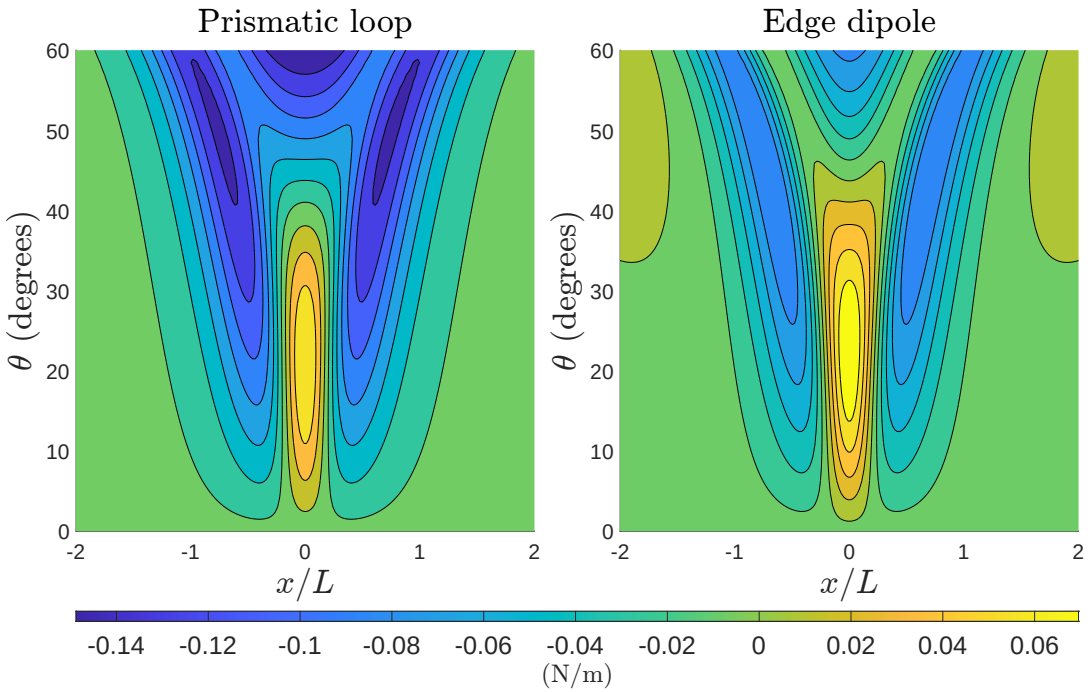


Figure 5.11: Contour plot of the Peach-Koehler force acting on an incoming dislocation due to a prismatic loop (left) and an edge dipole (right) for a range of tilt angles θ with $L = 10\,\text{nm}$.

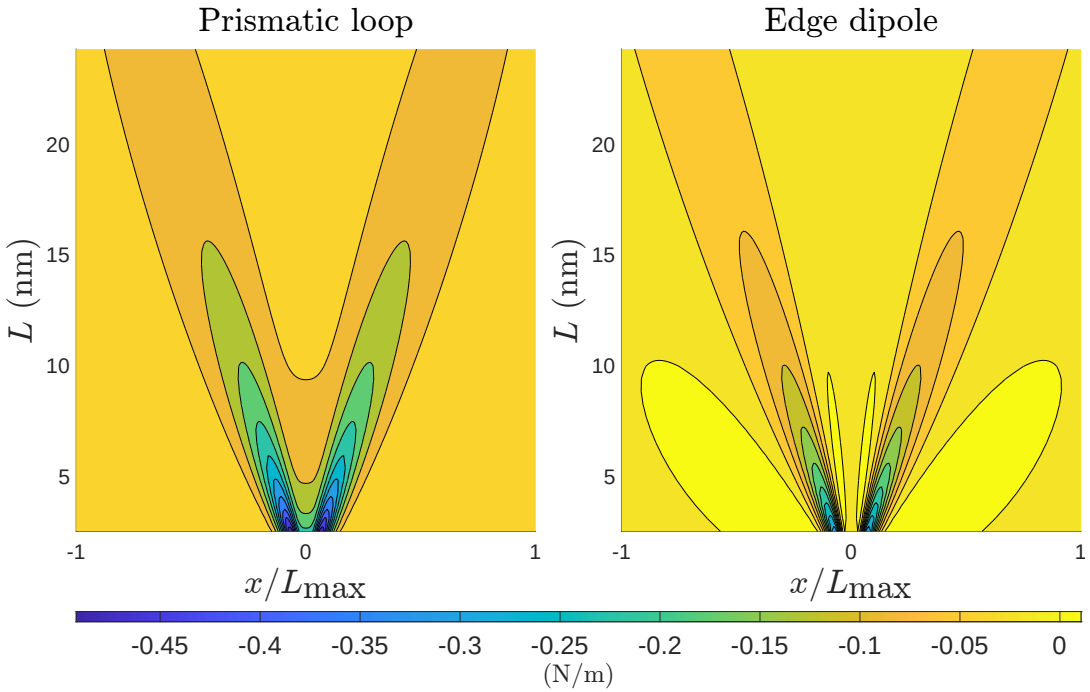


Figure 5.12: Contour plot of the Peach-Koehler force acting on an incoming dislocation due to a prismatic loop (left) and an edge dipole (right) for a range of loop sizes (from $L = 2.5\,\text{nm}$ to $L = L_{\text{max}} = 24.25\,\text{nm}$) with $\theta = 45°$.

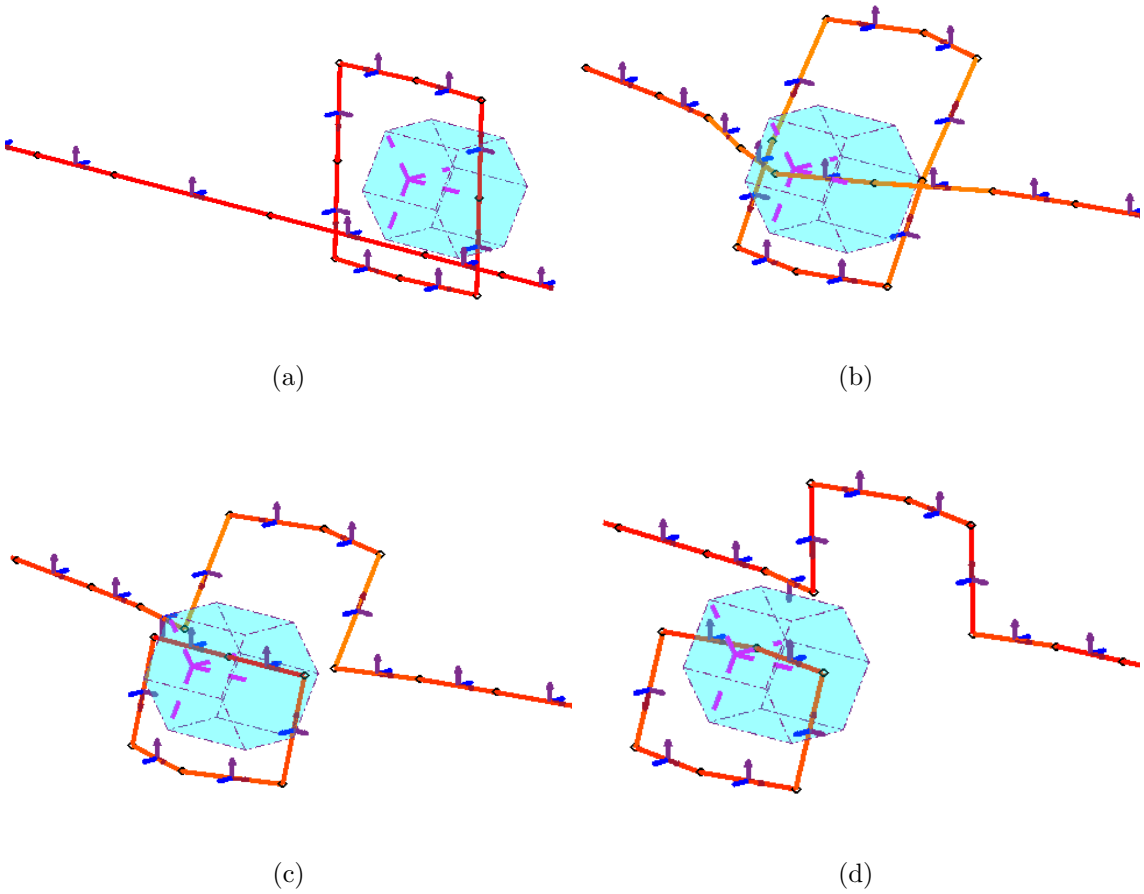
positions along the line of measurement with $L = 10\,\text{nm}$. The shapes of the contours are similar in both cases. However, the prismatic loop evidently exhibits greater repulsive PK forces at most tilt angles θ compared to the edge dipole. In addition, at low tilt angles both structures exhibit similar PK force curves. Note that at $\theta = 0$ both structures exhibit zero PK force.

Figure 5.12 displays a contour plot of the PK force for a range of sizes and positions along the line of measurement with $\theta = 45°$. As before, the shapes of the contours are similar in both cases, and the prismatic loop appears to exhibit greater repulsive PK forces at most loop sizes L compared to the edge dipole. In both cases, the magnitude of the repulsive PK force decreases as the loop size increases. Because of the valid plane strain assumption, it follows that edge dipoles of greater size indeed offer less resistance to dislocation motion[1]. However, note that this does not necessarily indicate that prismatic loops of greater size provide less resistance to dislocation motion. The reason for this difference is that single isolated prismatic loops violate the plane strain assumption, resulting in an incomplete depiction of the full interaction picture. This form of measurement does not properly capture the stress generated by the segments of the prismatic loop segments parallel to the simulation plane. As the loop size increases and all segments move farther away from the line of measurement, their contributions to the measured stress become increasingly diminished. Conventional 2D DD models cannot capture the non-planar stress distribution of single loops, and this phenomenon also falls beyond the scope of the current 2.5D DD model.

5.2 The dislocation-loop interaction

Idealised numerical and analytical studies of rigid dislocation-loop interactions are useful in understanding them, but 3D simulation is essential for capturing their full complexity. During a dislocation-loop interaction, the dislocation will often twist and bend to minimise the interaction energy, which will significantly impact the resulting dislocation reactions. In addition, the angle of the loop will also change dynamically as the dislocation passes through. Modelling dislocation curvature is outside of the scope of the currently considered 2.5D DD model. However, these microscopic dislocation reactions can be coarse-grained by determining a dislocation-loop interaction rule informed by a more thorough 3D analysis. In this section, 3D

[1]This is quite intuitive without any explicit calculation—consider that, as an edge dipole increases in size, every element of the dislocation moves away from every element of the sources of stress.



(a) (b)

(c) (d)

Figure 5.13: Formation of a double super-jog as a result of the collision between an edge dislocation and a vacancy prismatic loop. (a) An edge dislocation glides towards a vacancy prismatic loop. (b) The dislocation structures bend and rotate as they interact. (c) The edge dislocation collides with the loop, resulting in the formation of a double super-jog attached to the edge dislocation and a reduced vacancy prismatic loop. (d) The edge dislocation, now carrying a double super-jog, glides away from the loop. The hexagonal prism represents the orientation of the HCP crystal axes. At the centre of each segment is a blue, magenta, and black arrow which respectively represent the segment Burgers, normal, and line vectors. The colour of segments range between red, indicating pure edge, and yellow, indicating pure screw.

simulations are conducted to study the dislocation-loop interaction with the aim of producing such a rule.

All 3D DD simulations were performed assuming linear isotropic elasticity and used a shear modulus of $\mu = 37.1\,\text{GPa}$, Poisson's ratio of $\nu = 0.32$ [65], core energy density for a screw dislocation of $E_s^c = 0.125\,\text{eV}\,\text{Å}^{-1} \approx 0.05\mu b^2$ [122], HCP lattice parameters of $a = 3.233\,\text{Å}$ and $c = 1.593a$ [85], and isotropic Burgers vector spreading radius of $r_c = a$. The glissile glide drag coefficients were set to $B^{\text{glide}}_{\text{screw}}(2\text{Ba}) = 180 \times 10^{-6}\,\text{Pa}\,\text{s}$, $B^{\text{glide}}_{\text{screw}}(2\text{Pr}) = 85 \times 10^{-6}\,\text{Pa}\,\text{s}$, $B^{\text{glide}}_{\text{edge}}(2\text{Ba}) = 90 \times 10^{-6}\,\text{Pa}\,\text{s}$, and $B^{\text{glide}}_{\text{edge}}(2\text{Pr}) = 39 \times 10^{-6}\,\text{Pa}\,\text{s}$ [120], while the remaining drag coefficients were set to $B^{\text{line}} = 3.9 \times 10^{-6}\,\text{Pa}\,\text{s}$ and $B^{\text{climb}} = B^{\text{glide}}_{\text{sess}} = 10\,\text{Pa}\,\text{s}$. The line drag coefficient was selected such that its ratio relative to the glide drag coefficients was similar to that chosen by [84] Similarly, the climb drag coefficient was selected such that it had a similar order of magnitude to that chosen by [84].

In the 3D DD simulation an infinite domain was used. An $\langle a \rangle$-type Frank-Read source was introduced with length $L_G = 350\,\text{nm}$ of pure edge character with Burger's vector $\boldsymbol{b}_G = \frac{a}{3}[\bar{1}\bar{1}20]$ and which glides on the $(1\bar{1}00)$ prismatic plane. A square prismatic loop with Burger's vector $\boldsymbol{b}_L = -\boldsymbol{b}_G$ and side length (also referred to as a diameter) $L = 10\,\text{nm}$ is introduced $10\,\text{nm}$ ahead of the source such that its habit plane is perpendicular to the glide plane of the Frank-Read source (see figure 5.13a). The loop consists of four connected segments; two segments glide on the $(1\bar{1}00)$ prismatic plane while the other two segments glide on the (0001) basal plane. The line direction of a vacancy loop will correspond to the right-hand rule with respect to the Burger's vector $\boldsymbol{b}_L$; interstitial loops have an opposite line direction. Under an applied resolved shear stress τ, the edge dislocation will move towards the loop and interact with it.

Let us consider an applied resolved shear stress of $\tau = 100$ MPa in the $(1\bar{1}00)$ plane along the $\boldsymbol{b}_G$ direction. Let the glide plane of the edge dislocation cross the centre of the loop. The two segments of the prismatic loop gliding on the $(1\bar{1}00)$ prismatic plane will experience an induced Peach-Koehler force due to the external applied stress. Because these segments have the same Burger's vector but opposite line directions, these Peach-Koehler forces act in opposite directions, which induce a tilt in the glide cylinder of the loop. In isolation from other dislocation structures, the loop will continue tilting until it reaches an equilibrium angle due to a combination of multiple dynamic forces acting on its segments: the longitudinal and torsional core forces, the elastic self-forces, and the long-ranged elastic forces generated by each segment.

As the edge dislocation approaches the vacancy loop, the long-ranged elastic interaction of the edge dislocation will begin to take effect. The segment of the prismatic loop which has the same Burger's vector and line direction as the edge dislocation will experience an elastic repulsive force which will also contribute to the tilting of the loop (see figure 5.13b). Depending on the applied resolved shear stress and the tilt of the loop, the edge dislocation will either not react with the loop due to repulsive forces, react to form a single dislocation network consisting of a junction or crossed state [284], or react to form two distinct sets of dislocation structures (see figure 5.13c). If the applied resolved shear stress is insufficient, the loop will be pushed along its glide cylinder by the edge dislocation and they will not collide. Under a sufficiently great applied resolved shear stress, as is the case with $\tau = 100\,\text{MPa}$, the edge dislocation will react to form the last scenario: the outgoing structure consists of an edge dislocation with an attached double super-jog. This has been referred to as an R3 reaction by [149]. What remains consists of a rectangular prismatic loop which has half of the width of the square prismatic loop (see figure 5.13d). As the outgoing edge dislocation continues to travel due to the applied stress, it will experience elastic and core forces due to its attached double super-jog which will result in a dragging effect, effectively reducing its mobility (see section 5.3.3 for a discussion of this effect). Meanwhile, the remaining rectangular prismatic loop will reach a relaxation tilt angle which is dependent on the applied stress.

If an identical simulation is repeated except with an interstitial loop replacing the vacancy loop, a similar process will occur. The notable difference is that, as a result of the collision reaction, the outgoing edge dislocation will obtain an attached double-super jog which is removed from the half of the prismatic loop that is below the glide plane of the initial edge dislocation shown in figure 5.13a (instead of from the half of the prismatic loop above said glide plane, as is the process depicted in figure 5.13). This type of reaction will also occur if the same simulation is performed with a vacancy loop, but the edge dislocation is of opposite sign. Therefore, the position of the attached double super-jog on the outgoing edge dislocation is dependent on the relative sign of the two initial dislocation structures.

In general, if the glide plane of the edge dislocation crosses the vacancy loop and the two dislocation structures react, the part of the loop above (or, for an interstitial loop, below) said glide plane will be absorbed on the edge dislocation as a double super-jog. In addition, if the loop has some lateral tilt towards the basal plane, the edge dislocation will consecutively interact with each side of the loop one after

another, resulting in a temporary single intermediary dislocation structure consisting of a helical turn along an edge dislocation.

In MD simulations of an edge dislocation interacting with an $\langle a \rangle$-type prismatic loop performed by [157], results which match our DD simulations were reported. Of particular note, they observed the cutting and absorption of the loop by the edge dislocation via the same mechanisms as those observed in our DD simulation. They also observed the temporary single intermediary helical structure in the dislocation-loop interaction. In the case that the glide plane of the edge dislocation intersects the centre of the loop, they observed that the loop was pushed along its glide cylinder without colliding. In general, the critical stress required for edge dislocations to penetrate the loops was lower than in our DD simulations. However, it should be noted that the loops they investigated had a significantly smaller size ($L \approx 3\,\mathrm{nm}$) than the ones investigated in our study. Regardless, the similarities found in both studies employing different length scales is a testament to the effectiveness of DD in representing small-scale interactions which are significantly impacted by inelastic effects.

In addition, [85] performed a similar DD simulation of an edge dislocation interacting with a vacancy prismatic loop with identical relevant initial conditions. The key features of their simulation results which match ours are as follows. In their simulation, the prismatic loop, initially negligibly affected by the distant edge dislocation, first rotates in its glide cylinder due to the external applied stress, eventually reaching an equilibrium tilt angle. As the edge dislocation approaches the prismatic loop due to the external applied stress, both dislocations experience a mutual repulsion. For a high enough external applied stress (in this case, it is sufficient to give a resolved shear stress of $\tau = 100\,\mathrm{MPa}$), the dislocation collides with the loop, a double super-jog is formed on the outgoing edge dislocation in the same orientation as the one depicted in figure 5.13c, and a prismatic loop with half of the original width is left behind. Finally, if the simulation is repeated with the loop being of interstitial type instead of vacancy type, the outgoing dislocation obtains a double super-jog on the opposite side of its glide plane relative to the one depicted in figure 5.13c. Therefore, our simulation matches the simulation results obtained by [85], providing an independent validation of the HCP mobility law used in this text.

From this simulation the pertinent features of the microscopic dislocation-loop interaction mechanism can be identified so that they can be implemented in a 2.5D DD model to represent coarse-grained dislocation-loop collisions. This process is depicted schematically in figure 5.14. Most importantly, edge dislocations reduce the

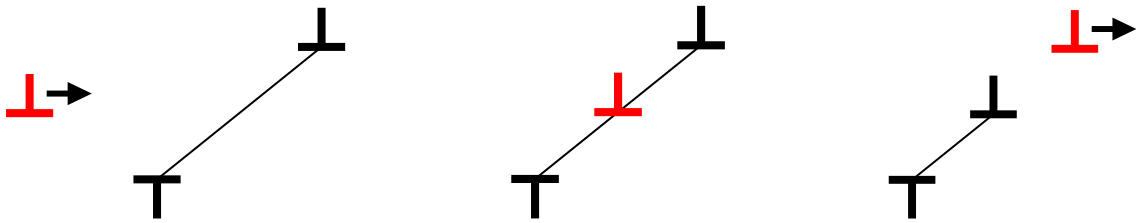


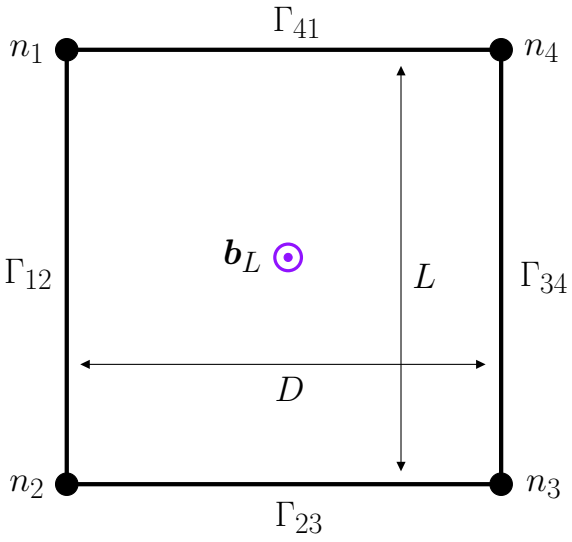
Figure 5.14: Schematic of a 2D dislocation-loop interaction rule. (a) The free incoming dislocation approaches the loop. (b) The free dislocation collides with the habit plane of the loop. (c) A dislocation which was once a constrained component of the loop becomes a free outgoing dislocation, and the once free incoming dislocation becomes a constrained component of the loop.

size of prismatic loops by an amount depending on the height at which they hit the loop and on the relative sign between both structures.

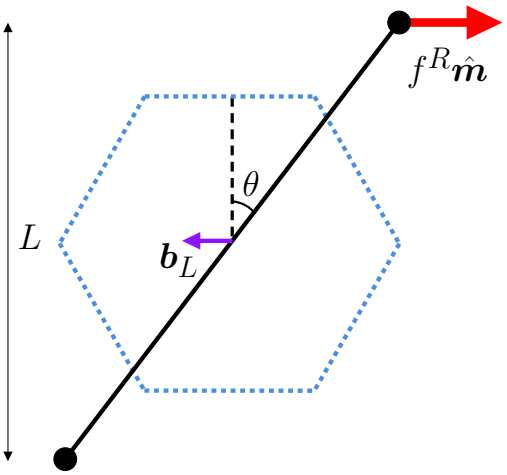
5.3 Prismatic loop dynamics and stability analysis

An important characteristic of prismatic loops that may influence irradiation hardening is their rotational dynamics. In this section, the angular stability of prismatic loops is investigated with the goal of obtaining expressions for their restoring force. These expressions are intended to inform the 2.5D DD model, enabling more realistic prismatic loop behaviour and enhancing irradiation hardening simulations. Let us once again consider the isolated square prismatic loop from section 5.1, and as in figures 5.15a and 5.15b. The loop consists of four segments: Γ_{41}, Γ_{12}, Γ_{23}, and Γ_{34}. The elastic and core forces on each node can be calculated via equations (3.13) and (3.7), respectively.

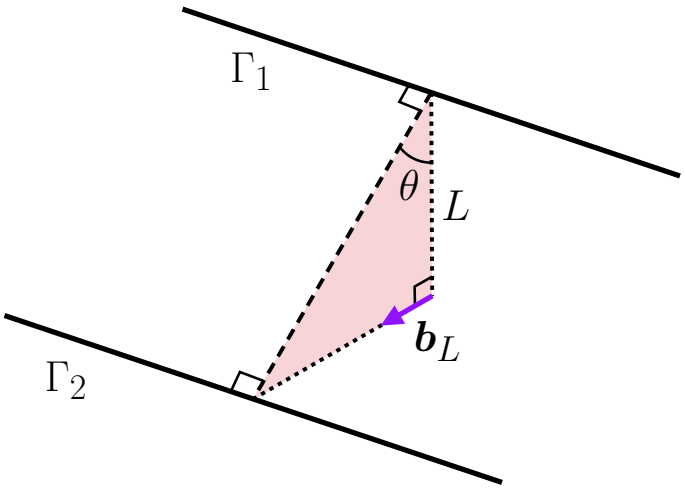
The aim is to derive an expression for the force responsible for the rotation of the loop and connect this to the 2D DD model. In 2D DD, the total forces on dislocations are infinite due to their infinite length, making them irrelevant. Instead, dislocation kinematics are determined by the PK force, defined as the product of the resolved shear stress and the Burgers vector, representing a force per unit length. Let us consider how one might calculate the relevant quantity for our application. Note that in our planar model, only the Γ_{41} and Γ_{23} segments (see figure 5.15) penetrate the 2D simulation plane, each at their midpoints. Therefore, our aim is to compute some quantity at some position associated with these two segments. By conservation of momentum during rotation, the forces acting on segment Γ_{41} must be equal and



(a) Prismatic loop in a $\theta = 0$ configuration. An initially square prismatic loop is always assumed in this text, i.e. $D = L$.



(b) Prismatic loop in a tilted configuration. The hexagonal prism represents the crystal axes, and represents a subset of the plane which would correspond to that of a 2D DD simulation. The red arrow represents the restoring force $f^{\mathrm{R}}\hat{\boldsymbol{m}} = \left(\tilde{\boldsymbol{F}} \cdot \hat{\boldsymbol{m}}\right)\hat{\boldsymbol{m}}$.



(c) Edge dipole in a tilted configuration. Segments Γ_1 and Γ_2 extend off to infinity. The red triangle represents a subset of the plane which would correspond to that of a 2D DD simulation. This dislocation structure can be understood to be the 2D approximation to the 3D prismatic loop case.

Figure 5.15: Diagrams of a prismatic loop and an edge dipole.

opposite to those acting on segment Γ_{23}. Therefore, symmetry dictates that analysing the dynamics of segment Γ_{41} alone is sufficient to fully characterise the rotational behavior.

One option is to determine the elastic stress field generated by the entire loop, evaluate it at the midpoint of segment Γ_{41}, and directly use this quantity as representative of the effective PK force for the 2D DD model. This method does not capture the non-uniform distribution of the stress along segment Γ_{41}, and is thus not suitable. Instead, we may find the average force per unit length $\tilde{\boldsymbol{F}}^{\mathrm{PK}}$ along segment Γ_{41} via

$$\tilde{\boldsymbol{F}}^{\mathrm{PK}} = \frac{1}{L} \int_{\Gamma_{41}} \boldsymbol{f}^{\mathrm{PK}}(\boldsymbol{x}) \ \mathrm{d}L(\boldsymbol{x}) \tag{5.1}$$

However, this calculation neglects contributions from core interactions. To include these, let us consider the total nodal forces, which incorporate both core and elastic effects, and express them in terms of some $\tilde{\boldsymbol{F}}$ which is yet to be determined and/or interpreted. Suppose that the total forces at nodes n_1 and n_4, respectively denoted by $\boldsymbol{f}_1$ and $\boldsymbol{f}_4$, are known. These forces arise from the combined elastic and core contributions of the entire loop. Suppose there exists a fictional force per unit length $\boldsymbol{F}(\boldsymbol{x})$ which is distributed solely along the segment Γ_{41}, and which itself alone exactly generates $\boldsymbol{f}_1$ and $\boldsymbol{f}_4$.

The forces can then be expressed as

$$\boldsymbol{f}_1 = \int_{\Gamma_{41}} N_1(\boldsymbol{x}) \boldsymbol{F}(\boldsymbol{x}) \ \mathrm{d}L(\boldsymbol{x}) \qquad \text{and} \qquad \boldsymbol{f}_4 = \int_{\Gamma_{41}} N_4(\boldsymbol{x}) \boldsymbol{F}(\boldsymbol{x}) \ \mathrm{d}L(\boldsymbol{x}) \tag{5.2}$$

It follows that

$$\frac{\boldsymbol{f}_1 + \boldsymbol{f}_4}{L} = \frac{1}{L} \int_{\Gamma_{41}} \boldsymbol{F}(\boldsymbol{x}) \ \mathrm{d}L(\boldsymbol{x}) \equiv \tilde{\boldsymbol{F}} \tag{5.3}$$

The desired restoring force is therefore the average force per unit length $\tilde{\boldsymbol{F}}$. The restoring force is then introduced as an additional force acting on the dipole of edge dislocations that represent the prismatic loop in the simulation plane. This modification effectively imparts a 2.5D character to the otherwise planar DDP model. The resulting structure can be interpreted as an edge dipole exhibiting the rotational dynamics characteristic of a single isolated prismatic loop.

Recall that in section 5.1 we established the conceptual connection between edge dipoles and arrays of prismatic loops. It is important to note that the rotational dynamics of prismatic loop arrays differs from those of isolated loops due to elastic interactions between adjacent loops. To be able to apply all of the approximations used in this chapter when considering prismatic loop arrays, one must assume that

the separation distance between adjacent loops is sufficiently large to render their mutual interactions negligible in terms of rotational dynamics, yet small enough for the edge dipole approximation to remain valid.

In order to investigate the angular stability of the loop, we shall analyse the total nodal forces $\boldsymbol{f}_1$ and $\boldsymbol{f}_4$ acting on nodes n_1 and n_4 as a function of the loop tilt angle θ. The average restoring force per unit length can then be calculated via $(\boldsymbol{f}_1(\theta) + \boldsymbol{f}_4(\theta))/L$. From the symmetry of the prismatic loop we have the relation $\boldsymbol{f}_1 \cdot \boldsymbol{b} = \boldsymbol{f}_4 \cdot \boldsymbol{b} = -\boldsymbol{f}_2 \cdot \boldsymbol{b} = -\boldsymbol{f}_3 \cdot \boldsymbol{b}$. Therefore, when projected into the glide plane $\hat{\boldsymbol{m}} = -\hat{\boldsymbol{b}}$ of segment Γ_{41} (see figure 5.15b), the restoring force expression becomes

$$f^{\mathrm{R}}(\theta) = -\frac{2\boldsymbol{f}_1(\theta) \cdot \hat{\boldsymbol{b}}}{L} \tag{5.4}$$

It is this expression that can be used by 2D DD codes to represent the corrective restoring forces acting on prismatic loops. The restoring force arising due to elastic and core contributions will be respectively denoted as $f^{\mathrm{R,e}}$ and $f^{\mathrm{R,c}}$. For reference, the restoring force acting on an edge dipole (as in figure 5.15c) is given by

$$f^{\mathrm{R}}_{\mathrm{ed}}(\theta) = \frac{\mu}{2\pi(1-\nu)L} \frac{\tan\theta\ (\tan^2\theta - 1)}{(\tan^2\theta + 1)^2} \tag{5.5}$$

and arises only due to elastic interactions. The stable equilibrium tilt angle of an edge dipole will always be $\theta_{eq} = \pi/4$, independent of the separation distance L.

Note that for this section we define three types of equilibrium tilt angles which apply only to isolated dislocation structures without the influence of external stress: θ^e_{eq}, θ^c_{eq}, and θ_{eq}. They are respectively the equilibrium tilt angles which would be induced by the isolated elastic forces of the structure, the isolated core forces, and the combined elastic and core forces.

5.3.1 Segment-segment interactions

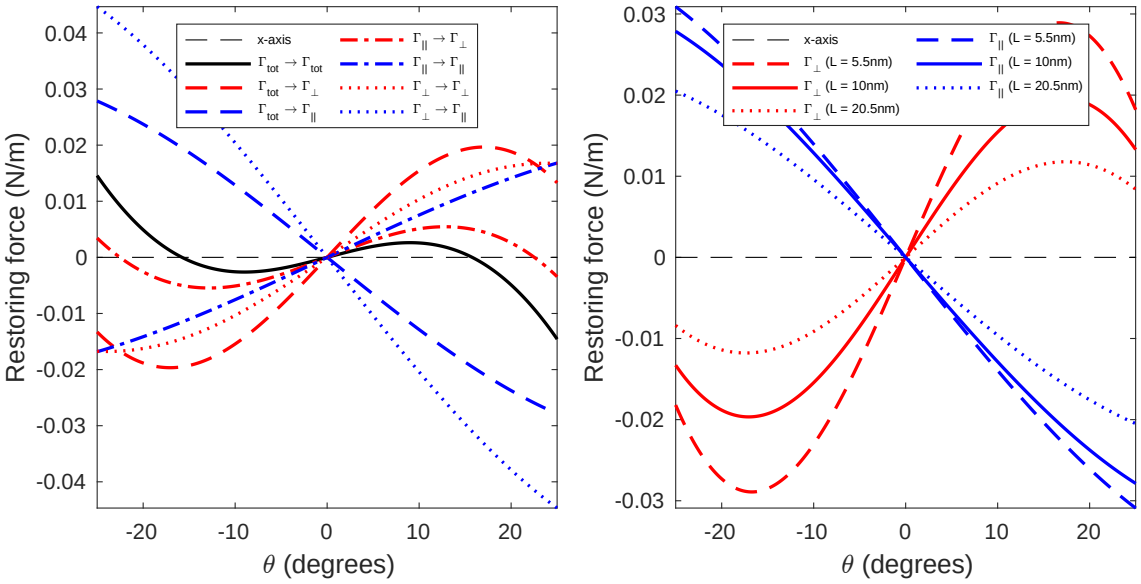
Let us now analyse the effect of each of the segments of the square prismatic loop on its stability. Motivated by the comparison to the 2D model, the four segments may be aggregated into two sets: the segments $\Gamma_\perp = \{\Gamma_{41}, \Gamma_{23}\}$ and the segments $\Gamma_\parallel = \{\Gamma_{12}, \Gamma_{34}\}$ which respectively represent the dislocations perpendicular and parallel to the plane of the 2D model. Let $\Gamma_{\mathrm{tot}} = \Gamma_\perp \cup \Gamma_\parallel$ denote the set of all the segments. Segments $\Gamma_\perp$ can be partially modelled by 2D DD models, while segments $\Gamma_\parallel$ cannot. We may investigate the individual effects of $\Gamma_\perp$ and $\Gamma_\parallel$ by calculating $f^R(\theta)$ for each isolated set. The elastic nodal force on node n_1 is given by

$$\boldsymbol{f}^{\mathrm{e}}_1 = \int_{\Gamma_{41}} N_1(\boldsymbol{x})\ \boldsymbol{f}^{\mathrm{PK}}(\boldsymbol{x})\ \mathrm{d}L(\boldsymbol{x}) + \int_{\Gamma_{12}} N_1(\boldsymbol{x})\ \boldsymbol{f}^{\mathrm{PK}}(\boldsymbol{x})\ \mathrm{d}L(\boldsymbol{x}) \tag{5.6}$$

Note that the Peach-Koehler force field $\boldsymbol{f}^{\mathrm{PK}}$ is generated by the precise structure of the entire loop. The first and second terms represent the contribution to the nodal force due to the action of the internal elastic stresses acting on the segments Γ_{41} and Γ_{12}, respectively. Due to the loop symmetry, this can be thought of as the action of the elastic restoring force on the segments $\Gamma_{\perp}$ and $\Gamma_{\parallel}$, respectively, up to a simple linear transformation given by equation (5.4). Let us denote these terms as $\boldsymbol{f}^{\mathrm{e}}_{\mathrm{tot}\to\perp}$ and $\boldsymbol{f}^{\mathrm{e}}_{\mathrm{tot}\to\parallel}$, respectively. The notation $G_{A\to B}$ can be understood as denoting the action on the set Γ_B due to the fields G arising from the set Γ_A. The elastic nodal force due to the total loop Γ_{tot} is given by $\boldsymbol{f}^{\mathrm{e}}_{\mathrm{tot}\to\perp} + \boldsymbol{f}^{\mathrm{e}}_{\mathrm{tot}\to\parallel}$.

The elastic stress fields arising from the dislocation structures considered in this section must be evaluated at points along the structures themselves. Classical expressions [193] yield singularities at these points, necessitating the use of non-singular expressions. Non-singular stress fields were obtained for finite length segments using the analytical expressions provided in Appendix B1, form 3, of Cai *et al.* [194]. These expressions were implemented analytically in MATLAB using the Symbolic Math Toolbox [285]. Next, the coordinate systems for the stress field expressions were translated and rotated into the appropriate orientation depending on the dislocation structure under consideration. This transformation process was applied to each segment comprising the dislocation structure. Once the analytical stress field σ was calculated, the PK force was calculated via $\boldsymbol{f}^{\mathrm{PK}}(\boldsymbol{x}) = (\sigma(\boldsymbol{x}) \cdot \boldsymbol{b}) \times \boldsymbol{l}$, where $\boldsymbol{b}$ and $\boldsymbol{l}$ respectively represent the Burgers and line vectors of the dislocation segment where the field is evaluated, and $\boldsymbol{x}$ is the field evaluation point. Finally, appropriately parametrised line integrals of the type shown in equation (5.6) were calculated numerically using the `vpaintegral` function in MATLAB [285].

Consider first the dynamics caused by the elastic interactions. Figure 5.16a displays plots of the elastic restoring forces arising from and acting on the different segments of a loop of side length $L = 10\,\mathrm{nm}$. Figure 5.16b displays plots of the elastic restoring forces arising from full loops of varying side lengths acting on $\Gamma_{\perp}$ and $\Gamma_{\parallel}$. Let us consider the elastic fields arising due to the full loop Γ_{tot}. In this case, the fields $\boldsymbol{f}^{\mathrm{R,e}}_{\mathrm{tot}\to\parallel}$ that act upon $\Gamma_{\parallel}$ induce loop stability, while the fields $\boldsymbol{f}^{\mathrm{R,e}}_{\mathrm{tot}\to\perp}$ that act upon $\Gamma_{\perp}$ induce loop instability. Next, consider the elastic fields arising due to segments $\Gamma_{\perp}$: the fields $\boldsymbol{f}^{\mathrm{R,e}}_{\perp\to\parallel}$ will induce loop stability in the $\Gamma_{\parallel}$ segments and the fields $\boldsymbol{f}^{\mathrm{R,e}}_{\perp\to\perp}$ will induce loop instability in the $\Gamma_{\perp}$ segments (i.e. in themselves). Finally, consider the elastic fields arising due to segments $\Gamma_{\parallel}$: both the fields $\boldsymbol{f}^{\mathrm{R,e}}_{\parallel\to\parallel}$ and $\boldsymbol{f}^{\mathrm{R,e}}_{\parallel\to\perp}$ will induce loop instability in the $\Gamma_{\parallel}$ and $\Gamma_{\perp}$ segments, respectively. This information is summarised in Table 5.1. In general, when only considering elastic



(a) (b)

Figure 5.16: Plots of elastic restoring forces acting on a square prismatic vacancy loop. (a) Elastic restoring forces arising from and acting on the different segments of a loop of side length $L = 10\,\text{nm}$. (b) Elastic restoring forces arising from loops of varying side lengths L, acting on the segments $\Gamma_{\perp}$ and $\Gamma_{\parallel}$.

effects, the loop stability is a consequence of a competing effect between segments $\Gamma_{\perp}$ and $\Gamma_{\parallel}$. The stabilising effect and reduction of the elastic stable equilibrium angle θ^{e}_{eq} arises mostly due to the stress fields which act upon segments $\Gamma_{\parallel}$. Therefore, the source of the stabilising effect cannot be properly captured by the 2D DD framework; an extension provided by a 3D theory of elasticity is required.

A stability analysis can also be applied to a double super-jog which is acquired by the edge dislocation. Figure 5.17 shows the elastic restoring force acting on segment Γ_{41} of the double super-jog (see figure 5.21b) which is created after a dislocation-loop interaction for different loop sizes. It can be shown (see section 5.3.3) that the structure will tend towards a stable equilibrium angle of $\theta_{eq} = 0$ in the absence of external forces. This contributes to the observed dragging effect which double super-jogs impart upon edge dislocations that they are attached to, which has been reported in the literature [85].

5.3.2 Core restoring force

Let us now analyse the contribution of the core restoring force to the stability of a prismatic loop and double super-jog. Consider the core force acting on node n_1

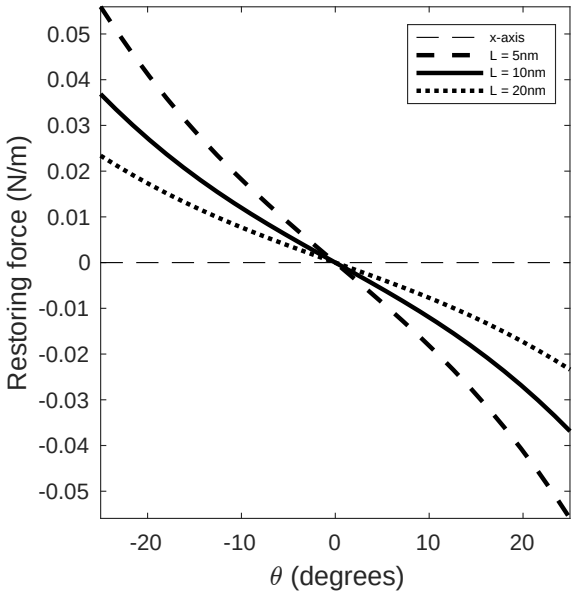


Figure 5.17: Elastic restoring force on double super-jogs of varying sizes.

Elastic segment interaction	Reaction outcome
$\Gamma_{\text{tot}} \rightarrow \Gamma_{\parallel}$	Stability
$\Gamma_{\text{tot}} \rightarrow \Gamma_{\perp}$	Instability
$\Gamma_{\perp} \rightarrow \Gamma_{\parallel}$	Stability
$\Gamma_{\perp} \rightarrow \Gamma_{\perp}$	Instability
$\Gamma_{\parallel} \rightarrow \Gamma_{\parallel}$	Instability
$\Gamma_{\parallel} \rightarrow \Gamma_{\perp}$	Instability

Table 5.1: Stability of the elastic interaction of different sets of segments with each other in a square prismatic loop.

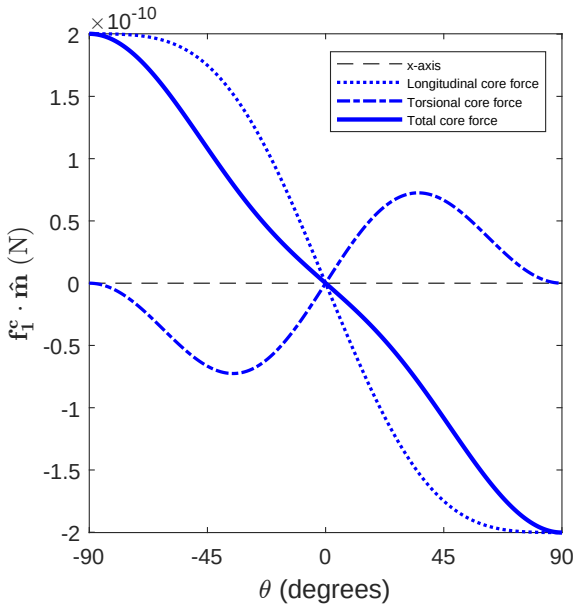


Figure 5.18: Core force acting on node n_1 of the prismatic loop from figure 5.15a, projected into its glide cylinder $\hat{\boldsymbol{m}} = -\boldsymbol{b}_L$, as a function of loop tilt angle.

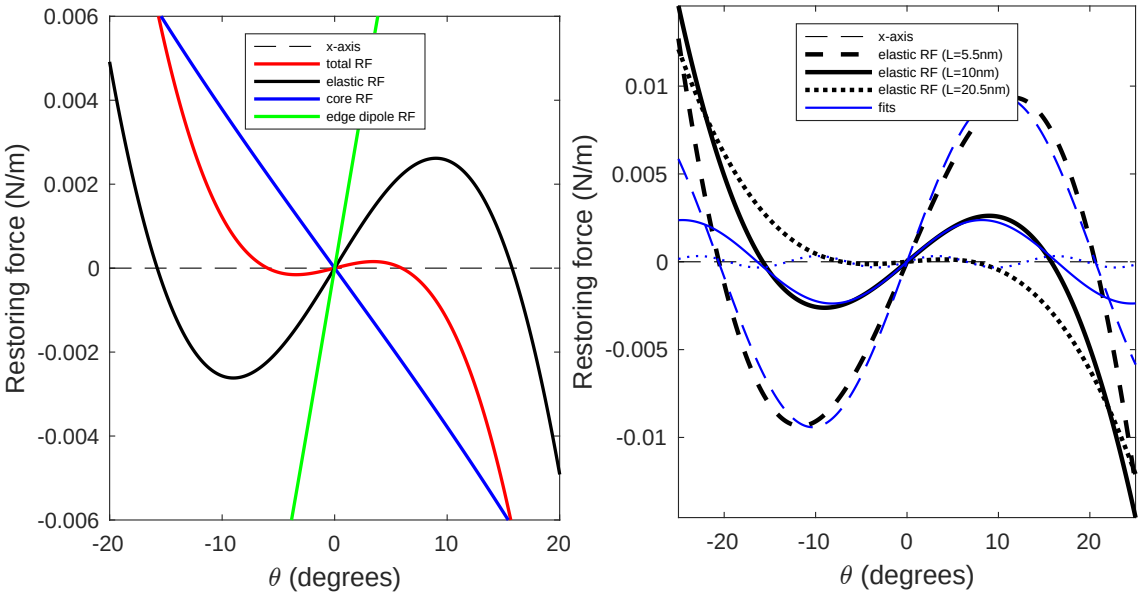
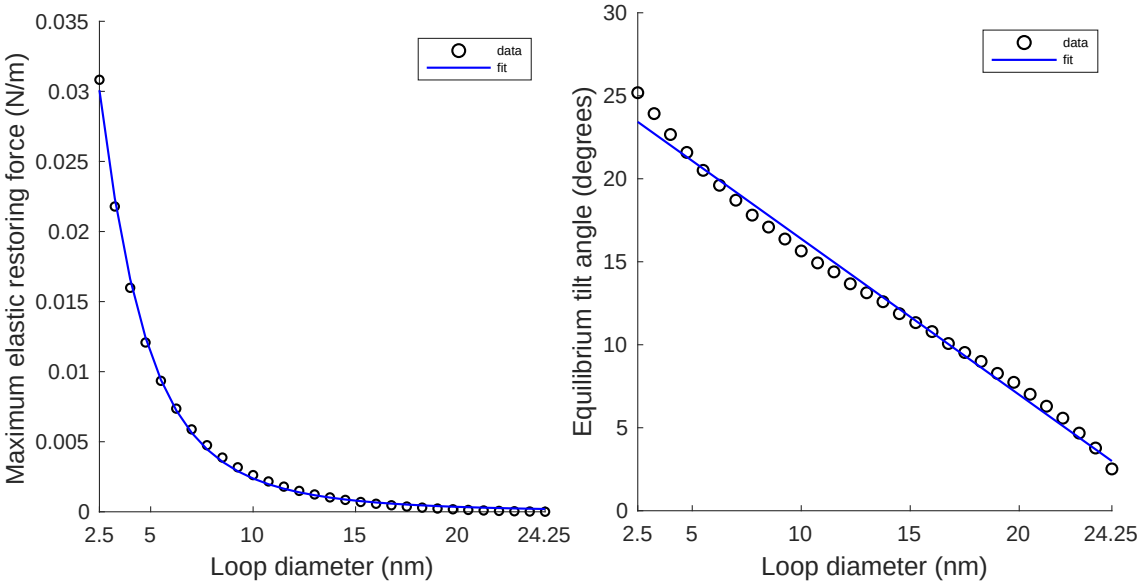


Figure 5.19: Plots containing restoring forces (RFs). (a) Restoring forces for a vacancy prismatic loop with $L = 10\,\text{nm}$. The total restoring force is the sum of the elastic and core restoring forces. The restoring force of an edge dipole of the same size is plotted for comparison. (b) Elastic restoring forces for loops of different sizes with corresponding fits. Blue curves of any pattern represent the plotted fits.



(a) Values of f_m for different loop diameters L. (b) Values of θ^e_{eq} for different loop diameters L.

Figure 5.20: Plots containing numerically-obtained data points with corresponding curves of best fit. Only elastic interactions were considered when collecting the data for these figures. Loop sizes of $L = 2.5\,\text{nm}$ to $L = 24.25\,\text{nm}$ were considered for these plots.

of figure 5.15a, projected into its glide cylinder $\hat{\boldsymbol{m}} = -\boldsymbol{b}_L$. Since this expression arises from equation (3.7), it consists of a superposition of a longitudinal component, which acts to shorten segments, and a torsional component, which acts to rotate segments into screw orientations. Because this study does not consider lateral habit plane rotations into the basal plane, and because segment Γ_{41} never changes length, the core force on n_1, represented by $\boldsymbol{f}^c_1$, will only depend on the dynamics of segment Γ_{12}. This projected core force on node n_1 is plotted in figure 5.18. As the loop begins to rotate from its pure edge configuration, the longitudinal component will always act to stabilise the extending segments and the torsional component will act to destabilise them.

The core restoring force has a simple analytical expression which can be obtained starting from equations (3.7) and (3.9). First, differentiating equation (3.9) with respect to $\boldsymbol{l}$ yields

$$\frac{\partial \epsilon^c}{\partial \boldsymbol{l}} = -\frac{2\nu E^c_s}{1-\nu}|\hat{\boldsymbol{b}} \cdot \boldsymbol{l}|\hat{\boldsymbol{b}} \tag{5.7}$$

where $\hat{\boldsymbol{b}}$ and $\boldsymbol{l}$ are respectively the unit Burgers and unit line vectors of segment Γ_{21}. Substituting this expression into equation (3.7), using the identity $(\boldsymbol{u} \otimes \boldsymbol{v})\,\boldsymbol{w} =$

$(\boldsymbol{v}\cdot\boldsymbol{w})\,\boldsymbol{u}$, and noting that the segment character angle is equivalent to $\pi/2-\theta$ yields

$$\boldsymbol{f}_1^c = \frac{E_s^c}{1-\nu}\left(\left(1-\nu\sin^2\theta\right)\boldsymbol{l} - 2\nu\sin\theta\left(\hat{\boldsymbol{b}} - \boldsymbol{l}\sin\theta\right)\right) \tag{5.8}$$

The first and second terms in expression (5.8) respectively represent the longitudinal and torsional core forces. Substituting this expression into equation (5.4) yields

$$f^{\mathrm{R,c}}(\theta, L) = \frac{2}{L}\frac{E_s^c}{1-\nu}\left((2\nu-1)\sin\theta - \nu\sin^3\theta\right) \tag{5.9}$$

This expression is plotted in figure 5.19a. From the geometry of the problem, it is evident that the core contribution acts to stabilise the structure. Changing the parameters L and E_s^c will only change the magnitude of the stabilising effect. Note that, since the only contribution to the core force on nodes n_1 and n_4 respectively come from segments Γ_{21} and Γ_{34}, the contributions to the core restoring force acting on segment Γ_{41} is the same for both the prismatic loop and double super-jog. Therefore, in this simplified representation, the core restoring force will also always act to stabilise double super-jogs. Consequently, for all dislocation structures considered, it is always true that $\theta_{eq}^c = 0$ and, furthermore, that $\theta_{eq} \leq \theta_{eq}^e$.

Suppose that a spatially uniform shear stress τ^{ext} is applied to the domain such that it acts entirely in the slip plane of segments Γ_{41} and Γ_{23}; consequently, it imparts a force on Γ_{12} and Γ_{34} which has no glide component, and can therefore be ignored on these segments. In the limit of negligible elastic contributions, one may assume that $f^{R,c} \gg f^{R,e}$. Two possible interpretations of this limit are: (1) that the core energy density E_s^c is sufficiently large such that the core restoring force dominates the elastic restoring force, and (2) that we in a sense operate within the line tension model in which nonlocal interaction forces are ignored. In the latter case, E_s^c is interpreted to additively subsume the elastic line tension, i.e. the elastic energy per unit length given by expression (3.4). Since EasyDD interpolates the inelastic core energy per unit length in the same manner as the elastic energy per unit length in the line tension model, no additional modifications are required.

In this limit, the equilibrium tilt angle θ_{eq} is then the solution of

$$0 = \tau^{\mathrm{ext}} b + f^{R,c}\left(\theta_{eq}, L\right) \tag{5.10}$$

where $b = |\boldsymbol{b}|$ is the Burgers vector magnitude. This equation is equivalent to the polynomial equation

$$0 = -\nu\sin^3\theta_{eq} + (2\nu-1)\sin\theta_{eq} + \frac{L}{2}\frac{1-\nu}{E_s^c}\tau^{\mathrm{ext}} b \tag{5.11}$$

The exact analytical solution to this polynomial is obtained via Cardano's solution to cubic equations [286], which yields

$$\theta_{eq} = \arcsin\left[\left(\mathcal{D}\frac{L\tau^{\text{ext}}b}{E_s^c}\right)^{\frac{1}{3}}\left[\left(1+(1+\mathcal{Q})^{\frac{1}{2}}\right)^{\frac{1}{3}}+\left(1-(1+\mathcal{Q})^{\frac{1}{2}}\right)^{\frac{1}{3}}\right]\right] \tag{5.12}$$

where

$$\mathcal{Q} := \frac{\mathcal{P}}{\left(\mathcal{D}\frac{L\tau^{\text{ext}}b}{E_s^c}\right)^2} \tag{5.13}$$

such that

$$\mathcal{P} := -\left(\frac{2\nu-1}{3\nu}\right)^3 \qquad \text{and} \qquad \mathcal{D} := \frac{1-\nu}{4\nu} \tag{5.14}$$

are constants. $\mathcal{P}$ is positive when $\nu < 0.5$ and $\mathcal{D}$ is always positive[2] ($\mathcal{P} \approx 0.05$ and $\mathcal{D} \approx 0.53$ for zirconium). For $\left(L\tau^{\text{ext}}b/E_s^c\right)^2 \gg \mathcal{P}/\mathcal{D}^2$, i.e. large $L\tau^{\text{ext}}/E_s^c$, the solution can be shown to behave as

$$\theta_{eq} \approx \arcsin\left[\left(\frac{(1-\nu)}{2\nu}\frac{L\tau^{\text{ext}}b}{E_s^c}\right)^{\frac{1}{3}}\right] \tag{5.15}$$

For $\left(L\tau^{\text{ext}}b/E_s^c\right) \ll \sqrt{\mathcal{P}/\mathcal{D}^2}$, i.e. small $L\tau^{\text{ext}}/E_s^c$, and upon performing binomial expansions, it is revealed that

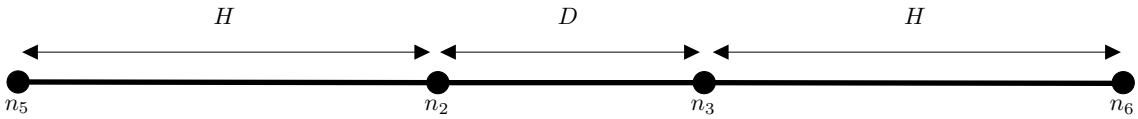
$$\theta_{eq} \approx \frac{(1-\nu)}{2\,(1-2\nu)}\frac{L\tau^{\text{ext}}b}{E_s^c} \tag{5.16}$$

is a suitable linear approximation.

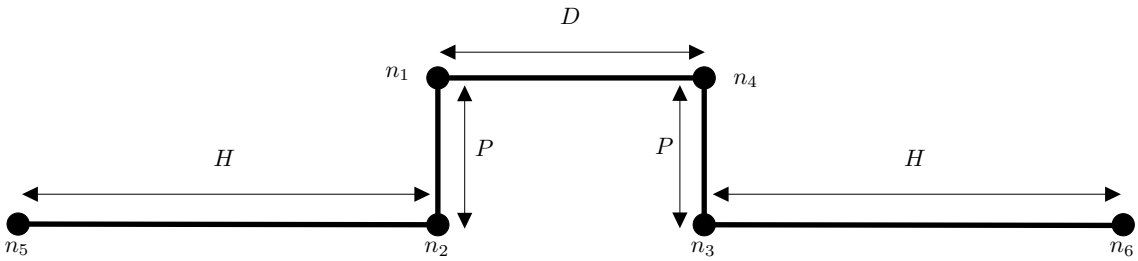
Taking values of $L = 10\,\text{nm} \approx 31b$, $\tau^{\text{ext}} = 100\,\text{MPa} \approx 0.0028\mu$, $E_s^c \approx 0.5\mu b^2$, and noting that $\sqrt{\mathcal{P}/\mathcal{D}^2} \approx 0.42$ for zirconium, one obtains $\left(L\tau^{\text{ext}}b/E_s^c\right) \approx 0.17 < \sqrt{\mathcal{P}/\mathcal{D}^2}$. Note that while this choice of E_s^c is roughly on the order of the elastic energy density in the line tension model, the inelastic core energy density can, in some cases, reach comparable magnitudes [205]. Taking a smaller core energy density of $E_s^c \approx 0.05\mu b^2$ results in $\left(L\tau^{\text{ext}}b/E_s^c\right) \approx 1.7 > \sqrt{\mathcal{P}/\mathcal{D}^2}$. Therefore, in the limit of negligible elastic interactions, for fairly large values of E_s^c, and for small values of $L\tau^{\text{ext}}$, θ_{eq} exhibits an approximately linear dependence with respect to $L\tau^{\text{ext}}$ as described by expression (5.16).

For zirconium, equation (5.15) was found to be a poor approximation of precise numeric values, and should only be used as a rough estimation of the limiting behaviour of the system. In general, as $\nu \to 0$, $\mathcal{P}/\mathcal{D}^2 \to \infty$, and so the corresponding

[2]Note that the Poisson's ratio of most real materials satisfies $0 \leq \nu \leq 0.5$.



(a) Edge dislocation.



(b) Edge dislocation with an acquired double super-jog. Only the $P = D$ case is considered in this text.

Figure 5.21: Diagrams of an edge dislocation before and after a collision with a prismatic loop has occurred.

regime of validity becomes smaller. On the other hand, as $\nu \to 0.5$, $\mathcal{P}/\mathcal{D}^2 \to 0$, and equation (5.16) diverges while equation (5.15) becomes exact for any value of $L\tau^{\text{ext}}/E_s^c$. For $\nu \approx 0.5$ and for small $L\tau^{\text{ext}}/E_s^c$, this system therefore exhibits the asymptotic behaviour given by

$$\theta_{eq} \sim \left(\frac{L\tau^{\text{ext}}b}{E_s^c}\right)^{\frac{1}{3}} \tag{5.17}$$

That is, in this regime, it is predicted that the equilibrium tilt angle θ_{eq} exhibits an approximately cubic root dependence with respect to $L\tau^{\text{ext}}/E_s^c$.

Consider a set of curves $\theta_{eq}(\tau^{\text{ext}})$, each corresponding to a different value of L, lying within a fixed domain interval $\tau^{\text{ext}} \in [\tau_1, \tau_2]$. Note that, according to equation (5.12), θ_{eq} is in general strictly monotonic with respect to $L\tau^{\text{ext}}b/E_s^c$ when $L\tau^{\text{ext}}b/E_s^c > 0$. It follows that the difference between the values of the endpoints of a codomain interval corresponding to a domain interval, i.e. the quantity given by $\theta_{eq}(\tau_2) - \theta_{eq}(\tau_1)$, will always increase as L increases. Therefore, this analysis predicts that, in the limit of negligible elastic interactions, the resistance of loops to rotation under external shear stress decreases as the loop size increases. These analytical results are supported with simulations in section 5.4.

5.3.3 Double super-jog dragging effect

Consider the two following cases: (1) a straight edge dislocation with a nodal arrangement as shown in figure 5.21a, and (2) an edge dislocation which has acquired

a double super-jog as in figure 5.21b. Suppose that in both cases a uniform external resolved shear stress τ is applied, and that each structure has a Burgers vector magnitude b. In case (1), the forces inducing motion in the network will be entirely due to the external stress. For the moment, ignore nodal dynamics acting in the climb and line directions, and thus assume that all nodal forces and velocities act along glide directions. The force acting on node n_2 is given by

$$f_2^{\text{edge}} = \frac{\tau b}{2}(H + D) \tag{5.18}$$

This will be balanced by equation (3.26), which can be expanded to obtain

$$f_2^{\text{edge}} = \frac{1}{2}(HB_{25} + DB_{32})\, v_2^{\text{edge}} \tag{5.19}$$

where B_{25} and B_{32} are the glide drag coefficients of segments Γ_{25} and Γ_{32}, respectively. Assuming that $B_{25} = B_{32}$, and after balancing equations (5.18) and (5.19), one obtains

$$v_2^{\text{edge}} = \frac{\tau b}{B_{32}} \tag{5.20}$$

In case (2), the elastic fields generated by the structure do not induce motion at this tilt angle (i.e. zero) as shown by figure 5.17. Therefore, the forces inducing motion will be entirely due to the external stress, as in case (1). Performing once again a balance of forces, and assuming that $H \to \infty$ and $D = P$, one obtains an expression for the velocities of node n_1 and n_2 given respectively by

$$v_1^{\text{dsg}} = \frac{\tau b}{(B_{41} + B_{12})} \tag{5.21}$$

and

$$v_2^{\text{dsg}} = \frac{\tau b}{(B_{41})} \tag{5.22}$$

Assuming that $B_{41} = B_{32}$, it is evident that $v_1^{\text{dsg}} < v_2^{\text{dsg}} = v_2^{\text{edge}}$. This will result in segments Γ_{25} and, via symmetry, Γ_{63}, to experience a greater mobility than segment Γ_{41}. As segment Γ_{41} is dragged behind and induces a non-zero tilt angle in the structure, the elastic fields generated will act to induce stability such that segments Γ_{25} and Γ_{63} experience a restorative force opposing their direction of motion. This effect will persist until a tilt angle of zero is achieved, after which this process will occur once again. The net effect is a reduction in the mobility of the entire structure.

5.3.4 Elastic restoring force

An analytical expression for the force exerted by a finite dislocation segment on the end node of a different finite dislocation segment with an arbitrary relative orientation has been derived and is given by Arsenlis *et al.* [101]. From this expression, it is possible to derive an exact analytical expression for $f^{\mathrm{R,e}}(\theta, L)$ using methods outlined in previous sections. However, such an expression is complicated and contains many terms, making it unwieldy for computational implementation. Therefore, in this section, a fitting procedure will be applied to data which has been collected via numerically computing line integrals of the type shown in equation (5.6). On the other hand, the core restoring force has a simple analytical expression which does not require a fitting procedure.

Our aim now is to obtain a simple analytical expression for $f^{\mathrm{R,e}}(\theta, L)$ which approximates the full complicated expression. In the following discussion, let us consider only elastic interactions, which corresponds to $E_s^c = 0$. Elastic restoring forces are numerically computed and shown in figure 5.19b for loops of different sizes. From these curves, θ_{eq}^e can be found by calculating their roots. These calculated roots were found to match the values of θ_{eq}^e obtained from performing direct 3D DD simulations. In general, as L increases, θ_{eq}^e decreases, and $f_m = \max_\theta\{|f^{\mathrm{R,e}}(\theta, L)| : -\theta_{eq}^e \leq \theta \leq \theta_{eq}^e\}$, the maximum magnitude of the amplitude of the elastic restoring force between the range $\theta \in [-\theta_{eq}^e, \theta_{eq}^e]$, also decreases. From this observation, and from looking at the behaviour of the elastic restoring force curves, we may deduce a local expression for the elastic restoring force given by

$$f^{\mathrm{R,e}}(\theta, L) = f_m\left(L\right) \sin\left(\frac{\pi}{\theta_{eq}^e\left(L\right)}\theta\right) \tag{5.23}$$

with a range of validity $\theta \in [-\theta_{eq}^e, \theta_{eq}^e]$. Since θ_{eq}^e is a stability point, this range of validity will represent many physical configurations of the prismatic loop found in simulations.

Values of $f_m(L)$ and $\theta_{eq}^e(L)$ were numerically computed for a range of loop sizes and are respectively shown in figures 5.20a and 5.20b. It is evident that $\theta_{eq}^e(L)$ may be approximated as a linear function. Several candidate functions exist to fit the maximum amplitude $f_m(L)$; taking inspiration from standard forms for non-singular field expressions, the chosen fits were given by

$$f_m\left(L\right) = \sigma_0 \frac{\beta}{\left(L^\lambda + \alpha^\lambda\right)^\lambda}, \qquad \theta_{eq}^e\left(L\right) = c_1 L + c_2 \tag{5.24}$$

where β, α, λ, c_1, and c_2 are fitting parameters. Note that $\sigma_0 = \mu/(2\pi(1-\nu))$ is not a fitting parameter, but rather a pre-factor that is the same as that found in typical elastic field expressions. The fitting parameters for $f_m(L)$ were obtained by solving a nonlinear least squares system via Gauss-Newton iteration [287]. Note that a unique global minimum for β, α, and λ was not found. The fitting parameters for θ^e_{eq} were obtained via simple linear regression. The corresponding fits for $f_m(L)$ and $\theta^e_{eq}(L)$ are superimposed on figure 5.20. The values and units of the five fitting parameters are given in Table 5.2. These fits were obtained from a data set of 30 loops consisting of loop sizes uniformly ranging from $L = 2.5\,\text{nm}$ to $L = 24.25\,\text{nm}$; greater loop sizes all had values of zero for θ^e_{eq}.

Fitting parameter	Value
β	$1.1741 \times 10^{-37} \cdot \text{m}^{\lambda^2+1}$
α	$3.8796 \times 10^{-9} \cdot \text{m}$
λ	$7/4$ (unitless)
c_1	$-1.6397 \times 10^{7} \cdot \text{m}^{-1}$
c_2	0.4499 (unitless)

Table 5.2: Fitting parameter values and units for the elastic restoring force shown in equations (5.24).

5.3.5 Total restoring force

We must now combine the core and elastic restoring forces to create a total restoring force expression which reflects the limited range of validity of the elastic component. One may use the piecewise expression given by

$$f^{\text{R}}(\theta, L) = \begin{cases} f^{\text{R,c}}(\theta, L) + f^{\text{R,e}}(\theta, L) & |\theta| \leq \theta^e_{eq} \\ f^{\text{R,c}}(\theta, L) & |\theta| > \theta^e_{eq} \end{cases} \tag{5.25}$$

where θ^e_{eq} is the equilibrium tilt angle of an isolated square prismatic loop which only endures elastic interactions. When large external stresses result in $\theta \gg \theta^e_{eq}$, equation (5.25) fails in supplying the sufficient restoring action to produce a realistic equilibrium tilt angle. In such a case, one possible correction to equation (5.25) and to the loop dynamics is to set the loop to be infinitely stiff with respect to external stresses which tend to increase its tilt angle outside of the range of validity $\theta \in [-\theta^e_{eq}, \theta^e_{eq}]$. This prevents the prismatic loop from obtaining values of θ outside

of the range of validity. Note that as the loop size increases, this method yields increasingly spurious results, since large prismatic loops will effectively lose most or all of their tilting capability. Alternatively, values for the total restoring force over the entire range of tilt angles from $-90°$ to $90°$ can be numerically computed and interpolated to provide the full behaviour if necessary, e.g. for 2.5D DDP codes.

5.4 Investigations using the 2.5D DDP model

The DDP code used in this section is a further enhancement of the one previously developed by [65], which uses the formulations established by [288, 109]. In the present DDP model, $\langle a \rangle$-type prismatic loops are idealised in the same way as described in previous sections of this text. The loop segments that intersect the simulation plane (see figure 5.15c) are represented as edge dipoles in either interstitial or vacancy orientations, i.e. with extra half planes aligned and either pointing towards or away from one another. To inform the planar model with the essential three-dimensional information that captures the effect of all loop segments on loop tilting, f^{R} is incorporated as an additional force acting on the dipole of edge dislocations that represent the prismatic loop in the simulation plane, hence making the planar DDP model 2.5D in character. However, the DDP model requires f^{R} to be evaluated for the full range of possible tilt angles, i.e. from $-90°$ to $90°$. Since the restoring force for a particular loop size already includes the effect of the elastic stress fields of the full square prismatic loop, the elastic interaction between the dipole of edge dislocations representing the prismatic loop in the planar DDP model is omitted from the computation to avoid double counting. For all of the simulations in this section, the elastic restoring force was numerically computed at 1000 points in the range $-90°$ to $90°$ from the non-singular elastic stress expressions given in [194], which was then added to the analytical core restoring force expression to obtain an angular discretisation of the total restoring force for all loop sizes simulated. These values were then linearly interpolated to capture the restoring force for all possible tilt angles θ. Numerically computed total restoring force curves over the full range of tilt angles and for various loop sizes are shown in figure 5.22. Note that core energy per unit length was set to $E_s^c = 0.125\,\mathrm{eV\,\AA^{-1}}$ for the plots in figure 5.22, as well as for all 2.5D DD simulations in this chapter. The restoring force was added to the Peach-Koehler force $\boldsymbol{f}^{\mathrm{PK}}$ to calculate the velocity of the loop dislocations, v_{loop}, according to:

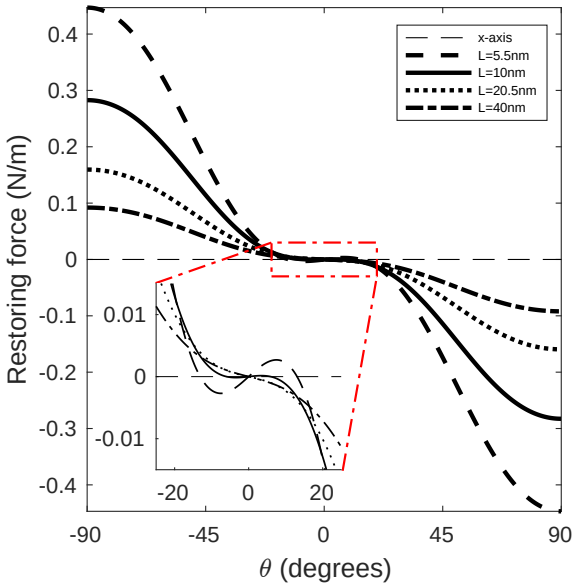


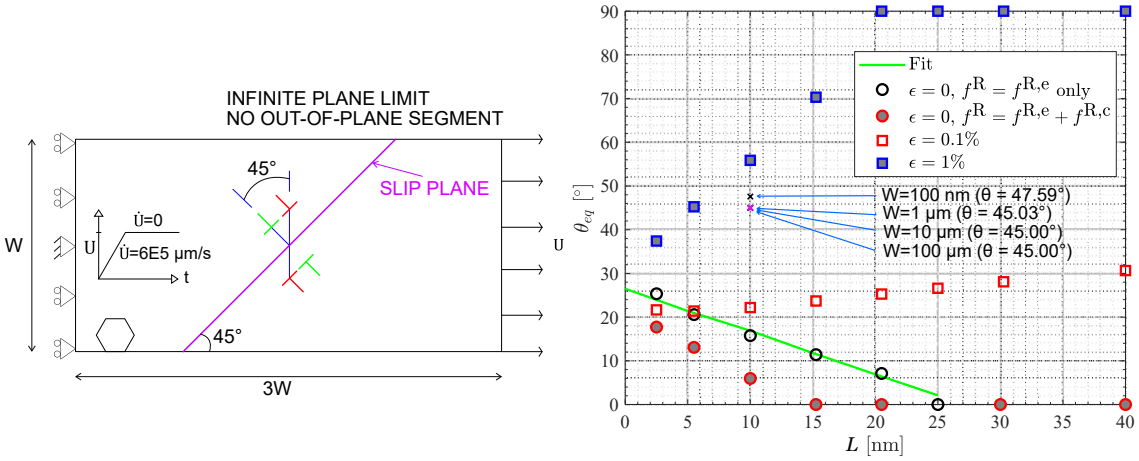
Figure 5.22: Plot containing numerically computed total restoring force curves for various loop sizes.

$$v_{\text{loop}} = \frac{f^{\text{PK}} + f^{\text{R}}(\theta, L)}{\text{B}_{\text{drag}}} \tag{5.26}$$

where the drag coefficient B_{drag} is assigned a typical value of $4 \times 10^{-4}\,\text{Pa}\,\text{s}$.

5.4.1 Loop stability analysis

To validate the 2.5D implementation and investigate the stability of prismatic loops for a range of loop sizes and applied strains, a simple uniaxial tension boundary value problem was used, as shown in the schematic of figure 5.23a. The simulation box contains only one prismatic slip system oriented 45° to the horizontal direction, which passes through the centre of the simulation box, and a single prismatic vacancy loop with its habit plane initially perpendicular to the slip direction. In this section, the loop size L is assumed to remain constant during a given simulation and is unaffected by the tilting. A simulation box large enough such that loop dislocations do not interact with the free surfaces was used in the simulations to mimic the situation in the three-dimensional dislocation dynamics model. In an infinite half plane, infinitely-long straight-line edge dislocations oriented as in figure 5.23a (i.e. an infinitely deep loop with elastic interactions but without the effect of core interactions) would tilt to an equilibrium angle of 45°. To determine an appropriate box size, the simulation box was maintained at a 3:1 aspect ratio and increased in size until a stable 45° was achieved for a loop with $L = 10\,\text{nm}$, as shown in figure 5.23b. The



(a) (b)

Figure 5.23: (a) A boundary value problem depicting a one loop – one slip system problem in a simulation box of size of $300 \times 100\,\mu m^2$. The vacancy loop shown as an edge dipole in climb configuration tilts by 45° degrees after the initial position (represented in green) of the loop is perturbed (represented in red). (b) DDP simulations are performed to understand the effect of loop size L on the evolution of equilibrium tilt angle θ_{eq} for one unstrained and two strained configurations. The unstrained θ_{eq} values match the values in Fig. 5.20b. The fit line for $\theta^e_{eq}(L)$ depicted in Fig. 5.20b is also plotted in green for reference. The simulation box size effect on the equilibrium angles of an edge dipole of size $L = 10\,nm$ is also shown; the smallest simulation box ($W = 100\,nm$) generates the highest boundary stresses that prompt the edge dipole to adopt an equilibrium angle furthest away from the 45° angular position.

smallest box size ($W = 100\,nm$) provides the highest instability to the equilibrium position ($\theta_{eq} = 47.59°$); a simulation box with size $W = 100\,\mu m$ was found to be more than sufficient ($\theta_{eq} = 45.000°$) to ensure that the loop dislocations were devoid of free surface interactions.

Simulations were performed using the 2.5D model to investigate the equilibrium tilt angles θ_{eq} under the action of the restoring force and applied loading for various loop sizes (ranging from $L = 2.5\,nm$ to $L = 40\,nm$) of $\langle a \rangle$-type prismatic loops in both unstrained and strained samples. In the zero applied strain simulations, the system is allowed to equilibrate until loop tilting terminates (i.e. until $v_{loop} < 1 \times 10^{-9}\,m\,s^{-1}$); this is a quasi-equilibrium state with respect to the timescale of the simulation. A constant time step of $\Delta t = 5 \times 10^{-10}\,s$ is generally used for the simulations but, due to the higher nonlinearity of the $f^R(\theta, L)$ versus θ curves shown in figure 5.22 for smaller loop sizes, a smaller time step is also selected in some cases. The open black circles on figure 5.23b depict the equilibrium tilt angles of loop dislocations

as a function of loop size when only considering the effect of the elastic restoring force (i.e. ignoring core effects). The equilibrium tilt angles calculated using the 2.5D model exactly match the ones obtained in figure 5.20b, which validates the 2.5D implementation. The fitting model presented in equation 5.23 is also shown for reference as a green line, which is the same as the line of fit presented in figure 5.20b. The effect of the total restoring force $f^{\mathrm{R}}(\theta, L)$, including both $f^{\mathrm{R,e}}(\theta, L)$ and $f^{\mathrm{R,c}}(\theta, L)$, is depicted by the red filled circles in figure 5.23b for the zero applied strain case, where it is observed that the equilibrium tilt angle decreases with an increase in loop size. Specifically, the $\langle a \rangle$-type prismatic loops with $L > 12\,\mathrm{nm}$ are observed to show no tilting and are stable at zero degrees. Although the full 3D situation is more complex, the trend that sufficiently large loops do not tilt (with respect to the timescale of the simulation) under zero applied strain is primarily a result of the weaker elastic interaction of the perpendicular loop segments for larger loop sizes (i.e. as those segments become further apart).

Further simulations were performed to investigate the effect of applied strain on the stable equilibrium tilt angles of $\langle a \rangle$-type prismatic loops as a function of loop size. Plot points corresponding to strain values of $\epsilon = 0.1\%$ and $\epsilon = 1\%$ are depicted by the red empty squares and blue filled squares, respectively, in figure 5.23b. The displacement rate is set to $\dot{\mathrm{U}} = 6 \times 10^5\,\mu\mathrm{m\,s^{-1}}$ to achieve a strain rate of $\dot{\epsilon} = 2000\,\mathrm{s^{-1}}$ for these simulations. After the completion of the loading step, the loops are allowed to equilibrate further with $\dot{\mathrm{U}} = 0\,\mu\mathrm{m\,s^{-1}}$, as shown in the schematic inset in figure 5.23a, until $v_{\mathrm{loop}} < 1 \times 10^{-9}\,\mathrm{m\,s^{-1}}$. In both strained cases, smaller loops are observed to have smaller equilibrium tilt angles compared to larger loops, which may indicate a higher resistance to certain types of deformation, e.g. a dislocation acting to drive a loop to a greater tilt angle will encounter greater resistance from a smaller loop, which in turn may have implications for the mechanics of irradiation hardening; this effect is due to the greater magnitude of the restoring force for smaller loops at larger angles (see figure 5.22), or more specifically, at angles considerably larger than the zero-strain equilibrium tilt angle for the smallest loop in the comparison. Moreover, in the $\epsilon = 1\%$ case the larger loops with $L > 15\,\mathrm{nm}$ show little resistance to the deformation and equilibrate at angles approaching 90°.

3D DD simulations investigating the impact of an external applied shear stress on the rotation of loops were performed to support the 2.5D DD simulations. Each simulation proceeds as follows. The initial condition consists of a square prismatic loop of size L comprised of four segments placed within an infinite domain. A slight rotational perturbation is applied to the loop to avoid the zero-angle unstable

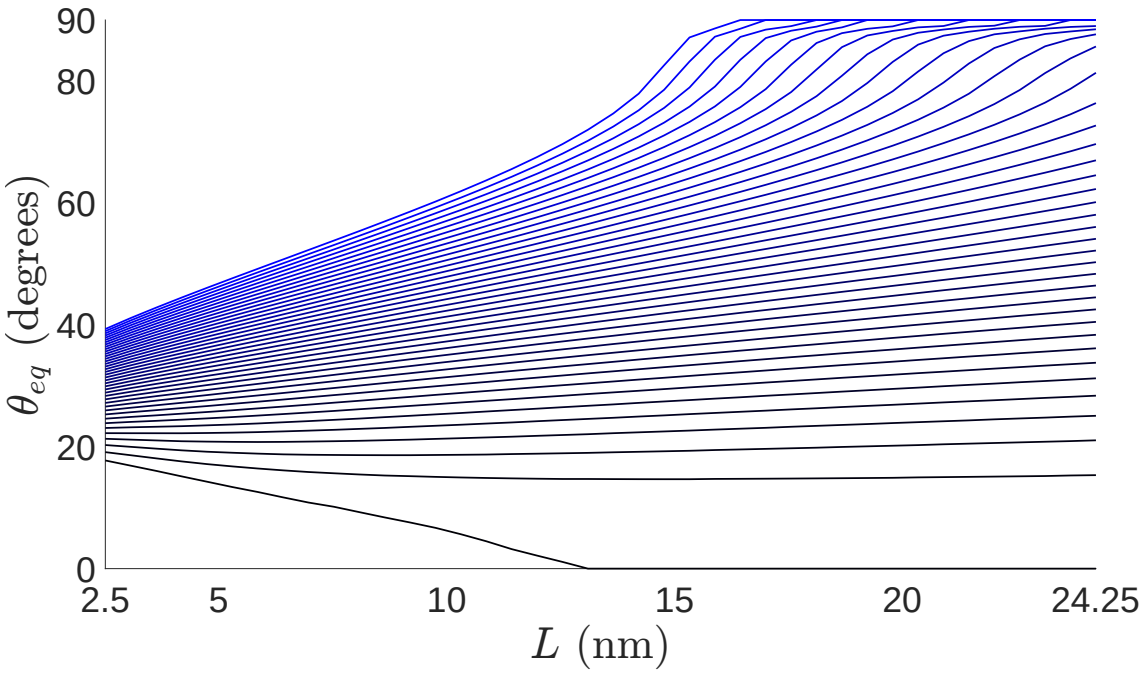


Figure 5.24: Plots of equilibrium tilt angles of prismatic loops as a function of loop size for a range of applied stresses τ^{ext} ranging from 0 MPa (pure black) to 600 MPa (pure blue). $E_s^c = 0.125\,\text{eV Å}^{-1} \approx 0.05\mu b^2$ is used.

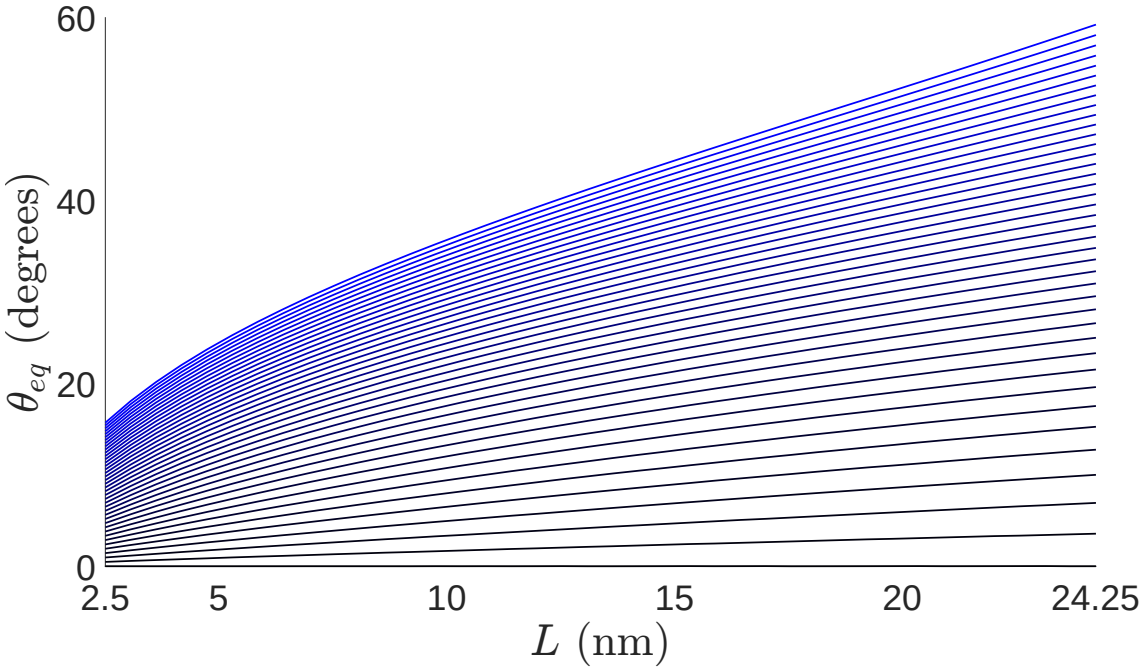


Figure 5.25: Plots of equilibrium tilt angles of prismatic loops as a function of loop size for a range of applied stresses τ^{ext} ranging from 0 MPa (pure black) to 600 MPa (pure blue). $E_s^c = 1.139\,\text{eV Å}^{-1} \approx 0.5\mu b^2$ is used.

equilibrium point. A spatially uniform shear stress τ^{ext} is applied to the domain. The nature of the external applied shear stress is such that it acts entirely in the slip plane of the Γ_{41} and Γ_{23} segments. As the loop rotates, segments Γ_{41} and Γ_{23} are never subdivided, but segments Γ_{12} and Γ_{34} are sometimes subdivided into pieces of smaller length as their lengths increase to sizes which are much larger than L. The simulation is interrupted after at least one of three cases occurs: (1) the speed of the fastest travelling node becomes smaller than $3 \times 10^{-1}\,\text{m}\,\text{s}^{-1}$, (2) the total simulation time exceeds $5 \times 10^{-9}\,\text{s}$, or (3) the tilt angle θ satisfies $|\pi/2 - \theta|/|\pi/2| < 10^{-2}$ (in which case θ_{eq} is set to $\pi/2$). The maximum speed condition is selected to be sufficiently large to ignore nodal oscillation modes which tend to arise due to minor lateral rotations towards the basal plane; it was found to be sufficiently small to properly capture the equilibrium tilt angles. The tilt angle is then calculated by adding $\pi/2$ to the maximum of the angles between the line vectors of all segments gliding in the basal plane and the Burgers vector. 40 loop sizes are tested, ranging uniformly from $L = 2.5\,\text{nm}$ to $L = 24.25\,\text{nm}$, and 40 applied stresses are tested, ranging uniformly from $\tau^{\text{ext}} = 0\,\text{MPa}$ to $\tau^{\text{ext}} = 600\,\text{MPa}$.

Figure 5.24 displays plots of the equilibrium tilt angle θ_{eq} as a function of the loop size L for all tested applied stresses using $E_s^c = 0.125\,\text{eV}\,\text{Å}^{-1} \approx 0.05\mu b^2$. As expected, the results match those found using the 2.5D DD model in figure 5.23b. Figure 5.25 displays similar plots, but instead using a value of $E_s^c = 1.139\,\text{eV}\,\text{Å}^{-1} \approx 0.5\mu b^2$, which is about an order of magnitude larger than before. In both cases, the equilibrium tilt angles of smaller sized loops lie within a smaller range, which indicates that they are more resistant to external shear stress. One could say that *the stable angle of smaller loops is less sensitive to external stresses.* It can also be seen that the loop stability is quite sensitive to E_s^c. In the case with smaller E_s^c, the curve behaviours are quite complex, which reflects the increased relevance of the elastic contribution. In the case with larger E_s^c, all equilibrium tilt angle curves increase monotonically with increasing size. In addition, the curves appear to exhibit near-linear behaviour at small τ^{ext} for all L. Figure 5.26 displays plots comparing the simulation results with the exact solution in the negligible elastic interaction limit given by equation (5.12) and its linear approximation (5.16). The simulation results appear to be fairly consistent with equation (5.12), especially for small L and/or τ^{ext}; their alignment decreases as L increases. Similarly, the linear approximation appears to be most useful for small applied stresses. It is expected that the analytical solution would increasingly match the simulation results as E_c^s increases, since the contributions

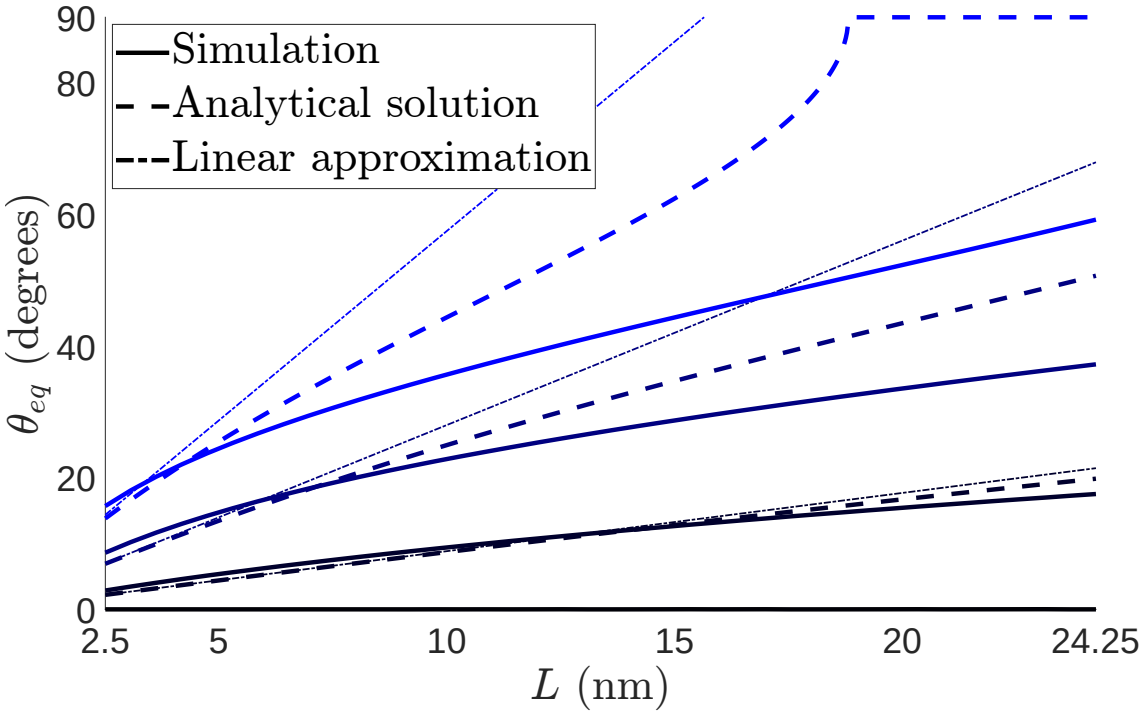
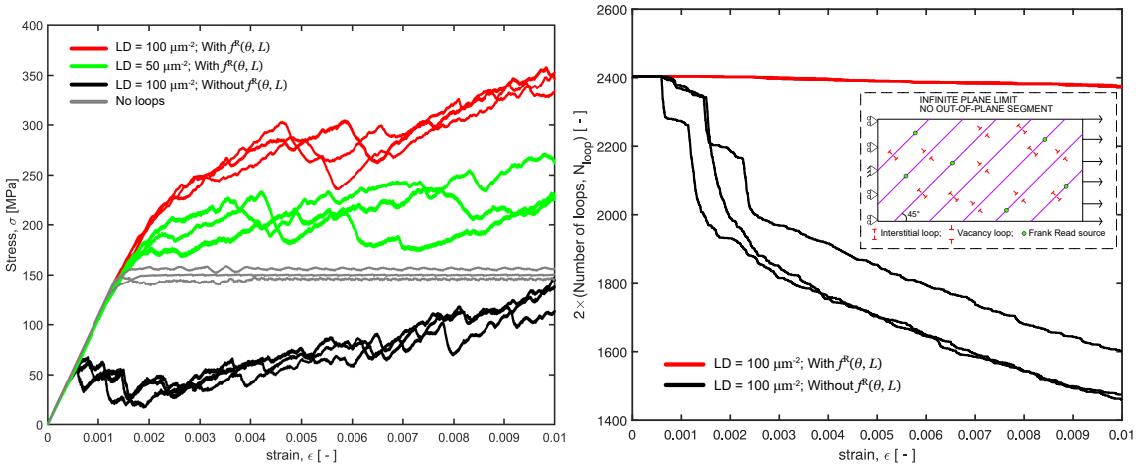


Figure 5.26: Plots of equilibrium tilt angles of prismatic loops as a function of loop size for applied stresses τ^{ext} given by 0 MPa (the x-axis), 92 MPa, 292 MPa, and 600 MPa. The colours range from pure black for 0 MPa, to pure blue for 600 MPa. The thick solid lines represent the data points obtained via simulation, the thick dotted lines represent the corresponding analytical solutions obtained from equation (5.12), and the thin half-dotted-half-solid lines represent the corresponding linear approximations obtained from equation (5.16). $E_s^c = 1.139\,\text{eV}\,\text{Å}^{-1} \approx 0.5\mu b^2$ is used.

from the elastic restoring force would become increasingly negligible in comparison to those from the core restoring force.

5.4.2 Restoring force and loop density effects on flow stress

In order to demonstrate the importance of $f^{\text{R}}(\theta, L)$ on the mobility of loop dislocations and the overall deformation behaviour via Eq. 5.26, the boundary value problem shown in the inset of figure 5.27b is simulated using the 2.5D DDP code with multiple loops present. Virtual samples are 6 µm × 2 µm in size, and a single slip (planes at 45°) situation without obstacles is chosen to elucidate the effect of $f^{\text{R}}(\theta, L)$. The slip plane spacing is taken to be $100b$, and there are a total of 170 slip planes in the sample. Frank-Read sources are randomly distributed on the slip planes with a density of 5 µm^{-2}. Their strength is taken from a Gaussian distribution with mean source strength 110 MPa and standard deviation 20 MPa. The loop sizes are also



(a) (b)

Figure 5.27: (a) The effect of restoring force $f^{\mathrm{R}}(\theta, L)$, with or without, on the evolution of flow stress for a loop density of $100\,\mu\mathrm{m}^{-2}$ in the DDP model. A case with a loop density of $50\,\mu\mathrm{m}^{-2}$ that considers the $f^{\mathrm{R}}(\theta, L)$ effect and a reference simulation without loops is also shown. (b) The effect of $f^{\mathrm{R}}(\theta, L)$ on the escape of loop dislocations from the sample surface. An inset shows a schematic of the boundary value problem used in the simulations.

taken from a distribution with mean 10 nm and standard deviation 0.1 nm. Loops are distributed randomly, but are centred about slip planes, and the total mass of loops is conserved (implying equal total vacancy and interstitial loop lengths). The dislocation-loop interaction is similar to the mechanism explained in section 5.2, whereby a loop may be cut by a dislocation nucleated from a Frank-Read source upon contact, but is restricted to a discretised reduction process that on average resolves the statistics of dislocation-loop interactions over the sample: a loop is initially at full length, is then cut to half its length, and is then reduced to zero length. Slip is not generated by loop dislocations until they move.

Two loop density cases of $50\,\mu\mathrm{m}^{-2}$ and $100\,\mu\mathrm{m}^{-2}$ were simulated, along with a reference simulation with no loops, for three realisations (same set of input parameters) each to capture the statistical scatter (see figure 5.27a). In the reference case (light black curves), it is evident that the flow stress is consistent with that required to activate dislocation sources on 45° planes with an average 110 MPa strength, with no apparent source of significant strengthening in this single-slip, no-obstacle, no-loop model setup. In the cases when loops and $f^{\mathrm{R}}(\theta, L)$ are included, there is a significant increase in flow stress observed relative to the reference case that increases with increasing loop density, as shown by the green and red curves, respectively,

in figure 5.27a. This trend is in agreement with the general observation in the literature that correlates greater loop density with greater irradiation hardening, and also demonstrates the significant role of $f^{\mathrm{R}}(\theta, L)$ in the 2.5D DDP model, even for this very simple case. In the simulations with $100\,\mu\mathrm{m}^{-2}$ loop density without $f^{\mathrm{R}}(\theta, L)$ included (dark black curves), in which loop dislocations are in effect edge dislocations interacting only with each other, the other dislocations in the system, and the boundary conditions, the flow stress is markedly lower compared to the case with no loops at all. The mechanism is that loops restrained from tilting by $f^{\mathrm{R}}(\theta, L)$ are able to remain in the system, are relatively difficult to tilt beyond their no-strain equilibrium angle, and therefore block slip from Frank-Read dislocations which elevates the flow stress, especially for higher loops densities; whereas when $f^{\mathrm{R}}(\theta, L)$ is not included, the two dislocations making a loop are free to glide away from each other easily, particularly as straining occurs and other dislocations are nucleated, which together imbalances the pair further. This, in turn, enhances slip, allowing the material to deform plastically at a lower flow stress compared to no loops at all. The mechanism is corroborated by the number of loop dislocations plotted against strain as shown in figure 5.27b. A very small, gradual decrease in loop dislocations is observed when $f^{\mathrm{R}}(\theta, L)$ is included (red curves), which indicates the restraining effect on loop dislocations of the out-of-plane segments captured by $f^{\mathrm{R}}(\theta, L)$; very few loop dislocations are able to escape at the free surfaces during the straining. This is in stark contrast to the case without $f^{\mathrm{R}}(\theta, L)$, in which a rapid decrease in loop dislocations is observed, particularly for lower strain values corresponding to a lower flow stress, which then stabilises but continues throughout the straining; the number of loop dislocations is reduced by roughly a third at 1% strain.

5.5 Conclusions and future work

This chapter introduces a new 2.5D DD method which informs a planar model with the essential 3D information pertaining to the rotational physics of prismatic loops. The primary application of this model is to study irradiation hardening of zirconium, although it could feasibly be extended to study other metals as well. However, there are limitations and general considerations associated with the present model which should be discussed. Some of these limitations are anticipated to be addressed in future research in order to refine and improve the 2.5D DD model.

In this text, 3D prismatic loops are considered to have a square (rectangular upon rotation) shape for simplicity. In reality, loops have been found to adopt roughly elliptical, square, and hexagonal shapes in experimental and theoretical studies [137, 135, 289, 166]. It is notable that hexagonal loops could feasibly be included in the current model by taking advantage of the presence of pyramidal planes—this could be an area of future investigation. However, at the scales relevant to dislocation dynamics, the precise shape of dislocation loops found in relevant engineering applications lacks a complete model. In addition, it is understood that the rotational dynamics of loops may be significantly influenced by both the elastic anisotropy of the crystal and the dislocation core energy density [280]. Regardless, piecewise segmented (i.e. polygonal) approximations to smooth curved dislocation loops have been found to agree well with exact constructions [276], which suggests that the results in this text are relevant. Although atomistic simulations may be necessary for a comprehensive understanding of loop rotational dynamics, in this text prismatic loops are studied in the framework of linear isotropic elasticity. Understanding loop behaviour in this regime provides a basic understanding of their dynamics, and serves as a foundation for interpreting more complex phenomena and identifying when non-elastic effects become significant.

The $D \neq L$ case is not considered in this model (see figure 5.15a). When a loop is cut by a dislocation, it reduces in size. In the current 2.5D DD model, this is represented by reducing both L and D, thereby maintaining $D = L$. However, in reality, only L is reduced, and D is unchanged. The physics of reduced loops has received limited attention in the literature. The method adopted by the current 2.5D DD model likely underestimates the dislocation resistance of reduced loops, potentially influencing the predicted behaviour of channel formation during irradiation hardening.

When a dislocation acquires a double super-jog, it experiences an increased effective drag, which is a phenomenon that cannot be explicitly captured by the current 2.5D DD model. This phenomenon has been studied recently by Dupuy *et al.*, who derived and implemented atomistically informed drag coefficients for jogged dislocations in zirconium [161]. This could be implemented into the current 2.5D DD model by appropriately increasing the drag coefficient of dislocations after they react with loops.

There are various other potential corrections and extensions which could feasibly be applied to the current 2.5D DD model. For example, in the simulations performed in this chapter, only one Burgers vector is incorporated. Future modifications could

incorporate multiple Burgers vectors, allowing for the simulation of cross-reactions between dislocations and loops of different Burgers vectors. Additionally, the model could be adapted to simulate basal slip and interactions with $\langle c \rangle$-type loops. However, further three-dimensional analytical, numerical, and/or simulation-based studies are required to fully understand the relationship between the size of prismatic loops (and particularly $\langle c \rangle$-type loops) and their ability to resist dislocation motion within the purely elastic regime.

An intriguing avenue for future research would be an in-depth study of the impact of the restoring force on irradiation hardening. For example, it would be interesting to compare the case where loops are infinitely stiff and cannot rotate to the case where the restoring force is applied to loops as usual. Such comparisons would help elucidate the role of loop rotational dynamics in contributing to dislocation motion resistance, dislocation channelling, and overall irradiation hardening.

One notable limitation of the current 2.5D DD model—and 2D DD models in general—is the inability to simulate screw dislocations. Screw dislocations are believed to play a critical role in irradiation hardening, as their interactions with prismatic loops often result in the formation of helical turns along the dislocation line, which serve as substantial barriers to its motion [197, 290, 85]. However, the edge-only regime provides a useful simplification that highlights fundamental dislocation interactions, providing a clearer insight into the role of edge dislocations in phenomena such as irradiation hardening. The current 2.5D DD model establishes a foundation for understanding the basic mechanics of irradiation hardening, facilitating future studies that incorporate screw dislocations and their more complex interactions.

Chapter 6

Simulations of zirconium tensile tests

Chapter introduction

In this chapter, 3D DD simulations are conducted and analysed to support experimental tensile tests of HCP zirconium. Note that all investigations in this section are limited to $\langle a \rangle$-type basal and prismatic slip systems. In section 6.1, all potential junction reactions in the considered system are analysed and discussed. In section 6.2, the experimental and computational methodologies, along with associated computer codes and bugs, are described. In section 6.3, dislocation dynamics simulations of tensile tests are conducted and analysed. In section 6.4, conclusions and potential directions for future work are discussed. Note that all of the content in this chapter is original work, although Alan Xu and Dhriti Bhattacharyya at the Australian Nuclear Science and Technology Organisation (ANSTO) conducted the tensile tests and provided the experimental data.

6.1 Dislocation junctions

The interactions between non-coplanar dislocations—also known as forest interactions—play a significant role in strain hardening. It is therefore important to understand the nature of the types of junction reactions that are possible in a given simulation. In preparation for the DD simulations conducted in this chapter, we shall first analyse the outcomes of possible dislocation-dislocation collision reactions in the relevant slip systems. In addition to providing a foundational understanding of junction formation, this analysis also serves to validate the EasyDD code. Note

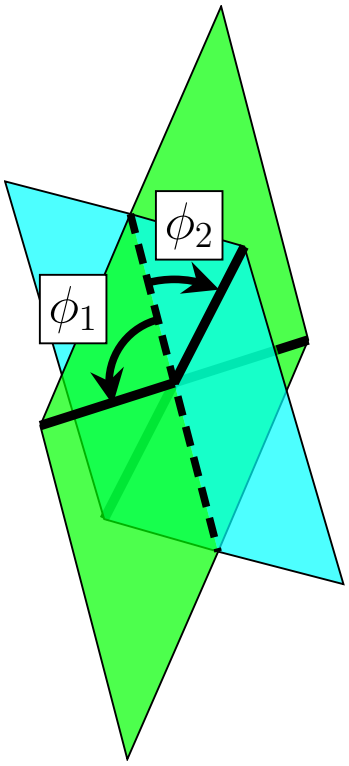


Figure 6.1: Schematic of an example of an initial configuration of a forest interaction. The thick solid lines represent the dislocations, the dotted line represents the line of intersection of the two non-coplanar glide planes, and the two intersecting parallelograms represent the glide planes.

that, in this chapter, all investigations are limited to $\langle a \rangle$-type basal and prismatic slip systems.

One important avenue of investigation is the analysis of *interaction maps*. Interaction maps generalise the well-known Frank's energy criterion for determining the outcome of a dislocation reaction [197] to non-parallel dislocation interactions. An interaction map (see, for example, figures 6.4, which will be discussed in detail later) is a depiction of the reaction outcomes of two initially straight non-coplanar dislocation lines, each belonging to specific slip systems and with line vectors at respective angles ϕ_1 and ϕ_2 relative to the line which defines the intersection of their respective glide planes, as shown in figure 6.1. An interaction map provides a useful first order classification of the strength of junctions between two slip systems. It can be interpreted, in an averaged sense, as relating to the probability of dislocation interaction outcomes within a crystal where dislocation orientations are randomly distributed. However, a more comprehensive analysis requires the computation of interaction coefficients, which is not performed in this text.

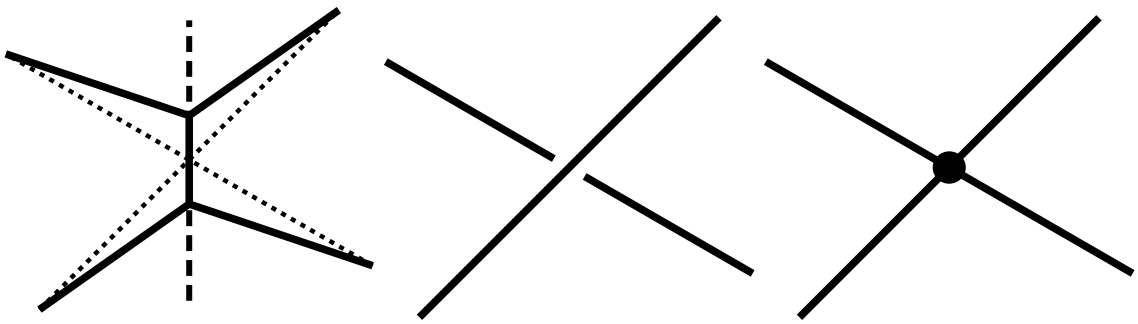


Figure 6.2: Schematic of the three possible outcomes of a forest interaction, from one of the following: (a) attractive, resulting in junction formation; (b) repulsive, resulting in no explicit reaction; (c) crossed, resulting in weak attraction and a single point of pinning at the black node. The thick solid lines represent the dislocations, the vertical dotted line represents the line of intersection of the two glide planes, and the diagonal dotted lines represent the initial dislocation configuration.

For each ϕ_1 and ϕ_2, the reaction outcome can be categorised as one of three separate types of states: attractive (figure 6.2a), repulsive (figure 6.2b), and crossed (figure 6.2c). An attractive state occurs when the dislocations come together and form a junction of some length. A repulsive state occurs when the two dislocations repel each other without undergoing an explicit reaction. A crossed state occurs when the dislocations weakly attract, typically becoming pinned at a single point of intersection without resulting in a junction. Let n and m denote Burgers vector indices. In a typical simulation conducted in this chapter, there are three possible types of collisions, denoted as follows: $n\text{Pr} - m\text{Pr}$, corresponding to a prismatic-prismatic collision with different Burgers vectors (resulting in junction formation if attractive), $n\text{Pr} - m\text{Ba}$, corresponding to a prismatic-basal collision with different Burgers vectors (resulting in junction formation if attractive), and $n\text{Pr} - n\text{Ba}$, corresponding to a prismatic-basal collision with the same Burgers vector (resulting in annihilation if attractive). The latter reaction is sometimes referred to as the collinear interaction, and in many systems provides the largest contribution to the critical stress for slip [29, 197].

In this chapter, all models are limited to $\langle a \rangle$-type basal and prismatic slip systems. Because of symmetry, obtaining all possible reaction information is possible by computing interaction maps corresponding to only three distinct forest interactions. Therefore, only the $1\text{Pr} - 2\text{Pr}$, $1\text{Pr} - 2\text{Ba}$, and $1\text{Pr} - 1\text{Ba}$ interactions are considered. If the interaction results in an attractive state, the respective junction outcomes are 3Pr, 3Ba, and annihilation (i.e. a junction with zero Burgers vector).

Interaction maps have been produced and analysed in a variety of systems such as FCC and BCC materials [284, 168, 169], HCP magnesium [170], HCP beryllium [171, 80], (effectively) HCP ice [173], and in prismatic HCP zirconium slip systems [129]. Interaction maps have been used to elucidate complex reactions which are composed of multiple simple dislocation-dislocation reactions [85] and to explain hardening related to forest interactions on a probabilistic basis [29, 173]. In this section, interaction maps are produced and analysed for HCP zirconium.

In this text, interaction maps are computed while neglecting external stress, as is typically done in the literature. However, it is notable that interaction maps have been found to be fairly insensitive to external stress, the initial dislocation curvature, and the initial distance between the dislocations [284]. In contrast, the initial dislocation length has been found to moderately impact the size of junction domains predicted by interaction maps, although the result converges as the initial dislocation length increases [169]. Note that only the case where the initial dislocations are of equal length was investigated in this text. However, the unequal length case has been associated with differences in junction strengths [291].

Before proceeding to a discussion of the computed interaction maps, it is important to discuss two simple criteria which can be used to predict the outcome of a forest interaction. These criteria are also useful in validating simulations used to create interaction maps. The first criterion predicts whether a junction is energetically favourable based on the local line tension energy [292]. This has been found to be quite accurate in predicting junction favourability, but inadequate for predicting crossed states. This is because a crossed state is a configuration in which the dislocations are attractive, but junction formation is not favourable. On the other hand, the prediction of crossed states can be enhanced by applying an additional criterion based on the mutual force between the two initial dislocations. This predicts whether the two dislocations are attractive. Combined together, these two criteria have been found to be remarkably robust and accurate in predicting reaction outcomes.

We shall first describe the line tension model. In this idealised model, it is assumed that all dislocation lines are rigid and that the interaction energy is ignored. Let us denote the dislocations which compose the initial configuration as dislocation (1) and dislocation (2). Let both dislocations each have the same initial length of H. Consider an intermediary stage in the evolution of a forest interaction as depicted in figure 6.3 (note that although only half of the configuration is depicted in this figure, the other half is equivalent by symmetry). Let $2L_1$, $2L_2$, and $2L_3$ denote the respective total lengths of (1), (2), and the junction during the evolution of the

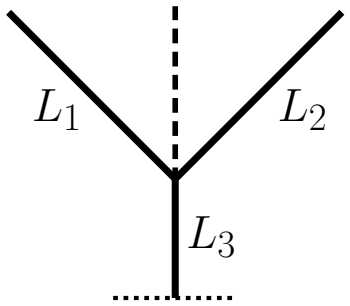


Figure 6.3: Schematic of an intermediary stage in the evolution of a forest interaction. The thick solid lines represent the dislocations, the vertical dotted line represents the line of intersection of the two glide planes, and the horizontal dotted line represents a line of symmetry which cuts the full configuration in half.

interaction; they will change during its progression. The energy of a single dislocation of length $2L_i$ with Burgers vector magnitude b_i and character angle θ_i is given by

$$E_i = \frac{\mu b_i^2}{4\pi(1-\nu)} \ln\left(\frac{\mathcal{R}_c}{r_c}\right) 2L_i g\left(\theta_i\right) \tag{6.1}$$

where

$$g\left(\theta_i\right) \coloneqq 1 - \nu\cos^2\theta_i \tag{6.2}$$

The total energy of a forest interaction is given by

$$U = \frac{2\mu}{4\pi(1-\nu)} \ln\left(\frac{\mathcal{R}_c}{r_c}\right) \sum_{i=1}^{3} b_i^2 L_i g\left(\theta_i\right) \tag{6.3}$$

Once the configuration reaches elastic relaxation, the length of the resulting junction is

$$L_{\text{junc}} = \underset{L_3\in[0,H/2]}{\arg\min}\left[U\left(L_3\right)\right] \tag{6.4}$$

Junction formation is considered favourable if the criterion

$$L_{\text{junc}} > \epsilon_{\text{junc}} \tag{6.5}$$

is fulfilled, where ϵ_{junc} is some minimum tolerance for the allowed junction length. The junction length L_{junc} can be obtained by solving $\frac{\partial U}{\partial L_3} = 0$ which leads to the equation

$$\sum_{i=1}^{3} b_i^2 \left(\frac{\partial L_i}{\partial L_3} g\left(\theta_i\right) + L_i \frac{\partial g\left(\theta_i\right)}{\partial L_3}\right) = 0 \tag{6.6}$$

Consequently, the conditions for junction formation depend on neither the shear modulus nor the logarithmic term in the energy.

We shall now describe the mutual force model. The total interaction force between two non-parallel, straight, infinitely long dislocation lines, acting on dislocation (2) due to dislocation (1), is given by

$$\boldsymbol{F}_{12} = \frac{\mu}{|\boldsymbol{l}_1 \times \boldsymbol{l}_2|}\hat{\boldsymbol{R}}_{12}\Bigg(\frac{1}{2}\left(\boldsymbol{b}_1 \cdot \boldsymbol{l}_1\right)\left(\boldsymbol{b}_2 \cdot \boldsymbol{l}_2\right) - \left(\boldsymbol{b}_1 \times \boldsymbol{b}_2\right) \cdot \left(\boldsymbol{l}_1 \times \boldsymbol{l}_2\right) + \frac{1}{1-\nu}\Big[\left(\boldsymbol{b}_1 \times \boldsymbol{l}_1\right) \cdot \hat{\boldsymbol{R}}_{12}\Big]\Big[\left(\boldsymbol{b}_2 \times \boldsymbol{l}_2\right) \cdot \hat{\boldsymbol{R}}_{12}\Big]\Bigg) \tag{6.7}$$

where $\hat{\boldsymbol{R}}_{12} = \boldsymbol{R}_{12}/|\boldsymbol{R}_{12}|$ is the unit vector corresponding to the shortest vector from dislocation (1) to dislocation (2) [293, 193]. This expression is valid when the distance between the two dislocations is much smaller than their lengths. The two dislocations are considered attractive when the criterion

$$\boldsymbol{F}_{12} \cdot \hat{\boldsymbol{R}}_{12} < 0 \tag{6.8}$$

is fulfilled. In this model, the conditions for mutual dislocation attraction or repulsion do not depend on the shear modulus.

We shall now discuss the methodology used to generate the interaction maps. The initial configurations (as shown in figure 6.1) necessary to produce the interaction maps were constructed as follows. Consider two dislocations, respectively denoted (1) and (2), each having the same length and each having a Burgers, normal, and line vector given by $(\boldsymbol{b}_1, \boldsymbol{n}_1, \boldsymbol{l}_1)$ and $(\boldsymbol{b}_2, \boldsymbol{n}_2, \boldsymbol{l}_2)$, respectively, such that their glide planes intersect. Each dislocation consisted of three nodes: two fixed nodes at the endpoints, and one mobile node at the centroid. Due to geometrical and glide constraints, if their collision reaction results in the formation of a junction, it will lie parallel to the line defined by the intersection of the two glide planes, given by $\boldsymbol{n}_1 \times \boldsymbol{n}_2$. First, the two dislocations were positioned parallel to this line, ensuring that they were perfectly aligned and fully overlapping; the centroid of this configuration was identified. Next, each dislocation was rotated about this centroid on its own glide plane by the angles ϕ_1 and ϕ_2, respectively. Note that the $(\phi_1, \phi_2) = (0, 0)$ configuration is always such that the line vectors of both dislocations are equivalent. Next, the centroid nodes of each dislocation were displaced by a distance ϵ_d in the respective directions $\boldsymbol{n}_1 \times \boldsymbol{l}_1$ and $\boldsymbol{n}_2 \times \boldsymbol{l}_2$ such that the final configuration was not intersecting. This final displacement step was conducted to properly resolve and distinguish mildly repulsive states from crossed states; the assignment $\epsilon_d = 10^{-2} r_{\text{ann}}$ was made. It was important that $\epsilon_d < r_{\text{ann}}$ for the purpose of accurately detecting

the outcome of a collision; if $\epsilon_d > r_{\text{ann}}$, then it was difficult to distinguish between a mildly repulsive state or a crossed state with a deterministic algorithm. Otherwise, this parameter was found to have little impact on the visually apparent outcomes of the simulations, which coincides with the findings of other authors [284].

In each simulation, the initial configuration was allowed to evolve until a relaxation criterion was met. The interaction state was determined at each time-step. If the number of 3-nodes[1] was greater or equal to two, the interaction state was determined to be attractive if the junction size was greater than approximately 3 nm; otherwise, the interaction state was determined to be crossed. If the number of 4-nodes was one, the interaction state was determined to be crossed. If the number of 4-nodes was greater or equal to two, the interaction state was determined to be repulsive. If the number of k-nodes where $k \geq 3$ was zero, the interaction state was determined to be repulsive if any of those k-nodes was attached to segments which all had the same normal vector; otherwise, the interaction state was determined to be attractive. The purpose of this final condition was to detect annihilation collisions.

EasyDD was used to conduct the simulations. For each run, the simulation was interrupted after at least one of three cases occurred: (1) the speed of the fastest travelling node became smaller than $3 \times 10^{-1}\,\mathrm{m\,s^{-1}}$, (2) the interaction state was constant for the previous 100 time-steps, or (3) the interaction oscillated substantially between states for the previous 100 time-steps, in which case the interaction was deemed a crossed state. For each interaction map, 20 values for ϕ_1 and ϕ_2 were tested respectively, each ranging uniformly from $-\pi\left(\frac{99}{100}\right)$ to $\pi\left(\frac{99}{100}\right)$, here expressed in radians. The Poisson's ratio corresponding to zirconium, $\nu = 0.32$, was used.

For the line tension model, the values $H = 32.33\,\mu\mathrm{m}$ and $\epsilon_{\text{junc}} = 10^{-4}H$ were used. For each forest interaction type, 100 values for ϕ_1 and ϕ_2 were solved respectively, each ranging uniformly from $-\pi$ to π, here expressed in radians. Equation (6.6) was not solved directly due to analytical difficulties. The MATLAB function `fminbnd` was instead used to numerically solve equation (6.4). Through graphical experimentation, the function $U(L_3)$ was found to be strictly convex within the considered domain. For the mutual force model, 100 values for ϕ_1 and ϕ_2 were evaluated, as before. The shortest distance vector $\boldsymbol{R}_{12}$ was always assigned to be parallel to $\boldsymbol{l}_1 \times \boldsymbol{l}_2$.

Interaction maps, along with the superimposed results from the line tension and mutual force models, are plotted in figures 6.4. The curves corresponding to the line tension model merely delineate domains in which junction formation is favourable—information pertaining to the resulting junction size is not conveyed.

[1] A k-node is a node with k connections.

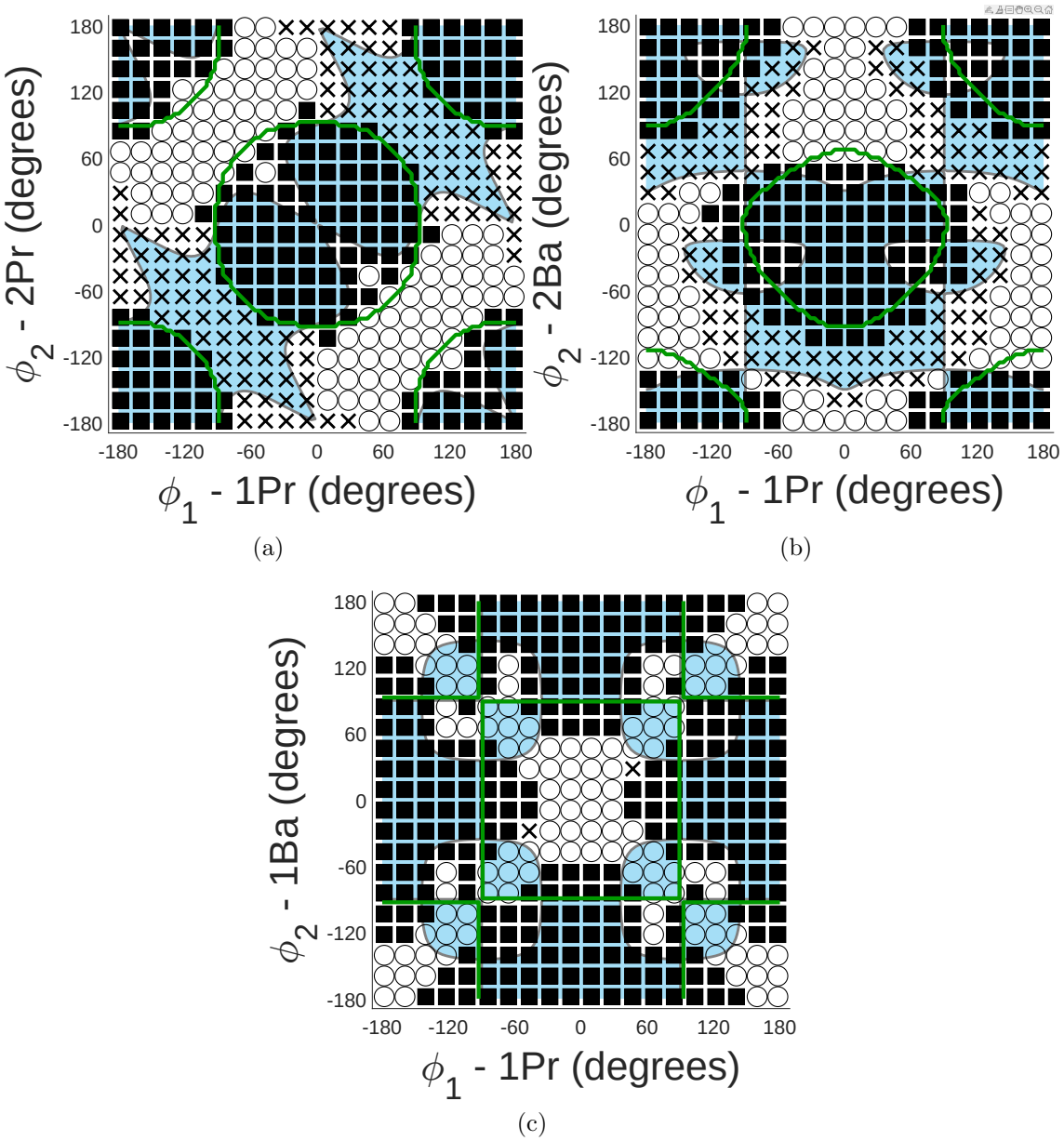
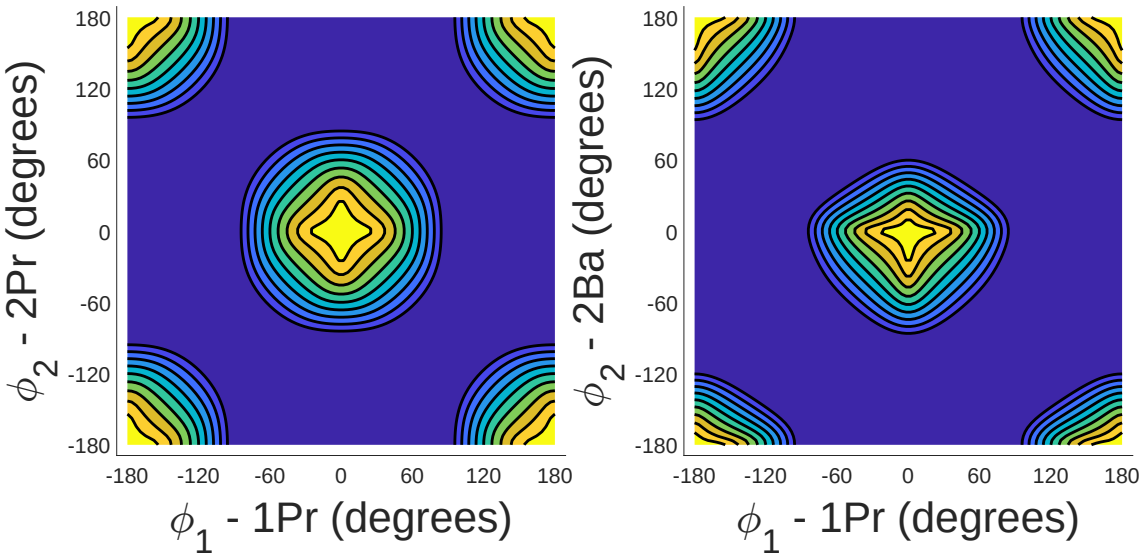
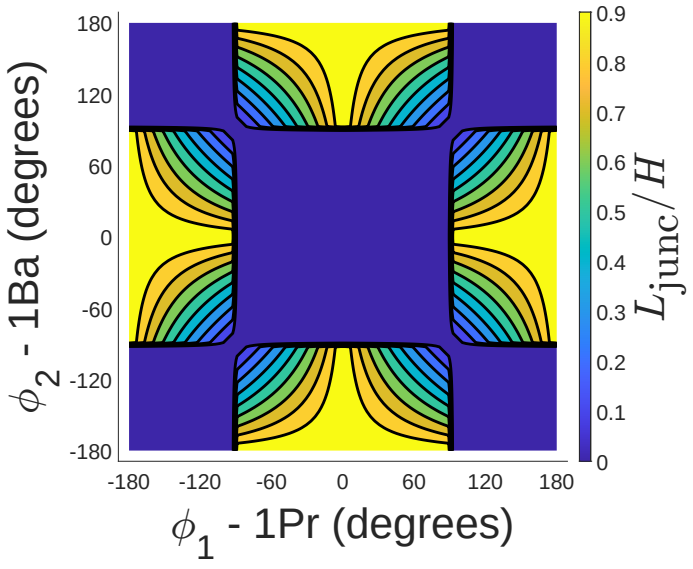


Figure 6.4: Plots containing interactions maps for forest interactions pertaining to the (a) nPr − mPr, (b) nPr − mBa, and (c) nPr − nBa slip systems. Filled rectangles, crosses, and empty circles respectively represent attractive, crossed, and repulsive states. The blue regions are attractive in the mutual force model; the gray lines delineate the blue regions. The green lines delineate regions in which junction formation is favourable in the line tension model.



(a) (b)



(c)

Figure 6.5: Contour plots containing junction size maps predicted by the line tension model for forest interactions pertaining to the (a) $n\text{Pr} - m\text{Pr}$, (b) $n\text{Pr} - m\text{Ba}$, and (c) $n\text{Pr} - n\text{Ba}$ slip systems. The final junction length L_{junc} is normalised with respect to the initial length of the dislocations H. The colour bar next to plot (c) applies to all three contour plots.

Therefore, these are hereafter referred to as *binary junction maps*. The $n\text{Pr} - m\text{Pr}$ case (figure 6.4a), the $n\text{Pr} - m\text{Ba}$ case (figure 6.4b), and the $n\text{Pr} - n\text{Ba}$ case (figure 6.4c) are plotted. The results agree very closely with interaction maps calculated for other HCP materials with similar or identical Poisson's ratios [129, 173]. For most interactions, the line tension model very accurately predicts regions corresponding to favourable junction formation. The mutual force model also predicts these regions. It is also evident that regions with crossed states correspond very closely with regions where the mutual force model is attractive and the line tension model simultaneously predicts no junction formation. This acts as a suitable validation of the results obtained from the DD simulations.

Note that, in the $n\text{Pr} - n\text{Ba}$ case, the alignment of the elastic solution predictions with the simulation results is not as clear. Upon further investigation it was found that, during these forest interactions, dislocations tend to significantly bend and twist to annihilate and minimise their energy. Dislocation lines are able to undergo local rotations which deviate up to approximately 40° from the rigid line model. Most visible deviations from the model predictions can plausibly be explained as arising due to this phenomenon.

The junction strength is determined in a probabilistic sense by the ratio of the number of junction formation occurrences to the total number of tested configurations. The interactions are given in order of increasing junction formation probability by $n\text{Pr} - m\text{Ba}$, $n\text{Pr} - m\text{Pr}$, and $n\text{Pr} - n\text{Ba}$, which is consistent with literature findings from similar HCP materials [173]. All interaction maps exhibit a periodic horizontal and vertical translational symmetry of 2π. For both the $n\text{Pr} - m\text{Pr}$ and $n\text{Pr} - n\text{Ba}$ cases, the two diagonals are additional lines of reflective symmetry, and hence initial condition (ϕ_1, ϕ_2) is equivalent in reaction outcome to initial condition (ϕ_2, ϕ_1). As has been noted by Devincre *et al.* [173] for the case of HCP ice, and as is also seen from figure 6.4b, this symmetry is not present in the $n\text{Pr} - m\text{Ba}$ case. Consequently, it is expected that there is an asymmetry with respect to the interaction coefficients corresponding to the basal-prismatic interaction, i.e. $a_{ij} \neq a_{ji}$.

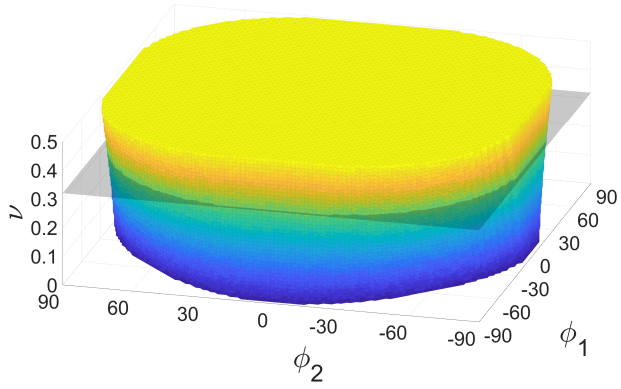
Junction sizes were not tracked during the simulations conducted in this text. However, predicted junction sizes were calculated using the line tension model. In figures 6.5, maps of the normalised junction sizes L_{junc}, hereafter referred to as *junction size maps*, are plotted as functions of ϕ_1 and ϕ_2 in a similar format to the previously presented interaction maps. By simple observation of the plots, the interactions are given in increasing order of junction formation probability by $n\text{Pr} - m\text{Ba}$ (figure 6.5b), $n\text{Pr} - m\text{Pr}$ (figure 6.5a), and $n\text{Pr} - n\text{Ba}$ (figure 6.5c),

which coincides with the results inferred from figures 6.4. In the junction size maps, some asymmetry is revealed which cannot be inferred from the binary junction maps alone. All junction size maps exhibit contour shapes resembling a four-pointed star which share the same class of symmetry as the corresponding binary junction maps.

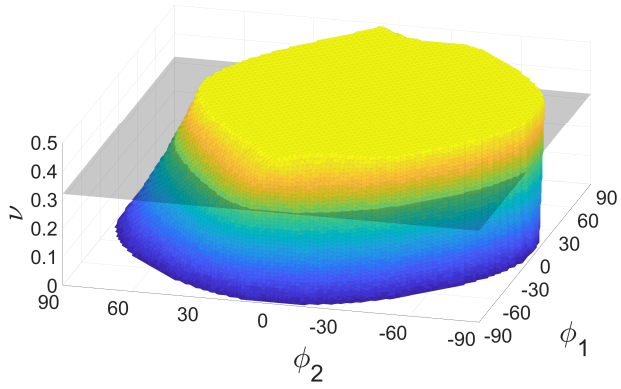
Because the Poisson's ratio parametrises the orientation-dependence via the function g from expression (6.2), it is expected that the symmetry of binary junction maps will increase as ν decreases to zero. The dependence of binary junction maps on the Poisson's ratio was determined via the following procedure. For each value of the Poisson's ratio, a binary junction map was generated as before, which consisted of a set of points (ϕ_1, ϕ_2) within a 2D domain, each of which corresponded to a binary value indicating whether that point corresponded to a junction formation or not. This was performed for a continuous range of Poisson's ratios, thereby creating a set of points within a continuous 3D domain, denoted $\mathcal{A}_\alpha$. The MATLAB function `alphaShape` was used to compute the alpha shape corresponding to $\mathcal{A}_\alpha$. An alpha shape is a generalisation of a convex hull—it is a surface which envelops a set of points [294]. The alpha shape is parametrised by a single parameter known as the alpha radius. As the alpha radius approaches infinity, the alpha shape progressively becomes decreasingly non-convex until it eventually converges to the convex hull. The alpha radius was chosen such that it corresponded to an alpha shape which enclosed the smallest possible volume such that it enclosed all of the points contained within the set $\mathcal{A}_\alpha$. As a result of the discretisation method, all of the produced alpha shapes were non-convex.

For each alpha shape, 40 values of the Poisson's ratio, ranging uniformly from 0 to 0.5, were solved. 100 values for ϕ_1 and ϕ_2 were solved respectively, each ranging uniformly from $-\pi/2$ to $\pi/2$. Note that the resulting alpha shape of the $n\text{Pr} - n\text{Ba}$ case was translated by $\phi_1 = \pi$ so that the resulting plot depicts all of the relevant interaction information. This is equivalent to assuming that both dislocations have opposite line directions when $(\phi_1, \phi_2) = (0, 0)$.

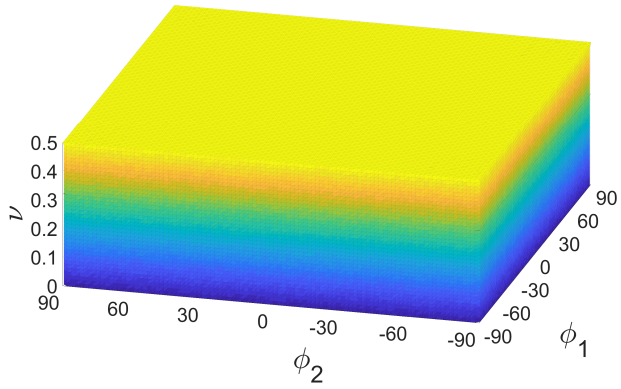
The alpha shapes corresponding to the three typical forest interactions are plotted in figures 6.6. All plots exhibit a periodic translational symmetry of 2π in both ϕ_1 and ϕ_2, as in previous plots. The conditions for junction formation vary in sensitivity with respect to the Poisson's ratio for the different forest interactions. The $n\text{Pr} - n\text{Ba}$ case (figure 6.6c) is completely insensitive to ν. The $n\text{Pr} - m\text{Pr}$ case (figure 6.6a) is only slightly sensitive to ν; as ν decreases, junction formation becomes less likely. In contrast, the $n\text{Pr} - m\text{Ba}$ case (figure 6.6b) is fairly sensitive to ν; as ν decreases, junction formation becomes more likely. In both the $n\text{Pr} - m\text{Pr}$ and $n\text{Pr} - m\text{Ba}$



(a)



(b)



(c)

Figure 6.6: Plots containing binary junction maps represented as alpha shapes corresponding to forest interactions of the (a) nPr $-$ mPr, (b) nPr $-$ mBa, and (c) nPr $-$ nBa slip systems. The colours correlate to the magnitude of the Poisson's ratio ν. The black translucent rectangular plane represents the cross section corresponding to the Poisson's ratio of Zr ($\nu = 0.32$).

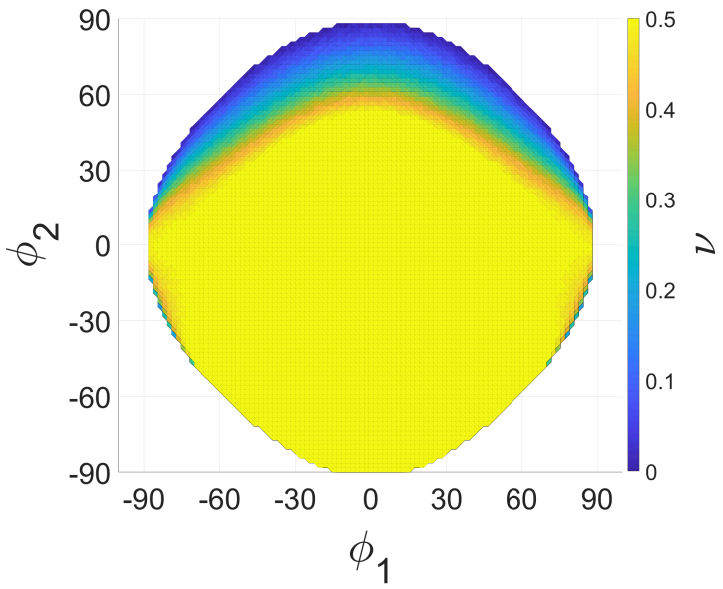


Figure 6.7: Plot containing a binary junction map represented as an alpha shape for the nPr $-$ mBa slip system interaction. The axes are shown in units of degrees. This plot holds the same information as in figure 6.6b, but is shown from a different perspective.

cases, their respective junction maps become increasingly symmetric as ν decreases, becoming completely radially symmetric at $\nu = 0$ (see figure 6.7). Therefore, as a rough approximation, it is expected that as the Poisson's ratio decreases, the nPr $-$ mBa forest interactions become stronger, while the other two interactions are minimally affected.

6.2 Methodology

6.2.1 Experimental setup

The experiment consisted of a uniaxial tensile test of a $L_x \times L_y \times L_z = 17\,\mu\text{m} \times 5\,\mu\text{m} \times 5\,\mu\text{m}$ cuboid sample of single crystal α-Zr, where L_x, L_y, and L_z are the dimensions of the sample in the x, y, and z directions, respectively. Upon being selected, the sample was chemically verified to be pure Zr ($\sim 100\%$). Subsequently, the sample was placed in storage where it was exposed to air at room temperature. The experiment was conducted under a vacuum at room temperature. The test was conducted three times on three separate samples of identical composition, size, and orientation. Figure 6.8 displays the stress-strain plots associated with these tests. The strains were determined using digital image correlation (DIC) [295]. For strains

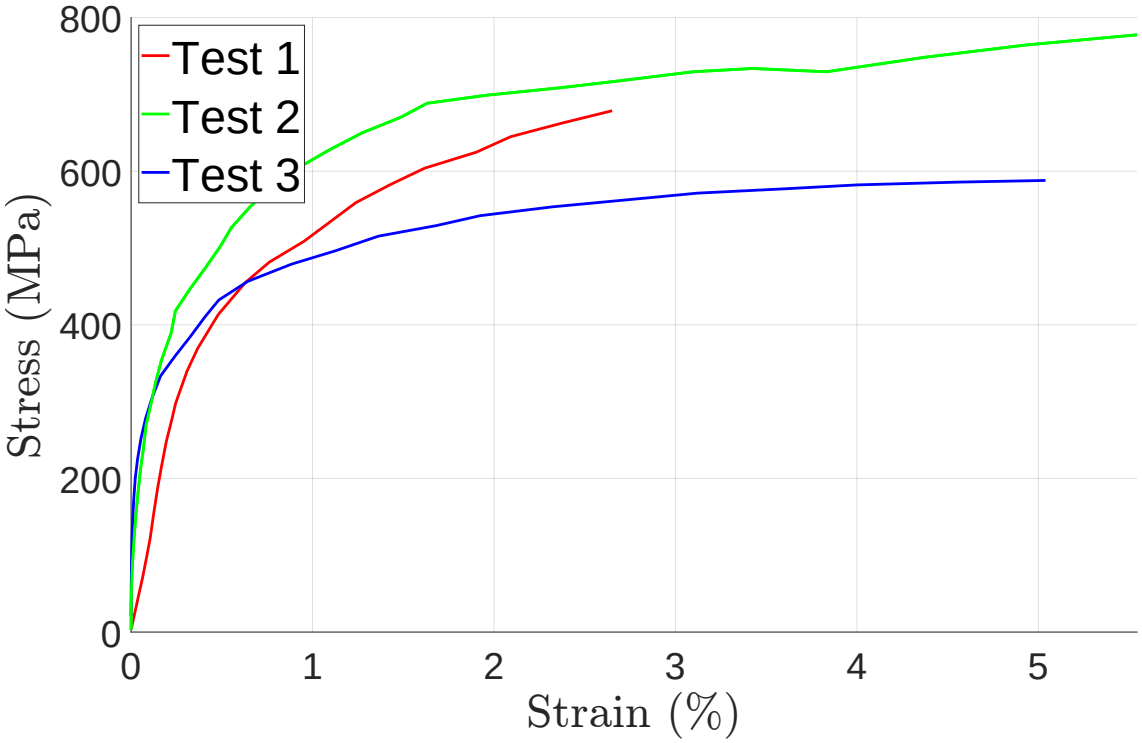


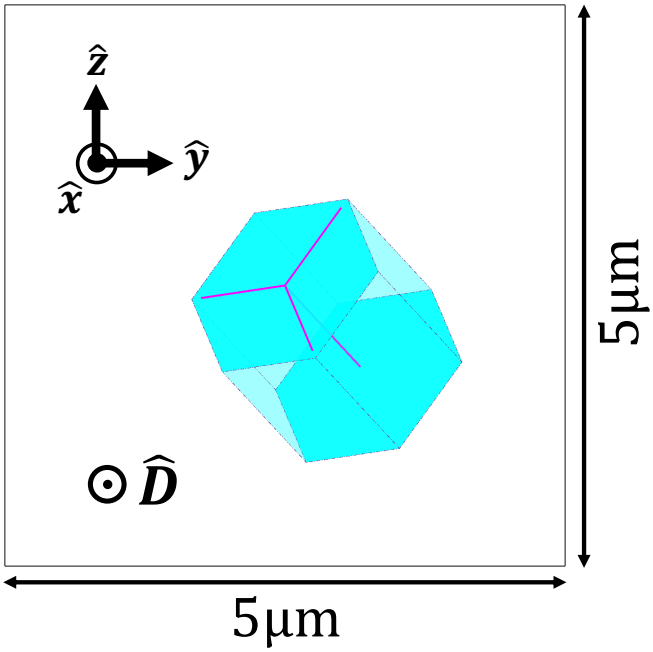
Figure 6.8: Plots containing stress-strain curves obtained from the tensile test experiments.

less than 0.3%, which lay mostly in the elastic regime, the resolution of DIC was not sufficiently fine to accurately determine the displacements. This is why there appears to be a large discrepancy in the behaviour of the stress-strain curves below this strain. In a future work, regions where the strain is below 0.3% will be combined together with the plastic region using the experimental value for the Young's modulus. Table 6.1 contains experimental variables associated with the tensile tests.

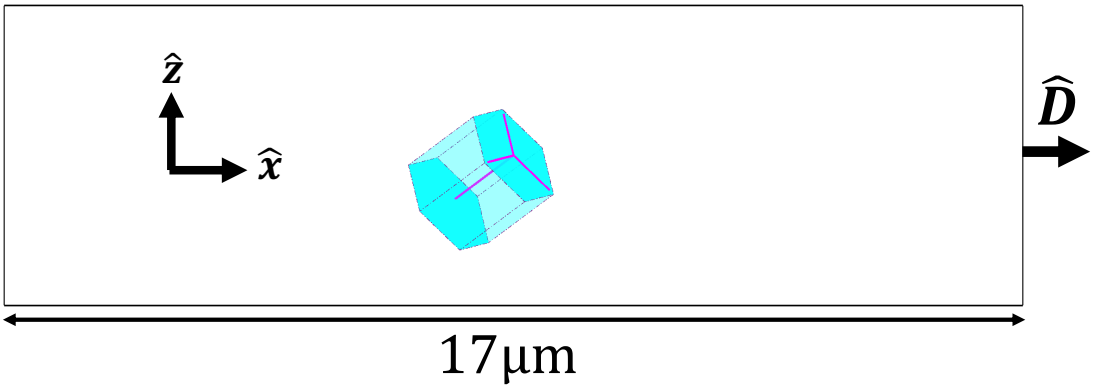
The HCP-based crystal orientation with respect to the sample and the laboratory coordinate system is as shown in figure 6.9. The loading direction $\hat{\boldsymbol{D}}$ is parallel to the $\hat{\boldsymbol{x}}$ axis. Using the extrinsic XYZ convention, the Euler angles are given by $\gamma_1 = 36°$, $\gamma_2 = 150.2°$, and $\gamma_3 = 8.5°$. The rotation matrix R_{ss} used to transform the crystal orientation is given by

$$R_{\text{ss}} = R_x(\pi/2)R_y(\pi/2)R_z(0)R_z(\gamma_3)R_y(\gamma_2)R_x(\gamma_1) \tag{6.9}$$

where $R_i(\theta)$ is the standard rotation matrix which rotates vectors by angle θ anti-clockwise about the i-axis. The first three rotation matrices in the product shown in equation (6.9) are not associated with the Euler angles, but are necessary to rotate the coordinate system into the one used in the experiment. The schmidt factors [296] for some relevant slip systems are given in table 6.2.



(a)



(b)

Figure 6.9: Setup of the geometry and crystal orientation for the zirconium tensile test. The hexagonal prism represents the orientation of the HCP crystal axes.

Variable	Test 1	Test 2	Test 3
Yield stress (MPa)	434.2	460.3	383.1
Failure stress (MPa)	678.7	777.6	587.9
Failure strain (m/m)	2.651×10^{-2}	5.544×10^{-2}	5.039×10^{-2}
Strain rate (s^{-1})	3.150×10^{-5}	3.876×10^{-5}	4.590×10^{-5}
Young's modulus (GPa)	125.1	103.1	100.8

Table 6.1: Table containing experimental data variables pertaining to the conducted tensile tests.

	Ba	Pr	PyI	PyII
$\boldsymbol{b}_1$	0.1357	0.1324	0.0516	0.1812
$\boldsymbol{b}_2$	0.3489	0.2535	0.3893	0.0561
$\boldsymbol{b}_3$	0.4846	0.1210	0.3378	0.1251

Table 6.2: Table containing Schmidt factors of different slip systems. Note that the PyI and PyII slip systems are not modelled in this text.

Since $\langle a \rangle$-type screw dislocations preferentially dissociate on prismatic planes due to a lower stacking fault energy, basal slip is believed to be largely mediated by thermally activated cross slip events, the rate of which increases with temperature [120, 122, 182]. Furthermore, basal-to-prismatic cross slip is energetically favourable, whereas prismatic-to-basal cross slip involves a large activation barrier [182]. Experiments [131] and DD modelling including cross slip [82] have shown that prismatic slip dominates at room temperature, while the basal slip fraction increases with increasing temperature. Therefore, for modelling purposes it is expected that basal slip can be largely neglected. Furthermore, experimental and *ab initio* evidence suggests that the rate-controlling mechanism of $\langle a \rangle$-type prismatic screw dislocations is pinning by oxygen atoms [297, 126, 111] and that, in pure Zr, the mobilities of edge and screw dislocations are otherwise athermal and comparable [120, 118]. Because the experimental sample contained very little oxygen content (and the oxygen diffusion coefficient in Zr is small [298]), a thermally activated mobility law was not used in this text.

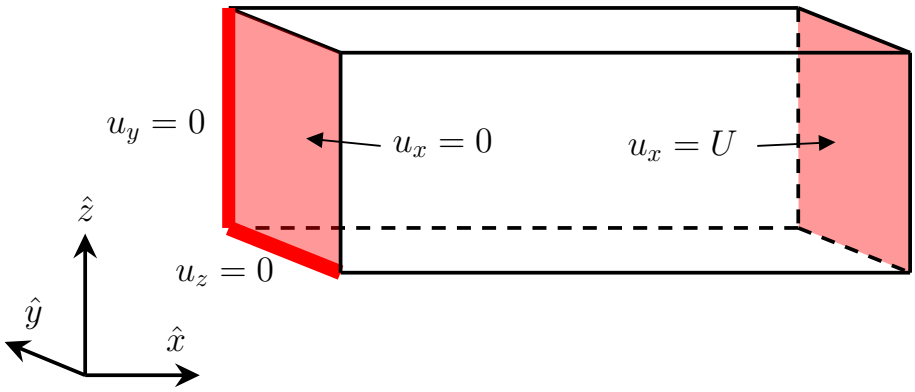


Figure 6.10: Schematic of the FE geometry used in the simulations conducted in this chapter. The two red planes are faces at which boundary conditions (6.10) and (6.11) are respectively applied. The two thick red lines are regions at which boundary conditions (6.12) and (6.13) are respectively applied.

6.2.2 Simulation setup

All simulations were conducted using EasyDD. The FE domain geometry was the same as that of the experiment: a cuboid with dimensions $L_x \times L_y \times L_z = 17\,\mu\text{m} \times 5\,\mu\text{m} \times 5\,\mu\text{m}$. The number of FE nodes in the x, y, and z directions are respectively given by N_x, N_y, and N_z. The boundary conditions were enforced in a manner which most accurately represented the experimental conditions. The applied displacement boundary conditions are given by

$$u_x\left(0, y, z\right) = 0 \tag{6.10}$$

$$u_x\left(L_x, y, z\right) = U \tag{6.11}$$

$$u_y\left(0, L_y, z\right) = 0 \tag{6.12}$$

$$u_z\left(0, y, 0\right) = 0 \tag{6.13}$$

The lateral boundary conditions (6.12) and (6.13) were introduced to enforce the symmetric deformation of the defect-free cuboid with respect to the plane orthogonal to the longitudinal axis that bisects the cuboid, and to prevent non-uniform contraction in the transverse directions. This avoids rigid body rotations and generates a uniform uniaxial tensile stress. All remaining degrees of freedom are subject to zero-traction (i.e. stress-free) boundary conditions. The geometry and boundary conditions are illustrated in figure 6.10.

Figure 6.11 provides a schematic representation of the spatial domains relevant to the experimental configuration. The region shaded in red, denoted V_1, represents the subdomain which is explicitly modelled by the 3D DD simulations conducted in

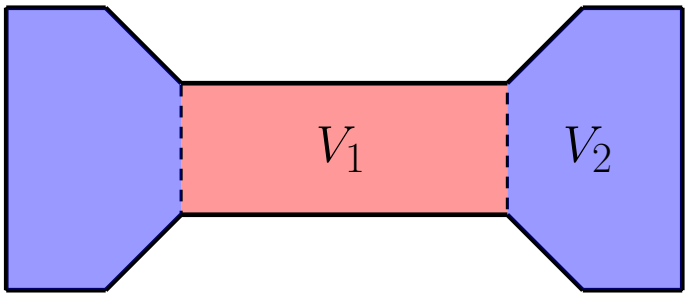


Figure 6.11: Schematic of a cross section of the specimen used in the experiment. The subdomain modelled by the DD simulations is filled in red and denoted V_1. The rest of the bulk of the specimen, which is not modelled by the DD simulations, is filled in blue and denoted V_2. In this figure, the loading direction is parallel to the longitudinal axis.

this chapter. The region filled in blue, denoted V_2, represents the remainder of the specimen domain. In the simulations, dislocations were permitted to exit through all surfaces of subdomain V_1 except for displacement-controlled surfaces (represented as dotted lines in figure 6.11). Within the model, any dislocation that collides with a displacement-controlled surface of V_1 becomes permanently fixed, which results in hard dislocation pile-ups. In contrast, during the physical experiment, a dislocation that migrates from V_1 into V_2 does not become fixed, but instead continues to traverse through the bulk while exerting mechanical influence—such as long-range stress fields—on the dislocation network within V_1. Furthermore, since the loading stress field is lower in V_2, soft dislocation pile-ups occur in this region. As a result, this discrepancy introduces an error to the model. Specifically, the treatment of the displacement-controlled faces as fully impenetrable is expected to lead to an underestimation of dislocation mobility in the simulations. However, since only a relatively small fraction of the dislocation network is expected to evolve near these surfaces during a typical simulation, the impact of this discrepancy on the overall dislocation behaviour should remain fairly limited.

In EasyDD, dislocations are typically first generated by a distribution of prismatic loop sources, each of which is associated with a single slip system. A prismatic loop source is a square prismatic loop with side length L_s wherein two parallel sides are fixed, and the remaining two parallel sides (which belong to the desired slip system) are free, as shown in figure 6.12. Prismatic loop sources are used instead of standard Frank-Read sources, which consist of a straight segment with two fixed ends, because dislocation-induced displacement related algorithms in EasyDD (see section 3.6.3) are specifically designed to operate on dislocations that form closed loops. The result

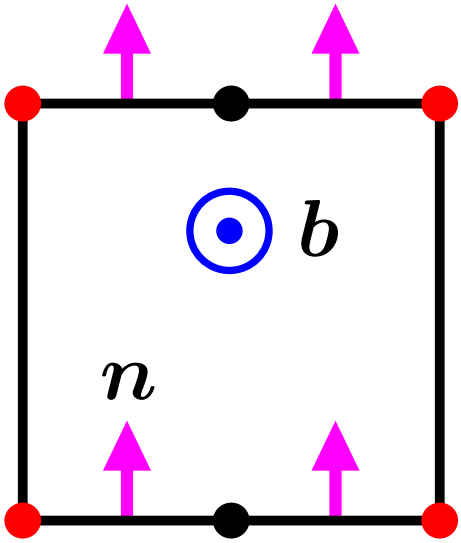


Figure 6.12: Schematic of a prismatic loop source. The red and black nodes are respectively fixed and mobile. The magenta arrows and blue annulus with a central disc respectively represent the normal vectors and Burgers vector of the active slip systems of the source.

is that, when the resolved shear stress is sufficiently large, the source acts as a pair of Frank-Read sources and generates dislocations in the desired slip system via the Frank-Read mechanism [299]. The size (or length) L_s and number N_s of sources are two parameters which can greatly impact the simulation output. The size of the source is related to the stress required for its activation σ_s via the Frank-Read generation criterion given approximately[2] by

$$L_s = \frac{2\mu b}{m\sigma_s} \tag{6.14}$$

where m is the Schmidt factor of the associated slip system, the list of which is given by table 6.2. The simulations conducted in this chapter always use prismatic loop sources to initialise the dislocation network. In a given simulation, all sources are of the same size. Note that, because $L_{\max} < L_s$ must be satisfied to allow for source nucleation, increasing the source size L_s permits a larger $L_{\max}$, which reduces the degrees of freedom of the simulation.

Although the use of isolated Frank-Read sources to initialise the dislocation structure is ubiquitous in the literature [129, 301, 302, 84, 249, 303, 304], they introduce unphysical artefacts such as increased network stabilisation [305] and the

[2]The exact form of the criterion depends on the underlying model, with predictions usually varying by up to a multiplicative constant of order unity [300]; equation (6.14) is the prediction of the simple line tension model [197].

inability to model dislocation starvation [306, 307] in finite domains. Some DD studies [308, 305, 309, 82] have instead generated the initial dislocation network through a relaxation procedure described as follows. A population of pinning point free (often straight, mobile, and surface-terminating) dislocations of varying orientation and slip system is introduced into the domain. This dislocation network is allowed to relax under zero applied loading until it reaches an equilibrium motionless state. This relaxed configuration is then used as the initial dislocation network for a virtual experiment. This is a more realistic method of constructing an initial network, and it avoids issues pertaining to the physical interpretation of the number N_s and size L_s of dislocation sources. In addition, the relaxation method reduces the coupling of the source size with the network resolution. However, it is challenging to implement in EasyDD due to the necessity of a proper treatment of virtual segments and their orientations in the pre-relaxed network. Although isolated Frank-Read sources are unphysical, DD studies [305] have shown that relaxed dislocation networks in finite domains exhibit highly stable pinning-like points which can be activated multiple times and are thus comparable to isolated Frank-Read sources. Furthermore, it has been reported that, for the same initial relaxed dislocation densities, these two approaches have yielded similar size-dependent macroscopic responses in some cases [305, 310].

Note that, since prismatic loop sources are usually never destroyed during a typical simulation, this method of introducing dislocations leads to permanent localised shear deformation along the planes defined by the initial source position; this phenomenon becomes increasingly pronounced as the dislocation density decreases. The artificial fixed segments of small sources will have a small impact on simulations. However, as the source size and number increases, the fixed segments will increasingly contribute a stress that acts on other dislocations and on the traction surfaces. Furthermore, the investigations conducted in chapter 5 imply that, to first order, the elastic interactions involved in the prismatic loop may act to decrease the activation stress of the source, and that this softening effect should be more pronounced for smaller sources. To avoid spurious hardening or softening effects, the stresses produced by the fixed segments are therefore disabled in some (but not all—it will be explicitly stated if so) of the simulations conducted in this chapter. On the other hand, these segments always contribute to the displacement calculation; however, since the sources are usually positioned away from the displacement faces, this will have a small impact.

Within the plastic flow regime (characterised by a nearly constant applied/flow stress), Fan *et al.* [309] developed a strain rate dependent plasticity model for the

resolved shear stress τ required to sustain plastic slip (e.g. at yield) given by

$$\tau = \frac{B\dot{\epsilon}}{m f_a \rho b^2} + \alpha \mu b \sqrt{\rho} \tag{6.15}$$

where $\dot{\epsilon}$ is the strain rate, B is the drag coefficient, m is the average or effective Schmidt factor, and f_a is the proportion of the dislocation density that is on active slip systems. This model has been validated against a range of FCC single crystal experiments [309]. The first and second terms are respectively the drag-controlled and Taylor hardening terms. At low dislocation densities, large crystal sizes, and high strain rates (known as the strain rate hardening regime), the drag-controlled term dominates. As the strain rate decreases and/or the dislocation density increases, strengthening processes become increasingly forest-dominated and the resolved shear strength follows a Taylor hardening power law (equation (1.1)). Equation (6.15) can be expressed equivalently in terms of the dimensionless parameters $\mathcal{P}$ and $\mathcal{T}$ via

$$\mathcal{T} = \frac{\tau \left(m f_a\right)^{1/3}}{\mu^{2/3} \left(B\dot{\epsilon}\right)^{1/3}} = \frac{1}{\mathcal{P}} + \alpha \sqrt{\mathcal{P}} \tag{6.16}$$

$$\mathcal{P} = \left(\frac{m f_a \mu b^3}{B}\right)^{2/3} \frac{\rho}{\dot{\epsilon}^{2/3}} \tag{6.17}$$

Here, $\mathcal{P}$ parametrises the transformation between the strain rate hardening regime ($\mathcal{P} < 1$), the Taylor hardening regime ($\mathcal{P} > 10$), and a transition regime ($1 < \mathcal{P} < 10$).

On the other hand, it is understood that at low dislocation densities and small crystal sizes (known as the source strengthening regime), size effects become significant and the crystal strength can in part be governed by the activation of the weakest dislocation sources [311, 256, 310], indicating that the distribution of L_s is very impactful. A complete understanding of crystal size effects with respect to dislocation-mediated plasticity has not yet been established [312]. Two explanations of size-dependent strengthening that are broadly accepted in the literature are provided as follows. First, the dislocation starvation model [306, 313] proposes that smaller crystals contain fewer sources, leading to mobile dislocations exiting free surfaces in discrete strain bursts faster than they can multiply. Second, the source truncation model [255, 314] proposes that smaller crystals contain shorter sources, leading to higher activation stresses. Experimental [315] and DD [302, 255] studies have reported that, for sufficiently small (usually sub-micron) domain sizes, Frank-Read sources can intersect free surfaces as they expand, thereby becoming single arm sources with decreased effective lengths and thus increased activation stresses. Furthermore, 2D DD studies have confirmed that the flow stress increases with decreasing crystal size

until a critical point is reached, below which source strengths dictate the flow stress [316, 317].

Several experimental [318, 319] and DD [302, 65] studies have proposed a size-dependent relationship describing the flow stress τ with a form given by

$$\tau = \frac{A}{\left(D\sqrt{\rho_s}\right)^q} + \tau_0 \tag{6.18}$$

where $\rho_s = N_s/V$ is the volumetric source density (with domain volume V), D is a characteristic length of the domain, q is a fitting parameter, and A is a constant that depends on the material, boundary conditions, and strain rate. The second term, τ_0, represents the limiting size-independent flow stress, which may include other strengthening effects such as a Taylor hardening term (equation (1.1)). Notably, 2D DD modelling has been used to ascertain that $q \approx 1$ for prismatic slip in HCP Zr in the case of cantilever bending [65].

Tang *et al.* [302] conducted a 3D DD investigation of the size dependence of micron and sub-micron scale FCC single crystal micro-pillars under compression at a high strain rate on the order of $10^5\,\mathrm{s}^{-1}$. Using isolated Frank-Read sources (as in this text), the authors identified a regime in which the flow stress depends solely on the source density in a manner that is independent of the source strength. In this regime, the system follows the relationship given by equation (6.18), with $q = 1$. They further reported that, once the average source strength exceeds a critical threshold, it begins to influence—or, if sufficiently strong, nearly entirely control—the flow stress.

More recently, El-Awady [310] applied 3D DD simulations using pinning point free dislocation networks to investigate FCC Ni single crystals under compression. The simulations revealed a size-dependent flow relationship—validated against a variety of micron and sub-micron single crystal experiments—given by

$$\tau = \frac{\beta\mu}{D\sqrt{\rho}} + \tau_0 \tag{6.19}$$

where ρ is the dislocation density[3] and β is a dimensionless constant that depends on the boundary conditions, crystallography, slip mobility, strain, and strain rate[4]. The first term effectively represents the strength of the weakest source [310].

[3] In the 3D DD simulations conducted by El-Awady [310], the dislocation density ρ was found to vary from its initial value ρ_0 by less than a factor of three below less than approximately 1% strain. Therefore, the author assumed that the dislocation density remains roughly constant.

[4] It has been determined via 3D DD simulations that $\beta \sim 10^{-3}$ for FCC Ni undergoing athermal slip [310]. Since prismatic-only slip in HCP Zr is in some ways analogous to slip in FCC materials [82], β may have a similar order of magnitude when restricted to these slip modes.

When the dislocation network is initialised using isolated prismatic loop sources, the initial dislocation density is $\rho_0 = 2\rho_s L_s$. Under these conditions, equation (6.19) exhibits the same form as equation (6.18) when the source length is fixed and size-independent terms are neglected. However, equation (6.19) also implies a dependence on L_s that is absent from equation (6.18). It should be noted that pinning point free dislocation networks exhibit complex evolving source distributions, characteristics, and mechanisms [308, 256] which cannot be fully captured by isolated Frank-Read sources. Furthermore, 3D DD simulations of small (especially sub-micron) crystals containing such networks often exhibit significant scatter, reflecting the statistical variability of source mechanisms [308, 305]. Consequently, the precise mechanistic connection between the formulations provided by equations (6.18) and (6.19) is complex and not entirely understood. Nonetheless, isolated Frank-Read sources remain valuable for simplifying and enabling the isolation, identification, and clarification of mechanisms involved in source-limited and size-dependent plasticity.

As discussed by El-Awady [310], by relating the first term in equation (6.19) with the stress necessary to operate a source (equation (6.14) up to a multiplicative constant), their model predicts that, in the source strengthening regime, the effective (mean) source size λ in a dislocation network at the onset of plastic flow is given by

$$\lambda = \frac{bD\sqrt{\rho_0}}{\beta} \tag{6.20}$$

where ρ_0 is the initial dislocation density. Although it is not immediately clear how the number N_s and size L_s of sources should be selected and related to maintain physical consistency, the model above provides sufficient information to derive a closing constraint. Initialising the network using isolated prismatic loop sources results in $\rho_0 = 2L_s N_s / D^3$, where a volume of $V = D^3$ is assumed. Furthermore, suppose one assumes that $\lambda = L_s$, i.e. that the Frank-Read source sizes represent the sizes of naturally forming pinning point free sources that are distributed within the relaxed dislocation network. It follows that, if one demands that the isolated Frank-Read source method be consistent with this size-dependent plasticity model, the source number and size must be

$$N_s = \frac{D^2\beta}{2b}\sqrt{\rho_0} \quad \text{and} \quad L_s = \frac{bD}{\beta}\sqrt{\rho_0} \tag{6.21}$$

For example, if one supposes a characteristic size of $D = (L_x L_y L_z)^{1/3} \approx 7.5\,\mu\text{m}$, an initial dislocation density of $\rho_0 = 10^{11}\,\text{m}^{-2}$, and $\beta = 10^{-3}$, the source number and mean source size must respectively be $N_s \approx 31$ and $L_s \approx 0.8\,\mu\text{m}$ to be consistent

with this model. Although some of the simulations conducted in this chapter roughly fulfill these constraints, they will not be strictly imposed since (1) a precise estimation (based on numerical studies or otherwise) of β for HCP Zr is not available at the time of writing and (2) we are not currently aiming to probe precise size-dependent relationships.

The strain rate is typically one of the largest bottlenecks in producing simulations which are able to access sufficiently large strains. As the strain rate decreases, the simulation increasingly approaches a quasistatic[5] loading state. In this state, dislocations are effectively always at equilibrium with respect to the time scale of the loading rate, and their velocities are on average low. As the strain rate increases at low dislocation densities, the dislocation velocity on average increases. Furthermore, as the strain rate increases, so does the prevalence of additional physical phenomena such as relativistic effects associated with high speed dislocations [320] and specimen acceleration [321], which are not incorporated in this text. For some purposes, dislocation inertia has been shown to be important at strain rates above $10^5\,\mathrm{s}^{-1}$ [322]. As implemented by some DD models [323, 309], high velocity (though still non-inertial) dislocation kinetics can be partially captured without incorporating a full elastodynamic simulation by applying a nonlinear (sometimes parameter-free) relativistic correction to the over-damped dislocation velocity that imposes an asymptotic upper bound given by the transverse sound wave velocity c_s [320, 324, 225] and that reduces to the linear mobility law at low velocities. DD studies [325, 322] have reported that, even at high strain rates ($> 10^6\,\mathrm{s}^{-1}$), only a small fraction of dislocations attain velocities near the transverse sound wave velocity. Therefore, a linear mobility law is expected to be adequate for many applications involving non-quasistatic loading conditions.

One purpose of the simulations conducted in this chapter is to calibrate the 3D DD model to the experiment by attempting to replicate the produced stress-strain plots. In principle, all of the DD parameters can affect the calibration, but, in practice, some are more important than others. The physical parameters, such as the Poisson's ratio and shear modulus, should be obtained based on data available for zirconium. The choice of most of the computational parameters, such as the minimum and maximum length of segments, should be supported by physical reasoning when

[5]In this text, the word "quasistatic" is used in two distinct ways: when the time scale associated with dislocation evolution is (1) much longer than that of elastic wave dissipation or (2) much shorter than that of the loading rate. When any confusion is possible, the latter is referred to as *quasistatic loading*.

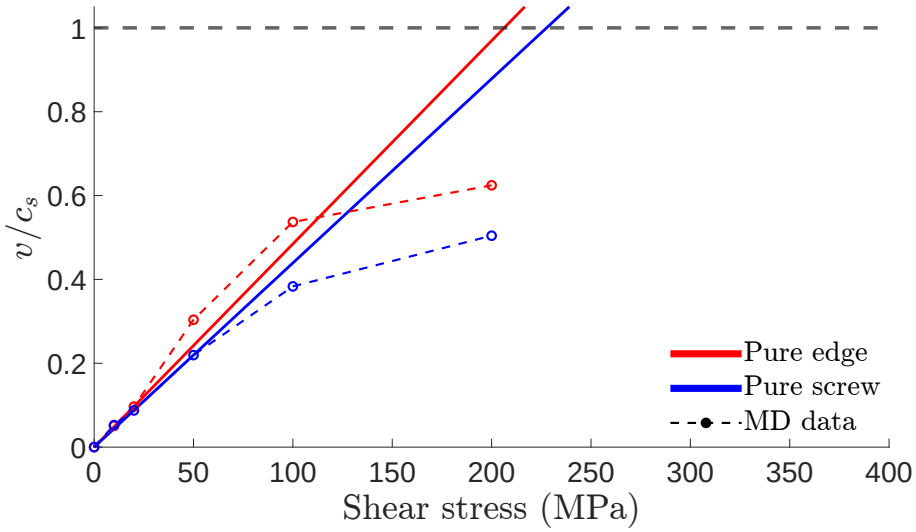


Figure 6.13: Dislocation velocity magnitude v normalised with respect to the prismatic transverse sound wave velocity $c_s = 2.3\,\mathrm{km\,s^{-1}}$ as a function of resolved shear stress for $\langle a \rangle$-type prismatic edge (red) and screw (blue) dislocations in pure Zr at room temperature. The linear mobility law is represented as solid lines, and the respective MD data points [120] are plotted for comparison.

possible, although they are often selected on an ad hoc basis. On the other hand, some parameters can be obtained via convergence testing.

Because α-Zr exhibits an HCP crystallographic phase, the HCP mobility law described in chapter 4 is used. Figure 6.13 compares this linear mobility law (using mobility parameters from table 6.3) with MD data pertaining to prismatic slip in pure Zr at room temperature; the prismatic transverse sound wave velocity is approximately $c_s = 2.3\,\mathrm{km\,s^{-1}}$ [120]. The corresponding velocities involved in the basal plane are not shown here, but are very similar when an athermal drag-based mobility is assumed [120]. Due to the spatially uniform nature of the stress associated with uniaxial tensile tests, the results of sections 4.3 and 4.4 are highly relevant for simulations conducted in this chapter. All conducted simulations use the parameter selection $(\eta, R_l) = (2, 1)$ for the various reasons given in the aforementioned chapter. The remaining most important parameters used in the simulations are equivalent to those presented in table 6.3 unless stated otherwise. Note that, in this text, the Burgers vector magnitude $|\boldsymbol{b}| = b$ is always equivalent to the lattice constant a.

6.2.3 Bug mitigation

EasyDD is a code which is in ongoing development and, as such, still contains some significant bugs. Certain computational parameters were chosen specifically

Material parameters
$\mu = 36.2\,\mathrm{GPa}$ [326]
$\nu = 0.336$ [326]
$a = 3.233\,\text{Å}$ [85]
$c/a = 1.593$ [85]
$r_c = 10a$
$E_s^c = 0.125\,\mathrm{eV\,Å}^{-1} \approx 0.05\mu b^2$ [122]
$B_{\mathrm{screw}}^{\mathrm{glide}}(\mathrm{Ba}) = 49 \times 10^{-6}\,\mathrm{Pa\,s}$ [120]
$B_{\mathrm{edge}}^{\mathrm{glide}}(\mathrm{Ba}) = 44 \times 10^{-6}\,\mathrm{Pa\,s}$ [120]
$B_{\mathrm{screw}}^{\mathrm{glide}}(\mathrm{Pr}) = 32 \times 10^{-6}\,\mathrm{Pa\,s}$ [120]
$B_{\mathrm{edge}}^{\mathrm{glide}}(\mathrm{Pr}) = 29 \times 10^{-6}\,\mathrm{Pa\,s}$ [120]
Computational parameters
$r_{\mathrm{ann}} = 6r_c$
$r_{\mathrm{tol}} = \frac{1}{2}r_{\mathrm{ann}}$
$r_{\mathrm{max}} = \frac{3}{4}r_{\mathrm{ann}}$
$L_{\mathrm{min}} = 400a$
$L_{\mathrm{max}} = 950a$
$A_{\mathrm{min}} = 4L_{\mathrm{min}}^2 \sin(\pi/3)$
$A_{\mathrm{max}} = 20A_{\mathrm{min}}$
$\Delta t_0 = 1 \times 10^{-7}\,\mathrm{s}$

Table 6.3: Table containing simulation parameters used to simulate HCP zirconium.

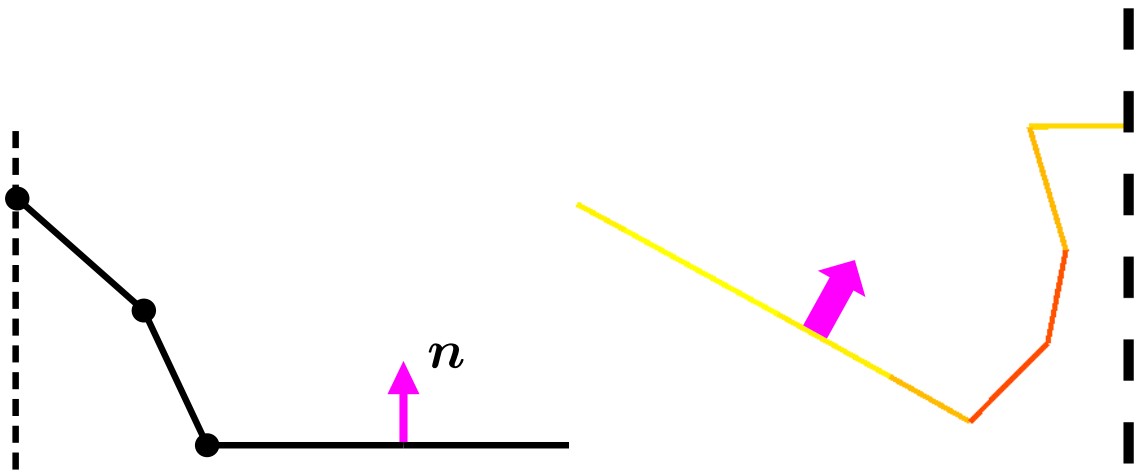


Figure 6.14: Surface hook depicted as: (a) stylised schematic and (b) part of a simulation. The black dotted line represents the trace of the surface and the magenta arrow represents the normal vector of the on-plane segments connected to the surface hook. The simulation image follows the red-edge and yellow-screw colour scheme.

to mitigate bugs. Beyond standard parameter selection, much effort went into the prevention and mitigation of these bugs, and they will be described in this section. In particular, two significant bugs were observed and identified for the first time during the simulations conducted in this chapter. Both of these bugs correspond to spurious processes that result in the build-up of large amounts of unphysical behaviour in the simulation. For both of these bugs, the unphysical behaviour leads to stable dislocation structures and tends to be self-amplifying, i.e. it leads to more of the same unphysical behaviour with no natural destabilising mode. This is unacceptable in a simulation.

Surface hooks

The first newly-discovered bug is the generation of so-called *surface hooks*. A surface hook is a chain of segments which have significant out-of-plane components and which ends on a surface, as shown in figure 6.14. Surface hooks tend to impede dislocation motion on glide planes which intersect the out-of-plane segments. In addition, they sometimes lead to the creation of a single armed source on a new glide plane. Both of these artefacts are detrimental to the simulation quality. Surface hook formation seems to be related to another problematic phenomenon, which is the occurrence of very fast surface nodes which are usually attached to short segments. These quick surface nodes are often at least an order of magnitude faster than any other node,

which severely impacts the numerical stiffness of the simulation. Surface hooks seem to arise due to the fast surface nodes which have large off-plane forces. The nature of the HCP mobility law interpolation method results in the compounding of surface hooks, since off-plane segments are treated as slipping into another available plane; as a segment slips off-plane, it becomes easier for it to slip further off-plane, thus extending the surface hook. It has been observed that surface hooks are more likely to appear as the strain rate decreases.

There are various ways of preventing and mitigating the influence of surface hooks. First, they can be mitigated by enforcing a strict interpolation tolerance between different slip planes and segment types. This can be implemented by asserting that a given segment decomposition coefficient L_{ij}^k only contributes to the full segment drag tensor $\boldsymbol{B}_i$ if it fulfills the criterion

$$\frac{|L_{ij}^k|^\iota}{|\boldsymbol{L}_{ij}|^\iota} > \epsilon_{\text{dec}} \tag{6.22}$$

where ι is a free parameter, ϵ_{dec} is the decomposition tolerance, and the superscript k denotes the type of segment, i.e. one of the coefficients in equation (4.5). As ι increases, the tolerance becomes more strict. For the simulations conducted in the present chapter, the selected parameter values were $\iota = 2$ and $\epsilon_{\text{dec}} = 10^{-2}$, which were found to have a minimal detrimental impact on the simulation quality and were helpful in preventing the formation of surface hooks.

As seen from section 3.6.2, the positions of surface nodes and the normal vectors of their internal connecting segments are coupled to the mobility law. In addition, these normal vectors are prone to spurious assignments in the pure screw case if the velocities of the exited and internal nodes are parallel to the segment line direction. To mitigate these issues, the normal vectors of newly-created internal surface connecting segments are instead assigned to be copies of those of their adjacent internal connecting segments. Furthermore, at every time-step, all surface nodes connected to internal off-plane segments are moved along the surface such that these segments are perpendicular to their normal vectors. Finally, disabling climb altogether further ensures that surface hooks never occur during simulations.

Unreliable normal vectors

A well-known bug that can massively impact the simulation quality is the incorrect assignment of pre-defined segment normal vectors. As discussed in sections 3.5.3 and 3.6.2, the issue primarily arises because the node splitting procedure—whether during

separation or surface node creation—is coupled to the mobility law. Throughout the course of a typical simulation, the spurious segments resulting from an incorrect normal vector assignment often give rise to further spurious segments through a combination of remeshing operations and spatial evolution. Spurious segments may become part of different, undesired slip systems which are otherwise restricted from activating, thus modifying the model in unreliable ways. Otherwise, a sessile segment will often form which acts as an obstacle for dislocation motion, thus leading to unphysical hardening. This is especially problematic if occurring in a system where sessile segments cannot otherwise form. In this chapter, sessile segment formation is always physically impossible within the simulated slip systems, meaning that sessile normal and Burgers vectors are assumed to be spurious. Because of this bug, pre-defined segment normal vectors were often unreliable in EasyDD. On the other hand, segment Burgers vectors are reliable.

Because the node splitting procedure is coupled to the mobility law, EasyDD in its present form is largely incompatible with climb when conducting large-scale simulations. Accordingly, climb is disabled for the simulations conducted in this chapter, which resolves the majority of the issues pertaining to unreliable normal vector assignments. However, even with climb disabled, the splitting procedure can lead to spurious normal vector assignments if all velocities involved in the splitting procedure are (1) near-zero in the non-screw case (in which case the new segment line direction and normal vector will be essentially random due to numerical noise) or (2) parallel to the segment line direction in the pure screw case (in which case the new segment normal vector will be zero). To mitigate this issue, in this chapter we restrict the set of admissible normal vectors $\mathcal{N}_{\text{adm}}$ to those that are physically possible in a given simulation[6]. For example, a simulation initialised with only prismatic slip admits only prismatic normal vectors; one initialised with both prismatic and basal slip admits both prismatic and basal normal vectors. The larger the set of admitted normal vectors $\mathcal{N}_{\text{adm}}$, the higher the risk of incorrect normal vector assignments. At every time-step, all non-zero normal vectors are re-assigned to the ones in $\mathcal{N}_{\text{adm}}$ to which they are most parallel to. If a segment has a glissile Burgers vector but zero normal vector, its normal vector is re-assigned to the vector in $\mathcal{N}_{\text{adm}}$ that is most parallel to $\boldsymbol{l} \times \hat{\boldsymbol{b}}$ in the non-screw case and re-assigned to a random vector in $\mathcal{N}_{\text{adm}}$ in the pure screw case.

[6]This slip system restriction does not apply to the segment decomposition procedure presented in section 4.2.

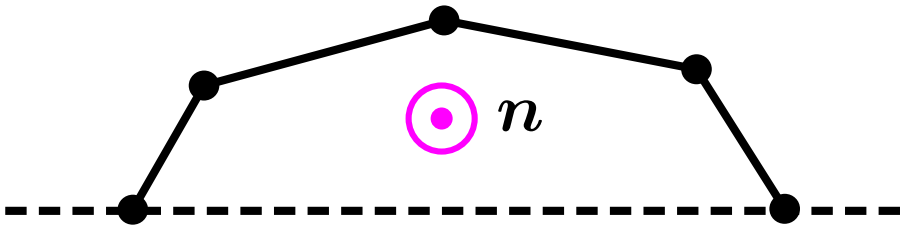


Figure 6.15: Schematic of a surface crescent. The black dotted line represents the trace of the surface and the normal vector of the segments composing the surface crescent is depicted in magenta.

Recall that in the HCP mobility law, dislocation segments are in general decomposed into one pure screw and two pure edge components. It can be advantageous to assume that the largest edge decomposition component lies on the unit edge vector corresponding to the pre-defined normal vector. This assumption can be beneficial for performance, because one decomposition is skipped. This assumption can also enhance simulation quality, because the influence of spurious out-of-plane segments can be mitigated if the pre-defined normal vector is correct. An alternative is to simply neglect this assumption, which makes the edge component decomposition procedure completely independent of the normal vector. Due to the aforementioned reasons, the former assumption is always made in the simulations conducted in this chapter.

Surface crescents

The second newly-discovered bug is the generation of so-called *surface crescents*, as shown in figure 6.15. A surface crescent is a fairly short (usually on the order of a single FEM mesh element) chain of dislocation segments that starts and ends at the surface, and which exhibits a roughly semi-circular shape orientated in a convex manner with respect to the surface. Surface crescents are very stable structures which are difficult to destroy once appeared. The presence of a single surface crescent will usually result in a pile-up of dislocations behind it, leading to a gradual localised accumulation of surface crescents (see figure 6.16), impeding further dislocation motion, resulting in an unphysical hardening of the associated slip system. It is hypothesised that the formation of surface crescents is a consequence of the inability of the FEM mesh to produce sufficiently refined forces required for ejection.

It should also be noted that the core energy density parameter E_c^s can be important in preventing surface crescents from forming. This is because the line tension force, the strength of which is determined by E_c^s, will always push surface crescents

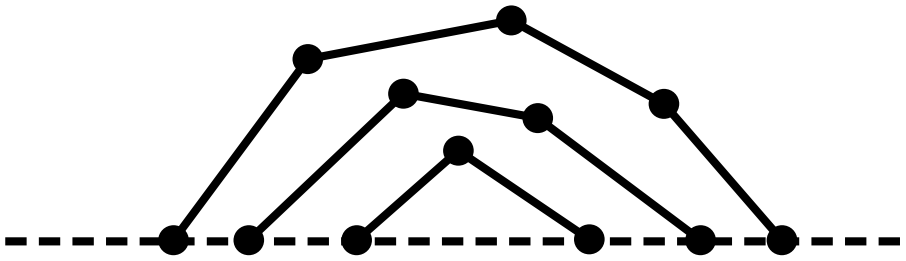


Figure 6.16: Schematic of a surface crescent pile-up. The black dotted line represents the trace of the surface.

towards the surface. By experimentation through simulation, it was determined that increasing E_c^s significantly reduced the frequency of formation of surface crescents (note that $0.01 < E_c^s/\mu b^2 < 0.1$ is a typical choice). However, modulating the parameter E_c^s is not sufficient in mitigating the issue, and some surface crescents form regardless. One potential solution is to refine the FEM mesh, the granularity of which may be otherwise reasonable. However, this may significantly increase the computational expense of the simulation, and is therefore unacceptable in cases where large strains must be accessed. An alternative solution is to implement a procedure which ejects surface crescents from the domain based on some detection criterion. In the simulations conducted in this chapter, the following detection criterion was implemented: all mobile nodes which are connected to solely surface nodes are ejected out of the domain. The already existing network meshing procedures in EasyDD will then safely take care of the ejected structure. During the advanced stages of a typical simulation, it was found that surface crescents are often ejected from the domain at a fairly constant rate. This appears to be an effective solution, and surface crescents no longer present an issue.

Overlapping segments

Occasionally—and especially during the nucleation of a Frank-Read source—two interacting segments fail to undergo the typical reaction procedure, and instead simply traverse through each other and overlap without the generation of a node at their intersection, as in figure 6.17. If this occurs, unphysical self-amplifying behaviour tends to follow. For instance, segments may accumulate and form dense overlapping tangles which are otherwise physically impossible. This phenomenon seems to be primarily controlled by the parameters $r_{\max}$, r_{tol}, $L_{\max}$, and $L_{\min}$. The selection of lower values of these parameters—which corresponds to finer resolution simulations—mitigates this phenomenon, albeit with a performance cost. This

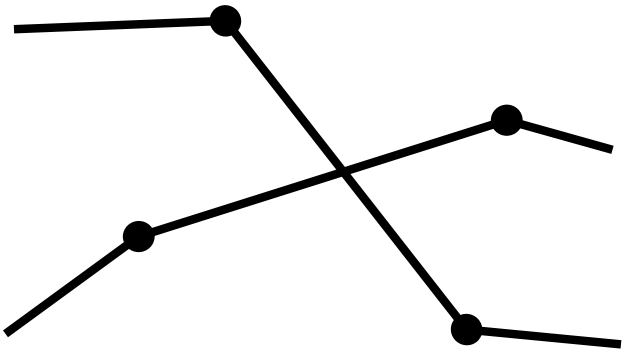


Figure 6.17: Schematic of two overlapping segments. Both segments are gliding on the same slip plane. Because there is no node at their intersection, this is a spurious arrangement.

accuracy-performance tradeoff is often worthwhile, and one should make the largest possible assignment for these parameters such that this phenomenon does not occur.

Omission of plastic displacements

The plastic displacement term (equation (3.44)) must be enabled to account for permanent plastic distortions and thereby produce physically accurate plasticity simulations. The EasyDD code was originally developed for cantilever bending, where the inclusion of dislocation-induced displacements has been observed to have a small impact to macroscopic response [249]. This is because cantilever bending conditions feature a neutral axis wherein dislocations form soft pile-ups. The surface tractions generated by these pile-ups often result in large softening effects. Furthermore, the calculation of dislocation-induced displacements is computationally expensive and exhibits poor time scaling[7], as discussed in section 3.6.3. For this reason, dislocation-induced displacements have been omitted in some previous applications of EasyDD.

In contrast, the inclusion of dislocation-induced displacements becomes crucial under tensile loading, where there are no natural pile-up zones. In such conditions, neglecting dislocation-induced displacements usually results in an unrealistic purely elastic macroscopic response. Therefore, dislocation-induced displacements (equations (3.44) and (3.45)) are always included in the simulations conducted in this chapter.

[7] In low dislocation density simulations, dislocation-induced displacements can consume more than $\sim 60\%$ of the computation time.

6.2.4 Computer codes and algorithms

In this section, details are presented of the implementation of some of the computer codes developed for the purpose of conducting the simulations in this chapter.

HCP mobility law

Pseudocode for the HCP mobility law implementation is presented in algorithm 1. During a typical simulation, the mobility law can consume approximately $5\% - 10\%$ of the simulation time. It is not unusual for the mobility law module to be called at least 10^6 times. It is therefore essential that it is computationally optimised.

Several optimisations have been implemented. For instance, previously, the reference crystal orientation was defined in the unrotated state and subsequently rotated every time the mobility law was called. To increase computational efficiency, the reference crystal orientation is now rotated only once at the initialisation stage of the simulation and provided as an input to the HCP mobility law. In addition, the number of glissile slip systems corresponding to each Burgers vector is precomputed for faster indexing. Furthermore, for every Burgers vector, the set of all unit edge vectors $\{\boldsymbol{l}_{e_q}\}$ into which an edge component may be decomposed (see section 4.2.1) is also precomputed.

As discussed in chapter 4, a segment Γ_{ij} is considered glissile if its Burgers vector $\boldsymbol{b}_{ij}$ and normal vector $\boldsymbol{n}_{ij}$ are parallel to the corresponding vectors in table 4.1. Let $\{\boldsymbol{V}_j\}$ be a reference set of vectors representing either Burgers or normal vectors. Denote by $\boldsymbol{v}_{ij}$ the Burgers or normal vector of segment Γ_{ij}, depending on whether $\{\boldsymbol{V}_j\}$ respectively represents a set containing Burgers or normal vectors. The glissile slip system to which Γ_{ij} belongs to is determined by using a criterion based on the cross product, given by

$$\boldsymbol{v}_{ij} \times \boldsymbol{V} < \boldsymbol{\epsilon}_c \tag{6.23}$$

for all vectors $\boldsymbol{V} \in \{\boldsymbol{V}_j\}$. Here, $\boldsymbol{\epsilon}_c = (\epsilon_c, \epsilon_c, \epsilon_c)$ is a tolerance vector; the assignment $\epsilon_c = 10^{-2}$ is usually adequate.

Time integrator

A new time integrator was developed for the simulations conducted in this chapter, and its pseudocode implementation is presented in algorithm 2. The time integrator uses the Euler-trapezoid method to compute the updated nodal positions. There are some new features which are intended to improve simulation quality, performance, and stiffness, which will be discussed in the following.

Algorithm 1: HCP mobility law

Initialise() `// Import slip system information in lab-frame crystal orientation`

`// Loop over every node provided in the input network:`

for $i = 1, \ldots, N$ **do**
- **if** n_i *is virtual* **then**
  - continue
- **end**
- $\boldsymbol{B}_i = \boldsymbol{0}$, $\boldsymbol{f}_i = \boldsymbol{0}$
- `// Loop over every connected segment:`
- **for** $j = 1, \ldots, k_i$ **do**
  - $\boldsymbol{f}_i = \boldsymbol{f}_i + \boldsymbol{f}_{ij}$
  - Determine glissile slip system of segment Γ_{ij} according to criterion (6.23)
  - **if** Γ_{ij} *is sessile* **then**
    - $\boldsymbol{B}_i = \boldsymbol{B}_i + \frac{1}{2}|\boldsymbol{L}_{ij}|\mathcal{B}_{ij}^{\text{sess}}$
    - continue
  - **else if** Γ_{ij} *is glissile* **then**
    - **if** L_{ij}^{s} *meets criterion* (6.22) **then**
      - $\boldsymbol{B}_i = \boldsymbol{B}_i + \frac{1}{2}|\boldsymbol{L}_{ij}|\mathcal{B}_{ij}^{s}$
    - **end**
    - **if** $L_{ij}^{e_a}$ *meets criterion* (6.22) **then**
      - $\boldsymbol{B}_i = \boldsymbol{B}_i + \frac{1}{2}|\boldsymbol{L}_{ij}|\mathcal{B}_{ij}^{e_a}$
    - **end**
    - **if** $L_{ij}^{e_b}$ *meets criterion* (6.22) **then**
      - $\boldsymbol{B}_i = \boldsymbol{B}_i + \frac{1}{2}|\boldsymbol{L}_{ij}|\mathcal{B}_{ij}^{e_b}$
    - **end**
- **end**
- **if** n_i *is a surface node* **then**
  - $\boldsymbol{B}_i = \mathcal{T}_s(\boldsymbol{B}_i)$
- **end**
- **if** $\boldsymbol{B}_i$ *is poorly conditioned* **then**
  - $\boldsymbol{B}_i = \mathcal{T}(\boldsymbol{B}_i)$
- **end**
- $\boldsymbol{v}_i = \boldsymbol{B}_i^{-1}\boldsymbol{f}_i$

end

The first improvement is the addition of a new parameter, Δt_p, which keeps track of the suggested time-step for the next cycle as opposed to the actual time-step applied in the final nodal position update in the current cycle Δt. In previous iterations of the time integrator used in EasyDD, this distinction was not made, and the suggested time-step (not necessarily the actual time-step) was simply assigned to Δt. The actual time-step used for the nodal position update and the suggested time-step—such as the one suggested by rule (3.33)—differed whenever the time-step increased between cycles. This means that there were likely small errors introduced to the global tracked time whenever the time-step was increased in the time integrator module. The implementation of the distinction between these two parameters provides a simple solution to this issue.

The second improvement is meant to maximise the time-step while minimising the number of expensive force evaluations by addressing a common phenomenon which occurred in the time-step size modulation. First, note that the $r_{\max}$ parameter imposes a fundamental a priori upper bound for the allowed time-step size in any given time integrator cycle given by

$$\Delta t_{\max} = \frac{r_{\max}}{\max\left(\{|\boldsymbol{v}_j|\}\right)} \tag{6.24}$$

Previously, when the time-step increased in size according to rule (3.33), it often overshot this upper bound, i.e. $\Delta t > \Delta t_{\max}$. After even a slight overshoot, the time-step must be halved to a value which is much further below what is necessary, and this is accompanied by unnecessary expensive force evaluations. The upper bound time-step $\Delta t_{\max}$ is particularly relevant in $r_{\max}$-dominated regions with low velocity gradients[8], which corresponds to low-density, early-stage plasticity simulations. In regions with high velocity gradients, r_{tol} will dominate if it is assigned appropriately and hence it will usually be the case that $\Delta t < \Delta t_{\max}$. To mitigate this phenomenon, the upper limit of Δt is set to be at most $\Delta t_{\max}\epsilon_t$, where $\epsilon_t = 1 - 10^{-5}$. The parameter ϵ_t ensures that no extra force evaluations are conducted by keeping the time-step slightly below the limiting value.

Figure 6.18 displays plots comparing the effects of the bounded time-step size modulation method discussed above with the standard unbounded method for two simulations which have otherwise identical initial conditions. The compared quantities are (1) the time-step size and (2) the cumulative wall clock time, which is decreased by about a factor of 43% in the bounded case. Note that there is a small period

[8] i.e., those which do not trigger the r_{tol}-related time-step decreases.

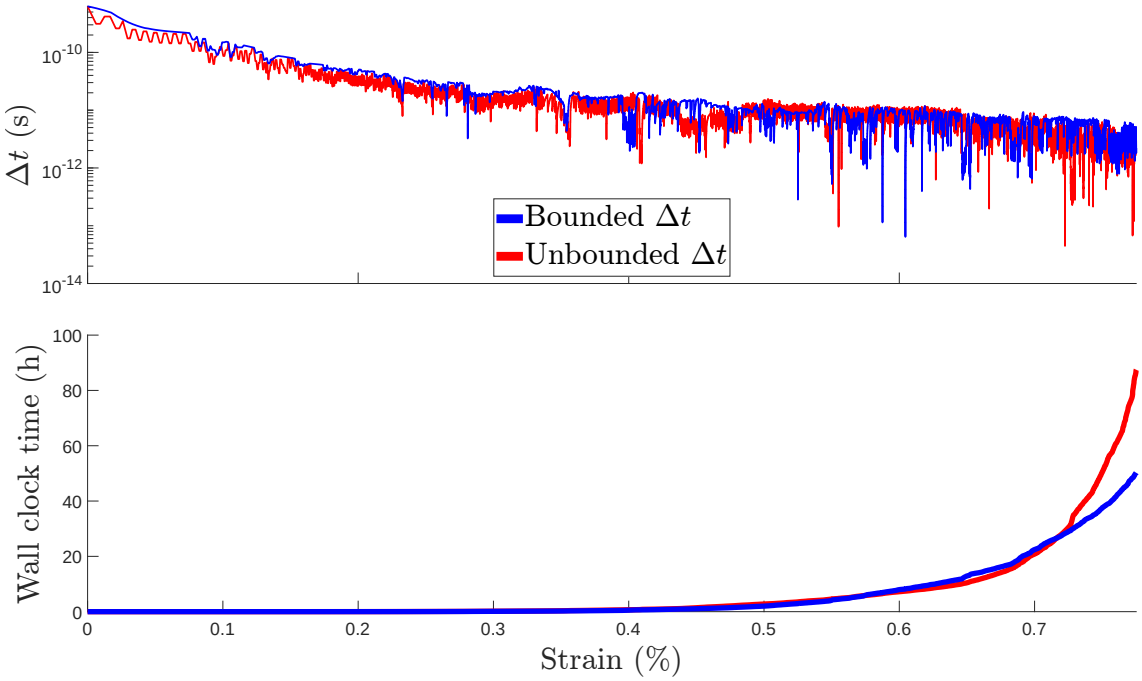


Figure 6.18: Plots depicting the results of two DD simulations which are identical except for: (1) one implements the time-step size bound given by equation (6.24) (blue solid line) and (2) the other does not implement this time-step bound (red solid line).

during the simulation in which the cumulative wall clock time of the bounded case is slightly larger. Compared to the unbounded case, the time-step size for the bounded case is roughly overall larger and undergoes fewer unnecessary decreases, which enables larger time-steps on average, fewer force evaluations, and thus corresponds to a reduced wall clock time. While further tests should be conducted to control for statistical scatter, it is evident that limiting the time-step size based on the parameter $r_{\max}$, and possibly based on other parameters, can result in significant improvements in computational efficiency.

The third feature is meant to minimise the impact of simulation stiffness. When there is a large disparity in speed between nodes, the time-step must decrease to accommodate the fastest nodes. This severely slows down the simulation since, in resolving the fast nodes, the slow nodes evolve negligibly while still being involved in expensive force evaluations. This large disparity in nodal speeds has been observed to occasionally greatly impact EasyDD simulations.

At the very beginning of the time integrator, the function `DetermineFastNodes()` determines which nodes are fast, as is described in the following. The nodal speeds are calculated, sorted, normalised, and log-transformed. Because this procedure

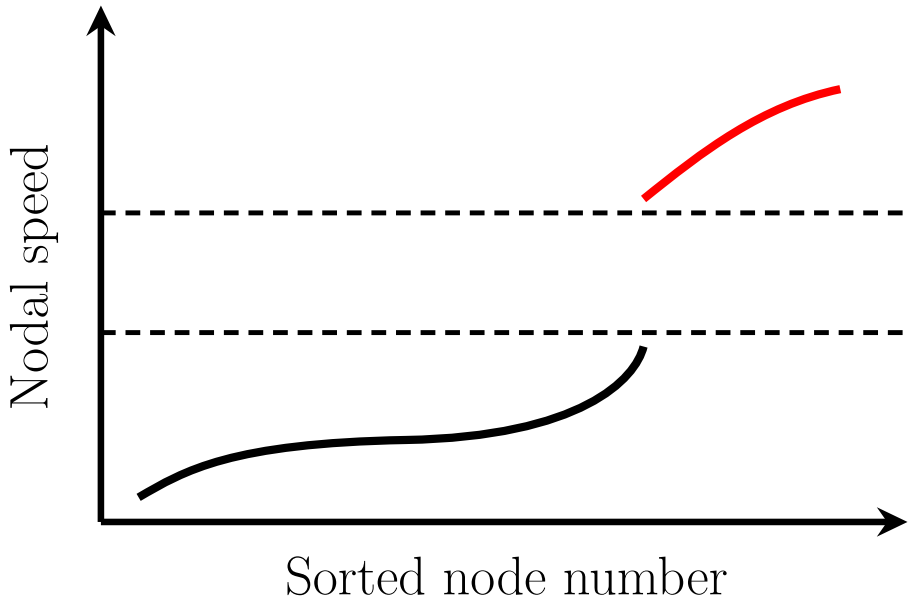


Figure 6.19: Schematic of an isolated speed regime identified in a set of nodes. The nodes are sorted from left to right in order of increasing speed. The fast nodes (in red) are separated from the slow nodes (in black) by a continuous band bounded by the two black dotted lines.

applies at every time-step, the sorting method should be considered carefully. As of the time of writing, MATLAB's default sorting function, `sort()`, uses the Quicksort algorithm which has a time complexity of $\mathcal{O}(N \log(N))$ for the best and average cases [327]. Since the force evaluations exhibit a worse time complexity of $\mathcal{O}(M^2)$, where the number of segments M usually satisfies $M \geq N$, this procedure will not introduce bottlenecks to the time integrator. Next, so-called "speed regimes" are identified. These are regimes in the speed-space which are completely isolated from each other by some factor, as shown in figure 6.19. When the largest speed regime is identified, the time-integrator proceeds normally for the nodes in that regime—the time-step is adjusted so that their velocity meets the r_{tol} and/or $r_{\max}$ tolerance. However, the velocities of all other nodes are assumed to stay constant in their respective neighbourhood, and so the tolerance procedure is not conducted for them. This alternative procedure is conducted by a new time integration function $\boldsymbol{g}_i^s$ which is used instead of $\boldsymbol{g}_i$. This assumption should be valid for the very small time-steps necessitated by the resolution of fast nodes. Although this is only done for the largest regime, in principle this method could be extended to act independently on multiple speed regimes.

It should be noted that at the time of writing, the force evaluations module is not optimised to handle the scenario wherein a specific subset of the links array with

Algorithm 2: Time integrator for stiffness mitigation

$\boldsymbol{v}_i^0 = \boldsymbol{g}_i\left(\{\boldsymbol{x}_j^0\}\right)$
$\texttt{fastnodeids} = \text{DetermineFastNodes}(\boldsymbol{v}_i^0)$ `// Determine which nodes are fast`
$\Delta t_{\max} = \frac{r_{\max}}{\max\left(\{|\boldsymbol{v}_j^0|\}\right)}\epsilon_t$ `// Maximum possible time-step imposed by` $r_{\max}$
$\Delta t_{\text{init}} = \Delta t$
$\Delta t = \min\left(\Delta t_p, \Delta t_{\max}\right)$
$\texttt{convergent} = false$
while $\texttt{convergent} == false$ **do**
  $\boldsymbol{x}_i^P = \boldsymbol{x}_i^0 + \boldsymbol{v}_i^0 \Delta t$
  if *there are fast nodes* **then**
    $\boldsymbol{v}_i^P = \boldsymbol{g}_i^s\left(\{\boldsymbol{x}_j^P\}, \texttt{fastnodeids}\right)$
  else
    $\boldsymbol{v}_i^P = \boldsymbol{g}_i\left(\{\boldsymbol{x}_j^P\}\right)$
  $\boldsymbol{v}_i^C = \left(\boldsymbol{v}_i^0 + \boldsymbol{v}_i^P\right)/2$
  $\boldsymbol{x}_i^C = \boldsymbol{x}_i^0 + \boldsymbol{v}_i^C \Delta t$
  $\epsilon_{\max} = \max\left(\{|\boldsymbol{x}_i^P - \boldsymbol{x}_i^C|\}\right)$ `// Maximum error magnitude`
  $d_{\max} = \max\left(\{|\boldsymbol{x}_i^P - \boldsymbol{x}_i^0|\}\right)$ `// Maximum distance travelled by any node`
  if $\epsilon_{max} \leq r_{tol}$ *and* $d_{max} \leq r_{max}$ **then**
    $\texttt{convergent} = true$
  else
    $\Delta t = \Delta t/2$
  $\texttt{counter} = \texttt{counter} + 1$
  if $\texttt{counter}$ *exceeds maximum iterations* **then**
    break
  end
end
$\boldsymbol{x}_i = \boldsymbol{x}_i^P$
$\boldsymbol{v}_i = \boldsymbol{v}_i^P$
if $\Delta t == \Delta t_{init}$ **then**
  $\Lambda = \Lambda_{\max}\left(1 + \frac{\epsilon_{\max}}{r_{\text{rol}}}\left(\Lambda_{\max}^q - 1\right)\right)^{-\frac{1}{q}}$
  $\Delta t_p = \min\left(\Lambda \Delta t, \Delta t_0\right)$
end

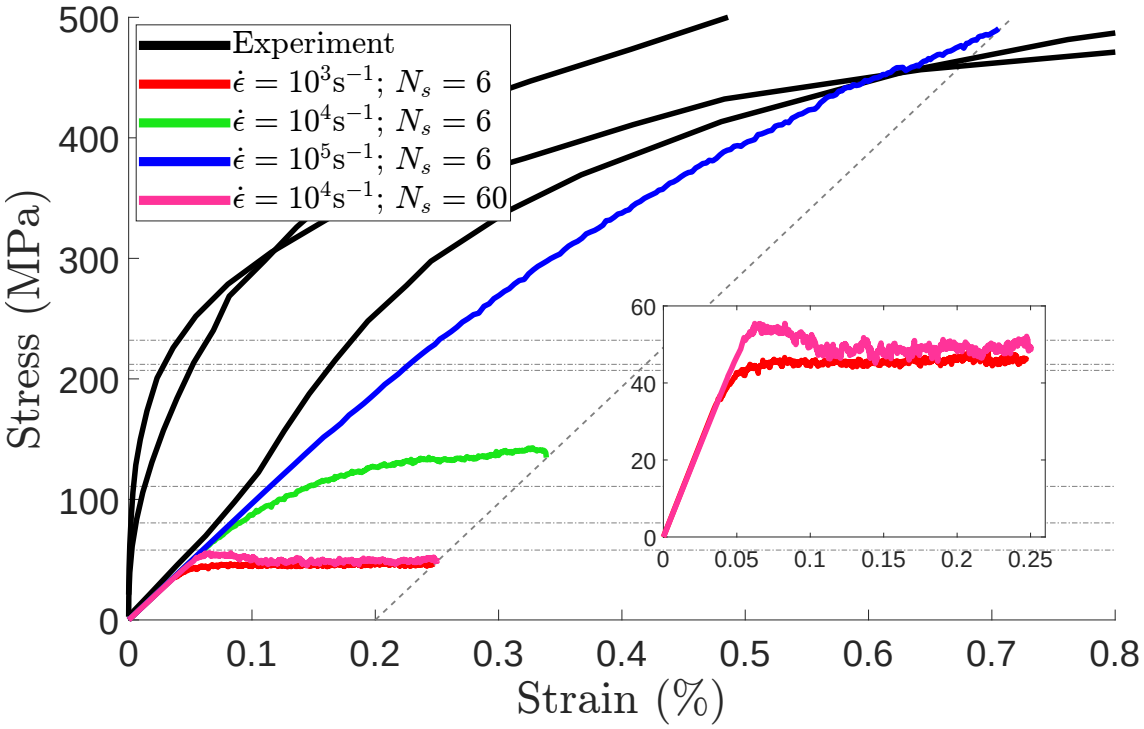


Figure 6.20: Stress-strain curves corresponding to all basal-prismatic simulations. The horizontal half-dotted-half-solid lines represent the activation stress of each slip system. The slanted dotted line represents the 0.2% offset yield criterion.

size greater than one is provided. When this occurs, the CPU is used to compute the forces, which can result in a significant bottleneck. Therefore, this method should only be applied if the number of relatively fast nodes is below approximately 400—this is the threshold above which force calculations are transferred from the CPU to the GPU in the standard case. The EasyDD forces subroutine should eventually be changed to accommodate this.

In the simulations conducted in this chapter, the criterion for fast node detection was that the band gap shown in figure 6.19 was such that the slowest node in the fast regime was at least 10^2 times faster than the fastest node in the slow regime. Using this criterion, it was found that fast nodes were detected quite sparingly. It is expected that reducing the threshold for fast node detection will increase this frequency. However, care should be taken that this threshold is not too low such that the constant velocity assumption of slow nodes is violated. More investigations are needed to determine the appropriate regimes of application of this new time integrator.

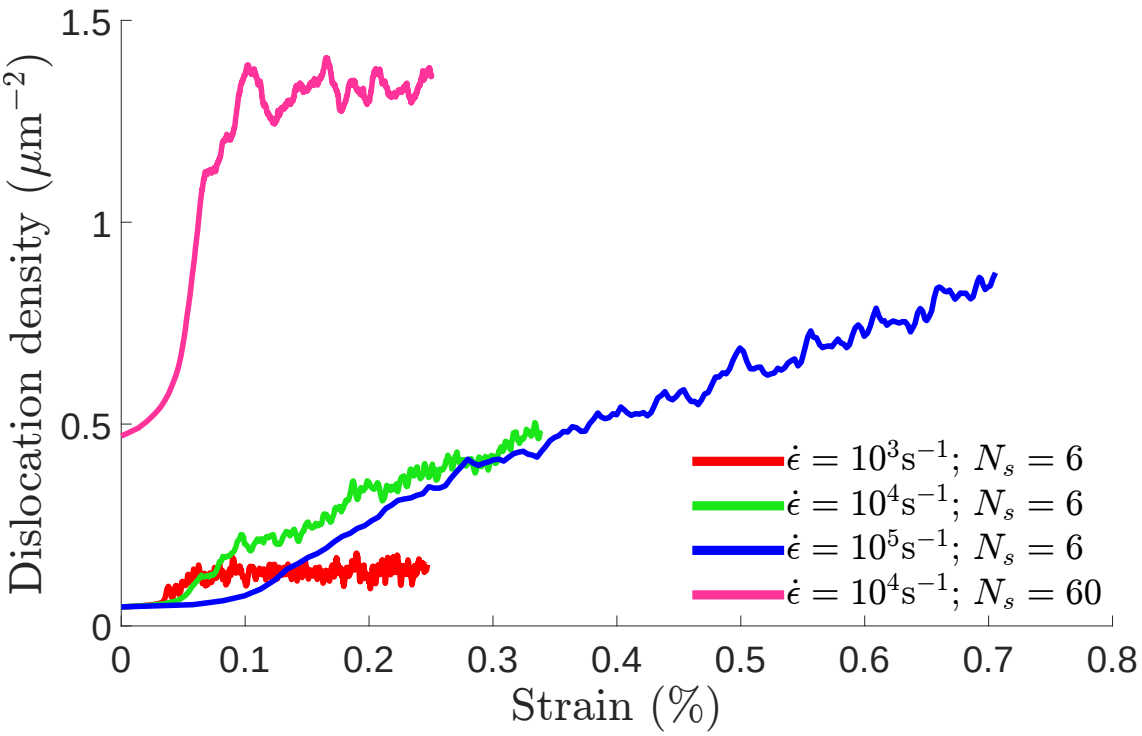


Figure 6.21: Plots of total dislocation densities corresponding to all basal-prismatic simulations.

6.3 Tensile simulations

In this section, 3D DD simulations of micro-tensile uniaxial loading are presented to support the experiments. All simulations were run on CPUs using computers equipped with either (1) dual Intel® Gold 6128 6-core CPUs and 192 GB RAM, (2) an Intel® Core™ i9-7900X 10-core CPU and 64 GB RAM, or (3) an Intel® Core™ i5-8500 CPU and 8 GB RAM.

Dislocation networks are initialised with prismatic loop sources of an equal size L_s that varies depending on the simulation. These sources are each associated with slip systems such that, in a given simulation, all modelled slip systems are always equally represented. For example, if $N_s = 6$ and six slip systems are included, then each possible slip system is initialised with one prismatic loop source. The initial slip planes are arranged such that they never intersect with displacement-controlled surfaces; this is not possible for the 3Pr slip system due to the crystal orientation. During initialisation, prismatic loop sources are distributed uniformly at random with the constraint that there is some minimum distance between any two parallel glide planes $d_{\mathrm{gp}} > 2r_{\mathrm{ann}}$ to avoid numerical issues which can affect the simulation quality. Furthermore, sources are restricted from being positioned within $0.1L_x$,

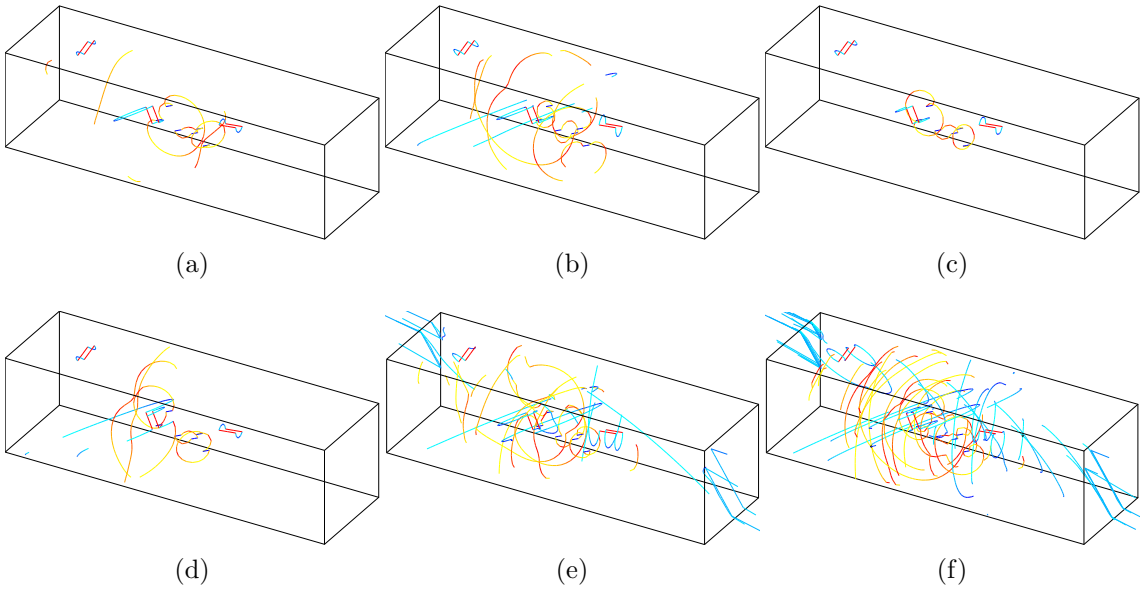


Figure 6.22: Internal dislocation network snapshots pertaining to the basal-prismatic $N_s = 6$ simulations at $\epsilon = 0.1\%$ strain (a-c) and at yield (d-f). (a) and (d): $10^3\,\mathrm{s}^{-1}$; (b) and (e): $10^4\,\mathrm{s}^{-1}$; (c) and (f): $10^5\,\mathrm{s}^{-1}$. In all figures, the leftmost $5\,\mu\mathrm{m} \times 5\,\mu\mathrm{m}$ face is the one corresponding to the zero-displacement boundary condition. Segments are respectively represented as red (pure edge) to yellow (pure screw) for basal dislocations and blue (pure edge) to cyan (pure screw) for prismatic dislocations. Thick black circles represent junction nodes.

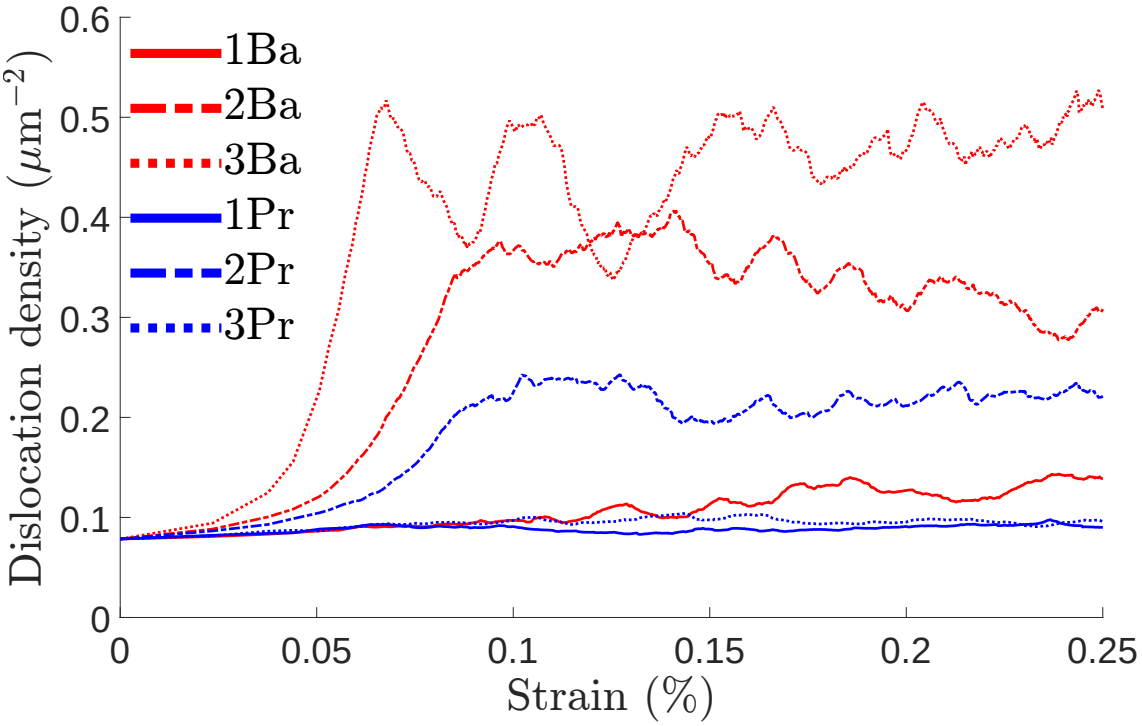
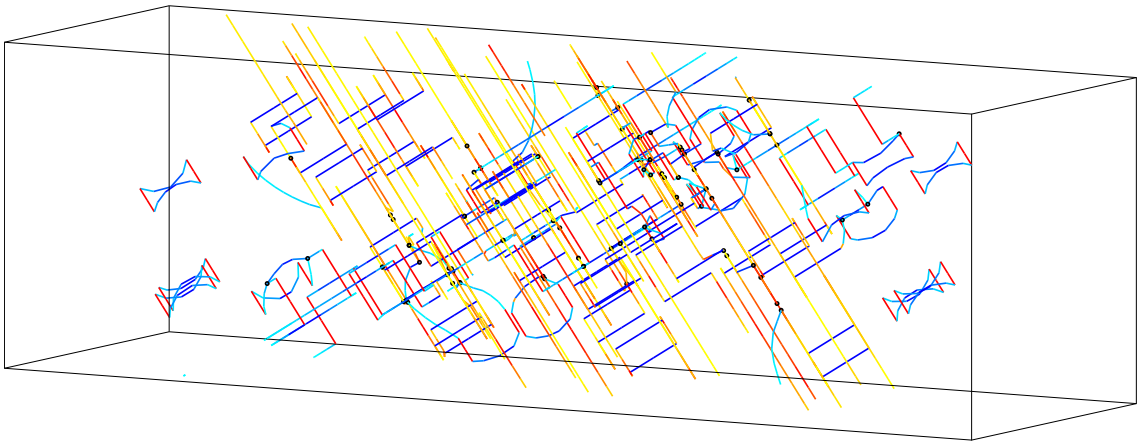


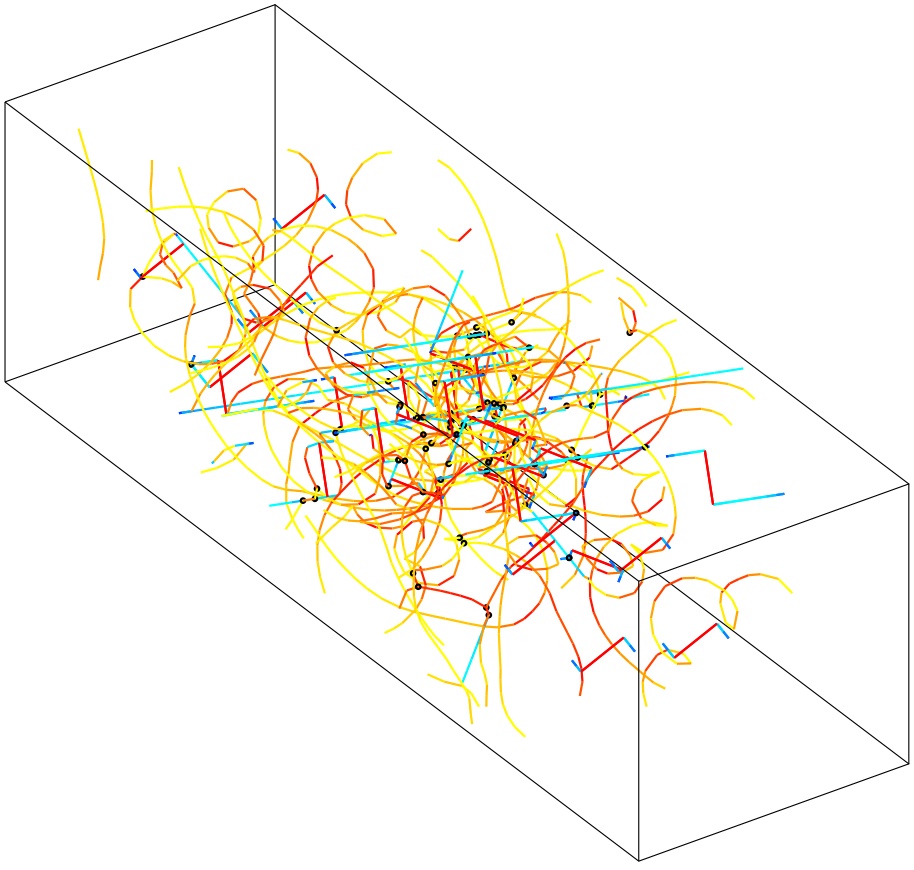
Figure 6.23: Plots of dislocation densities of individual slip systems corresponding to the basal-prismatic $N_s = 60$ simulation.

$0.1L_y$, and $0.1L_z$ of the respective surface faces perpendicular to the x, y, and z axes.

Unless stated otherwise, yield is defined according to the 0.2% offset criterion [39], which has been employed in DD studies across both strain rate dependent and forest hardening regimes [305, 309, 82]. Figure 6.36 displays the data at yield pertaining to all simulations conducted in this chapter plotted against the strain rate dependent model [309] prediction (equation (6.16)). Across all simulations, the mobile dislocation density fraction is assumed to be $f_a = 1$. The effective Schmidt factor is taken as the arithmetic mean of the Schmidt factors of each present slip system, resulting in $m \approx 0.246$ for simulations containing both basal and prismatic slip and $m \approx 0.169$ for simulations containing only prismatic slip. Furthermore, it is assumed that $\alpha = 0.3$, corresponding to the approximate prismatic-prismatic Taylor interaction strength in HCP ice [173], which exhibits mechanical properties similar to those of HCP Zr. Although some of the present simulations additionally include basal-prismatic interactions, none fall within the Taylor hardening regime, making this assumption inconsequential for those cases. Overall, the DD simulation results agree closely with the model prediction, which serves as a validation of the EasyDD code. It is evident that all simulations are within the strain rate hardening or transition regime.



(a)



(b)

Figure 6.24: Internal dislocation network snapshots pertaining to the basal-prismatic $N_s = 60$ simulation at yield. Lines of sight aligned with (a) $\boldsymbol{b}_2$ and (b) the basal plane normal vector. In all figures, the leftmost 5 µm × 5 µm face is the one corresponding to the zero-displacement boundary condition. Segments are respectively represented as red (pure edge) to yellow (pure screw) for basal dislocations and blue (pure edge) to cyan (pure screw) for prismatic dislocations. Thick black circles represent junction nodes.

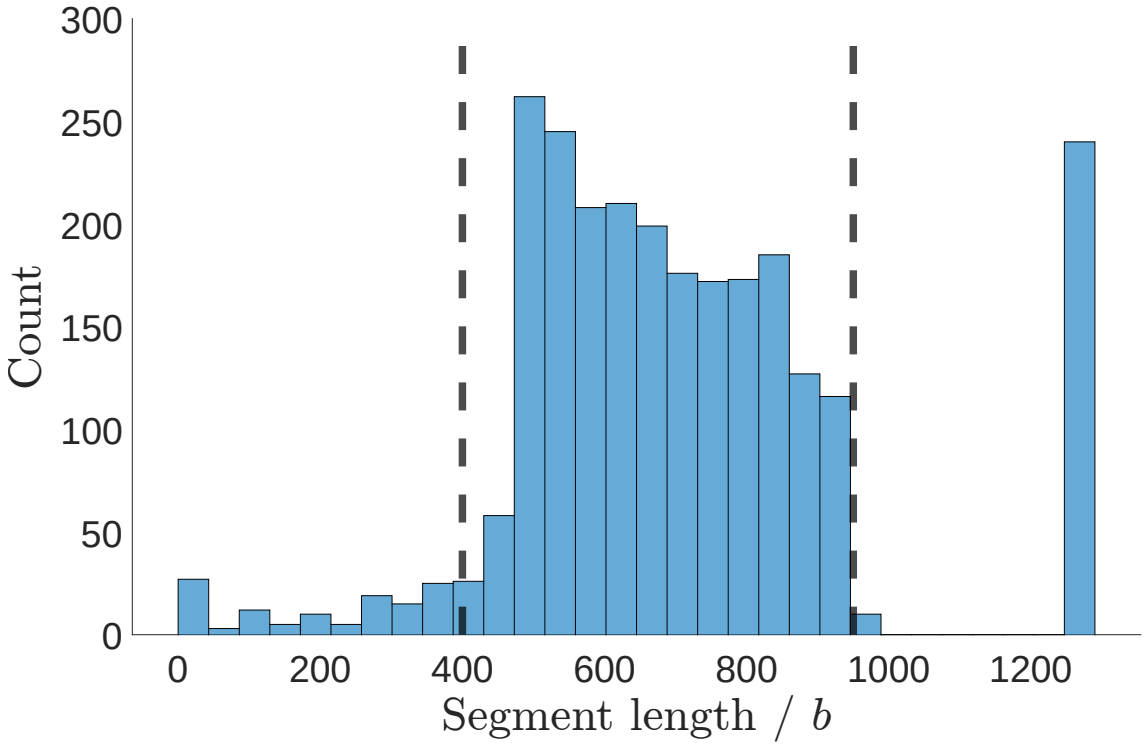


Figure 6.25: Histogram of segment lengths corresponding to the basal-prismatic $N_s = 60$ simulation at yield. The two dotted vertical lines respectively represent $L_{\min}$ and $L_{\max}$.

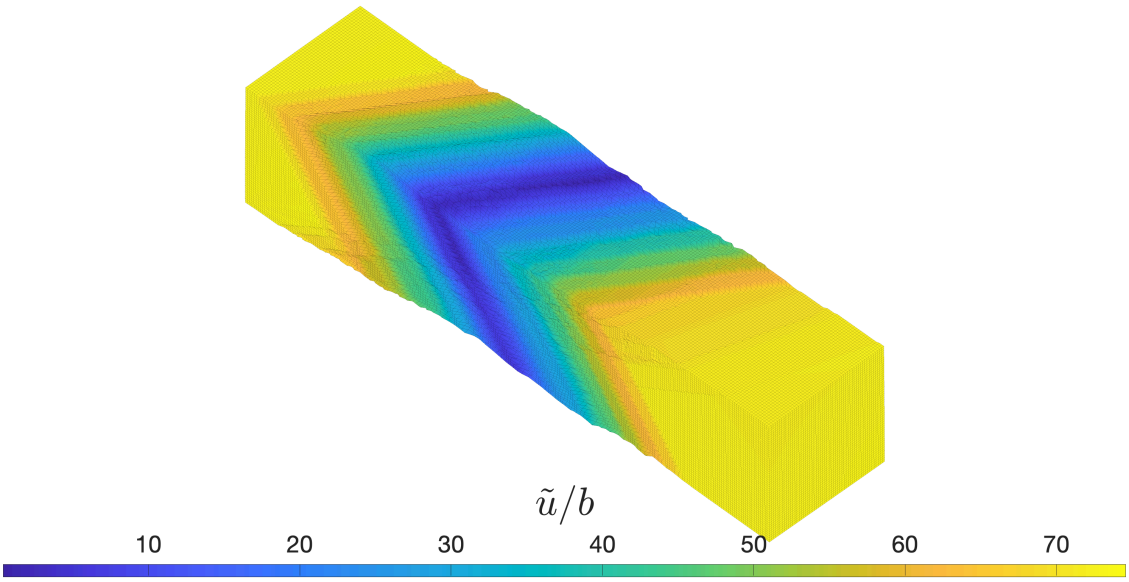
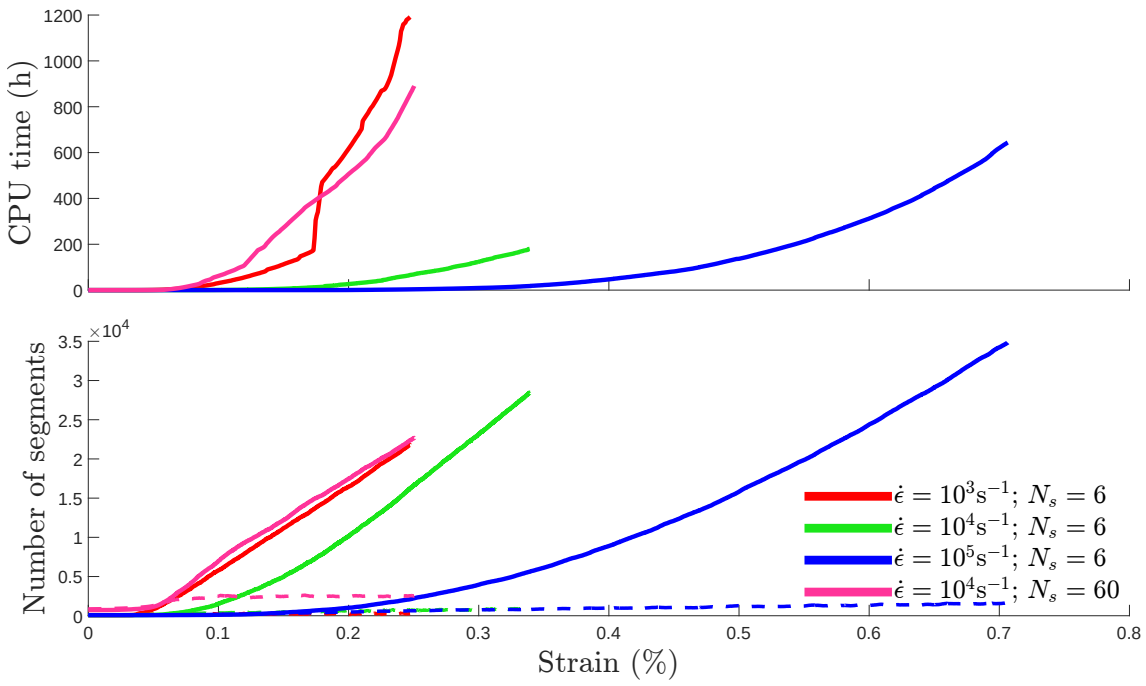


Figure 6.26: Plot of the dislocation-induced displacement field $\tilde{u}$ on the domain surface corresponding to the basal-prismatic $N_s = 60$ simulation at yield. Surface displacements are plotted on a mesh and are magnified by a factor of 100 for clarity, but the colour bar scale is unchanged. The leftmost $5\,\mu\text{m} \times 5\,\mu\text{m}$ face is the one corresponding to the zero-displacement boundary condition.

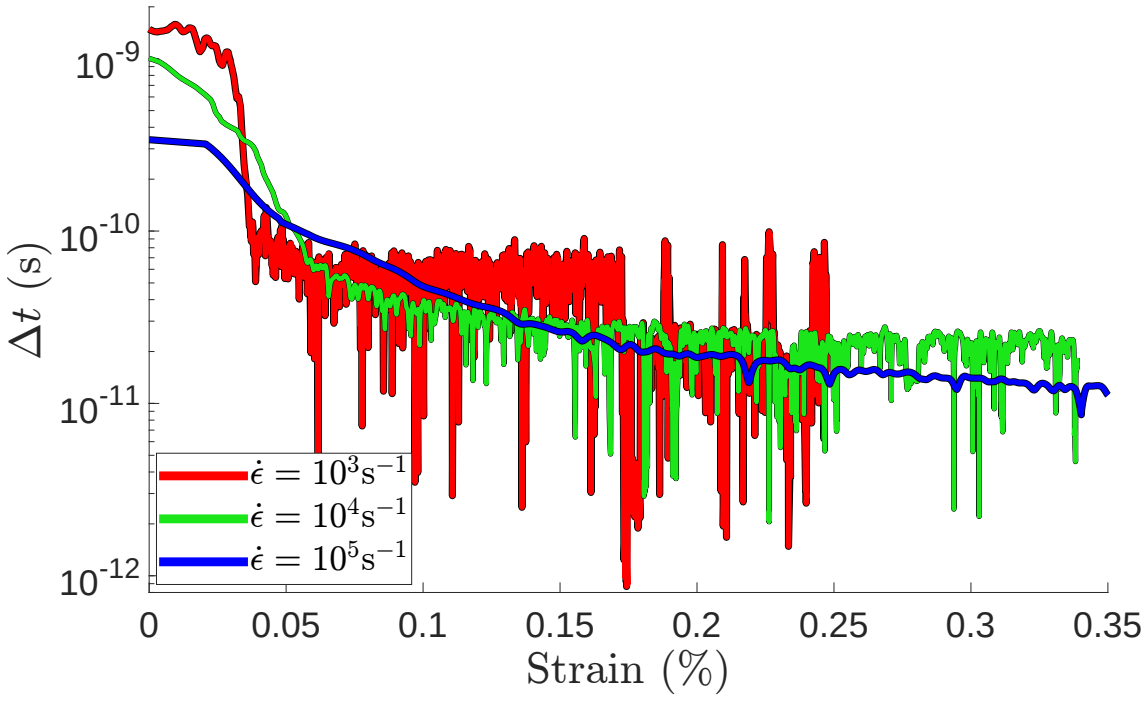
6.3.1 Basal-prismatic slip

As discussed in section 6.2.1, the experimental conditions are such that basal slip can likely be neglected for the present modelling purposes. However, to validate and explore the limits of the model, the simulations presented in this section include both $\langle a \rangle$-type basal and prismatic slip systems. This restricts the DD simulations to six slip systems: 1Ba, 2Ba, 3Ba, 1Pr, 2Pr, and 3Pr. The $n\text{Pr} - m\text{Pr}$, $n\text{Pr} - m\text{Ba}$, and $n\text{Pr} - n\text{Ba}$ non-coplanar reactions are possible. In this section, source sizes are always $L_s = L_y/6 \approx 0.83\,\mu\text{m}$; this choice mitigates the influence of stresses generated by fixed segments composing sources, and also avoids the regime in which the flow stress is entirely controlled by source strengths. The sensitivity of the macroscopic response on the source number and size will be studied in section 6.3.2. Following from table 6.2, the corresponding tensile stresses required for source activation in each slip system are: 207 MPa for 1Ba, 81 MPa for 2Ba, 58 MPa for 3Ba, 212 MPa for 1Pr, 111 MPa for 2Pr, and 232 MPa for 3Pr. Furthermore, the stresses generated by fixed segments are enabled. The number of FE nodes in each coordinate direction are given by $(N_x, N_y, N_z) = (30, 9, 9)$.

Throughout this section, basal dislocations are depicted with colours ranging

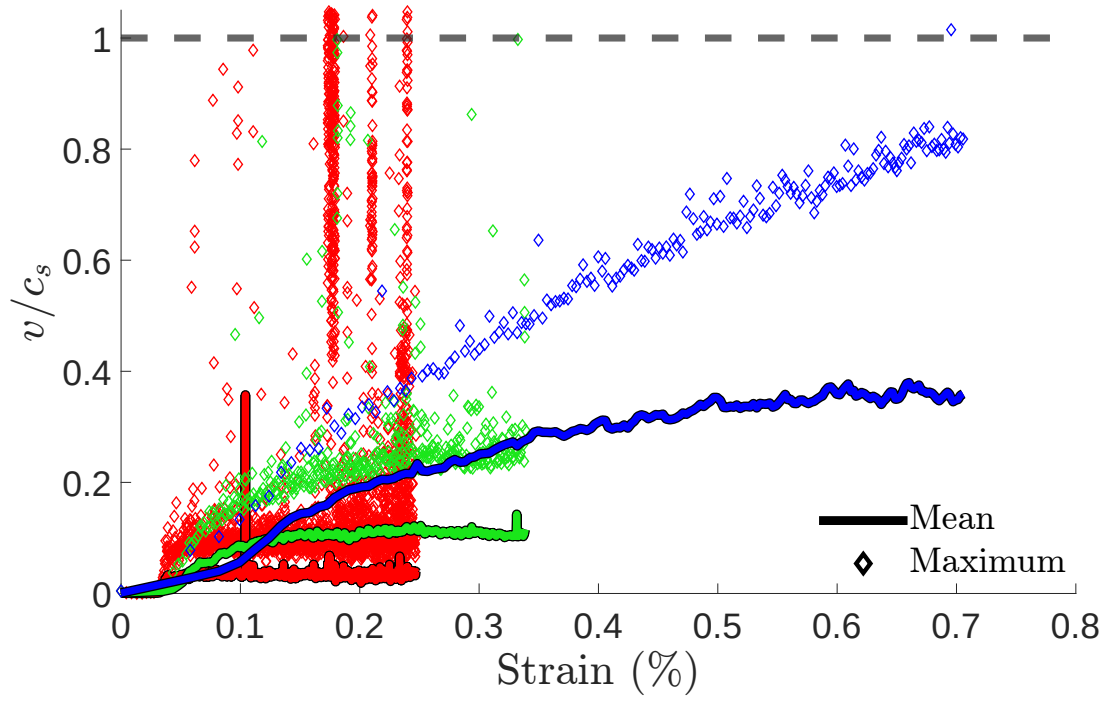


(a)

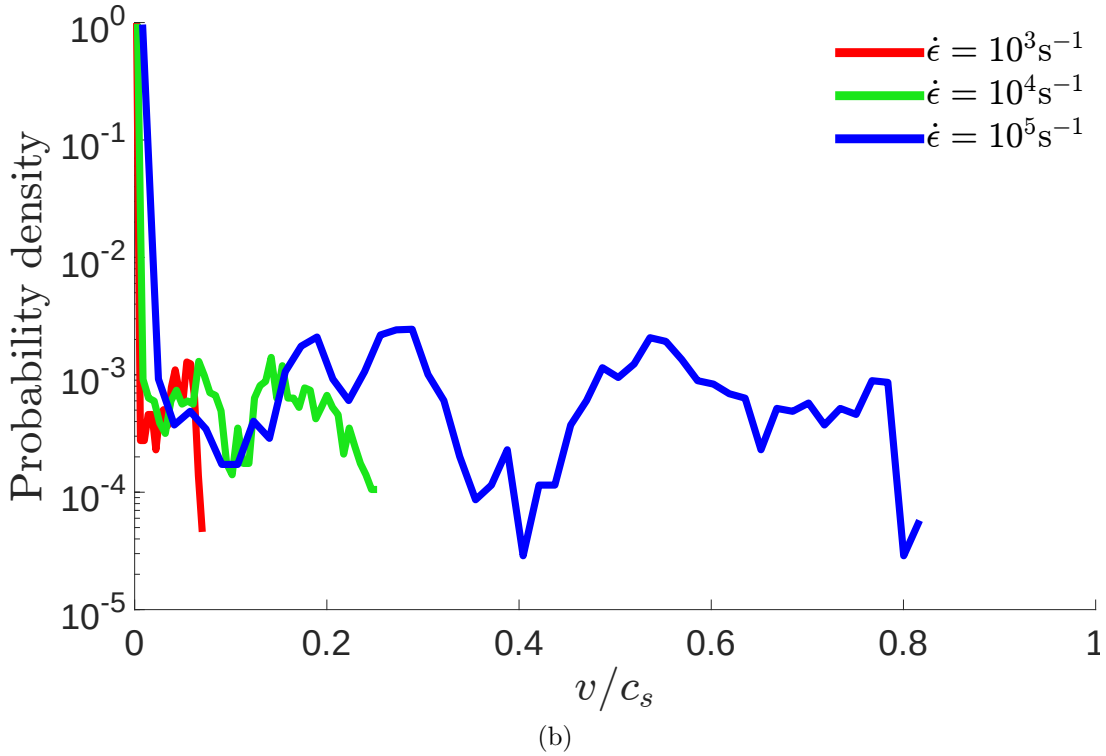


(b)

Figure 6.27: Plots pertaining to the basal-prismatic simulations. (a) The (1) cumulative CPU time and (2) number of internal (solid lines) and total (dashed lines) segments as a function of strain for all cases. (b) The time-step size as a function of strain for the $N_s = 6$ cases.



(a)



(b)

Figure 6.28: Plots pertaining to the basal-prismatic $N_s = 6$ simulations. (a) The mean (solid lines) and maximum (open diamonds) nodal speeds as a function of strain. The horizontal dotted line represents the prismatic transverse sound wave velocity $v = c_s$. (b) The probability densities of the nodal speeds at yield.

from red (pure edge) to yellow (pure screw) and prismatic dislocations are depicted with colours ranging from blue (pure edge) to cyan (pure screw). Junction nodes (those with more than 2 connections) are represented as thick black circles.

Four simulations were conducted by varying the strain rate $\dot{\epsilon}$ and number of sources N_s, and each was run until the yield point was reached. The simulated cases were:

$$(\dot{\epsilon}, N_s) = \left(10^3\,\mathrm{s}^{-1}, 6\right), \left(10^4\,\mathrm{s}^{-1}, 6\right), \left(10^5\,\mathrm{s}^{-1}, 6\right), \left(10^4\,\mathrm{s}^{-1}, 60\right)$$

Figure 6.20 displays all stress-strain curves for these simulations, while figure 6.21 displays the corresponding dislocation densities as functions of strain. Because of its high strain rate and the corresponding strain rate hardening, the $(\dot{\epsilon}, N_s) = (10^5\,\mathrm{s}^{-1}, 6)$ case appears to reproduce the experimental yield stress. However, the experiment was conducted under effectively quasistatic loading conditions and therefore did not exhibit any strain rate hardening effects. Simulating such low strain rates directly is computationally prohibitive. A common approach to approximate quasistatic loading is to conduct convergence tests on the strain rate parameter for a given initial dislocation density [237, 192]. In addition, a simulation can be configured such that its $\mathcal{P}$ parameter lies within the Taylor hardening regime, where the macroscopic response is independent of the strain rate.

Only the $(\dot{\epsilon}, N_s) = (10^3\,\mathrm{s}^{-1}, 6), (10^4\,\mathrm{s}^{-1}, 60)$ cases exhibit an approximately constant axial stress at yield, which corresponds to a steady dislocation density. It is expected that the remaining cases would also show this behaviour at higher strains. Figure 6.22 displays snapshots of the dislocation networks at $\epsilon = 0.1\%$ strain and at yield for the $N_s = 6$ cases. As expected, dislocations become fixed and accumulate at the displacement-controlled surfaces. However, at these surfaces, some non-fixed segments appear to exit the domain without correctly transforming into virtual segments. Although these segments lie outside the domain, they continue to exert stress as if they were internal segments. This behaviour represents a previously unreported bug in EasyDD of unknown origin. However, since typically only a fairly small number of non-virtual segments appear outside the domain, this bug is expected to have a small impact on the important results. Conversely, no surface hooks, spurious off-plane segments, surface crescents, or overlapping segments are present in any of the network snapshots.

A drop in axial stress is observed at the onset of plastic flow in the $(\dot{\epsilon}, N_s) = (10^4\,\mathrm{s}^{-1}, 60)$ case. Initially, dislocations are activated from the weakest slip system, the strength of which controls the point at which plastic flow begins. In conjunction with the subsequent activation of additional slip systems with little resistance, and owing

to the large number of sources, this leads to substantial plastic slip and a transient reduction in axial stress. The system gradually transitions into a steady-state plastic flow regime, in which a balance is reached between the multiplication and flow of dislocations, their escape from the crystal, and dislocation-dislocation interactions. It is expected that increasing the source sizes would reduce the magnitude of the axial stress drop. This interpretation is in part supported by the corresponding individual dislocation densities shown in figure 6.23, which show that the slip system with the lowest activation stress, 3Ba, is activated at the onset of plastic flow. This is followed by the activation of 2Ba and 2Pr at higher strains, coinciding with the reduction in axial stress and the transition into the steady-state plastic flow regime. Notably, these secondary slip systems are activated even though their activation stresses are considerably higher than the axial stress, suggesting that their activation may be enabled by local elastic stress concentrations. Some large initial oscillations can be seen in the 3Ba dislocation density which eventually subside. This oscillatory behaviour is likely unphysical and arises from the nature of the isolated prismatic loop sources. The initial activated slip systems repeatedly generate relatively unimpeded dislocation loops, temporarily increasing the dislocation density, while the subsequent exit of these loops from the domain leads to corresponding decreases. Although this phenomenon is unphysical, it disappears once the system enters the steady-state plastic flow regime, indicating that its impact on the important results is minor.

Figure 6.24 displays the dislocation network at yield for the $N_s = 60$ case. To facilitate the identification of surface hooks and other spurious artefacts, this network is visualised from a line of sight aligned with (1) $\boldsymbol{b}_2$ and (2) the basal plane normal vector, providing a view perpendicular to the normal of the basal and prismatic planes, respectively. Although a small fraction of the network consists of spurious off-plane segments, no other visually observable artefacts are present. Several junctions can also be identified. Figure 6.25 displays a histogram of the internal segment lengths. The majority of segment lengths are between L_{min} and L_{max}, but a small fraction have lengths below L_{min} which is necessary to accurately resolve separation reactions. Segments longer than L_{max} correspond to the fixed segments composing prismatic loop sources. Furthermore, the dislocation-induced surface displacement field is plotted in figure 6.26. In addition to elastic displacements, this plot includes plastic slip steps generated by dislocations exiting the domain. Note that, although the colour bar reflects total displacements at the correct scale, surface displacements are visually magnified by a factor of 100 for clarity. As expected, most slip steps lie parallel to the basal plane. Relative to the fixed end of the sample, the surface is

displaced primarily in the $\boldsymbol{b}_3$ direction, which is consistent with the 3Ba slip system being the first to activate and typically exhibiting the highest dislocation density.

Figure 6.27a displays the cumulative CPU time and number of segments (both total and internal) as functions of strain. The total number of segments was tracked during the simulations, but the number of internal segments was estimated by assuming that the average internal segment length for all cases was $709b$, which is the average internal segment length at yield in the $(\dot{\epsilon}, N_s) = (10^4\,\mathrm{s}^{-1}, 60)$ case. It is notable that, in all cases, the total number of segments appears to approach a stable linear growth as the strain increases.

The cumulative CPU time was calculated using the MATLAB function `cputime`, which returns the sum of computation time across all CPU threads and accounts for pauses caused by latency due to background computer processes. However, since the simulations were performed on different computers and CPUs, some ran slower than others, which obfuscates the comparison. Nevertheless, these plots still provide an approximate first comparison of computational efficiency.

Let us for the moment restrict our attention to the $N_s = 6$ cases. The corresponding cumulative CPU time curves generally exhibit smooth accelerating growth except for the $\dot{\epsilon} = 10^3\,\mathrm{s}^{-1}$ case, which shows irregularities beginning at approximately $\epsilon \approx 0.17\%$ strain. Figure 6.27b displays a comparison of the time-step sizes as functions of strain. For increased visibility, Gaussian smoothing was applied to each plot, using a moving average filter with a window containing 40 elements. At sufficiently high strain, the average time-step size decreases as the strain rate increases—this is likely due to higher resolved shear stresses and, consequently, higher dislocation velocities. In addition, as the strain rate decreases, the time-step size evolution becomes increasingly noisy. The $\dot{\epsilon} = 10^3\,\mathrm{s}^{-1}$ case exhibits a notable decrease in time-step size at approximately $\epsilon \approx 0.17\%$ strain, coinciding with the onset of irregularities in the corresponding cumulative CPU time curve.

Because the time-step size is closely related to the maximum nodal speed, this irregularity was further investigated through the maximum and mean nodal speeds, which are plotted as functions of strain in figure 6.28a. Since the tracked nodal velocities include components along segment line directions, they necessarily overestimate the actual dislocation velocity. However, it is encouraging that the mean nodal speeds all remain below $0.4c_s$, indicating that the employed linear mobility law agrees well with MD data on average (see figure 6.13). Furthermore, figure 6.28b displays nodal speed distributions at yield, which shows that the vast majority of nodes move relatively slowly (more than 96% are below $0.02c_s$ for $\dot{\epsilon} = 10^5\,\mathrm{s}^{-1}$), as

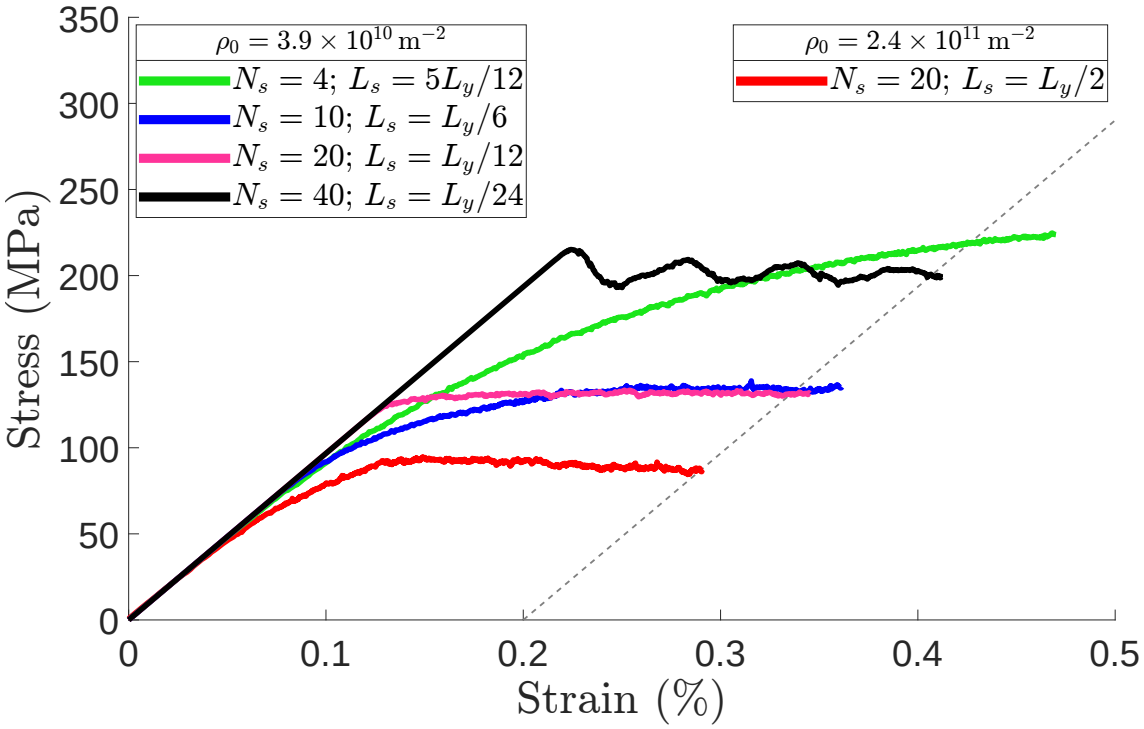


Figure 6.29: Stress-strain curves corresponding to all pure prismatic simulations. The slanted dotted line represents the 0.2% offset yield criterion.

expected. This supports the validity of applying the linear mobility law within this strain rate hardening regime.

As the strain rate increases, both the mean speed and the amount of noise in the maximum speed increases. At approximately $\epsilon \approx 0.17\%$ strain, the maximum speeds in the $\dot{\epsilon} = 10^3\,\mathrm{s}^{-1}$ case become very large and noisy relative to the mean speeds, explaining the decrease in time-step size and the irregularities in the cumulative CPU time observed at this strain level. At the time of writing, the cause of these unusually high nodal speeds at lower strain rates in EasyDD remains unclear. Since this behaviour leads to smaller time-step sizes, it may be a contributing factor to reduced computational efficiency.

6.3.2 Pure prismatic slip

Assuming pure prismatic slip, the critical resolved shear stress (CRSS) inferred from the current experiment is approximately 56 MPa – 108 MPa[9], which is substantially higher than the experimental value for room temperature pure Zr (less than 200 ppm

[9]This range of values was obtained by taking the average of the experimental yield stresses and using the range of Schmidt factors for prismatic slip.

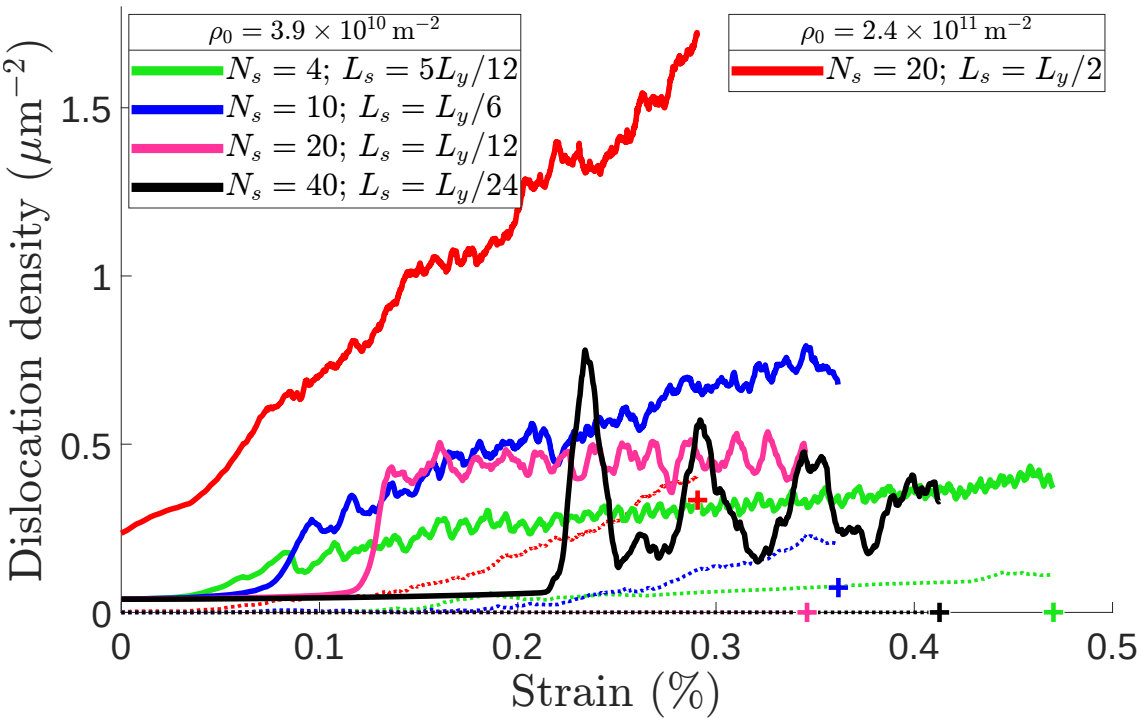


Figure 6.30: Plots of tracked total (solid lines) and 3Pr (dotted lines) dislocation densities corresponding to all pure prismatic simulations. The markers (plus signs) approximate the actual 3Pr dislocation density—computed post-simulation while neglecting all fixed segments—at the highest strain recorded in each case.

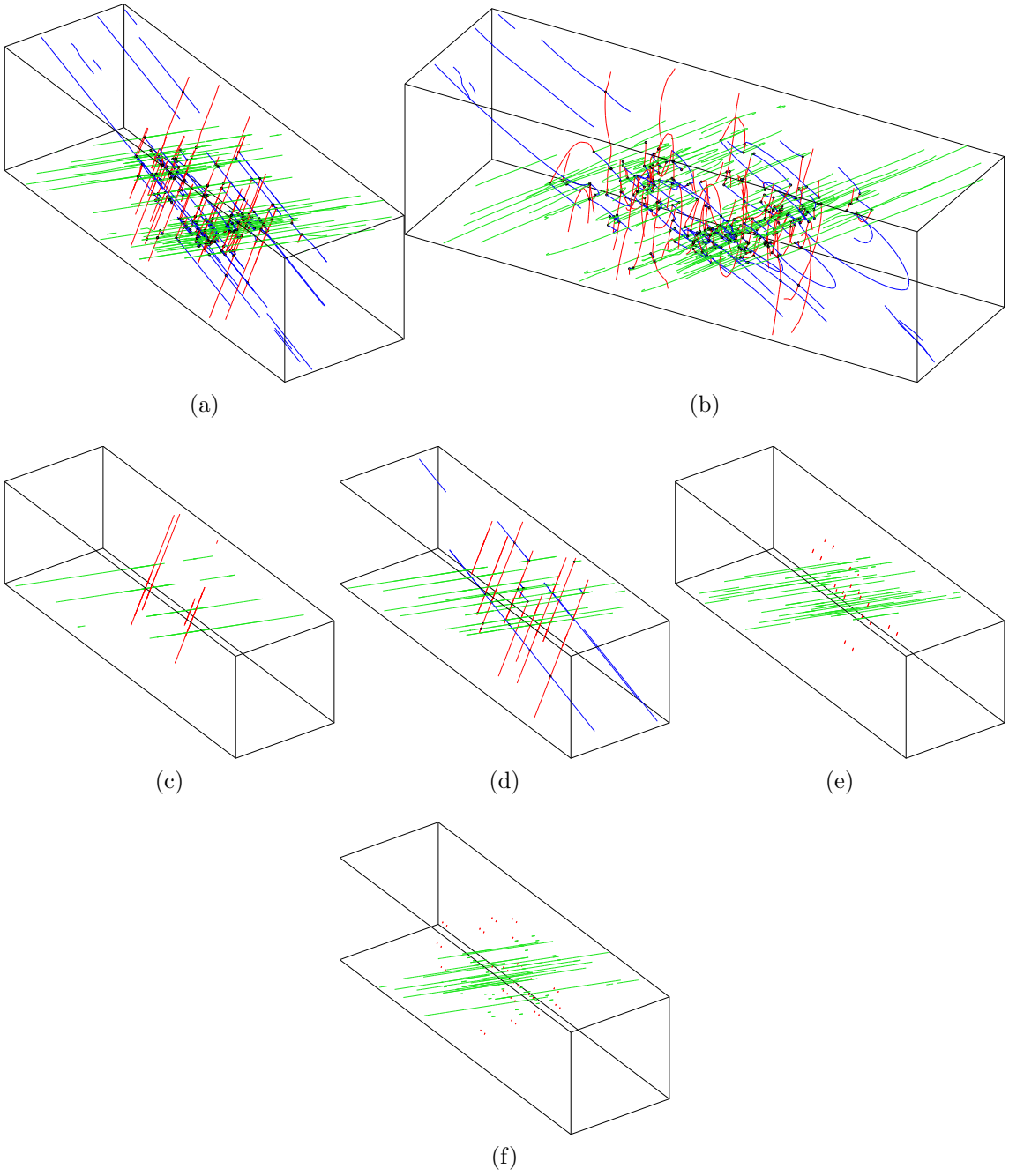


Figure 6.31: Internal dislocation network snapshots pertaining to all pure prismatic simulations at yield. (a) and (b): $(N_s, L_s) = (20, L_y/2)$; (c): $(N_s, L_s) = (4, 5L_y/12)$; (d): $(N_s, L_s) = (10, L_y/6)$; (e): $(N_s, L_s) = (20, L_y/12)$; (f): $(N_s, L_s) = (40, L_y/24)$. In all figures, the leftmost $5\,\mu\text{m} \times 5\,\mu\text{m}$ face is the one corresponding to the zero-displacement boundary condition. 1Pr, 2Pr, and 3Pr segments are respectively represented as red, green, and blue lines. Thick black circles represent junction nodes.

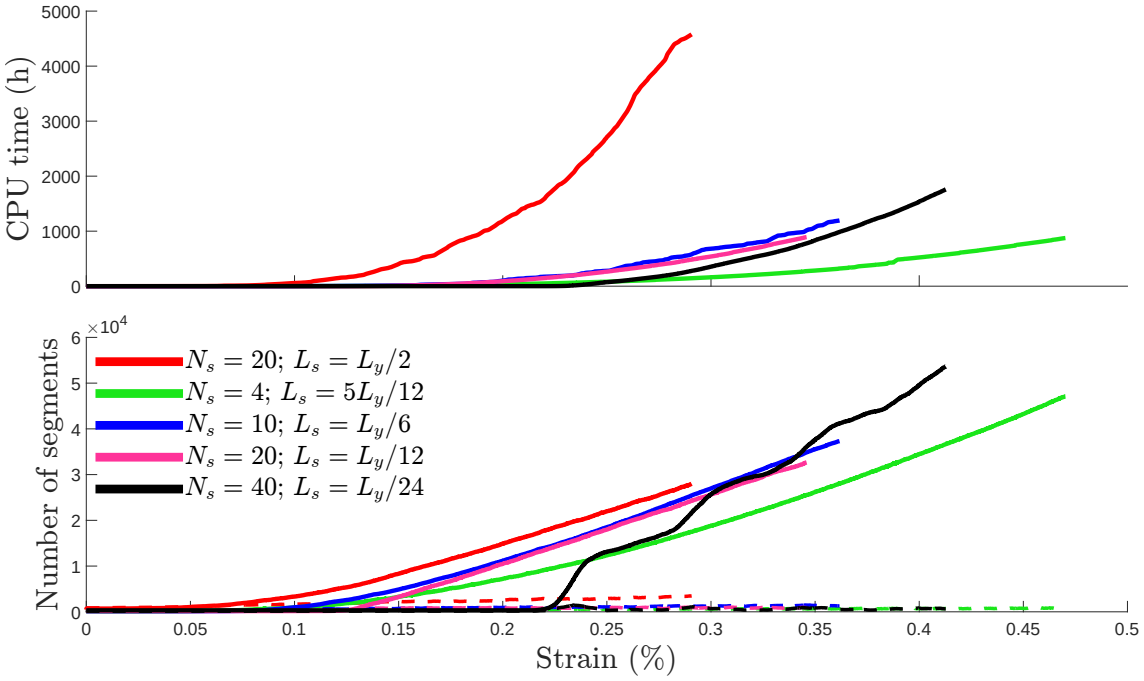


Figure 6.32: Plots of the (1) cumulative CPU time and (2) number of internal (solid lines) and total (dashed lines) segments as a function of strain corresponding to all pure prismatic simulations.

oxygen) of approximately 10 MPa – 20 MPa [328, 297, 113, 116]. On the other hand, as the loading direction aligns with the $\langle c \rangle$ direction at room temperature, mechanical twinning becomes the dominant deformation mode [113], which is associated with a higher CRSS than that of prismatic slip in untwinned HCP Zr [329]. Considering the relatively low Schmidt factors of the prismatic slip systems, it is therefore possible that twinning was present in the current experiment. Alternatively, the initial dislocation density could have been large—an estimate is not available at the time of writing.

Assuming that the crystal was untwinned and noting that the experiment was conducted under effectively quasistatic loading, the Taylor relation (equation (1.1)) predicts a dislocation density of approximately $\rho \approx 4 \times 10^{14}\,\mathrm{m}^{-2}$ ($\mathcal{P} \approx 3 \times 10^{8}$) at yield. Accessing useful strains at such high dislocation densities and large domain volumes is computationally infeasible with many available 3D DD frameworks [101], including EasyDD. At present we therefore abandon the goal of reproducing the experimental stress-strain curves within the Taylor hardening regime.

In this section, the objective is to (1) investigate the influence of the source number N_s and size L_s on the dislocation dynamics, and (2) generate additional simulation data to further validate the EasyDD code. Only $\langle a \rangle$-type prismatic slip systems

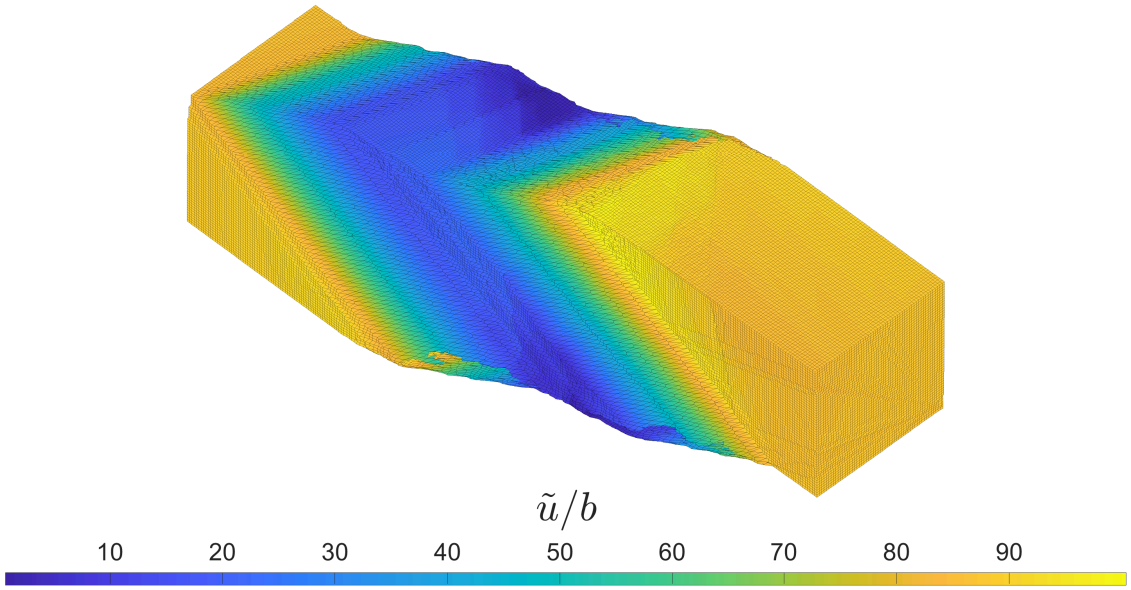


Figure 6.33: Plot of the dislocation-induced displacement field $\tilde{u}$ on the domain surface corresponding to the pure prismatic $(N_s, L_s) = (20, L_y/2)$ simulation at yield. Surface displacements are plotted on a mesh and are magnified by a factor of 100 for clarity, but the colour bar scale is unchanged. The rightmost 5 µm × 5 µm face is the one corresponding to the zero-displacement boundary condition.

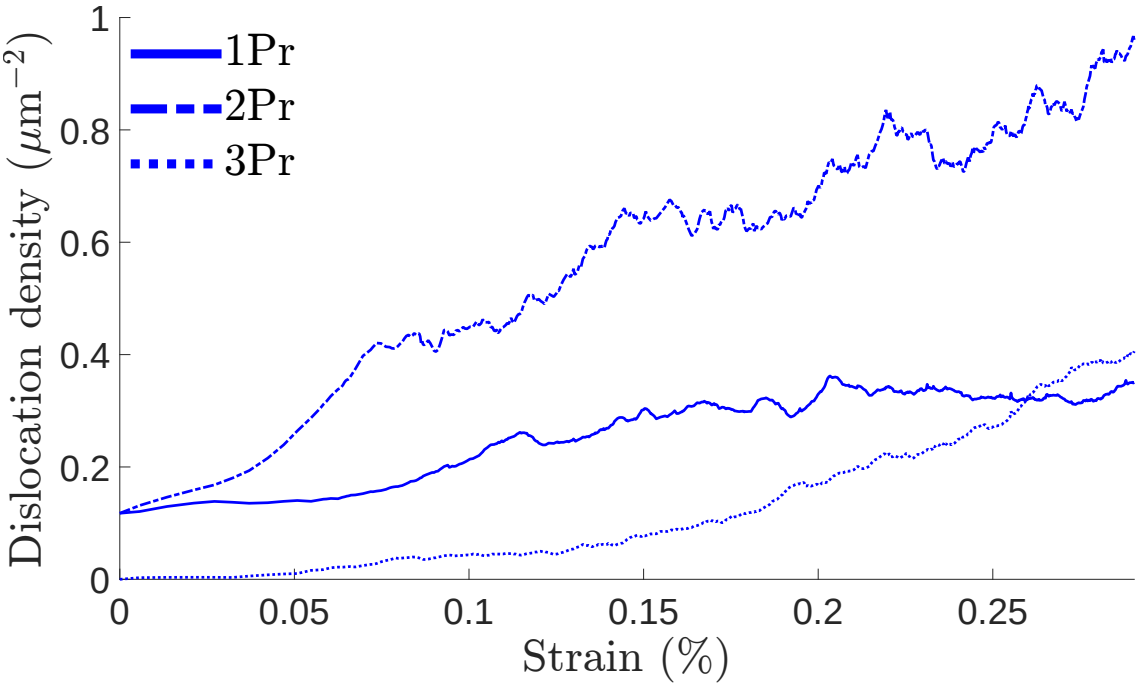
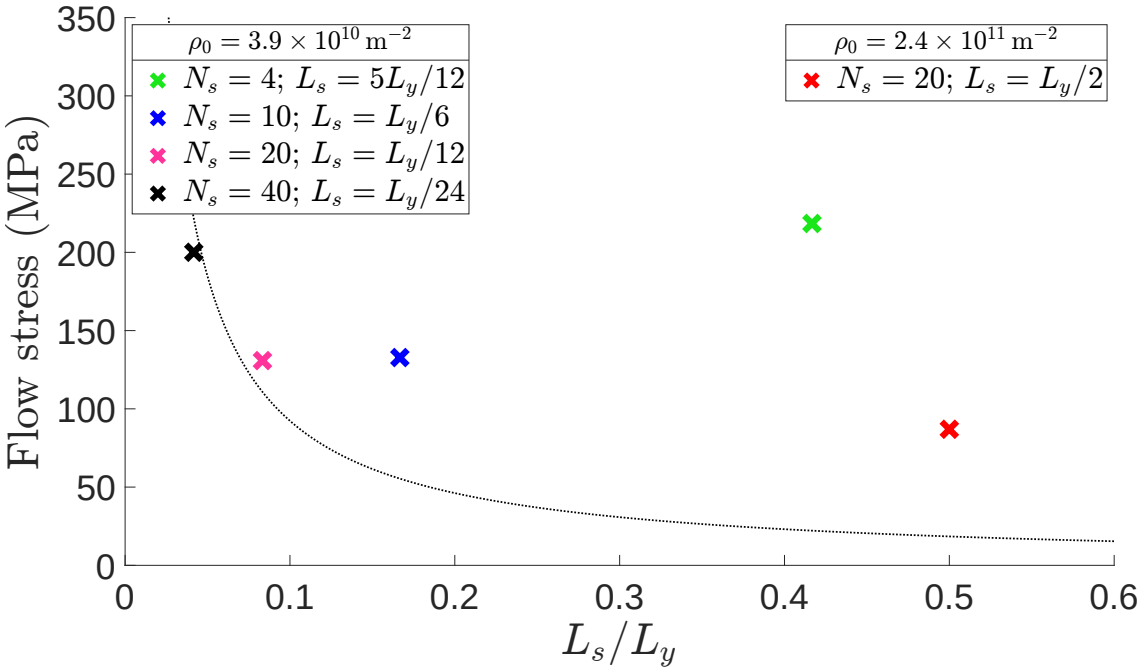
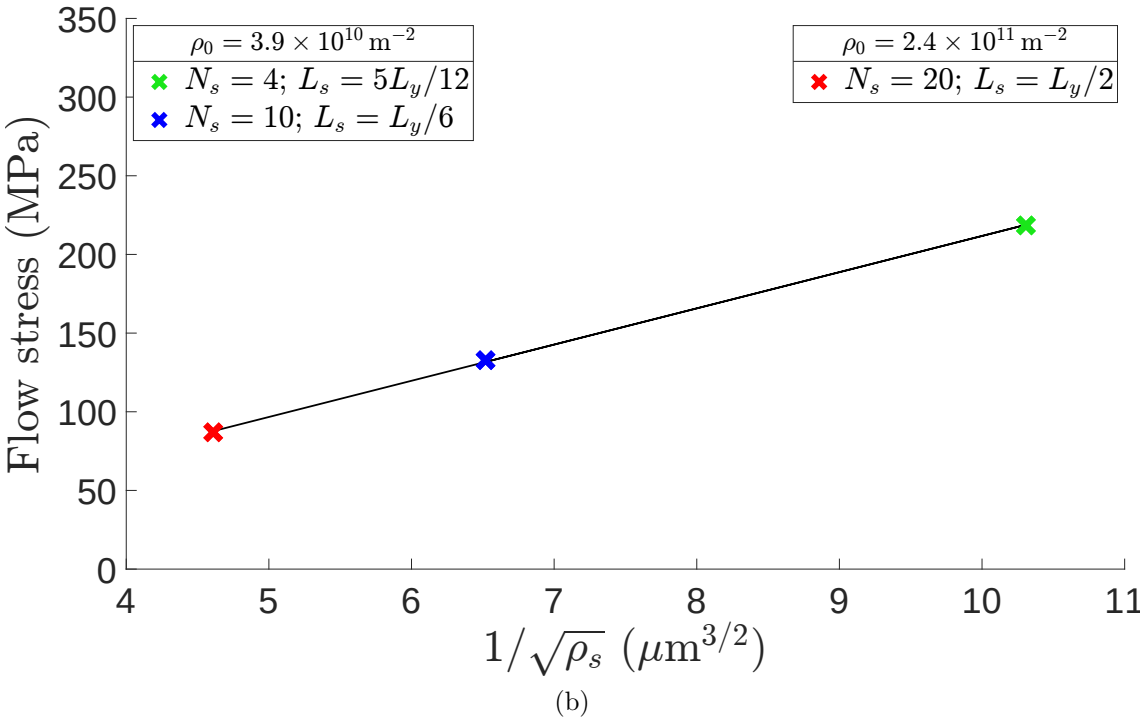


Figure 6.34: Plots of tracked dislocation densities of individual slip systems corresponding to the pure prismatic $(N_s, L_s) = (20, L_y/2)$ simulation.



(a)



(b)

Figure 6.35: (a) Flow stress at yield as a function of normalised source size corresponding to all pure prismatic simulations. The curved dotted line represents the source strength $\sigma_s \approx \mu b/mL_s$ of the weakest slip system (2Pr). (b) Flow stress at yield as a function of $1/\sqrt{\rho_s}$ corresponding to the pure prismatic simulations outside the source activation controlled regime. The straight line represents the line of best fit.

are included to more closely resemble the experimental conditions. This restricts the DD simulations to three slip systems: 1Pr, 2Pr, and 3Pr. Only the $n\text{Pr} - m\text{Pr}$ non-coplanar reaction is possible. The strain rate is always $\dot{\epsilon} = 10^4\,\text{s}^{-1}$. The number of FE nodes in each coordinate direction are given by $(N_x, N_y, N_z) = (30, 16, 16)$.

Because large prismatic loop sources are involved in the simulations conducted in this section, the stresses generated by fixed segments are disabled. Since EasyDD currently lacks the capability to distinguish between different types of fixed segments, the stresses generated by fixed segments that have collided with displacement-controlled surfaces are also disabled. This manner of treating displacement-controlled surfaces is expected to lead to an overestimation of dislocation mobility. However, since only a relatively small fraction of the dislocation network is expected to collide with these surfaces during a typical simulation, this discrepancy is expected to have a limited impact on the important dislocation dynamics. To minimise artefacts arising from such collisions and increase computational efficiency, sources associated with 3Pr slip systems are excluded, as the corresponding slip planes always intersect displacement-controlled surfaces. Consequently, the 1Pr and 2Pr slip systems are each always initialised with $N_s/2$ prismatic loop sources. However, the 3Pr slip systems naturally arise during the simulations though dislocation-dislocation reactions. Note that, although tracked dislocation densities exclude fixed segments composing prismatic loops, they include fixed segments that have collided with displacement-controlled surfaces, meaning that 3Pr dislocation densities (as depicted in figures 6.30 and 6.34) are often overestimated.

Throughout this section, the following colour scheme is used to represent dislocation lines: 1Pr dislocations are red, 2Pr dislocations are green, and 3Pr dislocations are blue. Junction nodes (those with more than 2 connections) are represented as thick black circles.

Five simulations were conducted by varying the number N_s and size L_s of sources, and each was run until the yield point was reached. The simulated cases were:

$$(N_s, L_s) = (20, L_y/2)\,, (4, 5L_y/12)\,, (10, L_y/6)\,, (20, L_y/12)\,, (40, L_y/24)$$

The $(N_s, L_s) = (20, L_y/2)$ case exhibits an initial dislocation density of $\rho_0 \approx 2.4 \times 10^{11}\,\text{m}^{-2}$, while the remaining four cases each exhibit identical initial dislocation densities of $\rho_0 \approx 3.9 \times 10^{10}\,\text{m}^{-2}$, but with varying source number and size. These parameter selections are intended to, in part, sample the statistical variation exhibited in a pinning point free dislocation network.

Figure 6.29 displays all stress-strain curves for these simulations, and figure 6.30 displays the corresponding dislocation densities (both total and 3Pr) as functions of strain. The dislocation density plots include markers approximating the actual 3Pr dislocation density—computed post-simulation while neglecting all fixed segments—at the highest strain recorded in each case. These markers provide a rough indication of the degree to which the 3Pr dislocation densities were overestimated. Evidently, the 3Pr slip system is at least moderately present in the $(N_s, L_s) = (20, L_y/2)\,, (10, L_y/6)$ cases, and at most negligibly present in the remaining cases. This observation, together with the approximately constant axial stresses at yield in the former cases, suggests that the 3Pr slip system becomes sufficiently active in those cases to sustain a steady-state plastic flow. Figure 6.31 displays snapshots of the dislocation networks at yield for all cases. Segments that are fixed or that lie outside the domain are not included in the visualisations. All networks are error-free except for the $(N_s, L_s) = (20, L_y/2)$ case, which contains a discernible fraction of spurious off-plane segments. This case exhibits more errors than the others due to its higher dislocation density, corresponding to an increased number of collisions and, consequently, an increased number of opportunities for the formation of spurious junction orientations and incorrect normal vector assignments.

Figure 6.32 displays the cumulative CPU time[10] and number of segments (both total and internal) as functions of strain. The number of internal segments was estimated by assuming that the average internal segment length for all cases was $740b$, which is the average internal segment length at yield in the $(N_s, L_s) = (20, L_y/2)$ case. The curves exhibit similar qualitative behaviours to those of most of the basal-prismatic simulations, and no major irregularities are present. The dislocation-induced surface displacement field for the $(N_s, L_s) = (20, L_y/2)$ case is plotted in figure 6.33. Most slip steps lie parallel to the 2Pr plane, although other slip step directions are faintly visible as well. Relative to the fixed end of the sample, the surface is displaced primarily in the $\boldsymbol{b}_2$ direction. This is consistent with the 2Pr slip system being the first to activate and exhibiting the highest dislocation density, as shown in figure 6.34.

Figure 6.35a displays the flow stress at yield for each simulation as a function of source size, with the source strength $\sigma_s \approx \mu b/mL_s$ corresponding to the weakest slip system (2Pr) superimposed. The $(N_s, L_s) = (10, L_y/6)\,, (20, L_y/12)$ cases, which have the same initial dislocation density ρ_0, exhibit nearly identical flow stresses even though all slip systems are active in the former case and only the weakest slip

[10]The $(N_s, L_s) = (20, L_y/2)$ simulation ran for a total of approximately 22 wall clock days.

system is active in the latter case. Both the $(N_s, L_s) = (20, L_y/12), (40, L_y/24)$ cases exhibit flow stresses close to the weakest source activation stress and contain only the weakest slip system as active, implying that they are partially or entirely controlled by the strength of the weakest sources. Notably, the $(N_s, L_s) = (20, L_y/12)$ case in particular has source characteristics that closely satisfy the constraints imposed by equations (6.21) and comes closest to achieving perfect plasticity.

The results presented in this section likely contain insufficient data to support robust, definitive conclusions regarding the connection between source characteristics and flow stress under the current conditions. Nevertheless, the available evidence suggests that, as source sizes become sufficiently small, the flow stress becomes controlled by the strength of the weakest sources in accordance with equation (6.14) up to a multiplicative constant. This trend is in agreement with prior 2D [316, 317] and 3D [302] DD studies. Furthermore, figure 6.35b displays the flow stress for the three cases outside the source activation controlled regime (i.e. cases $(N_s, L_s) = (20, L_y/12), (40, L_y/24)$ are excluded) as a function of $1/\sqrt{\rho_s}$; a line of best fit is superimposed. These results agree with the hypothesis presented by equation (6.18) with $q \approx 1$. Although these preliminary results are encouraging and partially validate the capability of EasyDD to capture source-limited strengthening, additional data collection is required to elucidate the relationship between source characteristics and flow stress in HCP Zr beyond the source activation controlled regime (i.e. within the source strength independent regime).

Because 3Pr sources are excluded, these slip systems can only arise from dislocation reactions, which is largely a statistical phenomenon that depends on relative source orientations. As N_s decreases, so does the probability per unit time that such a reaction will occur. In the $(N_s, L_s) = (20, L_y/2), (10, L_y/6)$ cases, in which there are many sources, all three slip systems are active in the limiting steady-state plastic flow regime. Conversely, in the $(N_s, L_s) = (4, 5L_y/12)$ case, in which there are few sources, the 3Pr slip system is unable to become sufficiently active to sustain a significant plastic flow at yield. Finally, in the $(N_s, L_s) = (20, L_y/12), (40, L_y/24)$ cases, only the slip system corresponding to the weakest sources activates, suggesting that 3Pr (i.e. the hardest slip system) sources would remain inactive even if present. The exclusion of 3Pr sources may influence the dislocation dynamics in the source strength independent regime. Nonetheless, it is notable that the simulation outcome of the $(N_s, L_s) = (4, 5L_y/12)$ case aligns with the trend prediction of the other data points plotted in figure 6.35a despite the absence of the 3Pr slip system. Future in-

vestigations should include 3Pr sources to ensure that the complete system dynamics and statistics are captured.

The stress-strain and dislocation density curves for the $(N_s, L_s) = (40, L_y/24)$ case exhibit an oscillatory mode that differs significantly from the other cases. This behaviour is associated with intermittent dislocation strain bursts which occur when the axial stress exceeds the activation stress of the weakest slip system. The bursts result in a transient increase of the dislocation density (see figure 6.30) and plastic flow, thus reducing the axial stress. When the axial stress falls below the activation stress of the weakest slip system, dislocation multiplication is interrupted, the remaining dislocations exit the crystal, the dislocation density decreases, plastic flow is diminished, and, in turn, the axial stress increases. This cycle repeats with decaying amplitudes, and the simulation appears to approach a roughly steady-state configuration when the yield point is reached. Noting that cases with larger sources exhibit smoother transitions from plastic flow onset to their limiting flow stress (see figure 6.29), the behaviour described here is expected to occur in the source activation controlled regime (cases $(N_s, L_s) = (20, L_y/12), (40, L_y/24)$), and oscillatory modes are hypothesised to become increasingly prominent as the source strength increases, although further simulations are required to confirm this. Such behaviour—associated with dislocation strain bursts—has been observed in experimental [306, 330] and DD [302, 308, 331, 332, 237] investigations of single crystal uniaxial loading, and has been in part correlated with smaller crystal and source sizes.

Although all simulations broadly follow the strain rate dependent model, the $(N_s, L_s) = (20, L_y/12)$ case deviates slightly more from its prediction compared to the other cases, as seen in figure 6.36. Both this case and the $(N_s, L_s) = (40, L_y/24)$ case exhibit zero 3Pr dislocation density and also notable oscillations in the total dislocation density. Furthermore, the axial stress at yield is roughly constant in these cases, indicating that deviations from the model prediction are largely controlled by the dislocation density parameter which fluctuates about a moving average. Although not directly shown here, the total dislocation density of the $(N_s, L_s) = (20, L_y/12)$ case at yield lies at the bottom of a trough—using its higher average dislocation density would bring this case closer to the model prediction. Therefore, although local deviations can occur, the simulation outcome generally agrees with the model prediction on average.

It should be noted that the dimensionless data transformation (equation (6.16)) depends (somewhat weakly) on the effective Schmidt factor. Because different slip system combinations were activated in different simulation cases, it is not clear

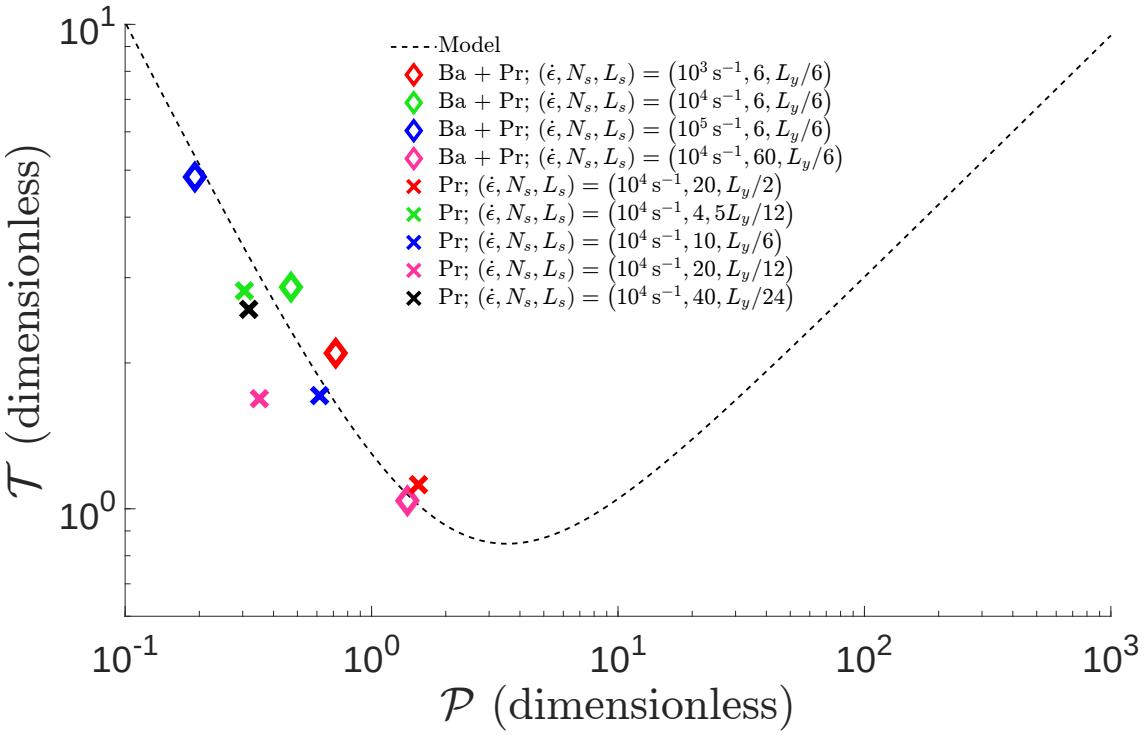


Figure 6.36: Comparison between the strain rate dependent model [309] prediction (equation (6.16)) and data at yield pertaining to all large-scale DD simulations presented in this chapter. It is assumed that $f_a = 1$, $\alpha = 0.3$, $B = B^{\mathrm{glide}}_{\mathrm{edge}}(\mathrm{Pr})$, $m \approx 0.246$ for simulations containing both basal and prismatic slip, and $m \approx 0.169$ for simulations containing only prismatic slip.

whether defining the effective Schmidt factor as the arithmetic mean of all three possible slip systems is appropriate. Perhaps a more consistent choice may be to define it as the mean of only the slip systems that are active in a given case. Such an adjustment would either increase or leave unchanged the effective Schmidt factor relative to the one used here. This may reveal a discrepancy that can be accounted for by including size effects into the model prediction. In future work, finite-domain simulations should be conducted with equal Schmidt factors across all slip systems through an appropriate choice of crystal orientation to eliminate this ambiguity. Nevertheless, as a first stage of validation, it is encouraging that both the position and slope trend of the simulation data agree well with the model prediction.

6.4 Conclusions

The main objective of this chapter was to model experimental tensile tests of HCP zirconium using the 3D DD code EasyDD. A range of strain rates, source numbers,

and source sizes were tested to assess the model's accuracy, stability, and capacity to yield a plastic response. This is a critical step towards building a physics-based understanding of mesoscopic-scale plasticity in zirconium, with the long-term goal of enabling extrapolation to regimes beyond those easily accessible through experiment.

In section 6.3.2, the impact of source number and size was investigated. It was found that below a critical source size—the specific value of which likely depends on at least the source density—the flow stress appeared to be largely controlled by the strength of the weakest sources. Above this critical source size, the flow stress was shown to scale proportionally with $1/\sqrt{\rho_s}$. These observations align with previous DD studies [316, 317, 302, 65], demonstrating the capability of EasyDD to represent source-limited strengthening. However, further data collection is required to draw definitive conclusions. At the time of writing, no studies have been identified which have validated the flow relation described by equation (6.18) in HCP materials using 3D DD modelling.

An important avenue for future extensions to this work would be to more clearly delineate how the source characteristics and strain rate together determine the flow stress in finite-domain HCP Zr, within the strain rate hardening regime or otherwise. In future work, 3Pr sources should be included to ensure that the full system dynamics are captured, and the distribution of source sizes could also be varied to understand its impact on the flow stress. This could provide insights into the distribution of source characteristics when the dislocation network topology is unknown, such as when only macroscopic data is available. It could also guide the selection of initial conditions for simulations that employ isolated Frank-Read sources so as to better reproduce the behaviour of more realistic dislocation networks featuring pinning point free sources.

Among all errors documented in section 6.2.3, only spurious off-plane segments were observed in the dislocation networks presented in this chapter. Simulations with fewer active non-coplanar slip systems contained fewer errors because they exhibited fewer non-coplanar collisions, and thus fewer opportunities for incorrect normal vector assignments. It is unlikely that further modifications to the mobility law alone can resolve this issue. The underlying problem lies in the nodal splitting procedures, and addressing it would require substantial investigation and redevelopment. Nevertheless, at the dislocation densities considered in this chapter (less than $2\times10^{12}\,\mathrm{m}^{-2}$), EasyDD exhibits an exceptional predictive accuracy that has been validated against the strain rate dependent model (equation (6.16)), as shown by figure 6.36. It is also notable that, although some of the stress-strain curves in this chapter do not reach a fully

constant axial stress at yield, the corresponding simulations still agree closely with this model, demonstrating its robustness. Furthermore, even though the model neglects size-dependent effects, it still accurately predicts the simulations presented in this chapter. Incorporating size-dependent plasticity terms may further enhance its predictive capability for smaller crystal sizes.

Stage II strain hardening [17] is largely governed by junction formation, and DD studies have reported that the associated strain hardening rate is fairly insensitive to the applied strain rate [174]. Junction-mediated strengthening becomes increasingly relevant as systems progress further into the Taylor hardening regime, where an increasing number of dislocation reactions results in an increasing number of junctions. Since the simulations conducted in this chapter exhibited fairly low dislocation densities and did not extend far beyond yield, junction statistics and their role in strain hardening could not be assessed robustly. Accessing the Taylor hardening regime within the present domain volume would require dislocation densities that are too high to be simulated within a reasonable elapsed time using EasyDD. Accordingly, the analyses conducted in section 6.1 could not be directly applied in this text. On the other hand, EasyDD is certainly capable of accessing larger dislocation densities in smaller domain volumes, such as a subset of the domain volume considered in this chapter. An aim of future studies is to compute interaction coefficients for various slip system combinations, which could enable a more quantitative assessment of the role of junction formation. The interaction maps developed in this chapter will help explain hardening pertaining to specific dislocation reactions on a probabilistic basis and clarify/predict the outcomes of complex small-scale reactions.

As simulations increasingly approach the Taylor hardening regime and dislocation interactions and collisions become increasingly prevalent, spurious junction orientations and incorrect normal vector assignments are expected to increasingly compromise the simulation quality. Addressing this issue should be an aim of future work so that EasyDD can more accurately resolve the microstructural mechanisms needed to investigate strain hardening at high dislocation densities. Otherwise, under such conditions it may be preferable to adopt a different dislocation dynamics code that is better established within the materials modelling community. Future work should also explore the use of alternative, community-validated DD codes—such as ParaDiS or OpenDiS—that may be better equipped to simulate high-density, multi-slip HCP systems with greater numerical robustness and computational efficiency.

Chapter 7

Conclusion

At the time of writing, no studies have been identified which conduct large-scale DD simulations of defect-induced irradiation hardening in HCP Zr. Owing to the inherently multi-scale nature of irradiation hardening, such simulations—particularly in three dimensions—are significantly constrained by computational cost. Furthermore, no studies have been identified which conduct large-scale simulations of HCP Zr using a 3D DD model that is fully coupled to FEM. The central aims of this text are therefore to (1) develop a computationally efficient 2.5D DD model which is capable of investigating irradiation-induced hardening in materials containing large densities of prismatic loop defects and (2) to lay the foundations for an experimentally validated 3D DD-FEM model to study mesoscopic-scale plasticity in zirconium. This thesis contains contributions towards both ends.

In chapter 4, the HCP mobility law—originally developed by Aubry *et al.* [84]—was described and thoroughly elucidated. The implications of the basic framework were described, including the fact that the HCP drag tensor of a segment is not in general diagonal in the $\{\boldsymbol{l}, \boldsymbol{n}, \boldsymbol{m}\}$ basis (where $\boldsymbol{l}$ and $\boldsymbol{n}$ are respectively the line and normal vectors of the segment, and $\boldsymbol{m} = \boldsymbol{l} \times \boldsymbol{n}$). This represents an important departure with respect to standard non-HCP mobility laws, which typically incorporate a diagonal drag tensor in this basis. Furthermore, an extension was provided via a new free parameter, η, the addition of which is necessary to reproduce the elliptical shape of dislocation loops growing at dynamic equilibrium. Finally, a framework was devised to derive analytical relationships between the equilibrium shapes of loops exhibiting self-similar growth and their corresponding drag functions.

In chapter 5, a new 2.5D DD model for capturing aspects of irradiation hardening was introduced. First, the reaction outcome between a vacancy/interstitial loop and an edge dislocation was simulated using EasyDD, from which a coarse-grained microscopic interaction mechanism was identified for use in the 2.5D DD model.

Second, the angular stability and restoring force of prismatic loops of various sizes was determined through analytical and numerical calculations using the theory of linear isotropic elasticity. In addition, a mechanistic explanation for the dragging effect observed in double super-jogs is provided. Third, 2.5D DDP analyses of the stability of prismatic loops of differing sizes in samples strained to varying amounts were performed. In these 2.5D simulations, prismatic loops are represented as edge dipoles in which the effect of one dislocation on the other is replaced by the numerically calculated 3D restoring force to emulate realistic prismatic loop rotation physics. It was observed that the equilibrium tilt angle of smaller loops is less sensitive to external loading than that of larger loops, which may point to a mechanistic effect of loop size on irradiation hardening and dislocation channelling leading to local plastic strain softening. Using a simple single-slip model, loops were shown to demonstrably elevate flow stress, observed to increase with increasing loop density in accord with experimental observations of irradiation hardening. Furthermore, the important role of the out-of-plane loop segments, captured by the restoring force obtained from the 3D analyses, was revealed. It is concluded that the introduced 2.5D model captures many of the salient effects of dislocation-loop interactions, and hence provides a basis for examining these effects in detail in larger, more realistic boundary value problems relevant to irradiation damage in nuclear power applications.

In chapter 6, junction configurations relevant to $\langle a \rangle$-type basal and prismatic slip systems in Zr were investigated. Corresponding interaction maps for $n\text{Pr} - m\text{Pr}$, $n\text{Pr} - m\text{Ba}$, and $n\text{Pr} - n\text{Ba}$ were obtained using 3D DD simulations. It is notable that, for Zr, only the prismatic-prismatic interaction maps are available in the literature—the basal-prismatic interaction map calculations are new results. These interaction maps appear to closely match the ones calculated for other materials with similar elastic constants, such as HCP ice (which has a Poisson's ratio of approximately 0.33 [173], compared to 0.32 in Zr), which is expected. Furthermore, junction size maps were calculated using the line tension model, revealing asymmetries which cannot be inferred from binary junction maps alone—this is another new calculation. In addition, binary junction maps were calculated as a function of all physically realistic Poisson's ratios—the direct visual evidence of this dependence is a new result. These calculations also verify the expected conclusion that, as the Poisson's ratio decreases, the binary junction map symmetry increases for $n\text{Pr} - m\text{Pr}$ and $n\text{Pr} - m\text{Ba}$ interactions. For most interactions, the combined line tension and mutual force model very accurately predicted reaction outcomes, which serves as a validation of the DD code. It should be noted that the resistance of junctions to

external stress was not calculated in this text, although this has been included in the work of other authors [80] for a range of HCP materials. In a future work, other characteristics pertaining to forest interactions in Zr should be investigated—for instance, interaction maps which include pyramidal slip systems could be calculated. Furthermore, interaction coefficients incorporated in a Taylor hardening law could also be calculated, although this may require amendments to the functionality of EasyDD to enable bulk simulations.

Subsequently, large-scale 3D DD-FEM simulations were conducted to support experimental tensile tests of pure HCP Zr, thereby constituting the first of this kind of computational investigation. For this purpose, the HCP mobility law described in chapter 4 was implemented. Furthermore, several challenges were encountered and addressed during the development process. For instance, large efforts went into the mitigation of bugs which severely impact the simulation quality and lead to errors and unphysical phenomena. After a significant amount of tuning of the model—and particularly upon disabling climb—most of these bugs were repaired. Among all documented bugs, only spurious off-plane segments were observed in the simulations conducted in chapter 6; it is encouraging that, even in the worst case, these constituted only a small fraction of the entire dislocation network. Spurious off-plane segments were especially apparent when including large proportions of non-coplanar slip systems in the simulations. These types of errors fundamentally originate from the topological operations module of EasyDD, and it is unlikely that they can be properly addressed via further simple changes to the mobility law. Future work should address this issue to ensure that EasyDD can fully and accurately capture the microstructural mechanisms involved in simulations exhibiting high dislocation densities. Nevertheless, within the strain rate hardening regime, EasyDD was found to exhibit an excellent predictive capability that was validated against a strain rate dependent model [309].

For the large domain volume at which the experiment operated, the Taylor hardening regime remains computationally intractable with EasyDD. Consequently, the experiment could not be reproduced at quasistatic strain rates. In addition, because the DD simulations were conducted at fairly low dislocation densities and were interrupted at yield, the role of junction formation in strain hardening could not be assessed quantitatively. To access higher strains within the Taylor hardening regime, EasyDD may require further development to improve computational efficiency and to address the presence of spurious off-plane segments associated with junction formation events. Otherwise, it may be preferable to explore the use of alternative,

community-validated DD codes, which may be more robust for such applications. The investigations fulfilled in this chapter will also inform improvements to other DD codes to enhance their modelling predictive capabilities.

In chapter 6, source-limited strengthening of the experimental domain was investigated through large-scale 3D DD simulations. The results suggest that, when source sizes are sufficiently small, the flow stress is largely governed by the strength of the weakest sources. Outside this source activation controlled regime, the flow stress appears to scale with the inverse square root of the volumetric source density. These trends are consistent with current predictions of size-dependent and source-limited dislocation-mediated plasticity, providing an encouraging initial validation of EasyDD in accurately capturing these regimes. However, additional 3D DD simulation data is needed to robustly verify these findings. Future DD-based studies will focus on more comprehensively delineating the respective influences of source characteristics and strain rate on the flow stress in finite-domain HCP materials. Such investigations will help elucidate micro-mechanical deformation mechanisms in Zr, which is crucial for advancing its continued development as a nuclear material.

A fully experimentally validated 3D DD-FEM model for HCP Zr would provide a powerful tool for probing dislocation-mediated plasticity under varied conditions. Once validated, the model can be extrapolated to predict behaviour for different crystal orientations and loading geometries beyond the initial micro-tensile test case. For instance, due to the complex deformation mechanisms in Zr, the experimental determination of its CRSS values—which are particularly useful as inputs to crystal plasticity models—is a difficult endeavour [329]. A validated DD-FEM model can therefore be used to predict the CRSS of slip modes that are experimentally challenging to isolate. In addition, such a model would enable detailed studies of comparisons of deformation mechanisms in both unirradiated and irradiated zirconium by introducing a population of prismatic loop defects. Furthermore, the influence of thermally activated mobility mechanisms can be explored by comparing different mobility laws, such as those incorporating an Arrhenius-type dependence.

In summary, this thesis has provided contributions to the development of enhanced large-scale DD models for the investigation of dislocation-mediated phenomena and irradiation hardening in HCP zirconium. The foundations for improved mesoscopic-scale computational models of material plasticity have been established.

Appendix A

A level set approach for investigating dislocation evolution

A.1 Mathematical framework

Let us investigate the problem of an evolving closed dislocation loop using a level set approach. We represent the closed dislocation loop by a smooth compact[1] hypersurface[2] Γ_t embedded in $\mathbb{R}^2$ which is assumed to evolve smoothly with time t [333]. The hypersurface Γ_t is the boundary of a bounded open set D_t, which represents the region on the interior of the dislocation loop. A surface evolution equation is one that prescribes the normal velocity $V = \boldsymbol{v} \cdot \hat{\boldsymbol{m}}$ at every point on Γ_t in the glide direction $\hat{\boldsymbol{m}}$ which is oriented outwards from D_t, via

$$V = F(\boldsymbol{x}, t) \quad \text{on} \quad \Gamma_t \tag{A.1}$$

where the function F can in general depend on various intrinsic factors (e.g. line curvature) and extrinsic factors (e.g. external forces) [333].

In the level set method, the hypersurface Γ_t is represented as a zero level set of an auxiliary time-dependent scalar function $u : \mathbb{R}^2 \times [0, \infty) \to \mathbb{R}$. A class of PDEs for which all level sets of their solutions evolve according to equation (A.1) is given by

$$u_t - |\nabla u| V = 0 \tag{A.2}$$

such that the glide direction is $\hat{\boldsymbol{m}} = -\boldsymbol{\nabla} u / |\boldsymbol{\nabla} u|$ [334]. The relevant domains are

[1] Informally speaking, a compact space (in this case a subset of Euclidean space) is one that includes all of its boundary points and points within its boundary, i.e. it has no "holes".

[2] A hypersurface is the generalisation of a surface of dimension $d-1$ that is embedded in a space of dimension d.

defined by

$$\Gamma_t = \{\boldsymbol{x} \in \mathbb{R}^2 : u(\boldsymbol{x}, t) = 0\} \tag{A.3}$$

$$D_t = \{\boldsymbol{x} \in \mathbb{R}^2 : u(\boldsymbol{x}, t) > 0\} \tag{A.4}$$

In the level set approach, we must first choose an initial condition $u(\boldsymbol{x}, t = 0)$ and then solve the corresponding initial value problem for equation (A.2). Note that there is a significant amount of freedom in the choice of initial condition: Γ_t and D_t are uniquely determined by Γ_0 and D_0 in a manner which is otherwise independent of $u(\boldsymbol{x}, t = 0)$ [333].

The discrete nodal framework provides a set of tools which are limited for the purposes of perspicuous level set analysis. Equation (4.46)—and other similar discrete nodal equations—can be transformed into their continuous counterparts by taking the dislocation loop to approach an infinitely fine nodal discretisation such that $\tilde{L}_i \to 0$. All quantities which depend linearly on the segment length—such as the nodal force—tend towards zero under this continuum-casting approach, and so must be transformed via $G_i/\tilde{L}_i \to G$, where G_i represents the discrete variable evaluated at node n_i and G represents the continuous variable. For instance, the nodal force is transformed via $\boldsymbol{f}_i/\tilde{L}_i \to \boldsymbol{f}$ such that $\boldsymbol{f} = \boldsymbol{f}(\boldsymbol{x})$ is a continuous force per unit length evaluated at every point $\boldsymbol{x}$ on the dislocation line. However, quantities which are independent of the segment length—such as the drag tensor, nodal velocity, glide vector, and drag function—transform simply via $G_i \to G$. Upon applying this continuum-casting procedure, the normal velocity becomes

$$V = \beta^{-1} f \hat{\boldsymbol{v}} \cdot \hat{\boldsymbol{m}} \quad \text{on} \quad \Gamma_t \tag{A.5}$$

which is the relevant surface evolution equation for a dislocation loop. The spatially continuous variables $V = V(\boldsymbol{x})$, $f = |\boldsymbol{f}(\boldsymbol{x})|$, $\hat{\boldsymbol{v}} = \hat{\boldsymbol{v}}(\boldsymbol{x})$, and $\hat{\boldsymbol{m}} = \hat{\boldsymbol{m}}(\boldsymbol{x})$ are only defined on the dislocation line.

We restrict the problem to one in which the only force on the dislocation loop is due to the external applied shear stress; interaction and line tension forces are ignored and all forces act codirectional to $\hat{\boldsymbol{m}}$ at every point on Γ_t. Furthermore, the magnitude f of the resulting force is spatially uniform and the drag function β may be interpreted as the resolved glide drag coefficient β^{glide}. In principle, the quantity $\hat{\boldsymbol{v}} \cdot \hat{\boldsymbol{m}}$ can be determined analytically, but for simplicity we shall assume that $\hat{\boldsymbol{v}} \cdot \hat{\boldsymbol{m}} = 1$. As discussed previously, this is always true in the non-HCP formulation, and is a valid approximation in the HCP formulation. In this situation, the relevant level set equation for the evolution of a dislocation loop is given by equation (4.57).

A.2 Example: a self-similarly evolving superelliptical loop

In order to further study this problem, we consider the regime of self-similar (or homothetic) evolution, defined as the state during which the spatial dislocation loop shape is uniformly scaled as the time increases (see figure 4.16b). Under such a condition, the proportions of the shape of a dislocation loop do not change during its growth, thus maintaining self-similarity. In this example, the aim is to search for self-similar superelliptical [335] solutions of equation (4.57) and identify the form of β necessary to admit such solutions. We assume a particular form of the solution given by

$$u(\boldsymbol{x}, t) = t - g(S(\boldsymbol{x})) \tag{A.6}$$

for some monotonic function $g : \mathbb{R} \to \mathbb{R}$ such that

$$S(\boldsymbol{x}) = \left|\frac{x_1}{a_1}\right|^{\lambda} + \left|\frac{x_2}{a_2}\right|^{\lambda}, \quad a_1 > 0, \quad a_2 > 0, \quad \lambda > 0 \tag{A.7}$$

where x_1 and x_2 are the Cartesian spatial coordinates of the domain. The level sets of the function $S : \mathbb{R}^2 \to \mathbb{R}$ are self-similar superellipses. Furthermore, S bestows an elliptical symmetry to the function g, and since g is assumed to be monotonic[3], its level sets are self-similar and must have the same shape as those of S. Note that the assumed form of the solution u is such that, if the level sets of g are self-similar, then each level set of u necessarily evolves self-similarly with time. Inserting equation (A.6) into equation (4.57) yields

$$1 = |\boldsymbol{\nabla} g| \beta^{-1} f \tag{A.8}$$

$$= g'(S) \, |\boldsymbol{\nabla} S| \beta^{-1} f \tag{A.9}$$

which is in fact an eikonal equation. Here, we have used the notation $g'(S) \coloneqq \frac{\mathrm{d}g}{\mathrm{d}S}$. A calculation reveals that

$$|\boldsymbol{\nabla} S| = \lambda S^{\frac{\lambda-1}{\lambda}} \Phi(\Theta) \tag{A.10}$$

where

$$\Phi(\Theta) \coloneqq \frac{\sqrt{|\cos\Theta|^{2\lambda-2} / a_1^{2\lambda} + |\sin\Theta|^{2\lambda-2} / a_2^{2\lambda}}}{\left[|\cos\Theta|^{\lambda} / a_1^{\lambda} + |\sin\Theta|^{\lambda} / a_2^{\lambda} \right]^{\frac{\lambda-1}{\lambda}}} \tag{A.11}$$

[3]Consider that if g were *not* monotonic, the solution could admit multiple loops, or even regions of space containing a smeared out dislocation "area" instead of a line.

It therefore follows that

$$g'(S)\, S^{\frac{\lambda-1}{\lambda}} = \frac{\beta}{\lambda f \Phi(\Theta)} \tag{A.12}$$

Because the left hand side of equation (A.12) is solely dependent on S, its right hand side must also be solely dependent on S if we wish to admit self-similar solutions. The equation is therefore inconsistent unless we impose a specific functional form on the drag function given by $\beta = K\Phi(\Theta)\mathcal{H}(S)$, where $\mathcal{H}(S)$ is an arbitrary function to be selected. Because we are not interested in expressions of β which depend on radial distance, but rather only those which depend solely on Θ, we must select $\mathcal{H}(S) = 1$. Furthermore, assuming that $g(0) = 0$, we obtain

$$g(S) = \frac{K}{f} S^{1/\lambda} \tag{A.13}$$

and therefore the full solution is given by

$$u(\boldsymbol{x}, t) = t - \frac{K}{f}\left(\left|\frac{x_1}{a_1}\right|^{\lambda} + \left|\frac{x_2}{a_2}\right|^{\lambda}\right)^{1/\lambda} \tag{A.14}$$

The level sets of the solution indeed correspond to superellipses which grow self-similarly with a size proportional to ft/K, as expected.

The unique class of drag functions β that admit self-similar superelliptical solutions to the surface evolution equation corresponding to an evolving dislocation loop is given by $\beta(\Theta) = K\Phi(\Theta)$. What remains is to determine the relationship between the polar angle Θ and the dislocation character angle θ. Consider a specific level set of the solution, which corresponds to a possible dislocation loop configuration. Let us denote $R_s = R_s(\Theta)$ as the radial equation of the target dislocation loop. Note that we restrict the treatment of this system to dislocation loops for which the function R_s is injective.

The target dislocation loop shape is

$$R_s(\Theta) = \gamma\left(\left|\frac{\cos\Theta}{a_1}\right|^{\lambda} + \left|\frac{\sin\Theta}{a_2}\right|^{\lambda}\right)^{-1/\lambda} \tag{A.15}$$

where γ is a parameter which determines the size of the loop. Using relation (4.55) (and noting that, in the self-similar evolution regime, said relation is independent of the size of the considered dislocation loop and thus the choice of level set), the relationship between the polar angle Θ and the Burgers vector θ can be determined analytically, and is given by

$$|\tan\Theta| = \left(\frac{a_2}{a_1}\right)^{\frac{\lambda}{\lambda-1}} |\cot\theta|^{\frac{1}{\lambda-1}} \tag{A.16}$$

Furthermore, upon imposing $K = a_1 a_2$ to achieve the desired interpolation bounds, the drag function becomes

$$\beta(\theta) = \left(\left| \frac{\cos\theta}{a_1} \right|^{\frac{\lambda}{\lambda-1}} + \left| \frac{\sin\theta}{a_2} \right|^{\frac{\lambda}{\lambda-1}} \right)^{-\frac{\lambda-1}{\lambda}} \tag{A.17}$$

Upon assigning the respective screw and edge drag coefficients $a_1 = B_{\text{screw}}$ and $a_2 = B_{\text{edge}}$, this expression represents an interpolation of the glide drag coefficient between pure screw and pure edge orientations. The $\lambda = 2$ case, which corresponds to the self-similar elliptical solution, is the standard radial equation of an ellipse in terms of the character angle θ. This is the only value of λ for which the corresponding form of the self-similar solution matches the form of the drag function. This is also the only value of λ for which the isotropic drag case (i.e. $B_{\text{screw}} = B_{\text{edge}}$) corresponds to an isotropic loop, which is an important physical requirement.

Bibliography

[1] Daniel Hortelano-Roig, Rakesh Kumar, Daniel S. Balint, and Edmund Tarleton. Discrete dislocation dynamics simulations of ⟨a⟩-type prismatic loops in zirconium. *International Journal of Plasticity*, 171:103802, December 2023.

[2] Vito Volterra. Sur l'équilibre des corps élastiques multiplement connexes. *Annales scientifiques de l'École Normale Supérieure*, 3e série, 24:401–517, 1907.

[3] Geoffrey Ingram Taylor. The mechanism of plastic deformation of crystals. part i.—theoretical. *Proceedings of the Royal Society of London. Series A, Containing Papers of a Mathematical and Physical Character*, 145(855):362–387, 1934.

[4] E. Orowan. Zur Kristallplastizität. III. *Zeitschrift fur Physik*, 89(9-10):634–659, September 1934.

[5] Michael Polanyi. Über eine art gitterstörung, die einen kristall plastisch machen könnte. *Zeitschrift für Physik*, 89:660–664, 1934.

[6] J. M. Burgers. Some considerations on the fields of stress connected with dislocations in a regular crystal lattice. i. *Proceedings of the Koninklijke Nederlandse Akademie van Wetenschappen*, 42:293–378, 1939.

[7] M. Peach and J. S. Koehler. The Forces Exerted on Dislocations and the Stress Fields Produced by Them. *Physical Review*, 80(3):436–439, November 1950.

[8] J. Blin. Energie mutuelle de deux dislocations. *Acta Metallurgica*, 3(2):199–200, 1955.

[9] P. B. Hirsch, R. W. Horne, and M. J. Whelan and. Lxviii. direct observations of the arrangement and motion of dislocations in aluminium. *The Philosophical Magazine: A Journal of Theoretical Experimental and Applied Physics*, 1(7):677–684, 1956.

[10] P. Hirsch, Cockayne , D., Spence , J., , and M. Whelan. 50 Years of TEM of dislocations: Past, present and future. *Philosophical Magazine*, 86(29-31):4519–4528, October 2006. Publisher: Taylor & Francis _eprint: https://doi.org/10.1080/14786430600768634.

[11] Andreas N. Danilewsky. X-Ray Topography—More than Nice Pictures. *Crystal Research and Technology*, 55(9):2000012, 2020. _eprint: https://onlinelibrary.wiley.com/doi/pdf/10.1002/crat.202000012.

[12] Dongzhu Lu, Quantong Jiang, Xiumin Ma, Qichao Zhang, Xiaole Fu, and Liang Fan. Defect-Related Etch Pits on Crystals and Their Utilization. *Crystals*, 12(11):1549, November 2022. Number: 11 Publisher: Multidisciplinary Digital Publishing Institute.

[13] R. v. Mises. Mechanik der festen körper im plastisch- deformablen zustand. *Nachrichten von der Gesellschaft der Wissenschaften zu Göttingen, Mathematisch-Physikalische Klasse*, 1913:582–592, 1913.

[14] R. Sowerby, D. K. Uko, and Y. Tomita. A review of certain aspects of the Bauschinger effect in metals. *Materials Science and Engineering*, 41(1):43–58, November 1979.

[15] W. Blum, P. Eisenlohr, and F. Breutinger. Understanding creep—a review. *Metallurgical and Materials Transactions A*, 33(2):291–303, February 2002.

[16] Andrea C. Levi and Miroslav Kotrla. Theory and simulation of crystal growth. *Journal of Physics: Condensed Matter*, 9(2):299, January 1997.

[17] A. D. Rollett and U. F. Kocks. A review of the stages of work hardening. *Dislocations '93,Assois (France),1-9 Apr 1993*, January 1993. Number: LA-UR–93-2339 Publisher: Los Alamos National Laboratory.

[18] Martin Bechthold and James C. Weaver. Materials science and architecture. *Nature Reviews Materials*, 2(12):1–19, December 2017. Publisher: Nature Publishing Group.

[19] K. M. Gupta and Nishu Gupta. Semiconductor Materials: Their Properties, Applications, and Recent Advances. In K.M. Gupta and Nishu Gupta, editors, *Advanced Semiconducting Materials and Devices*, pages 3–40. Springer International Publishing, Cham, 2016.

[20] W.F. Chen. *Plasticity in Reinforced Concrete*. J. Ross Publishing Classics. J. Ross Pub., 2007.

[21] J. Knaster, A. Moeslang, and T. Muroga. Materials research for fusion. *Nature Physics*, 12(5):424–434, May 2016. Publisher: Nature Publishing Group.

[22] Zhengang Duan, Huilong Yang, Yuhki Satoh, Kenta Murakami, Sho Kano, Zishou Zhao, Jingjie Shen, and Hiroaki Abe. Current status of materials development of nuclear fuel cladding tubes for light water reactors. *Nuclear Engineering and Design*, 316:131–150, 2017.

[23] A. H. Cottrell. Commentary. A brief view of work hardening. In F. R. N. Nabarro and M. S. Duesbery, editors, *Dislocations in Solids*, volume 11, pages vii–xvii. Elsevier, January 2002.

[24] F.R.N. Nabarro, Z.S. Basinski, and D.B. Holt and. The plasticity of pure single crystals. *Advances in Physics*, 13(50):193–323, 1964.

[25] Placid Rodriguez. Sixty years of dislocations. *Bulletin of Materials Science*, 19(6):857–872, December 1996.

[26] Georges Saada and Patrick Veyssière. Chapter 61 Work hardening of face centred cubic crystals. Dislocations intersection and cross slip. In F. R. N. Nabarro and M. S. Duesbery, editors, *Dislocations in Solids*, volume 11, pages 413–458. Elsevier, January 2002.

[27] L.P. Kubin, B. Devincre, and M. Tang. Mesoscopic modelling and simulation of plasticity in fcc and bcc crystals: Dislocation intersections and mobility. *Journal of Computer-Aided Materials Design*, 5(1):31–54, January 1998.

[28] R. Madec, B. Devincre, and L. P. Kubin. From Dislocation Junctions to Forest Hardening. *Physical Review Letters*, 89(25):255508, December 2002. Publisher: American Physical Society.

[29] R. Madec, B. Devincre, L. Kubin, T. Hoc, and D. Rodney. The Role of Collinear Interaction in Dislocation-Induced Hardening. *Science*, 301(5641):1879–1882, September 2003.

[30] B. Devincre, L. Kubin, and T. Hoc. Physical analyses of crystal plasticity by DD simulations. *Scripta Materialia*, 54(5):741–746, March 2006.

[31] Vasily V. Bulatov, Luke L. Hsiung, Meijie Tang, Athanasios Arsenlis, Maria C. Bartelt, Wei Cai, Jeff N. Florando, Masato Hiratani, Moon Rhee, Gregg Hommes, Tim G. Pierce, and Tomas Diaz de la Rubia. Dislocation multijunctions and strain hardening. *Nature*, 440(7088):1174–1178, April 2006. Publisher: Nature Publishing Group.

[32] P. Franciosi, M. Berveiller, and A. Zaoui. Latent hardening in copper and aluminium single crystals. *Acta Metallurgica*, 28(3):273–283, March 1980.

[33] H. Mughrabi. Dislocation wall and cell structures and long-range internal stresses in deformed metal crystals. *Acta Metallurgica*, 31(9):1367–1379, September 1983.

[34] G. V. S. S. Prasad, M. Goerdeler, and G. Gottstein. Work hardening model based on multiple dislocation densities. *Materials Science and Engineering: A*, 400-401:231–233, July 2005.

[35] Ladislas Kubin, Benoit Devincre, and Thierry Hoc. The deformation stage II of face-centered cubic crystals: Fifty years of investigations. *International Journal of Materials Research*, 100(10):1411–1419, October 2009. Publisher: De Gruyter.

[36] D. Peirce, R. J. Asaro, and A. Needleman. An analysis of nonuniform and localized deformation in ductile single crystals. *Acta Metallurgica*, 30(6):1087–1119, June 1982.

[37] R. J. Asaro and A. Needleman. Overview no. 42 Texture development and strain hardening in rate dependent polycrystals. *Acta Metallurgica*, 33(6):923–953, June 1985.

[38] Franz Roters, Philip Eisenlohr, Thomas R. Bieler, and Dierk Raabe. *Crystal Plasticity Finite Element Methods: In Materials Science and Engineering*. Wiley, 1 edition, October 2010.

[39] Andreas Öchsner. *Elements of Classical Plasticity Theory*. Springer International Publishing, Cham, 2022.

[40] F. Roters, P. Eisenlohr, L. Hantcherli, D. D. Tjahjanto, T. R. Bieler, and D. Raabe. Overview of constitutive laws, kinematics, homogenization and multiscale methods in crystal plasticity finite-element modeling: Theory, experiments, applications. *Acta Materialia*, 58(4):1152–1211, February 2010.

[41] Xiazi Xiao, Dmitry Terentyev, Haijian Chu, and Huiling Duan. Theoretical models for irradiation hardening and embrittlement in nuclear structural materials: a review and perspective. *Acta Mechanica Sinica*, 36(2):397–411, April 2020.

[42] legislation.gov.uk. Climate Change Act 2008. https://www.legislation.gov.uk/ukpga/2008/27/contents. [Accessed 13-04-2025].

[43] G.S. Was. *Fundamentals of Radiation Materials Science: Metals and Alloys*. Springer Berlin Heidelberg, 2007.

[44] Chris Llewellyn Smith. The need for fusion. *Fusion Engineering and Design*, 74(1):3–8, November 2005.

[45] J.R. Lamarsh and A.J. Baratta. *Introduction to Nuclear Engineering*. Addison-Wesley series in nuclear science and engineering. Pearson Prentice Hall, 2011.

[46] C. R. F. Azevedo. Selection of fuel cladding material for nuclear fission reactors. *Engineering Failure Analysis*, 18(8):1943–1962, December 2011.

[47] Steven J. Zinkle and Jeremy T. Busby. Structural materials for fission & fusion energy. *Materials Today*, 12(11):12–19, November 2009.

[48] J. A. L. Robertson. Zirconium—an international nuclear material. *Journal of Nuclear Materials*, 100(1):108–118, September 1981.

[49] L. Xu, Y. Xiao, A. van Sandwijk, Q. Xu, and Y. Yang. Production of nuclear grade zirconium: A review. *Journal of Nuclear Materials*, 466:21–28, 2015.

[50] C. Lemaignan. 2.07 - Zirconium Alloys: Properties and Characteristics. In Rudy J. M. Konings, editor, *Comprehensive Nuclear Materials*, pages 217–232. Elsevier, Oxford, January 2012.

[51] C.E. Coleman. *The Metallurgy of Zirconium*. Non-serial Publications. INTERNATIONAL ATOMIC ENERGY AGENCY, Vienna, 2023.

[52] Khushahal Thool, K. U. Yazar, V. Kavimani, Aman Gupta, and Shi-Hoon Choi. Microstructural and Textural Evolution in Hexagonal Close-Packed Metals: The Case of Zirconium, Magnesium, and Titanium. *Crystals*, 14(8):727, August 2024. Number: 8 Publisher: Multidisciplinary Digital Publishing Institute.

[53] Arthur T. Motta, Laurent Capolungo, Long-Qing Chen, Mahmut Nedim Cinbiz, Mark R. Daymond, Donald A. Koss, Evrard Lacroix, Giovanni Pastore, Pierre-Clément A. Simon, Michael R. Tonks, Brian D. Wirth, and Mohammed A. Zikry. Hydrogen in zirconium alloys: A review. *Journal of Nuclear Materials*, 518:440–460, May 2019.

[54] F. Onimus and J.L. Béchade. 4.01 - radiation effects in zirconium alloys. In Rudy J.M. Konings, editor, *Comprehensive Nuclear Materials*, pages 1–31. Elsevier, Oxford, 2012.

[55] Alan Xu, Michael Saleh, Joel Davis, Lyndon Edwards, and Dhriti Bhattacharyya. In-situ micro-tensile investigation of strain rate response along <100> and <110> directions in single crystal nickel. *International Journal of Plasticity*, 106:129–144, July 2018.

[56] C. Motz, D. Weygand, J. Senger, and P. Gumbsch. Micro-bending tests: A comparison between three-dimensional discrete dislocation dynamics simulations and experiments. *Acta Materialia*, 56(9):1942–1955, May 2008.

[57] Zachary H. Aitken, Haidong Fan, Jaafar A. El-Awady, and Julia R. Greer. The effect of size, orientation and alloying on the deformation of AZ31 nanopillars. *Journal of the Mechanics and Physics of Solids*, 76:208–223, March 2015.

[58] G.S Was, J.T Busby, T Allen, E.A Kenik, A Jensson, S.M Bruemmer, J Gan, A.D Edwards, P.M Scott, and P.L Andreson. Emulation of neutron irradiation effects with protons: validation of principle. *Journal of Nuclear Materials*, 300(2):198 – 216, 2002.

[59] D. Kiener, P. Hosemann, S. A. Maloy, and A. M. Minor. In situ nanocompression testing of irradiated copper. *Nature Materials*, 10(8):608–613, AUG 2011.

[60] P. Hosemann, C. Shin, and D. Kiener. Small scale mechanical testing of irradiated materials. *Journal of Materials Research*, 30(9):1231–1245, May 2015.

[61] Vikram Jayaram. Small-Scale Mechanical Testing. *Annual Review of Materials Research*, 52(Volume 52, 2022):473–523, July 2022. Publisher: Annual Reviews.

[62] E. Arzt. Size effects in materials due to microstructural and dimensional constraints: a comparative review. *Acta Materialia*, 46(16):5611–5626, October 1998.

[63] HHM Cleveringa, E Van der Giessen, and A Needleman. A discrete dislocation analysis of bending. *International Journal of Plasticity*, 15(8):837–868, 1999.

[64] J. Senger, D. Weygand, P. Gumbsch, and O. Kraft. Discrete dislocation simulations of the plasticity of micro-pillars under uniaxial loading. *Scripta Materialia*, 58(7):587–590, APR 2008.

[65] E. Tarleton, D. S. Balint, J. Gong, and A. J. Wilkinson. A discrete dislocation plasticity study of the micro-cantilever size effect. *Acta Materialia*, 88:271–282, April 2015.

[66] Nasr M. Ghoniem†, Esteban P. Busso, Nicholas Kioussis, and Hanchen Huang. Multiscale modelling of nanomechanics and micromechanics: an overview. *Philosophical Magazine*, 83(31-34):3475–3528, October 2003. Publisher: Taylor & Francis _eprint: https://doi.org/10.1080/14786430310001607388.

[67] Erik van der Giessen, Peter A Schultz, Nicolas Bertin, Vasily V Bulatov, Wei Cai, Gábor Csányi, Stephen M Foiles, M G D Geers, Carlos González, Markus Hütter, Woo Kyun Kim, Dennis M Kochmann, Javier LLorca, Ann E Mattsson, Jörg Rottler, Alexander Shluger, Ryan B Sills, Ingo Steinbach, Alejandro Strachan, and Ellad B Tadmor. Roadmap on multiscale materials modeling. *Modelling and Simulation in Materials Science and Engineering*, 28(4):043001, March 2020. Publisher: IOP Publishing.

[68] A. G. Mylonakis, M. Varvayanni, N. Catsaros, P. Savva, and D. G. E. Grigoriadis. Multi-physics and multi-scale methods used in nuclear reactor analysis. *Annals of Nuclear Energy*, 72:104–119, October 2014.

[69] Jörg Neugebauer and Tilmann Hickel. Density functional theory in materials science. *WIREs Computational Molecular Science*, 3(5):438–448, 2013. _eprint: https://onlinelibrary.wiley.com/doi/pdf/10.1002/wcms.1125.

[70] John A. Moriarty, Vaclav Vitek, Vasily V. Bulatov, and Sidney Yip. Atomistic simulations of dislocations and defects. *Journal of Computer-Aided Materials Design*, 9(2):99–132, May 2002.

[71] J.F Nye. Some geometrical relations in dislocated crystals. *Acta Metallurgica*, 1(2):153–162, 1953.

[72] Ekkehart Kröner. Allgemeine kontinuumstheorie der versetzungen und eigenspannungen. *Archive for Rational Mechanics and Analysis*, 4(1):273–334, Jan 1959.

[73] E. Kröner. Benefits and shortcomings of the continuous theory of dislocations. *International Journal of Solids and Structures*, 38(6):1115–1134, February 2001.

[74] A. El-Azab. Statistical mechanics treatment of the evolution of dislocation distributions in single crystals. *Physical Review B*, 61(18):11956–11966, May 2000. Publisher: American Physical Society.

[75] Thomas Hochrainer and M. Zaiser. Fundamentals of a continuum theory of dislocations. *Proceedings of the International conference on Statistical Mechanics of Plasticity and Related Instabilities*, 2006.

[76] Anter El-Azab and Giacomo Po. Continuum Dislocation Dynamics: Classical Theory and Contemporary Models. In Wanda Andreoni and Sidney Yip, editors, *Handbook of Materials Modeling: Methods: Theory and Modeling*, pages 1583–1607. Springer International Publishing, Cham, 2020.

[77] S. Groh and H. M. Zbib. Advances in Discrete Dislocations Dynamics and Multiscale Modeling. *Journal of Engineering Materials and Technology*, 131(4), 09 2009. 041209.

[78] Ryan B. Sills, William P. Kuykendall, Amin Aghaei, and Wei Cai. Fundamentals of Dislocation Dynamics Simulations. In Christopher R. Weinberger and Garritt J. Tucker, editors, *Multiscale Materials Modeling for Nanomechanics*, Springer Series in Materials Science, pages 53–87. Springer International Publishing, Cham, 2016.

[79] Zhuo Zhuang, Zhanli Liu, and Yinan Cui. Chapter 7 - discrete-continuous model of crystal plasticity at the submicron scale. In Zhuo Zhuang, Zhanli Liu, and Yinan Cui, editors, *Dislocation Mechanism-Based Crystal Plasticity*, pages 177–217. Academic Press, 2019.

[80] Chi-Chin Wu, Sylvie Aubry, Athanasios Arsenlis, and Peter W. Chung. Binary dislocation junction formation and strength in hexagonal close-packed crystals. *International Journal of Plasticity*, 79:176–195, April 2016.

[81] A. Arsenlis, M. Rhee, G. Hommes, R. Cook, and J. Marian. A dislocation dynamics study of the transition from homogeneous to heterogeneous deformation in irradiated body-centered cubic iron. *Acta Materialia*, 60(9):3748–3757, May 2012.

[82] Yang Li, Giacomo Po, Yinan Cui, and Nasr Ghoniem. Prismatic-to-basal plastic slip transition in zirconium. *Acta Materialia*, 242:118451, January 2023.

[83] Haidong Fan, Sylvie Aubry, Athanasios Arsenlis, and Jaafar A. El-Awady. The role of twinning deformation on the hardening response of polycrystalline magnesium from discrete dislocation dynamics simulations. *Acta Materialia*, 92:126–139, June 2015.

[84] S. Aubry, M. Rhee, G. Hommes, V. V Bulatov, and A. Arsenlis. Dislocation dynamics in hexagonal close-packed crystals. *Journal of the Mechanics and Physics of Solids*, 94:105–126, September 2016.

[85] Julie Drouet, Laurent Dupuy, Fabien Onimus, Frédéric Mompiou, Simon Perusin, and Antoine Ambard. Dislocation dynamics simulations of interactions between gliding dislocations and radiation induced prismatic loops in zirconium. *Journal of Nuclear Materials*, 449(1):252–262, 2014.

[86] Vasily V. Bulatov, Moon Rhee, and Wei Cai. Periodic Boundary Conditions for Dislocation Dynamics Simulations in Three Dimensions. *MRS Online Proceedings Library (OPL)*, 653:Z1.3, January 2000.

[87] L. Z Sun, N. M Ghoniem, S. H Tong, and B. N Singh. 3D dislocation dynamics study of plastic instability in irradiated copper. *Journal of Nuclear Materials*, 283-287:741–745, December 2000.

[88] Tamer Crosby, Giacomo Po, and Nasr M. Ghoniem. Modeling plastic deformation of post-irradiated copper micro-pillars. *Journal of Nuclear Materials*, 455(1):126–129, December 2014.

[89] Yinan Cui, Giacomo Po, and Nasr Ghoniem. Does irradiation enhance or inhibit strain bursts at the submicron scale? *Acta Materialia*, 132:285–297, June 2017.

[90] S. I. Rao, C. Woodward, B. Akdim, E. Antillon, T. A. Parthasarathy, J. A. El-Awady, and D. M. Dimiduk. Large-scale dislocation dynamics simulations

of strain hardening of Ni microcrystals under tensile loading. *Acta Materialia*, 164:171–183, February 2019.

[91] Haiyang Yu, Alan C. F. Cocks, and Edmund Tarleton. Formation of prismatic dislocation loops during unloading in nanoindentation. *Scripta Materialia*, 189:112–116, December 2020.

[92] Phu Cuong Nguyen and Ill Ryu. Mesoscale dislocation dynamics modeling of incipient plasticity under nanoindentation. *Materialia*, 32:101956, December 2023.

[93] M Verdier, M Fivel, and I Groma. Mesoscopic scale simulation of dislocation dynamics in fcc metals: Principles and applications. *Modelling and Simulation in Materials Science and Engineering*, 6(6):755, nov 1998.

[94] Benoit Devincre. Modeling crystal plasticity with dislocation dynamics simulations: the 'micromegas' code. *Mechanics of Nano-objects*, pages 81–89, 01 2011.

[95] C. Lemarchand, B. Devincre, and L.P. Kubin. Homogenization method for a discrete-continuum simulation of dislocation dynamics. *Journal of the Mechanics and Physics of Solids*, 49(9):1969–1982, 2001. The JW Hutchinson and JR Rice 60th Anniversary Issue.

[96] Hussein M. Zbib, Moono Rhee, and John P. Hirth. On plastic deformation and the dynamics of 3D dislocations. *International Journal of Mechanical Sciences*, 40(2):113–127, February 1998.

[97] K. W. Schwarz. Simulation of dislocations on the mesoscopic scale. i. methods and examples. *Journal of Applied Physics*, 85(1):108–119, 01 1999.

[98] N. M. Ghoniem, S.-H. Tong, and L. Z. Sun. Parametric dislocation dynamics: A thermodynamics-based approach to investigations of mesoscopic plastic deformation. *Physical Review B*, 61(2):913–927, January 2000.

[99] H. M. Zbib, M. Shehadeh, S. M. A. Khan, and G. Karami. Multiscale dislocation dynamics plasticity. *International Journal for Multiscale Computational Engineering*, 1(1):17, 2003.

[100] Vasily Bulatov, Wei Cai, Jeff Fier, Masato Hiratani, Gregg Hommes, Tim Pierce, Meijie Tang, Moono Rhee, Kim Yates, and Tom Arsenlis. Scalable line dynamics in paradis. In *Proceedings of the 2004 ACM/IEEE Conference on Supercomputing*, SC '04, page 19, USA, 2004. IEEE Computer Society.

[101] A Arsenlis, W Cai, M Tang, M Rhee, T Oppelstrup, G Hommes, T G Pierce, and V V Bulatov. Enabling strain hardening simulations with dislocation dynamics. *Modelling and Simulation in Materials Science and Engineering*, 15(6):553–595, jul 2007.

[102] M. Tang, G. Hommes, S. Aubry, A. Arsenlis, and Livermore Lawrence Livermore National Laboratory. ParaDiS-FEM dislocation dynamics simulation code primer. Technical Report LLNL-TR–501662, Lawrence Livermore National Laboratory, Livermore, CA (United States), September 2011.

[103] Javier Antonio Gonzalez Joa, Laurent Dupuy, Peter Råback, Marc Fivel, Michel Perez, and Jonathan Amodeo. El-Numodis: a new tool to model dislocation and surface interactions. *Modelling and Simulation in Materials Science and Engineering*, 31(5):055003, 2023.

[104] Lawrence Livermore National Laboratory. OpenDiS. https://github.com/OpenDiS/OpenDiS, 2024.

[105] University of Oxford Materials. EasyDD. https://github.com/TarletonGroup/EasyDD, 2021.

[106] R. B. Sills and S. Aubry. Line Dislocation Dynamics Simulations with Complex Physics. In Wanda Andreoni and Sidney Yip, editors, *Handbook of Materials Modeling : Methods: Theory and Modeling*, pages 1–23. Springer International Publishing, Cham, 2018.

[107] D. S. Balint, V. S. Deshpande, A. Needleman *, and E. Van der Giessen. Discrete dislocation plasticity analysis of crack-tip fields in polycrystalline materials. *Philosophical Magazine*, 85(26-27):3047–3071, 2005.

[108] V S Deshpande, D S Balint, A Needleman, and E Van der Giessen. Size effects in single asperity frictional contacts. *Modelling and Simulation in Materials Science and Engineering*, 15(1):S97, dec 2006.

[109] E. Van der Giessen and A. Needleman. Discrete dislocation plasticity: a simple planar model. *Modelling and Simulation in Materials Science and Engineering*, 3(5):689–735, September 1995. Publisher: IOP Publishing.

[110] E Tenckhoff. *Deformation mechanisms, texture, and anisotropy in zirconium and zircaloy*. ASTM,Philadelphia, PA, 01 1988.

[111] D. Caillard, M. Gaumé, and F. Onimus. Glide and cross-slip of a-dislocations in Zr and Ti. *Acta Materialia*, 155:23–34, August 2018.

[112] E. J. Rapperport and C. S. Hartley. DEFORMATION MODES OF ZIRCONIUM AT 77, 575, AND 1075 K. *Trans. Met. Soc. AIME*, Vol: 218, October 1960. Institution: Nuclear Metals, Inc., Concord, Mass.

[113] A Akhtar and A Teghtsoonian. Plastic deformation of zirconium single crystals. *Acta Metallurgica*, 19(7):655–663, July 1971.

[114] Fei Long, Feng Xu, and Mark R. Daymond. Temperature Dependence of the Activity of Deformation Modes in an HCP Zirconium Alloy. *Metallurgical and Materials Transactions A*, 44(9):4183–4193, September 2013.

[115] Jicheng Gong, T. Benjamin Britton, Mitchell A. Cuddihy, Fionn P. E. Dunne, and Angus J. Wilkinson. ⟨a⟩ Prismatic, ⟨a⟩ basal, and ⟨c+a⟩ slip strengths of commercially pure Zr by micro-cantilever tests. *Acta Materialia*, 96:249–257, September 2015.

[116] A. Akhtar. Prismatic slip in zirconium single crystals at elevated temperatures. *Metallurgical Transactions A*, 6(6):1217–1222, June 1975.

[117] J. I. Dickson and G. B. Craig. Room-temperature basal slip in zirconium. *Journal of Nuclear Materials*, 40(3):346–348, September 1971.

[118] Emmanuel Clouet, Daniel Caillard, Nermine Chaari, Fabien Onimus, and David Rodney. Dislocation locking versus easy glide in titanium and zirconium. *Nature Materials*, 14(9):931–936, September 2015. Publisher: Nature Publishing Group.

[119] Marko Knezevic, Beyerlein , Irene J., Nizolek , Thomas, Mara , Nathan A., , and Tresa M. Pollock. Anomalous Basal Slip Activity

in Zirconium under High-strain Deformation. *Materials Research Letters*, 1(3):133–140, September 2013. Publisher: Taylor & Francis _eprint: https://doi.org/10.1080/21663831.2013.794375.

[120] H.A. Khater and D.J. Bacon. Dislocation core structure and dynamics in two atomic models of α-zirconium. *Acta Materialia*, 58(8):2978–2987, 2010.

[121] D. J. Bacon and V. Vitek. Atomic-scale modeling of dislocations and related properties in the hexagonal-close-packed metals. *Metallurgical and Materials Transactions A*, 33(3):721–733, March 2002.

[122] Emmanuel Clouet. Screw dislocation in zirconium: An *ab initio* study. *Physical Review B*, 86(14):144104, October 2012.

[123] Émile Maras and Emmanuel Clouet. Secondary slip of screw dislocations in zirconium. *Acta Materialia*, 223:117398, January 2022.

[124] Nermine Chaari, Emmanuel Clouet, and David Rodney. First order pyramidal slip of 1/3 <1-210> screw dislocations in zirconium. *Metallurgical and Materials Transactions A*, 45(13):5898–5905, December 2014. arXiv:1410.1121 [cond-mat].

[125] Nermine Chaari, Emmanuel Clouet, and David Rodney. First-Principles Study of Secondary Slip in Zirconium. *Physical Review Letters*, 112(7):075504, February 2014. Publisher: American Physical Society.

[126] Nermine Chaari, David Rodney, and Emmanuel Clouet. Oxygen - Dislocation interaction in zirconium from first principles. *Acta Materialia*, 132:416–424, June 2017.

[127] G. Schoeck. The Activation Energy of Dislocation Movement. *physica status solidi (b)*, 8(2):499–507, 1965. _eprint: https://onlinelibrary.wiley.com/doi/pdf/10.1002/pssb.19650080209.

[128] S. P. Fitzgerald. Kink pair production and dislocation motion. *Scientific Reports*, 6(1):39708, December 2016. Publisher: Nature Publishing Group.

[129] G. Monnet, B. Devincre, and L. P. Kubin. Dislocation study of prismatic slip systems and their interactions in hexagonal close packed metals: application to zirconium. *Acta Materialia*, 52(14):4317–4328, August 2004.

[130] Daniel Caillard, Martin Rautenberg, and Xavier Feaugas. Dislocation mechanisms in a zirconium alloy in the high-temperature regime: An *in situ* TEM investigation. *Acta Materialia*, 87:283–292, April 2015.

[131] A. Akhtar. Basal slip in zirconium. *Acta Metallurgica*, 21(1):1–11, January 1973.

[132] M. H Yoo, S. R Agnew, J. R Morris, and K. M Ho. Non-basal slip systems in HCP metals and alloys: source mechanisms. *Materials Science and Engineering: A*, 319-321:87–92, December 2001.

[133] Thomas Soyez, Daniel Caillard, Fabien Onimus, and Emmanuel Clouet. Mobility of ⟨c+a⟩<math><mrow is="true"><mo is="true">⟨</mo><mi is="true">c</mi><mo linebreak="goodbreak" is="true">+</mo><mi is="true">a</mi><mo is="true">⟩</mo></mrow></math> dislocations in zirconium. *Acta Materialia*, 197:97–107, September 2020.

[134] Jean François Stohr, , and Jean Paul Poirier. Etude en microscopie electronique du glissement pyramidal 1122 ⟨1123⟩ dans le magnesium. *The Philosophical Magazine: A Journal of Theoretical Experimental and Applied Physics*, 25(6):1313–1329, June 1972. Publisher: Taylor & Francis _eprint: https://doi.org/10.1080/14786437208223856.

[135] D.O. Northwood, R.W Gilbert, L.E. Bahen, P.M. Kelly, R.G. Blake, A. Jostsons, P.K. Madden, D. Faulkner, W. Bell, and R.B. Adamson. Characterization of neutron irradiation damage in zirconium alloys — an international "round-robin" experiment. *Journal of Nuclear Materials*, 79(2):379–394, 1979.

[136] Si-Mian Liu and Wei-Zhong Han. Transmission electron microscopy characterization of dislocation loops in irradiated zirconium. *Tungsten*, 3(4):470–481, December 2021.

[137] A. Jostsons, P.M. Kelly, and R.G. Blake. The nature of dislocation loops in neutron irradiated zirconium. *Journal of Nuclear Materials*, 66(3):236–256, 1977.

[138] P. M. Kelly and R. G. Blake. The characterization of dislocation loops in neutron irradiated zirconium. *The Philosophical Magazine: A Journal of Theoretical Experimental and Applied Physics*, 28(2):415–426, 1973.

[139] Takeo ONCHI, Hideo KAYANO, and Yasuhiro HIGASHIGUCHI. Effect of Neutron Irradiation on Deformation Behavior of Zirconium. *Journal of Nuclear Science and Technology*, 14(5):359–369, May 1977. Publisher: Taylor & Francis _eprint: https://www.tandfonline.com/doi/pdf/10.1080/18811248.1977.9730770.

[140] A. Luft. Microstructural processes of plastic instabilities in strengthened metals. *Progress in Materials Science*, 35(2):97–204, 1991.

[141] F. Kroupa and P. B. Hirsch. Elastic interaction between prismatic dislocation loops and straight dislocations. *Discussions of the Faraday Society*, 38:49, 1964.

[142] L. P. Kubin and J. Kratochvil. Elastic model for the sweeping of dipolar loops. *Philosophical Magazine A*, 80(1):201–218, January 2000. Publisher: Taylor & Francis _eprint: https://doi.org/10.1080/01418610008212049.

[143] H.R. Higgy and F.H. Hammad. Effect of neutron irradiation on the tensile properties of zircaloy-2 and zircaloy-4. *Journal of Nuclear Materials*, 44(2):215–227, 1972.

[144] RB Adamson. Effects of Neutron Irradiation on Microstructure and Properties of Zircaloy. In GD Moan, editor, *Zirconium in the Nuclear Industry: Twelfth International Symposium*, pages 15–31. ASTM International, West Conshohocken, PA, 2000.

[145] Suresh Yagnik and Anand Garde. Chapter 7 - zirconium alloys for lwr fuel cladding and core internals. In G. Robert Odette and Steven J. Zinkle, editors, *Structural Alloys for Nuclear Energy Applications*, pages 247–291. Elsevier, Boston, 2019.

[146] F Onimus, I Monnet, J. L Béchade, C Prioul, and P Pilvin. A statistical TEM investigation of dislocation channeling mechanism in neutron irradiated zirconium alloys. *Journal of Nuclear Materials*, 328(2):165–179, July 2004.

[147] F. Onimus, J. L. Béchade, and D. Gilbon. Experimental Analysis of Slip Systems Activation in Neutron-Irradiated Zirconium Alloys and Comparison with Polycrystalline Model Simulations. *Metallurgical and Materials Transactions A*, 44(1):45–60, January 2013.

[148] D.J. Bacon and Yu.N. Osetsky. Modelling dislocation–obstacle interactions in metals exposed to an irradiation environment. *Materials Science and Engineering: A*, 400-401:353–361, 2005. Dislocations 2004.

[149] D.J. Bacon, Y.N. Osetsky, and D. Rodney. Chapter 88 dislocation–obstacle interactions at the atomic level. In J.P. Hirth and L. Kubin, editors, *Dislocations in Solids*, volume 15, pages 1–90. Elsevier, 2009.

[150] David Rodney. Molecular dynamics simulation of screw dislocations interacting with interstitial frank loops in a model fcc crystal. *Acta Materialia*, 52(3):607–614, 2004.

[151] Marion Borde, Laurent Dupuy, Adrien Pivano, Bruno Michel, David Rodney, and Jonathan Amodeo. Interaction between 1/2¡110¿{001} dislocations and {110} prismatic loops in uranium dioxide: Implications for strain-hardening under irradiation. *International Journal of Plasticity*, 168:103702, 2023.

[152] Akiyoshi Nomoto, Naoki Soneda, Akiyuki Takahashi, and Shiori Ishino. Interaction analysis between edge dislocation and self interstitial type dislocation loop in bcc iron using molecular dynamics. *MATERIALS TRANSACTIONS*, 46(3):463–468, 2005.

[153] Y. N. Osetsky D. J. Bacon and Z. Rong. Computer simulation of reactions between an edge dislocation and glissile self-interstitial clusters in iron. *Philosophical Magazine*, 86(25-26):3921–3936, 2006.

[154] X.-Y. Liu and S.B. Biner. Molecular dynamics simulations of the interactions between screw dislocations and self-interstitial clusters in body-centered cubic fe. *Scripta Materialia*, 59(1):51–54, 2008.

[155] Dmitry Terentyev, P. Grammatikopoulos, D.J. Bacon, Yu.N. Osetsky, and Rachid Chaouadi. Simulation of the interaction between an edge dislocation and a interstitial dislocation loop in a-iron. *Acta Materialia*, 56(18):5034–5046, June 2008. Score = 10.

[156] R.E. Voskoboynikov, Yu.N. Osetsky, and D.J. Bacon. Self-interstitial atom clusters as obstacles to glide of 1/3 $\langle 11\bar{2}0\rangle$ $\{1\bar{1}00\}$ edge dislocations in α-zirconium. *Materials Science and Engineering: A*, 400-401:54–58, 2005. Dislocations 2004.

[157] A Serra and D J Bacon. Atomic-level computer simulation of the interaction between dislocations and interstitial loops in α-zirconium. *Modelling and Simulation in Materials Science and Engineering*, 21(4):045007, apr 2013.

[158] Can Erel, Giacomo Po, Tamer Crosby, and Nasr Ghoniem. Generation and interaction mechanisms of prismatic dislocation loops in fcc metals. *Computational Materials Science*, 140:32–46, 2017.

[159] X.J. Shi, L. Dupuy, B. Devincre, D. Terentyev, and L. Vincent. Interaction of $\langle 100 \rangle$ dislocation loops with dislocations studied by dislocation dynamics in α-iron. *Journal of Nuclear Materials*, 460:37–43, 2015.

[160] Fabien Onimus, Laurent Dupuy, Marine Gaumé, Wassim Kassem, and Frederic Mompiou. Deformation mechanisms of zirconium alloys after irradiation studied by dislocation dynamics simulations and in situ straining experiments in TEM. In *Zirconium in the Nuclear Industry: 19th International Symposium*, pages 319–342. ASTM International100 Barr Harbor Drive, PO Box C700, West Conshohocken, PA 19428-2959, 100 Barr Harbor Drive, PO Box C700, West Conshohocken, PA 19428-2959, July 2021.

[161] L. M. Dupuy, W. Kassem, E. Clouet, and F. Onimus. Atomistically informed dislocation dynamics simulations: application to dislocation-loop interactions in zirconium. *Modelling and Simulation in Materials Science and Engineering*, 32(3):035015, February 2024. Publisher: IOP Publishing.

[162] J. Drouet, L. Dupuy, F. Onimus, and F. Mompiou. A direct comparison between in-situ transmission electron microscopy observations and Dislocation Dynamics simulations of interaction between dislocation and irradiation induced loop in a zirconium alloy. *Scripta Materialia*, 119:71–75, July 2016.

[163] D. J. Bacon. The elastic energies of elliptical dislocation loops. *The Philosophical Magazine: A Journal of Theoretical Experimental and Applied Physics*, 14(130):715–729, 1966.

[164] W. G. Wolfer, T. Okita, and D. M. Barnett. Motion and rotation of small glissile dislocation loops in stress fields. *Phys. Rev. Lett.*, 92:085507, Feb 2004.

[165] Cong Dai, Levente Balogh, Zhongwen Yao, and Mark R. Daymond. The habit plane of $\langle a \rangle$-type dislocation loops in α-zirconium: an atomistic study. *Philosophical Magazine*, 97(12):944–956, 2017.

[166] R. Hulse and C. P. Race. An Atomistic Modelling Study of the Properties of Dislocation Loops in Zirconium. *Journal of Nuclear Materials*, 546:152752, April 2021.

[167] Alexandre Mussi, Ahmed Addad, and Fabien Onimus. Dislocation electron tomography: A technique to characterize the dislocation microstructure evolution in zirconium alloys under irradiation. *Acta Materialia*, 213:116964, 2021.

[168] R Madec, B Devincre, and L. P Kubin. On the nature of attractive dislocation crossed states. *Computational Materials Science*, 23(1):219–224, April 2002.

[169] Ladislas P. Kubin, Ronan Madec, and Benoit Devincre. Dislocation Intersections and Reactions in FCC and BCC Crystals. *MRS Online Proceedings Library (OPL)*, 779:W1.6, January 2003.

[170] L. Capolungo. Dislocation junction formation and strength in magnesium. *Acta Materialia*, 59(8):2909–2917, May 2011.

[171] Chi-Chin Wu, Sylvie Aubry, Peter W. Chung, and Athanasius Arsenlis. Dislocation Dynamics Simulations of Junctions in Hexagonal Close-Packed Crystals. *MRS Online Proceedings Library*, 1424(1):67–72, December 2012.

[172] C. C. Wu, P. W. Chung, S. Aubry, L. B. Munday, and A. Arsenlis. The strength of binary junctions in hexagonal close-packed crystals. *Acta Materialia*, 61(9):3422–3431, May 2013.

[173] B. Devincre. Dislocation dynamics simulations of slip systems interactions and forest strengthening in ice single crystal. *Philosophical Magazine*, 93(1-3):235–246, January 2013. Publisher: Taylor & Francis _eprint: https://doi.org/10.1080/14786435.2012.699689.

[174] Ryan B. Sills, Nicolas Bertin, Amin Aghaei, and Wei Cai. Dislocation Networks and the Microstructural Origin of Strain Hardening. *Physical Review Letters*, 121(8):085501, August 2018. Publisher: American Physical Society.

[175] S. Naka, Lasalmonie , A., Costa , P., , and L. P. Kubin. The low-temperature plastic deformation of α-titanium and the core structure of a-type screw dislocations. *Philosophical Magazine A*, 57(5):717–740, May 1988. Publisher: Taylor & Francis _eprint: https://doi.org/10.1080/01418618808209916.

[176] N. Bertin, C. N. Tomé, I. J. Beyerlein, M. R. Barnett, and L. Capolungo. On the strength of dislocation interactions and their effect on latent hardening in pure Magnesium. *International Journal of Plasticity*, 62:72–92, November 2014.

[177] Hussein M. Zbib and Tomas Diaz de la Rubia. A multiscale model of plasticity. *International Journal of Plasticity*, 18(9):1133 – 1163, 2002.

[178] L. Capolungo, I. J. Beyerlein, and Z. QWang. The role of elastic anisotropy on plasticity in hcp metals: a three-dimensional dislocation dynamics study. *Modelling and Simulation in Materials Science and Engineering*, 18(8):085002, October 2010. Publisher: IOP Publishing.

[179] Haidong Fan, Sylvie Aubry, A. Arsenlis, and Jaafar A. El-Awady. Orientation influence on grain size effects in ultrafine-grained magnesium. *Scripta Materialia*, 97:25–28, March 2015.

[180] Haidong Fan, Sylvie Aubry, Athanasios Arsenlis, and Jaafar A. El-Awady. Grain size effects on dislocation and twinning mediated plasticity in magnesium. *Scripta Materialia*, 112:50–53, February 2016.

[181] M. R. Barnett, Z. Keshavarz, A. G. Beer, and D. Atwell. Influence of grain size on the compressive deformation of wrought Mg–3Al–1Zn. *Acta Materialia*, 52(17):5093–5103, October 2004.

[182] Yang Li, Sabyasachi Chatterjee, Enrique Martinez, Nasr Ghoniem, and Giacomo Po. On the cross-slip of screw dislocations in zirconium. *Acta Materialia*, 208:116764, April 2021.

[183] Luca Reali, Mark R Wenman, Adrian P Sutton, and Daniel S Balint. Plasticity of zirconium hydrides: a coupled edge and screw discrete dislocation model. *Journal of the Mechanics and Physics of Solids*, 147:104219, 2021.

[184] Luca Reali, Daniel S. Balint, Adrian P. Sutton, and Mark R. Wenman. Plastic relaxation and solute segregation to β-Nb second phase particles in Zr-Nb alloys: A discrete dislocation plasticity study. *Journal of the Mechanics and Physics of Solids*, 156:104581, November 2021.

[185] Luca Reali, Daniel S. Balint, and Mark R. Wenman. Dislocation modelling of the plastic relaxation and thermal ratchetting induced by zirconium hydride

precipitation. *Journal of the Mechanics and Physics of Solids*, 167:104988, October 2022.

[186] Jaime Marian, Steve Fitzgerald, and Giacomo Po. *Discrete Dislocation Dynamics Simulations of Irradiation Hardening in Nuclear Materials*, pages 1–29. Springer International Publishing, Cham, 2018.

[187] Thomas Nogaret, David Rodney, Marc Fivel, and Christian Robertson. Clear band formation simulated by dislocation dynamics: Role of helical turns and pile-ups. *Journal of Nuclear Materials*, 380(1):22–29, October 2008.

[188] K. Gururaj and C. Robertson. Plastic Deformation in ODS Ferritic Alloys: A 3D Dislocation Dynamics Investigation. *Energy Procedia*, 7:279–285, January 2011.

[189] K. Gururaj, Robertson , C., , and M. Fivel. Channel formation and multiplication in irradiated FCC metals: a 3D dislocation dynamics investigation. *Philosophical Magazine*, 95(12):1368–1389, April 2015. Publisher: Taylor & Francis _eprint: https://doi.org/10.1080/14786435.2015.1029560.

[190] Yinan Cui, Nasr Ghoniem, and Giacomo Po. Plasticity of irradiated materials at the nano and micro-scales. *Journal of Nuclear Materials*, 546:152746, April 2021.

[191] Yinan Cui, Giacomo Po, and Nasr Ghoniem. Suppression of Localized Plastic Flow in Irradiated Materials. *Scripta Materialia*, 154:34–39, September 2018.

[192] Bruce Bromage. *Dislocation Based Modelling of Engineering Alloys*. PhD thesis, University of Oxford, 2022.

[193] J.P. Hirth and J. Lothe. *Theory of Dislocations*. A Wiley-Interscience publication. Wiley, 1982.

[194] Wei Cai, Athanasios Arsenlis, Christopher R. Weinberger, and Vasily V. Bulatov. A non-singular continuum theory of dislocations. *Journal of the Mechanics and Physics of Solids*, 54(3):561 – 587, 2006.

[195] R. Bullough and E. A. J. Foreman. The elastic energy of a rhombus-shaped dislocation loop. *The Philosophical Magazine: A Journal of Theoretical Experimental and Applied Physics*, 9(98):315–329, 1964.

[196] Emmanuel Clouet. Elastic energy of a straight dislocation and contribution from core tractions. *Philosophical Magazine*, 89(19):1565–1584, July 2009. Publisher: Taylor & Francis _eprint: https://doi.org/10.1080/14786430902976794.

[197] D. Hull and D.J. Bacon. *Introduction to Dislocations*. Materials science and technology. Elsevier Science, 2011.

[198] H. B. Huntington, J. E. Dickey, and Robb Thomson. Dislocation Energies in NaCl. *Physical Review*, 100(4):1117–1128, November 1955. Publisher: American Physical Society.

[199] X. W. Zhou, R. B. Sills, D. K. Ward, and R. A. Karnesky. Atomistic calculations of dislocation core energy in aluminium. *Physical Review B*, 95(5):054112, February 2017. Publisher: American Physical Society.

[200] J. P Hirth. Some current topics in dislocation theory. *Acta Materialia*, 48(1):93–104, January 2000.

[201] Charles H Henager and Richard G Hoagland. Dislocation core fields and forces in FCC metals. *Scripta Materialia*, 50(7):1091–1095, April 2004.

[202] C. H. Henager Jr., , and R. G. Hoagland. Dislocation and stacking fault core fields in fcc metals. *Philosophical Magazine*, 85(36):4477–4508, December 2005. Publisher: Taylor & Francis _eprint: https://doi.org/10.1080/14786430500300181.

[203] B A Szajewski, F Pavia, and W A Curtin. Robust atomistic calculation of dislocation line tension. *Modelling and Simulation in Materials Science and Engineering*, 23(8):085008, October 2015. Publisher: IOP Publishing.

[204] S P Fitzgerald and S Aubry. Self-force on dislocation segments in anisotropic crystals. *Journal of Physics: Condensed Matter*, 22(29):295403, July 2010.

[205] Yi Hu, B A Szajewski, D Rodney, and W A Curtin. Atomistic dislocation core energies and calibration of non-singular discrete dislocation dynamics. *Modelling and Simulation in Materials Science and Engineering*, 28(1):015005, November 2019. Publisher: IOP Publishing.

[206] V.V. Bulatov, V. Bulatov, and W. Cai. *Computer Simulations of Dislocations*. Osmm Series. OUP Oxford, 2006.

[207] A. N. Gulluoglu, D. J. Srolovitz, R. LeSar, and P. S. Lomdahl. Dislocation distributions in two dimensions. *Scripta Metallurgica*, 23(8):1347–1352, August 1989.

[208] Josh Barnes and Piet Hut. A hierarchical O(N log N) force-calculation algorithm. *Nature*, 324(6096):446–449, December 1986. Publisher: Nature Publishing Group.

[209] Susanne Pfalzner and Paul Gibbon. *Many-Body Tree Methods in Physics*. Cambridge University Press, 1996.

[210] V Rokhlin. Rapid solution of integral equations of classical potential theory. *Journal of Computational Physics*, 60(2):187–207, September 1985.

[211] J. Carrier, L. Greengard, and V. Rokhlin. A Fast Adaptive Multipole Algorithm for Particle Simulations. *SIAM Journal on Scientific and Statistical Computing*, 9(4):669–686, July 1988. Publisher: Society for Industrial and Applied Mathematics.

[212] Leslie Greengard and Vladimir Rokhlin. A new version of the Fast Multipole Method for the Laplace equation in three dimensions. *Acta Numerica*, 6:229–269, January 1997. Publisher: Cambridge University Press.

[213] H. Y. Wang and R. Lesar. O(N) algorithm for dislocation dynamics. *Philosophical Magazine A*, 71(1):149–164, January 1995. Publisher: Taylor & Francis _eprint: https://doi.org/10.1080/01418619508242962.

[214] Degang Zhao, Jingfang Huang, and Yang Xiang. A new version fast multipole method for evaluating the stress field of dislocation ensembles. *Modelling and Simulation in Materials Science and Engineering*, 18(4):045006, June 2010.

[215] Pierre Blanchard, Olivier Coulaud, Arnaud Etcheverry, Laurent Dupuy, and Eric Darve. An Efficient Interpolation Based FMM for Dislocation Dynamics Simulations. In *Platform for Advanced Scientific Computing*, Lausanne, Switzerland, June 2016. USI and CSCS and EPFL.

[216] J. P. Hirth, T. Jo/ssang, and J. Lothe. Dislocation Energies and the Concept of Line Tension. *Journal of Applied Physics*, 37(1):110–116, January 1966.

[217] E. Orowan. Problems of plastic gliding. *Proceedings of the Physical Society*, 52(1):8, January 1940.

[218] J. P. Hirth, H. M. Zbib, and J. Lothe. Forces on high velocity dislocations. *Modelling and Simulation in Materials Science and Engineering*, 6(2):165, March 1998.

[219] I. I. Novikov, V. V. Roshchupkin, M. M. Lyakhovitskii, M. A. Pokrasin, N. A. Minina, A. I. Chernov, N. L. Sobol', A. G. Kol'tsov, and S. A. Klimenko. Investigation of the acoustic properties of zirconium. *Inorganic Materials: Applied Research*, 5(2):184–188, March 2014.

[220] Beñat Gurrutxaga–Lerma, Jonas Verschueren, Adrian P. Sutton, and Daniele Dini. The mechanics and physics of high-speed dislocations: a critical review. *International Materials Reviews*, 66(4):215–255, May 2021. Publisher: Taylor & Francis _eprint: https://doi.org/10.1080/09506608.2020.1749781.

[221] Beñat Gurrutxaga-Lerma, Daniel S. Balint, Daniele Dini, Daniel E. Eakins, and Adrian P. Sutton. Chapter Two - Dynamic Discrete Dislocation Plasticity. In Stéphane P. A. Bordas, editor, *Dynamic Discrete Dislocation Plasticity*, volume 47 of *Advances in Applied Mechanics*, pages 93–224. Elsevier, 2014. ISSN: 0065-2156.

[222] Junjie Yang, Ali Rida, Yejun Gu, Daniel Magagnosc, Tamer A. Zaki, and Jaafar A. El-Awady. The three-dimensional elastodynamic solution for dislocation plasticity and its implementation in discrete dislocation dynamics simulations. *Acta Materialia*, 253:118945, July 2023.

[223] Wei Cai and Vasily V. Bulatov. Mobility laws in dislocation dynamics simulations. *Materials Science and Engineering: A*, 387-389:277–281, 2004. 13th International Conference on the Strength of Materials.

[224] Jaehyun Cho, Jean-François Molinari, and Guillaume Anciaux. Mobility law of dislocations with several character angles and temperatures in FCC aluminum. *International Journal of Plasticity*, 90:66–75, March 2017.

[225] Giacomo Po, Yinan Cui, David Rivera, David Cereceda, Tom D. Swinburne, Jaime Marian, and Nasr Ghoniem. A phenomenological dislocation mobility law for bcc metals. *Acta Materialia*, 119:123–135, 2016.

[226] Sergei Starikov and Vasily Tseplyaev. Two-scale simulation of plasticity in molybdenum: Combination of atomistic simulation and dislocation dynamics

with non-linear mobility function. *Computational Materials Science*, 179:109585, 2020.

[227] Ladislas P. Kubin, G. Canova, M. Condat, Benoit Devincre, V. Pontikis, and Yves Bréchet. Dislocation Microstructures and Plastic Flow: A 3D Simulation. *Solid State Phenomena*, 23-24:455–472, 1992. Publisher: Trans Tech Publications Ltd.

[228] Fengxian Liu, Alan C. F. Cocks, and Edmund Tarleton. A new method to model dislocation self-climb dominated by core diffusion. *Journal of the Mechanics and Physics of Solids*, 135:103783, February 2020.

[229] Fengxian Liu, Alan C. F. Cocks, Simon P. A. Gill, and Edmund Tarleton. An improved method to model dislocation self-climb. *Modelling and Simulation in Materials Science and Engineering*, 28(5):055012, June 2020. Publisher: IOP Publishing.

[230] Fengxian Liu, Alan C. F. Cocks, and Edmund Tarleton. Dislocation climb driven by lattice diffusion and core diffusion. *Journal of the Mechanics and Physics of Solids*, 176:105300, July 2023.

[231] W.H. Press, S.A. Teukolsky, W.T. Vetterling, and B.P. Flannery. *Numerical Recipes with Source Code CD-ROM 3rd Edition: The Art of Scientific Computing*. Numerical Recipes: The Art of Scientific Computing. Cambridge University Press, 2007.

[232] D. Weygand, L. H. Friedman, E. Van der Giessen, and A. Needleman. Aspects of boundary-value problem solutions with three-dimensional dislocation dynamics. *Modelling and Simulation in Materials Science and Engineering*, 10(4):437, June 2002.

[233] Ryan B. Sills and Wei Cai. Efficient time integration in dislocation dynamics. *Modelling and Simulation in Materials Science and Engineering*, 22(2):025003, January 2014. Publisher: IOP Publishing.

[234] D. J. Gardner, C. S. Woodward, D. R. Reynolds, G. Hommes, S. Aubry, and A. Arsenlis. Implicit integration methods for dislocation dynamics. *Modelling and Simulation in Materials Science and Engineering*, 23(2):025006, January 2015. Publisher: IOP Publishing.

[235] Ryan B. Sills, Amin Aghaei, and Wei Cai. Advanced time integration algorithms for dislocation dynamics simulations of work hardening. *Modelling and Simulation in Materials Science and Engineering*, 24(4):045019, April 2016. Publisher: IOP Publishing.

[236] N Bertin, S Aubry, A Arsenlis, and W Cai. GPU-accelerated dislocation dynamics using subcycling time-integration. *Modelling and Simulation in Materials Science and Engineering*, 27(7):075014, October 2019.

[237] Daniel Celis Garza. *Dislocation Based Modelling of Fusion Relevant Materials*. PhD thesis, University of Oxford, 2021.

[238] J. Erickson. *Algorithms*. Jeff Erickson, 2019.

[239] M.H. Yoo. c + a dislocation reactions in h.c.p. metals. *Scripta Metallurgica*, 2(10):537–540, 1968.

[240] M. H. Yoo, J. R. Morris, K. M. Ho, and S. R. Agnew. Nonbasal deformation modes of HCP metals and alloys: Role of dislocation source and mobility. *Metallurgical and Materials Transactions A*, 33(3):813–822, March 2002.

[241] Zhaoxuan Wu and W. A. Curtin. Mechanism and energetics of $\langle$c + a$\rangle$ dislocation cross-slip in hcp metals. *Proceedings of the National Academy of Sciences*, 113(40):11137–11142, October 2016. Publisher: Proceedings of the National Academy of Sciences.

[242] M. Verdier, M. Fivel, and I. Groma. Mesoscopic scale simulation of dislocation dynamics in fcc metals: Principles and applications. *Modelling and Simulation in Materials Science and Engineering*, 6(6):755, November 1998.

[243] M. C. Fivel and G. R. Canova. Developing rigorous boundary conditions to simulations of discrete dislocation dynamics. *Modelling and Simulation in Materials Science and Engineering*, 7(5):753, September 1999.

[244] C. Lemarchand, B. Devincre, and L.P. Kubin. Homogenization method for a discrete-continuum simulation of dislocation dynamics. *Journal of the Mechanics and Physics of Solids*, 49(9):1969 – 1982, 2001. The JW Hutchinson and JR Rice 60th Anniversary Issue.

[245] A. Vattré, B. Devincre, F. Feyel, R. Gatti, S. Groh, O. Jamond, and A. Roos. Modelling crystal plasticity by 3d dislocation dynamics and the finite element method: The discrete-continuous model revisited. *Journal of the Mechanics and Physics of Solids*, 63:491 – 505, 2014.

[246] Yinan Cui, Zhanli Liu, and Zhuo Zhuang. Quantitative investigations on dislocation based discrete-continuous model of crystal plasticity at submicron scale. *International Journal of Plasticity*, 69:54 – 72, 2015.

[247] O. Jamond, R. Gatti, A. Roos, and B. Devincre. Consistent formulation for the Discrete-Continuous Model: Improving complex dislocation dynamics simulations. *International Journal of Plasticity*, 80:19–37, May 2016.

[248] O.C. Zienkiewicz and R.L. Taylor. *The Finite Element Method for Solid and Structural Mechanics*. The Finite Element Method. Butterworth-Heinemann, 2013.

[249] B. Bromage and E. Tarleton. Calculating dislocation displacements on the surface of a volume. *Modelling and Simulation in Materials Science and Engineering*, 26(8):085007, October 2018. Publisher: IOP Publishing.

[250] S Queyreau, J Marian, B D Wirth, and A Arsenlis. Analytical integration of the forces induced by dislocations on a surface element. *Modelling and Simulation in Materials Science and Engineering*, 22(3):035004, February 2014. Publisher: IOP Publishing.

[251] Roland de Wiť. The Continuum Theory of Stationary Dislocations*. In Frederick Seitz and David Turnbull, editors, *Solid State Physics*, volume 10, pages 249–292. Academic Press, January 1960.

[252] D. M. Barnett. The displacement field of a triangular dislocation loop. *Philosophical Magazine A*, 51(3):383–387, March 1985. Publisher: Taylor & Francis _eprint: https://doi.org/10.1080/01418618508237562.

[253] D. M. Barnett and R. W. Balluffi. The displacement field of a triangular dislocation loop–a correction with commentary. *Philosophical Magazine Letters*, 87(12):943–944, December 2007. Publisher: Taylor & Francis _eprint: https://doi.org/10.1080/09500830701601748.

[254] Marc Fivel and Christophe Depres. An easy implementation of displacement calculations in 3D discrete dislocation dynamics codes. *Philosophical Magazine*, 94(28):3206–3214, October 2014. Publisher: Taylor & Francis _eprint: https://doi.org/10.1080/14786435.2014.949326.

[255] Triplicane A. Parthasarathy, Satish I. Rao, Dennis M. Dimiduk, Michael D. Uchic, and Dallas R. Trinkle. Contribution to size effect of yield strength from the stochastics of dislocation source lengths in finite samples. *Scripta Materialia*, 56(4):313–316, February 2007.

[256] Jaafar A. El-Awady, Ming Wen, and Nasr M. Ghoniem. The role of the weakest-link mechanism in controlling the plasticity of micropillars. *Journal of the Mechanics and Physics of Solids*, 57(1):32–50, January 2009.

[257] D. Hull and D.J. Bacon. 6 - Dislocations in Other Crystal Structures. In D. Hull and D.J. Bacon, editors, *Introduction to Dislocations (Fifth Edition)*, pages 109 – 136. Butterworth-Heinemann, Oxford, fifth edition, 2011.

[258] J. P. Hirth and J. Lothe. GLIDE OF JOGGED DISLOCATIONS. *Canadian Journal of Physics*, 45(2):809–826, February 1967.

[259] Wei Cai, Vasily V. Bulatov, Jinpeng Chang, Ju Li, and Sidney Yip. Chapter 64 - dislocation core effects on mobility. In F.R.N. Nabarro and J.P. Hirth, editors, *Dislocations in Solids*, volume 12 of *Dislocations in Solids*, pages 1–80. Elsevier, 2004.

[260] Emmanuel Clouet. Predicting dislocation climb: Classical modeling versus atomistic simulations. *Physical Review B*, 84(9):092106, September 2011. Publisher: American Physical Society.

[261] Aaron A. Kohnert and Laurent Capolungo. The kinetics of static recovery by dislocation climb. *npj Computational Materials*, 8(1):104, May 2022.

[262] Yang Li, Nasr Ghoniem, Kristopher Baker, Benjamin Ramirez Flores, Thomas Black, James Hollenbeck, and Giacomo Po. A coupled vacancy diffusion-dislocation dynamics model for the climb-glide motion of jogged screw dislocations. *Acta Materialia*, 244:118546, January 2023.

[263] H Strunk and R Frydman. Jog dragging in edge dislocations with application to plastic deformation and internal friction. *Materials Science and Engineering*, 18(1):143–148, March 1975.

[264] A. K. Cline, C. B. Moler, G. W. Stewart, and J. H. Wilkinson. An estimate for the condition number of a matrix. *SIAM Journal on Numerical Analysis*, 16(2):368–375, 1979.

[265] R. Tyrrell Rockafellar. *Convex Analysis*. Princeton University Press, 1970.

[266] S. D. Gavazza and D. M. Barnett. The self-force on a planar dislocation loop in an anisotropic linear-elastic medium. *Journal of the Mechanics and Physics of Solids*, 24(4):171–185, August 1976.

[267] G. J. O. Jameson. Inequalities for the perimeter of an ellipse. *The Mathematical Gazette*, 98(542):227–234, 2014. Publisher: The Mathematical Association.

[268] J. A. Carrillo, J. Mateu, M. G. Mora, L. Rondi, L. Scardia, and J. Verdera. The ellipse law: Kirchhoff meets dislocations, March 2017. arXiv:1703.07013.

[269] J. Mateu, M. G. Mora, L. Rondi, L. Scardia, and J. Verdera. Energy minimisers of perturbed dislocation energies. *Nonlinear Analysis*, 231:113014, June 2023.

[270] Peter J Cameron. *Introduction to Algebra*. Oxford University Press, 01 1997.

[271] Yang Xiang, Li-Tien Cheng, David J. Srolovitz, and Weinan E. A level set method for dislocation dynamics. *Acta Materialia*, 51(18):5499–5518, October 2003.

[272] S. S. Quek, Y. Xiang, Y. W. Zhang, D. J. Srolovitz, and C. Lu. Level set simulation of dislocation dynamics in thin films. *Acta Materialia*, 54(9):2371–2381, May 2006.

[273] Jun Pan and Yoji Shibutani. Formation of Prismatic Dislocation Loop around a Spherical Inclusion Using Level Set Dislocation Dynamics. *Journal of Solid Mechanics and Materials Engineering*, 6:913–924, January 2012. ADS Bibcode: 2012JSMME...6..913P.

[274] R. Tyrrell Rockafellar and Roger J.-B. Wets. *Variational Analysis*. Springer Verlag, Heidelberg, Berlin, New York, 1998.

[275] T.A. Khraishi, J.P. Hirth, H.M. Zbib, and M.A. Khaleel. The displacement, and strain–stress fields of a general circular volterra dislocation loop. *International Journal of Engineering Science*, 38(3):251–266, 2000.

[276] H.M. Zbib T.A. Khraishi, J.P. Hirth and T. Diaz de La Rubia. The stress field of a general circular volterra dislocation loop: Analytical and numerical approaches. *Philosophical Magazine Letters*, 80(2):95–105, 2000.

[277] F. Kroupa. Circular edge dislocation loop. *Cechoslovackij fiziceskij zurnal B*, 10(4):284–293, Apr 1960.

[278] P. Kroupa. The interaction between prismatic dislocation loops and straight dislocations. part i. *The Philosophical Magazine: A Journal of Theoretical Experimental and Applied Physics*, 7(77):783–801, 1962.

[279] JJ Gilman. Influence of dislocation dipoles on physical properties. *Discussions of the Faraday Society*, 38:123–137, 1964.

[280] F Kroupa. DISLOCATION DIPOLES AND DISLOCATION LOOPS. *J. Phys., Colloq.*, 27(C3):C3–154–C3–167, July 1966.

[281] N.M. Ghoniem, S.H. Tong, B.N. Singh, and L.Z. Sun. On dislocation interaction with radiation-induced defect clusters and plastic flow localization in fcc metals. *Phil. Mag. A*, 81:2743–2764, 2001.

[282] Z. Rong, V. Mohles, D.J. Bacon *, and Yu. N. Osetsky. Dislocation dynamics modelling of dislocation–loop interactions in irradiated metals. *Philosophical Magazine*, 85(2-3):171–188, January 2005. Publisher: Taylor & Francis _eprint: https://doi.org/10.1080/14786430412331315644.

[283] Z. Rong, Y. N. Osetsky †, and D. J. Bacon *. A model for the dynamics of loop drag by a gliding dislocation. *Philosophical Magazine*, 85(14):1473–1493, May 2005. Publisher: Taylor & Francis _eprint: https://doi.org/10.1080/14786430500036371.

[284] L. K. Wickham, K. W. Schwarz, and J. S. Stölken. Rules for Forest Interactions between Dislocations. *Physical Review Letters*, 83(22):4574–4577, November 1999. Publisher: American Physical Society.

[285] Inc. The MathWorks. *Symbolic Math Toolbox*. Natick, Massachusetts, United State, 2019.

[286] Jasbir S. Chahal. Solution of the cubic. *Resonance*, 11(8):53–61, Aug 2006.

[287] Åke Björck. *Numerical Methods for Least Squares Problems*. Society for Industrial and Applied Mathematics, 1996.

[288] V. A. Lubarda, J. A. Blume, and A. Needleman. An analysis of equilibrium dislocation dislocations. *Acta metall. mater.*, 41(2):625–642, 1993.

[289] Steven P. Fitzgerald and Zhongwen Yao. Shape of prismatic dislocation loops in anisotropic α-Fe. *Philosophical Magazine Letters*, 89(9):581–588, September 2009. Publisher: Taylor & Francis _eprint: https://doi.org/10.1080/09500830903199012.

[290] David Rodney. Atomic modeling of irradiation-induced hardening. *Comptes Rendus Physique*, 9(3-4):418–426, 2008.

[291] R. C. Picu and M. A. Soare. Asymmetric dislocation junctions exhibit a broad range of strengths. *Scripta Materialia*, 62(7):508–511, April 2010.

[292] L. Dupuy and M. C. Fivel. A study of dislocation junctions in FCC metals by an orientation dependent line tension model. *Acta Materialia*, 50(19):4873–4885, November 2002.

[293] F. Kroupa. The force between non-parallel dislocations. *Cechoslovackij fiziceskij zurnal B*, 11(11):847–848, November 1961.

[294] Herbert Edelsbrunner and Ernst P. Mücke. Three-dimensional alpha shapes. *ACM Trans. Graph.*, 13(1):43–72, January 1994.

[295] Markus G. R. Sause. Digital Image Correlation. In Markus G.R. Sause, editor, *In Situ Monitoring of Fiber-Reinforced Composites: Theory, Basic Concepts, Methods, and Applications*, pages 57–129. Springer International Publishing, Cham, 2016.

[296] R. E. Smallman. Plasticity of crystals with special reference to metals by e. schmid and w. boas. *Journal of Applied Crystallography*, 2(3):147–147, 1969.

[297] P Soo and G. T Higgins. The deformation of zirconium-oxygen single crystals. *Acta Metallurgica*, 16(2):177–186, February 1968.

[298] I. G Ritchie and A Atrens. The diffusion of oxygen in alpha-zirconium. *Journal of Nuclear Materials*, 67(3):254–264, August 1977.

[299] F. C. Frank and W. T. Read. Multiplication Processes for Slow Moving Dislocations. *Physical Review*, 79(4):722–723, August 1950. Publisher: American Physical Society.

[300] A. J. E. Foreman. The bowing of a dislocation segment. *The Philosophical Magazine: A Journal of Theoretical Experimental and Applied Physics*, 15(137):1011–1021, May 1967. Publisher: Taylor & Francis _eprint: https://doi.org/10.1080/14786436708221645.

[301] G. Monnet. Investigation of precipitation hardening by dislocation dynamics simulations. *Philosophical Magazine*, 86(36):5927–5941, December 2006. Publisher: Taylor & Francis _eprint: https://doi.org/10.1080/14786430600860985.

[302] H. Tang, K. W. Schwarz, and H. D. Espinosa. Dislocation escape-related size effects in single-crystal micropillars under uniaxial compression. *Acta Materialia*, 55(5):1607–1616, March 2007.

[303] Haiyang Yu, Alan Cocks, and Edmund Tarleton. Discrete dislocation plasticity HELPs understand hydrogen effects in bcc materials. *Journal of the Mechanics and Physics of Solids*, 123:41–60, February 2019.

[304] Haiyang Yu, Alan C. F. Cocks, and Edmund Tarleton. Simulating hydrogen in fcc materials with discrete dislocation plasticity. *International Journal of Hydrogen Energy*, 45(28):14565–14577, May 2020.

[305] C. Motz, D. Weygand, J. Senger, and P. Gumbsch. Initial dislocation structures in 3-D discrete dislocation dynamics and their influence on microscale plasticity. *Acta Materialia*, 57(6):1744–1754, April 2009.

[306] Julia R. Greer, Warren C. Oliver, and William D. Nix. Size dependence of mechanical properties of gold at the micron scale in the absence of strain gradients. *Acta Materialia*, 53(6):1821–1830, April 2005.

[307] Z. W. Shan, Raja K. Mishra, S. A. Syed Asif, Oden L. Warren, and Andrew M. Minor. Mechanical annealing and source-limited deformation in submicrometre-diameter Ni crystals. *Nature Materials*, 7(2):115–119, February 2008.

[308] H. Tang, K. W. Schwarz, and H. D. Espinosa. Dislocation-Source Shutdown and the Plastic Behavior of Single-Crystal Micropillars. *Physical Review Letters*, 100(18):185503, May 2008. Publisher: American Physical Society.

[309] Haidong Fan, Qingyuan Wang, Jaafar A. El-Awady, Dierk Raabe, and Michael Zaiser. Strain rate dependency of dislocation plasticity. *Nature Communications*, 12(1):1845, March 2021. Publisher: Nature Publishing Group.

[310] Jaafar A. El-Awady. Unravelling the physics of size-dependent dislocation-mediated plasticity. *Nature Communications*, 6(1):5926, January 2015. Publisher: Nature Publishing Group.

[311] Jaafar A. El-Awady, S. Bulent Biner, and Nasr M. Ghoniem. A self-consistent boundary element, parametric dislocation dynamics formulation of plastic flow in finite volumes. *Journal of the Mechanics and Physics of Solids*, 56(5):2019–2035, May 2008.

[312] Julia R. Greer and Jeff Th. M. De Hosson. Plasticity in small-sized metallic systems: Intrinsic versus extrinsic size effect. *Progress in Materials Science*, 56(6):654–724, August 2011.

[313] Julia R. Greer and William D. Nix. Nanoscale gold pillars strengthened through dislocation starvation. *Physical Review B*, 73(24):245410, June 2006. Publisher: American Physical Society.

[314] D. M. Norfleet, D. M. Dimiduk, S. J. Polasik, M. D. Uchic, and M. J. Mills. Dislocation structures and their relationship to strength in deformed nickel microcrystals. *Acta Materialia*, 56(13):2988–3001, August 2008.

[315] Michael D. Uchic, Paul A. Shade, and Dennis M. Dimiduk. Plasticity of Micrometer-Scale Single Crystals in Compression. *Annual Review of Materials Research*, 39(Volume 39, 2009):361–386, August 2009. Publisher: Annual Reviews.

[316] V. S. Deshpande, A. Needleman, and E. Van der Giessen. Plasticity size effects in tension and compression of single crystals. *Journal of the Mechanics and Physics of Solids*, 53(12):2661–2691, December 2005.

[317] D S Balint, V S Deshpande, A Needleman, and E Van Der Giessen. Size effects in uniaxial deformation of single and polycrystals: a discrete dislocation plasticity analysis. *Modelling and Simulation in Materials Science and Engineering*, 14(3):409–422, April 2006.

[318] S. Korte and W.J. Clegg. Discussion of the dependence of the effect of size on the yield stress in hard materials studied by microcompression of MgO. *Philosophical Magazine*, 91(7-9):1150–1162, March 2011. Publisher: Taylor & Francis _eprint: https://doi.org/10.1080/14786435.2010.505179.

[319] D. J. Dunstan and A. J. Bushby. The scaling exponent in the size effect of small scale plastic deformation. *International Journal of Plasticity*, 40:152–162, January 2013.

[320] R.G. McQueen, S.P. Marsh, J.W. Taylor, J.N. Fritz, and W.J. Carter. Chapter vii - the equation of state of solids from shock wave studies. In Ray Kinslow, editor, *High-Velocity Impact Phenomena*, pages 293–417. Academic Press, 1970.

[321] Meyrick Hockly and Clive R. Siviour. Specimen Inertia in high strain rate tensile testing. *EPJ Web of Conferences*, 94:01050, 2015. Publisher: EDP Sciences.

[322] Z. Q. Wang, I. J. Beyerlein, and R. Lesar. Dislocation motion in high strain-rate deformation. *Philosophical Magazine*, 87(16):2263–2279, June 2007. Publisher: Taylor & Francis _eprint: https://doi.org/10.1080/14786430601153422.

[323] Z. L. Liu, X. C. You, and Z. Zhuang. A mesoscale investigation of strain rate effect on dynamic deformation of single-crystal copper. *International Journal of Solids and Structures*, 45(13):3674–3687, June 2008.

[324] K. M Jassby and T Vreeland. On the measurement of dislocation damping forces at high dislocation velocity. *Acta Metallurgica*, 20(4):611–615, April 1972.

[325] M. A. Shehadeh *, H. M. Zbib, and T. Diaz De La Rubia. Modelling the dynamic deformation and patterning in fcc single crystals at high strain rates: dislocation dynamics plasticity analysis. *Philosophical Magazine*, 85(15):1667–1685, May 2005. Publisher: Taylor & Francis _eprint: https://doi.org/10.1080/14786430500036470.

[326] Desmond Tromans. Elastic anisotropy of hcp metal crystals and polycrystals. *Int. J. Res. Rev. Appl. Sci.*, 6, 01 2011.

[327] C. A. R. Hoare. Algorithm 64: Quicksort. *Commun. ACM*, 4(7):321, July 1961.

[328] D Mills and G B Craig. Plastic deformation of zirconium–oxygen alloy single crystals in the range 77° to 950°K. *Trans. Met. Soc. AIME, 242: 1881-90(Sept. 1968)*, 12 1967.

[329] Jean-Sébastien Lecomte, Jérôme Crépin, and Pierre Barberis. Critical Resolved Shear Stress and Work Hardening Determination in HCP Metals: Application to Zr Single Crystals. *Metals*, 14(10):1101, October 2024. Number: 10 Publisher: Multidisciplinary Digital Publishing Institute.

[330] Zhang-Jie Wang, Qing-Jie Li, Zhi-Wei Shan, Ju Li, Jun Sun, and Evan Ma. Sample size effects on the large strain bursts in submicron aluminum pillars. *Applied Physics Letters*, 100(7):071906, February 2012.

[331] Ferenc F. Csikor, Christian Motz, Daniel Weygand, Michael Zaiser, and Stefano Zapperi. Dislocation Avalanches, Strain Bursts, and the Problem of Plastic Forming at the Micrometer Scale. *Science*, 318(5848):251–254, October 2007. Publisher: American Association for the Advancement of Science.

[332] Y. N. Cui, P. Lin, Z. L. Liu, and Z. Zhuang. Theoretical and numerical investigations of single arm dislocation source controlled plastic flow in FCC micropillars. *International Journal of Plasticity*, 55:279–292, April 2014.

[333] Yoshikazu Giga. *Surface evolution equations*. Monographs in Mathematics. Birkhauser Verlag AG, Basel, Switzerland, 2006 edition, January 2006.

[334] Yoshikazu Giga and Shun'ichi Goto. Motion of hypersurfaces and geometric equations. *Journal of the Mathematical Society of Japan*, 44(1):99–111, 1992.

[335] N. T. Gridgeman. Lamé Ovals. *The Mathematical Gazette*, 54(387):31–37, 1970. Publisher: Mathematical Association.